ADVANCED PHOTONICS | ADVANCED PHOTONICS NEXUS

Theme Issue on

Optical Orbital Angular Momentum

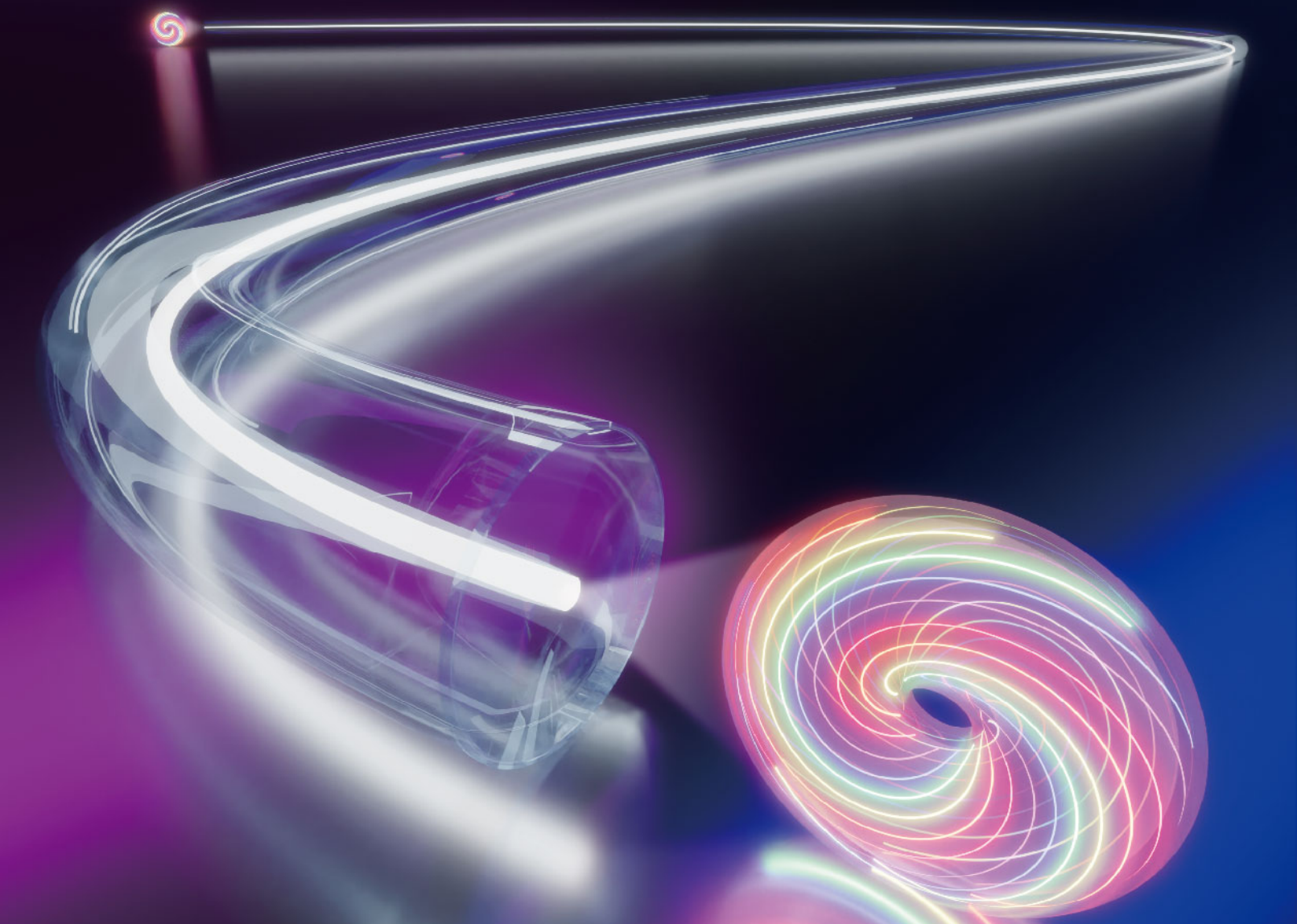

CHINESE LASER PRESS 中国激光杂志社 | SPIE.

CONTENTS

ADVANCED PHOTONICS | ADVANCED PHOTONICS NEXUS

Theme Issue on
Optical Orbital Angular Momentum

On the cover — The image illustrates the propagation of a spatiotemporal optical vortex wavepacket through an optical fiber. This article presents the first demonstration of spatiotemporal optical vortex pulse propagation through a few-mode optical fiber. The authors note that the wavepacket maintains its spatiotemporal phase structure well, demonstrating the new possibility of transmitting transverse orbital angular momentum inside fiber.

CONTENTS

ADVANCED PHOTONICS | ADVANCED PHOTONICS NEXUS

Theme Issue on
Optical Orbital Angular Momentum

SPECIAL EDITORIAL

Optical Orbital Angular Momentum: Thirty Years and Counting

Guixin Li
Southern University of Science and Technology
Shenzhen, China

Junsuk Rho
Pohang University of Science and Technology (POSTECH)
POSCO-POSTECH-RIST Convergence Research Center for Flat Optics and Metaphotonics
Pohang, Republic of Korea

Xiao-Cong Yuan
Shenzhen University
College of Optoelectronics, Nanophotonics Research Center
Shenzhen, China

In 1992, Professor Allen's paper published in *Physical Review A* indicated that laser light with a Laguerre-Gaussian amplitude distribution has an orbital angular momentum (OAM). Since then, conceptual studies on OAM of photons have been attracting continual attention in physics and optics communities. In recent years, we have witnessed the birth and fast development of many break-through technologies driven by the concept of OAM, from advanced light-field manipulation to super-resolution imaging, classical and quantum optical communications, and many others.

In this connection, we are honored to organize a theme issue to pay our respect to Professor Allen for his pioneering study on OAM, as well as the great achievements by other scientists and scholars in this field. This special collection focuses on optical orbital angular momentum and its role in optical science and applications. One review article and nine original ones are assembled in *Advanced Photonics* and its sister journal *Advanced Photonics Nexus*. The topics of these contributions include torsion pendulum driven by OAM of light, time-varying OAM, optical interconnects for OAM modes, retrieval of OAM spectrum, free-electron lasers for OAM generation, reconfigurable structured light modes, OAM multiplexed optical holography, phase aperture for transforming vortex beam, and OAM modes in a Janus optical parametric oscillator.

We hope the readers, whether early career or established scientists, will enjoy the collection of articles in this joint theme issue and find them helpful and inspiring.

A list of the articles is provided here:

- Torsion pendulum driven by the angular momentum of light: Beth's legacy continues, Etienne Brasselet, University of Bordeaux, CNRS
- Generation of time-varying orbital angular momentum beams with space-time-coding digital metasurface, Jensen Li, Hong Kong University of Science and Technology
- Propagation of transverse photonic orbital angular momentum through few-mode fiber, Qiwen Zhan, University of Shanghai for Science and Technology
- Tailoring light on three-dimensional photonic chips: a platform for versatile OAM mode optical interconnects, Jian Wang, Huazhong University of Science and Technology
- Single-shot Kramers–Kronig complex orbital angular momentum spectrum retrieval, Siyuan Yu, Sun Yat-sen University
- Self-seeded free-electron lasers with orbital angular momentum, Gianluca Geloni, European XFEL GmbH
- Reconfigurable structured light generation and its coupling to air–core fiber, Jian Wang, Huazhong University of Science and Technology
- Multiparameter encrypted orbital angular momentum multiplexed holography based on multiramp helicoconical beams, Xiao Yuan, Soochow University
- Characteristics of a Gaussian focus embedded within spiral patterns in common-path interferometry with phase apertures, Ying Gu, Chinese PLA General Hospital
- Generation of high-efficiency, high-purity, and broadband Laguerre-Gaussian modes from a Janus optical parametric oscillator, Yong Zhang, Nanjing University; Min Xiao, Nanjing Univ./Univ. of Arkansas

COMMENTARY

Advent of torsional optomechanics from Beth's legacy

Jaehyuck Jang,[a] Jungho Mun,[b] and Junsuk Rho[a,b,c,*]
[a]Pohang University of Science and Technology (POSTECH), Department of Chemical Engineering, Pohang, Republic of Korea
[b]Pohang University of Science and Technology (POSTECH), Department of Mechanical Engineering, Pohang, Republic of Korea
[c]POSCO-POSTECH-RIST Convergence Research Center for Flat Optics and Metaphotonics, Pohang, Republic of Korea

Torsional optomechanics, which involves the transfer of angular momentum from light to matter, has been a vibrant research area since Beth's pioneering contribution in 1935. Beth proposed a method to measure the transfer of spin angular momentum using a torsional pendulum,[1] laying the foundation for classical and quantum optomechanics related to particle levitation, trapping, and cooling in modern optics.[2]

In the article recently published in *Advanced Photonics*, Brasselet reviewed the Beth's discovery legacy and looked how this idea has continued over the years.[3] Beth successfully detected the spin angular momentum of light using a torsion pendulum consisting of half-wave plates and a mirror.[1] Years later, Carrara proposed a modified configuration making the detection easier by introducing the system in the microwave domain.[4] In 1966, Allen devised an experimental setup with a drop-suspended aluminum dipole hanging on a support, enclosed by a circular waveguide.[5] The rotation of the dipole was measured by monitoring the rotational spectral shift of dipole radiation. This optically induced rotation is now considered as a cornerstone of optical tweezers. In 1992, Allen et al. conducted an orbital analog of the spin experiment by Beth, measuring the mechanical torque induced by the transfer of orbital angular momentum from a paraxial Laguerre-Gaussian beam to a suspended pair of cylindrical lenses.[6] In 2007, Battacharya and Meystre achieved the quantization of a vibrational and rotational mode of a classical oscillator through angular momentum transfer,[7] which is an important contribution to the field of quantum optomechanics.

Beth's accomplishment a century ago has directly or indirectly influenced various fields, including classical and quantum optomechanics, spin-orbit interactions, as well as acoustomechanics (Fig. 1). Torsional optomechanics, driven by the exchange of orbital angular momentum, has been actively investigated in recent days, particularly with the advent of the field of optical vortices.[8] Cavity quantum optomechanics offers a potential playground for exploring the fundamental principles of quantum mechanics in macroscopic systems, with potential applications in highly sensitive devices for detecting forces, displacements, and other physical quantities.[9] With the advent of optical vortices with orbital angular momentum,[6,8] the spin and orbital parts of angular momentum have been distinguished, and their interplay, or the optical spin-orbit interactions, have been actively investigated[10] for spin and orbital Hall effect of light, spin-orbit conversion, and chiral sensing. Similarly, exchanges of angular momentum were found in acoustics,[11,12] and the spin part of angular momentum of acoustics has recently been noted.[13] Recently, there has been investigation into the torsional dynamics driven by acoustic radiation torque.[11] Wireless torsional mechanics driven by acoustic fields has been applied to ultrasound elastography and viscoelastic tensor imaging.[12] Additionally, recent studies in acoustomechanics hold promise for the development of new imaging technologies in metrology and biomedical imaging.[12] The detailed overviews and perspectives on these fields can be found in Brasselet's article.[3] In conclusion, we would like to quote Brasselet, who aptly states that "Beth's legacy is not yet over." As such, Beth's pioneering contribution continues to bloom as it has for over a century.

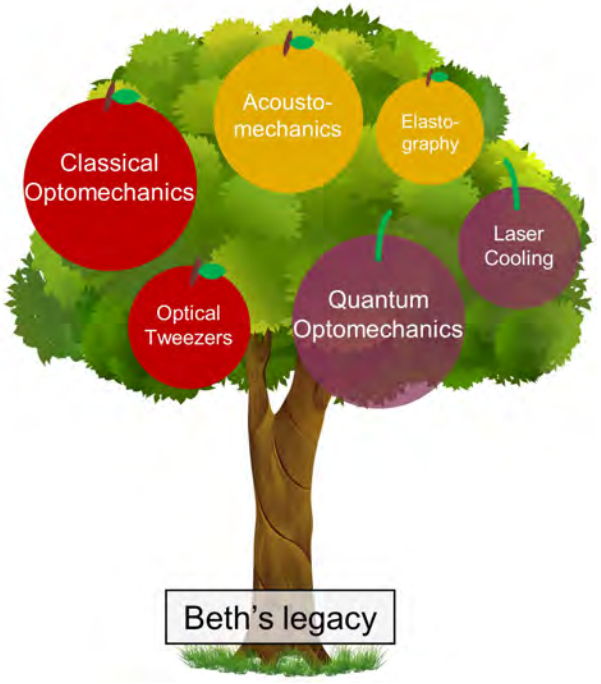

Fig. 1 Illustration of the impact of Beth's accomplishment on diverse fields.

Acknowledgments

This work was financially supported by the POSCO-POSTECHRIST Convergence Research Center program funded by POSCO, and the National Research Foundation (NRF) grant (NRF2022M3C1A3081312) funded by the Ministry of Science and ICT (MSIT) of the Korean government. J.J. acknowledges the NRF Sejong Science fellowship (NRF-RS-2023-00209560) funded by the Ministry of Science and ICT (MSIT) of the Korean government. J.M. acknowledges the POSTECH PIURI postdoctoral fellowship, and the NRF *Sejong* Science fellowship funded by the MSIT of the Korean government.

References

1. R. A. Beth, "Direct detection of the angular momentum of light," *Phys. Rev.* **48**(5), 471–471 (1935).
2. E. Collin, "Mesoscopic quantum thermo-mechanics: a new frontier of experimental physics," *AVS Quantum Sci.* **4**(2), 020501 (2022).
3. E. Brasselet, "Torsion pendulum driven by the angular momentum of light: Beth's legacy continues," *Adv. Photonics* **5**(3), 034003 (2023).
4. N. Carrara, "Torque and angular momentum of centimetre electromagnetic waves," *Nature* **164**(4177), 882–884 (1949).

*Address all correspondence to Junsuk Rho, jsrho@postech.ac.kr

5. P. J. Allen, "A radiation torque experiment," *Am. J. Phys.* **34**(12), 1185–1192 (1966).
6. L. Allen et al., "Orbital angular momentum of light and the transformation of Laguerre-Gaussian laser modes," *Phys. Rev. A* **45**(11), 8185–8189 (1992).
7. M. Bhattacharya and P. Meystre, "Using a Laguerre-Gaussian beam to trap and cool the rotational motion of a mirror," *Phys. Rev. Lett.* **99**(15), 153603 (2007).
8. Y. Shen et al., "Optical vortices 30 years on: OAM manipulation from topological charge to multiple singularities," *Light Sci. Appl.* **8**(1), 90 (2019).
9. A. Pontin et al., "Simultaneous cavity cooling of all six degrees of freedom of a levitated nanoparticle," *Nat. Phys.*, in press (2023).
10. K. Y. Bliokh et al., "Spin-orbit interactions of light," *Nat. Photonics* **9**(12), 796–808 (2015)
11. K. Volke-Sepúlveda, A. O. Santillán, and R. R. Boullosa, "Transfer of angular momentum to matter from acoustical vortices in free space," *Phys. Rev. Lett.* **100**(2), 024302 (2008).
12. N. Jiménez, J. M. Benlloch, and F. Camarena, "A new elastographic technique using acoustic vortices," in *IEEE Int. Ultrason. Symp.*, IEEE, pp. 1–4 (2020).
13. K. Y. Bliokh and F. Nori, "Spin and orbital angular momenta of acoustic beams," *Phys. Rev. B* **99**(17), 174310 (2019)

Jaehyuck Jang is a postdoctoral fellow in Chemical Engineering at Pohang University of Science and Technology (POSTECH). His research interests include planar optics and its applications for next-generation displays, high-*Q* optical resonators, and light-matter interactions between resonators and quantum emitters.

Jungho Mun is a POSTECH PIURI postdoctoral fellow in Mechanical Engineering at POSTECH. His current research interests include sub-wavelength electromagnetics, scattering, structured lights, and meta-optics.

Junsuk Rho is a Mu-Eun-Jae Endowed Chair Associate Professor and Young Distinguished Professor with a joint appointment in Mechanical Engineering and Chemical Engineering at POSTECH. He received his BS (2007) and MS (2008) degrees in Mechanical Engineering from Seoul National University and the University of Illinois, Urbana-Champaign, respectively. After getting his PhD (2013) in mechanical engineering and nanoscale science & engineering from the University of California Berkeley, he worked as a postdoctoral fellow in the Materials Sciences Division at Lawrence Berkeley National Laboratory and was an Ugo Fano Fellow in the Nanoscience and Technology Division at Argonne National Laboratory.

Review Article

ADVANCED PHOTONICS

Torsion pendulum driven by the angular momentum of light: Beth's legacy continues

Etienne Brasselet*
University of Bordeaux, CNRS, Laboratoire Ondes et Matière d'Aquitaine, Talence, France

Abstract. The optical angular momentum is ubiquitous to the science of light, especially whenever the polarization state and the spatial distribution of the phase are involved, which are most often associated with the spin and orbital parts of the total angular momentum, respectively. Notably, the independent introduction of these two contributions to the total optical angular momentum was accompanied by suggestions regarding the possible detection of their mechanical effects using a torsion pendulum. Today, the classical and quantum mechanical aspects of spin and orbital angular momentum of light and their mutual coupling remain active research topics offering exciting perspectives for photonic technologies. Our brief historical overview shows how the torsion pendulum has accompanied scientific advances on mechanical effects based on the angular degrees of freedom of light since Beth's pioneering contribution published in 1935.

Keywords: light; polarization; optical angular momentum; optomechanics.

Received Apr. 18, 2023; accepted for publication Jun. 1, 2023; published online Jun. 30, 2023.

[DOI: 10.1117/1.AP.5.3.034003]

1 Historical Context

The present paper is dedicated to the 30th anniversary of Allen et al.'s paper[1] that kickstarted a fruitful research topic related to the orbital angular momentum of light. Interestingly, the latter work not only identified that a Laguerre–Gaussian paraxial field with azimuthal integer order l carries $l\hbar$ angular momentum per photon of an orbital nature, $\hbar$ being the reduced Planck constant. Inspired by Beth's spin angular momentum experiment,[2] it also suggested a way to detect and measure it using a torsion pendulum equipped with a Laguerre–Gaussian mode converter. This motivates the present aim at highlighting the place taken by the torsion pendulum since the advent of the concept of angular momentum associated with the polarization state of light, which dates back to Sadovskiĭ's work[3] in the late 19th century, according to Vulf'son.[4] The previous motivation is further supported by the fact that, a few years before Sadovskiĭ's work, Righi[5] mentioned an experimental attempt to detect the mechanical effects of circularly polarized waves on matter using a torsion pendulum, yet unsuccessful.

Independently from earlier works from Sadovskiĭ, Poynting conjectured from a mechanical analogy that the torque per unit surface exerted on an absorbing target by a circularly polarized (CP) paraxial light field equals the optical energy per unit volume multiplied by $\lambda/(2\pi)$ with λ the optical wavelength and is oriented along the propagation direction of light.[6] Said differently, noting that the optical energy per unit volume corresponds to the optical pressure, Poynting suggested that the optical torque and force surface densities are proportional with a proportionality factor $\lambda/(2\pi)$, which highlights $\lambda/2\pi$ as the intrinsic lever arm of light. Recalling that the optical energy per unit volume in vacuum is I/c, where I is the optical intensity and c is the speed of light, Poynting thus stated that a paraxial light beam with power P propagating along the z axis and impinging on a perfectly absorbing target exerts on it a total torque $\mathbf{\Gamma} = (\sigma P/\omega)\mathbf{z}$, where the $\sigma = \pm 1$ refers to the left/right-handedness of the circular polarization state, ω is the optical angular frequency, and $\mathbf{z}$ is the unit vector along the z axis. Since Einstein extended Planck's quantization of energy to the light by stating that the quantum of optical energy is $\hbar\omega$, Poynting's suggestion is reformulated at the level of a quantum of energy as the fact that the projection of the photon spin angular momentum associate to free space CP light field along its propagation direction is $\sigma\hbar$, where the $\sigma = \pm 1$ defines the photon helicity.

In his paper,[6] Poynting also suggested the use of a torsion pendulum for the mechanical detection of the torque arising from nondissipative rather than dissipative spin angular momentum transfer from light to matter. This is done using a linearly

*Address all correspondence to Etienne Brasselet, etienne.brasselet@u-bordeaux.fr

polarized (LP) light beam passing through a quarter-wave plate (QWP) whose neutral axes are oriented at $\pm\pi/4$ from the incident polarization direction. Aware that the mechanical detection is challenging, Poynting proposed to illuminate with an LP light beam a series of QWPs suspended by a torsion wire, intercalating between each of them a fixed QWP hold by external means to restore the initial linear polarization state before light passes through the next suspended wave plate, as depicted in Fig. 1(a). The use of N suspended QWPs and $N-1$ fixed ones enables the incident light to exert a total torque oriented along the torsion wire with magnitude NP/ω, provided that the optical axes of two subsequent QWPs are mutually orthogonal, while the sign of the torque depends on the $\pm\pi/4$ orientation of the incident linear polarization with respect to the slow axis of the first QWP. Such a trick nevertheless left Poynting rather dubious about a possible experimental success, as he reported "even with such multiplication, my present experience of optical forces does not give me much hope that the effect could be detected, if it has the value suggested by the mechanical model."[6]

It was not until 1935 that Beth announced the successful detection of the (spin) angular momentum of light[7] from a variant of the latter approach. In fact, Beth used a circular instead linear incident polarization state, a half-wave plate (HWP) instead of a QWP as the suspended birefringent element, and a reflective rather than transmissive multiplication approach owing to a fixed set of a QWP and a mirror, as illustrated in Fig. 1(b). In doing so, Beth obtained a multiplication factor $N=4$, and the torque sign is controlled by the incident circular polarization handedness. The added value of Beth's apparatus is that both wave plates do not require either absolute or relative orientation of their optical axis, at least when using incident CP light. This allowed Beth not only to detect the sought-after mechanical effect[7] but also to measure it in the near-infrared domain with nominal wavelength of 1.2 μm. This was done by placing the torsion pendulum apparatus in vacuum (10^{-9} bar) and assessing the differential angular deviation of the pendulum around its revolution axis obtained under in-phase and out-of-phase optical forcing. This is thoroughly reported in Ref. 2, where the dependence of the optical torque on wavelength and ellipticity of the incident light is studied.

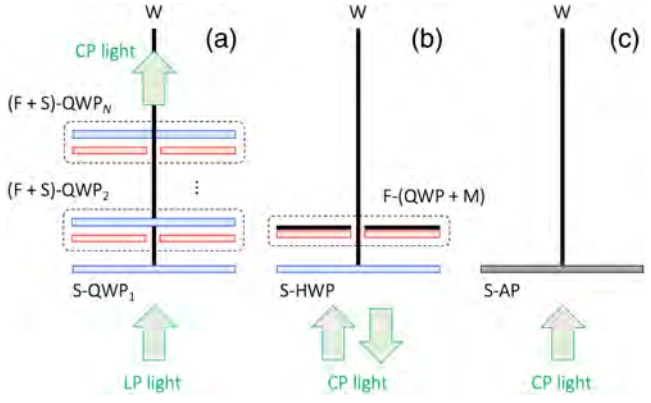

Fig. 1 Selection of a set of pioneering sketches of torsion pendulum arrangements enabling mechanical detection of the transfer of $\pm N\hbar$ spin angular momentum per photon, N integer, from fully polarized incident beam. (a) Poynting's suggestion based on the use of $2N-1$ QWPs and LP incident light within a nondissipative process. Prefixes F and S hold for fixed and suspended wave plates, respectively. (b) Beth's experimental approach providing $N=4$ using a CP incident beam within a nondissipative process. (c) Carrara's experimental approach providing $N=1$ using a CP incident beam within a dissipative process. W, torsion wire; M, mirror; AP, absorbing plate.

In short, using a torsion pendulum consisting essentially of a 25.4 mm diameter HWP suspended from a 25 cm long quartz fiber, Beth demonstrated experimentally by mechanical means, up to a few percents precision, that the angular momentum carried by free space elliptically polarized paraxial light along the direction of propagation is $s_3\hbar$ per photon, where s_3 is the reduced third Stokes parameter.[8] Beth's experiment, which was quantitatively confirmed by Holbourn a few months later using a transmission scheme associated with $N=2$,[9] has entered the history of sciences and is chosen as the starting experimental milestone of the present contribution.

Remarkably, the experimental demonstration of spin angular momentum transfer to matter was in fact achieved, albeit unnoticed, by Righi in 1883 when he observed and analyzed frequency shifts experienced by light as it passes through rotating optical elements.[10] These frequency shifts, now known as rotational Doppler frequency shifts, have been also identified in the presence of orbital angular momentum transfer[11] and in the presence of both spin and orbital contributions.[12] Rotational Doppler frequency shifts are indeed the signature of the rotational mechanical action of light on matter and are the angular counterpart of Doppler frequency shifts associated with light-matter linear momentum transfer. This was pointed out by Henriot[13] in 1934 and subsequently discussed by Atkinson[14] shortly before Beth's announcement.

2 Microwave and Radiowave Experiments

Several years after Beth's and Holbourn's experiments dealing with nondissipative spin angular momentum transfer from light to birefringent media, Carrara reported a dissipative variant of it where the incident angular momentum from CP field is absorbed by the suspended element, as depicted in Fig. 1(c), which corresponds to $N=1$. The experiment was performed in the microwave domain at 9.36 GHz frequency using an absorbing screen made of two subunits placed at the output of a waveguide.[15] The decrease in frequency by 6 orders of magnitude compared to Beth's experiment implies an increase in the applied torque by a factor of 10^6 for a given input power, which makes *a priori* the detection of the effect much easier. Carrara also reported on the nondissipative approach using a reflective scheme. Indeed, by adapting the nature and the relative distance between the two subunits, the suspended system behaved as an effective suspended eighth-wave plate or QWP endowed with a reflective output facet, which, respectively, corresponds to $N=1$ for incident LP wave (provided an appropriate polarization direction) and $N=2$ for incident CP wave. Nevertheless, even though the mechanical detection of angular momentum transfer was successful and the observed angular deviation of the torsion pendulum corresponds to the expected order of magnitude, its quantitative assessment remained an issue. In particular, the ratio between the 3.2 cm wavelength and the transverse characteristic size of the suspended element (in the shape of a disk or a square) being near unity, the knowledge of the geometrical section of the absorber is not sufficient to determine with precision the amount of angular momentum transferred. This issue was addressed analytically by Toraldo Di Francia, who also pointed

out the potentially important consequences of even a small deviation from the ideal circular polarization state on the applied torque.[16]

The latter diffraction effects associated with finite beam size effects can be avoided using waveguides, which attracted attention in the 1960s. According to Allen,[17] the first experimental demonstration of the mechanical effect of angular momentum transfer using a torsional pendulum placed in a waveguide, although not published, was made by Lahart. This experiment consisted in measuring the angular displacement of a suspended macroscopic dipole placed in the course of a CP microwave propagating inside a metallic waveguide. An experimental demonstration of it was reported by Steven and Cullen, who provided a precise measurement of the angular momentum $\sigma\hbar$ per photon carried by a CP transverse electric (TE) mode TE_{11} in a cylindrical waveguide.[18] In addition to this fundamental experimental demonstration, Steven and Cullen proposed an application of it as a power meter based on electromagnetic radiation torque at the frequency of ~35 GHz. This extended previous concept of power meters based on electromagnetic radiation force.[19]

Independently from previously mentioned works, Lahart's early attempt was picked up by Allen, who reported a full study at 9.3 GHz frequency.[17] For his study, he replaced the torsion wire with a needle pivot support or liquid drop suspension technique and used a 1.65 cm long (i.e., almost half-wavelength long) dipole made of aluminum foil. It was thus a rotating rather than an oscillating device, which appears today as a pioneering work in the field of optically induced rotational dynamics of objects, a subject that has blossomed with the advent of optical tweezers.[20] Allen adapted his apparatus to situations that correspond to $N = 1$ and $N = 2$ by working in transmission and reflection, respectively. However, the observed ratio 1/2.8 between the corresponding steady rotation frequencies under constant irradiation power, assessed by monitoring the rotational frequency shifts rather than the rotation of the dipole itself, was surprisingly far from the expected value of 1/2. Allen indeed reported that "the discrepancy, as yet unaccounted for, is much too large to be attributable to experimental error."[17] This problem remained unresolved for almost three decades before Kristensen et al.[21] revisited this experiment, this time with a torsion pendulum.

The starting point was to notice the crucial role of the angular momentum transfer cross section and possible mode conversion processes, which alter the spin-only picture for CP light in free space. In fact, in circular waveguides, TE modes labeled as TE_{mn} (or H_{mn}) with integers m and n referring to azimuthal and radial indices, when CP, carry $\sigma m\hbar$ total angular momentum per quantum of energy for $m > 0$;[18] see also Ref. 22 for detailed calculation. Elaborating a carefully designed setup, Kristensen et al.[21] solved the problem faced by Allen and also extended the experimental approach to higher-order modes ($m > 1$). However, although this work highlighted the role of spin and orbital contributions in the transfer of electromagnetic angular momentum to matter, it was not until 2014 that a pure orbital experiment was performed in the microwave domain. This was done by Emile et al.[23] at 870 MHz frequency based on an earlier proposal by Vul'fson.[4] This proposal results from the analysis of the energy and angular momentum fluxes radiated by a rotating dipole, which was carried out to illustrate that these fluxes may not be collinear in the case of nonplanar waves and also to motivate their experimental evaluation.[4] In particular, outside the near-field zone, the spin and orbital angular momenta fluxes radiated by a rotating dipole flow perpendicularly to the plane of rotation and the in-plane angular momentum is purely orbital in nature.[23,24] The mechanical detection and measurement of the latter was achieved according to the apparatus depicted in Fig. 2(a), where a turnstile antenna is placed in the plane and in the center of a suspended ring absorber. The turnstile antenna radiates like an uniformly rotating dipole when the two orthogonal dipoles radiate in phase quadrature.[23] Alternatively, a source radiating angular momentum experiences a torque, as expected from angular momentum conservation.[18,26] This has been experimentally detected by Chute[25] in the radiowave domain at 14 MHz frequency, using a rotating dipole made of two loop antennas [see Fig. 2(b), where a turnstile antenna is depicted as an alternative option discussed in Ref. 25]. Noteworthy, beyond the fundamental aspect of the latter demonstration, the concomitant reaction torque exerted on the radiating antenna itself has been proposed to control the orientation of space vehicles.[25,27]

To conclude this section, we recall that the principle and realization of contactless mechanical torque induced by rotating electromagnetic fields date back to the end of the 18th century with the advent of the asynchronous electric motor. This was noticed in a few works dealing with microwave experiments; see, for instance, Refs. 26 and 28. The analogy is indeed striking, since a rotor absorbing a power P from rotating fields generated by an m-pole pair machine experiences a radiation torque mP/ω.[26] Recalling the quantum description of the latter classical formulation, which states that the field energy quantum carries an angular momentum of $m\hbar$, this is an interesting opportunity to rethink the way we look at a photon—usually associated with the optical domain—when it comes to everyday electric motors.

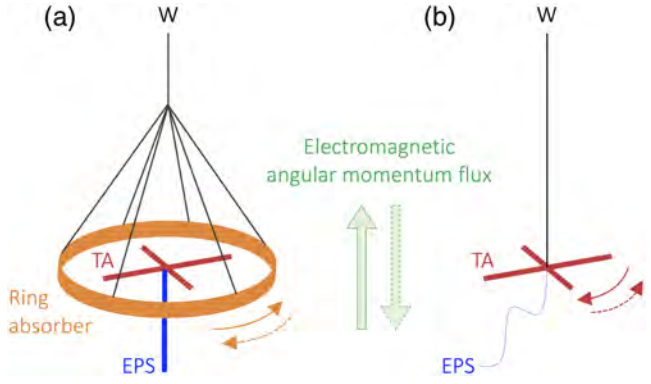

Fig. 2 Illustrative sketches of torsion pendulum experiments dealing with the study of the mechanical effects of angular momentum radiation from a rotating dipole. (a) Apparatus to detect and measure the in-plane orbital angular momentum of the field from dissipative angular momentum transfer to matter in the microwave domain from a cotton wire pendulum.[23] (b) Apparatus to detect and measure the torque exerted on the source itself in the radiowave domain from a steel wire pendulum.[25] The electromagnetic angular momentum flux flows up or down depending on the direction of rotation of the dipole; see the corresponding mechanical motion indicated by solid/dashed arrow. TA, turnstile antenna; EPS, electric power supply connected to the antenna that is (a) fixed to a rigid post or (b) left free to rotate.

3 Optical Experiments

Despite the advent of lasers in the 1960s, Beth's and Holbourn's experiments were not replicated for decades in the field of optics, although they inspired the development of rotational optical manipulation of matter, as discussed in Section 4. This was done by Delannoy et al.[29] in the mid-infrared domain using a 10.6 μm wavelength CO_2 laser with a power of several tens of watts and a HWP suspended by a spider silk thread acting as a torsion wire. The obtained optical torque reached 10^{-12} N · m level, which corresponds to an increase by 3 orders of magnitude compared to the original experiment.[2] The observation of large angular deviations, up to 1 deg, allowed direct real-time monitoring and accurate measurement of the expected uniform angular acceleration of the suspended macroscopic device as a result of stationary spin angular momentum transfer from light to matter. Recently, Yasuda and Hatakeyama[30] reported a torque sensitivity level of 2×10^{-17} N · m close to the thermal noise limit of the apparatus owing to the use of two torsion pendulum in series, one of them acting as a vibration isolator. This device was quantitatively tested by driving the pendulum at its resonance frequency via the absorption of CP light beam at 852 nm wavelength and ∼0.1 W optical power.

Besides these modern macroscopic experimental demonstrations based on the original strategies depicted in Figs. 1(b) and 1(c), alternative torsion pendulum strategies have also been developed at much smaller spatial scales both for nondissipative and dissipative angular momentum transfer processes. This is illustrated in Fig. 3 in two situations where the torsion wire itself undergoes polarization-controlled mechanical effects driven at resonance as a result of time-dependent angular momentum transfer from light to matter. Figure 3(a) refers to the work by He et al.,[31] where the torsion wire is a birefringent waveguide. Optical torque sensing is mediated by the position-dependent optical coupling between a static waveguide [not shown in Fig. 3(a)] and a nanobeam fixed perpendicularly to the suspended torsion waveguide. Indeed, as the nanobeam is set into motion by light-induced torsion of the suspended waveguide, the gap between the nanobeam and the static waveguide varies, which leads to intensity modulation detected at the output of the static waveguide. Optical torque below 10^{-18} N · m at 0.1 mW power level and ∼1.5 μm wavelength is measured. Such an optomechanical fully integrated approach was then extended to optical nanofibers by Fenton el al.[32] where, according to the authors, spin-based torsional optomechanics relies on optical angular momentum transfer by absorption rather than conversion. Torsional dynamics driven by near-infrared pump light induces time-dependent strain-induced birefringence that is monitored by analyzing the polarization state changes experienced by a probe light field guided through the nanofiber; see Fig. 3(b). Experimental investigations of torsional optomechanics of suspended waveguides now go beyond the detection and measurement of the mechanical effects of optical angular momentum transfer, for instance toward the elaboration of quantum experiments in the macroscopic world. This requires preparing the system as close as possible to its motional ground state, and one can mention very recent experimental attempts using either passive[33] or active[34] feedback approaches.

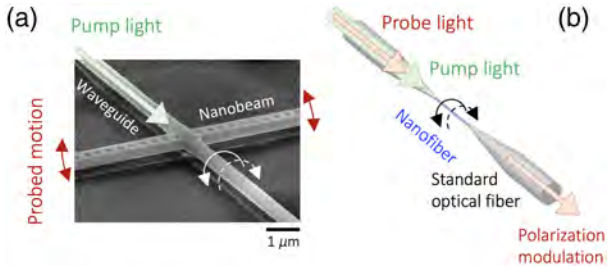

Fig. 3 Illustration of two kinds of fully integrated optomechanical torsional dynamics experiments driven by a waveguided pump light exciting torsional motion of the waveguide itself. (a) Suspended birefringent silicon waveguide, for nondissipative angular momentum transfer demonstration. Scanning electron microscope image from Ref. 31. (b) Suspended isotropic optical nanofiber (subwavelength diameter) obtained by pulling a standard optical fiber locally molten using a flame brushing technique, for dissipative angular momentum transfer demonstration.[32] In both cases, the torsional dynamics is monitored by optical means via (a) nanobeam motion and (b) strain-induced birefringence; see text for details.

Notably, spin-driven torsional optomechanics of waveguides does not tell *a priori* about the spin or orbital nature of the transferred angular momentum from the propagating optical waves to the waveguide through which it propagates. In fact, anisotropic and/or inhomogeneous media can couple the polarization state of light with its spatial degrees of freedom, thereby redistributing the total angular momentum into its spin and orbital parts. This has been addressed numerically in the framework of torsional optomechanics of suspended silicon waveguides.[35] As far as the optical orbital angular momentum is concerned, this brings us to the work of Allen et al.[1] that formally extended Beth's torsion pendulum to the spatial degrees of freedom of light, as discussed hereafter.

Allen et al.[1] indeed proposed an orbital analog of the spin Beth's experiment to detect and measure the mechanical effect of the nondissipative transfer of orbital angular momentum from a paraxial Laguerre–Gaussian beam passing through a suspended afocal pair of cylindrical lenses; see Fig. 4(a). Such a refractive system reverses the sign of the azimuthal index l of the incident paraxial Laguerre–Gaussian beam, hence depositing $2l\hbar$ orbital angular momentum per photon into the system.[1] The total torque exerted on the suspended system is thus oriented along the torsion wire and has a magnitude $2|l|P/\omega$ whatever the incident polarization state. Interestingly, the question of where does the mechanical effect occur for this two-part system was addressed a few months later by several authors; see Refs. 38 and 39. Still, it was not until 2005 that an experimental attempt in the visible domain was reported by Beijersbergen and Woerdman using the original macroscopic proposal depicted in Fig. 4(a), however unsuccessfully.[36] The authors concluded that the lack of rotational symmetry in the system makes it more sensitive to nonideal conditions, which ultimately prevents systematic errors from being overcome. The dissipative analog of this experiment allows recovering axisymmetry, for instance, using a suspended disk-shaped absorber plate and LP beams to cancel the contribution from spin angular momentum. This is depicted in Fig. 4(b), and its implementation was reported by Emile and Emile.[37]

In the same way that Beth's macroscopic spin-based experiments have been transposed to the field of integrated photonics, several orbital analogs have been discussed, but only theoretically so far to our knowledge. A recent example was reported by Kaviani et al.,[40] who discussed the expected optomechanical

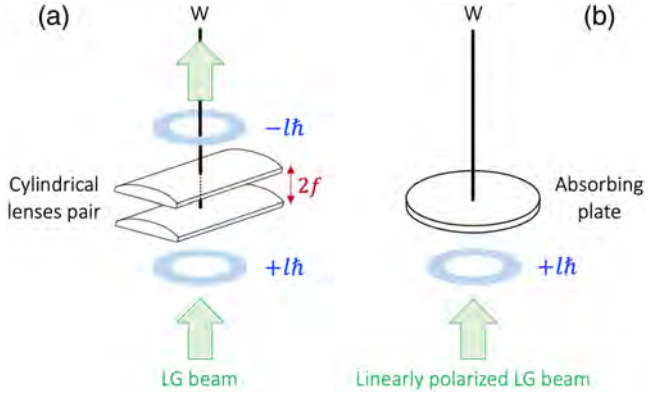

Fig. 4 Macroscopic torsion pendulum systems for the mechanical demonstration of orbital angular momentum transfer from light to matter. (a) Nondissipative approach consisting of a suspended pair of cylindrical lenses distant by $2f$ with f the focal length, which was proposed in Ref. 1 and implemented in Ref. 36, yet unsuccessfully. (b) Dissipative approach implemented in Ref. 37. The blue rings refer to the doughnut-shaped transverse intensity profile of a Laguerre–Gaussian beam with azimuthal index $\pm l$, which carries $\pm l\hbar$ per photon along the beam propagation direction.

performances of a on-chip torsional pendulum driven by optical orbital angular momentum transfer, be it of dissipative or nondissipative origin. Notably, an important contribution was made by Battacharya and Meystre,[41] who demonstrated the possible trapping and cooling of the rotational motion of a massive system to its ground state, considering the case of a 10 μm radius mirror with 10 μg. This proposal relies on an optical cavity made of two helical mirrors imparting orbital angular momentum changes for the reflected light, one of them being suspended to a torsion wire, as depicted in Fig. 5.

We note, however, that this approach left open the question of the role of the spatial distribution of the intracavity field when defining the nature and size of the helical mirror for a given operating wavelength, which seems particularly relevant when large values of l are involved. By further exploiting the same cavity design, Battacharya et al.[42] showed that the optical torque exerted on the reflective orbital torsion pendulum can entangle the latter with a cavity mode. Since then, several variants have been discussed theoretically while exploring the manifestation of quantum effects using macroscopic systems. For instance, placing a ferrimagnetic sphere into the cavity, Cheng et al.[43] reported the tripartite entanglement between a cavity mode, the reflective orbital torsion pendulums, and a magnon, whereas Chen et al.[44] showed that replacing the static helical mirror of the original design by a suspended one, light–matter orbital angular momentum transfer can entangle the two reflective orbital torsion pendulums.

4 Wireless Optical Approaches

Torsional distortions of material systems caused by the transfer of optical angular momentum are of course not limited to the torsional pendulum as such. In fact, it is sufficient to have a restoring torque, which opposes the optical torque at the origin of the motion. Several experimental demonstrations of wireless torsional optomechanics driven by the angular momentum of light have been reported to date.

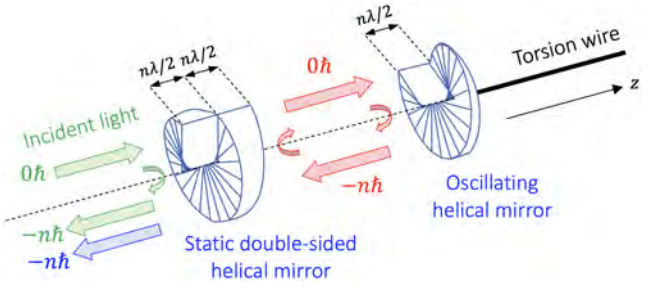

Fig. 5 Revised illustration of the helical mode cavity design proposed by Battacharya and Meystre[41] (in Ref. 41, the displayed handedness of the helical mirrors do not match the required self-consistency for the building up of a cavity mode and here we also provide the correct orbital angular momentum content for the field inside and outside the optical cavity. Similar issues appear in Ref. 42.) that opened up the prediction of various kinds of entanglements involving light and matter and light–matter.[42–44] All helical reflective surfaces have the same handedness and $n\lambda/2$ step height (n positive integer). The incident field is a Gaussian beam and the colored arrows refer to contributions of various kinds: purely extracavity (green), purely intracavity (red), extracavity arising from intracavity (blue). In the sketched example, on the one hand, the reflection on the oscillating helical mirror removes $n\hbar$ orbital angular momentum per photon along **z**. On the other hand, the static helical element, which is a partially reflective split-disk mirror with a helical ramp, preserves the orbital state in transmission while its extracavity (intracavity) side removes (adds) $n\hbar$ orbital angular momentum per photon along **z** upon reflection. Using helical mirrors with opposite handedness reverses the sign of the orbital angular momentum changes.

An illustrative example is the case of a thin film of liquid crystals, usually a few tens of micrometers thick, interacting with a focused laser beam. Indeed, the spin and orbital parts of the total angular momentum of paraxial light can be transferred independently or simultaneously to liquid crystals by nondissipative means. Liquid crystals, being birefringent viscoelastic fluids, can be set into rotational motion from spin angular momentum transfer as demonstrated by Santamato et al.[45] and Zolot'ko et al.,[46] and torsional dynamics for the collective molecular orientation can take place for incident elliptical polarization state.[47] Notably, the restoring torque can qualified as not being of a purely material origin as it depends on the light-matter interaction. The elastic restoring torque indeed depends on the light-induced orientational state of the liquid crystal. Torsional distortions of liquid crystals can also occur due to orbital angular momentum transfer when the excitation laser beam has a noncircular intensity cross section, as reported by Piccirillo et al.[48] Moreover, these authors also demonstrated that torsional dynamics can also result from the competition between spin and orbital optical angular momentum transfer.[48] However, the orientational viscosity of liquid crystals causes the system to be overdamped, preventing amplification of the oscillatory motion by periodic forcing, which nevertheless enriches the spectral response of the system, which is intrinsically nonlinear.[49]

Another example is that of transparent nanorods optically trapped in liquid by a tightly focused LP laser beam whose polarization azimuth rotates sufficiently faster. As shown by Bonin et al.,[50] this leads to the oscillatory motion of the nanorod

orientation in a plane perpendicular to the beam propagation direction. The experimental demonstration of light-induced torsional dynamics of transparent elongated nanoparticles in vacuum came only more than one decade later; see, for instance, Refs. 51 and 52. These works were an important step toward the experimental realization of torsional cooling of nonspherical objects based on the polarization state rather than the spatial degrees of freedom, as had been proposed theoretically.[53,54] The most recent advances bring us even closer to the sought-after ground-state cooling of all 6 degrees of freedom of a levitated nonspherical nanoparticle.[55]

Finally, the wireless situation involving an optical torque that results from the interaction between the spin and orbital degrees of freedom has also been demonstrated experimentally. This was reported in Ref. 56, where a piecewise space-variant anisotropic plate with 6 mm diameter deposited at a bounded air–water interface is shown to behave as a light-driven overdamped in-plane torsional spring as CP light passes through it.

5 Beyond Electromagnetic Waves

A notable feature of scalar waves is that a paraxial field propagating along the z axis (toward $z > 0$) and having an amplitude proportional to $\exp[i(-\omega t + kz + l\varphi)]$, where ω is the angular frequency, k is the wave vector, and φ is the azimuthal angle, carries orbital angular momentum. In particular, the ratio l/ω between the angular momentum and energy fluxes in electromagnetism[1] applies as well in acoustics.[57] Accordingly, the acoustic radiation torque exerted on a material system absorbing a sound wave endowed with a phase singularity with topological charge l according to the preceding expression is $\mathbf{\Gamma} = (lP/\omega)\mathbf{z}$. Its mechanical detection and measurement using Beth's torsion pendulum approach [see Fig. 6(a)] was reported by Volke-Sepúlveda et al.[59] and Skeldon et al.[60] in the audible domain, in the air. The demonstration of a resonant torsional mechanical oscillator driven by acoustic orbital angular momentum transfer was reported only recently.[58] This was also done in the air, however, via a nondissipative process, using an ultrasonic acoustic field carrying zero angular momentum that reflects off a helical mirror imparting nonzero orbital angular momentum to the reflected field, as illustrated in Fig. 6(b).

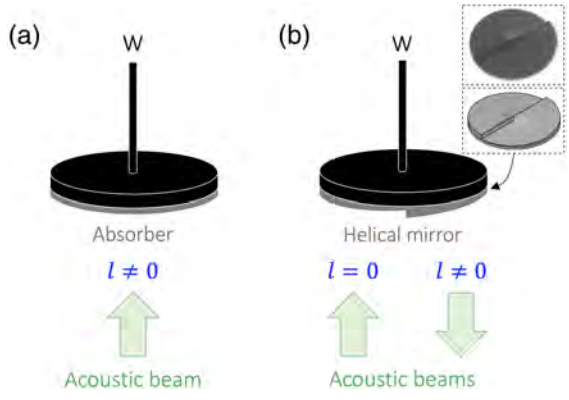

Fig. 6 Sketches of torsion pendulum arrangements enabling mechanical detection of the transfer of orbital angular momentum from sound to matter by (a) dissipative and (b) nondissipative means. The inset of panel (b) shows the designed (bottom) and fabricated (top) 3D printed helically corrugated plates acting as a reflective acoustic vortex generator used for experimental demonstration.[58]

Interestingly, the wireless torsional dynamics driven by acoustic radiation torque has also been studied for some years in the context of ultrasound elastography, which is a technique used for noncontact quantitative palpation in medical diagnosis. The idea is to transiently twist a soft sound-absorbing medium through irradiation with a focused ultrasonic pulse that generates an orthoradial shear wave.[61,62] These works lay the foundation for a new imaging technique capable of determining the viscoelastic tensor of soft media in a way that goes beyond what can be done by ultrasonic elastography based solely on acoustic radiation forces.

6 Summary

Nearly 90 years after Beth's experimental demonstration that light can act mechanically on matter as a consequence of the transfer of spin angular momentum from light to matter, torsional optomechanics driven by the optical angular momentum remains a lively research topic in many respects, as has been discussed here. Notably, the transfer of angular momentum can also be of orbital or spin-orbit origin, depending on the nature of the light–matter interaction involved. In particular, angular momentum-based cavity optomechanics has paved the way for a whole range of attractive quantum mechanical experiments with material systems that are diversifying in nature and size thanks to ever-improving instrumentation and manufacturing technologies.[63] Finally, the exploration of mechanical torsional effects driven by the angular momentum of waves beyond electromagnetic ones has begun with sound waves, which already suggests interesting applications in metrology and biomedical imaging. Beth's legacy is not yet over.

Acknowledgment

The author declares no conflicts of interest.

References

1. L. Allen et al., "Orbital angular momentum of light and the transformation of Laguerre-Gaussian laser modes," *Phys. Rev. A* **45**, 8185–8189 (1992).
2. R. A. Beth, "Mechanical detection and measurement of the angular momentum of light," *Phys. Rev.* **50**, 115–125 (1936).
3. A. I. Sadovskiĭ, ZhRFKhO. Ch. Fiz. 9, 82 (1897). (The author was unable to obtain this publication.)
4. K. S. Vul'fson, "Angular momentum of electromagnetic waves," *Sov. Phys. Usp.* **30**(8), 724 (1987).
5. A. Righi, "Sulle oscillazioni elettriche a piccola lunghezza d'onda e sul loro impiego nella produzione di fenomeni analoghi ai principali fenomeni dell'ottica," Tipografia Gamberini e Parmeggiani, Bologna (1894).
6. J. H. Poynting, "The wave motion of a revolving shaft, and a suggestion as to the angular momentum in a beam of circularly polarised light," *Proc. R. Soc. London A* **82**(557), 560–567 (1909).
7. R. A. Beth, "Direct detection of the angular momentum of light," *Phys. Rev.* **48**(5), 471 (1935).
8. M. Born and E. Wolf, *Principles of Optics: Electromagnetic Theory of Propagation, Interference and Diffraction of Light*, Elsevier (2013).
9. A. H. S. Holbourn, "Angular momentum of circularly polarized light," *Nature* **137**(3453), 31 (1936).
10. A. Righi, "Sur les changements de longueur d'onde obtenus par la rotation d'un polariseur, et sur le phénomène des battements

produits avec les vibrations lumineuses," *J. Phys. Theor. Appl.* **2**(1), 437–446 (1883).
11. J. Courtial et al., "Measurement of the rotational frequency shift imparted to a rotating light beam possessing orbital angular momentum," *Phys. Rev. Lett.* **80**(15), 3217–3219 (1998).
12. J. Courtial et al., "Rotational frequency shift of a light beam," *Phys. Rev. Lett.* **81**(22), 4828–4830 (1998).
13. E. Henriot, "Les couples exercés par la lumière polarisée circulairement," *Comptes rendus de l'Académie des sciences* **198**, 1146 (1934).
14. R. D. E. Atkinson, "Energy and angular momentum in certain optical problems," *Phys. Rev.* **47**(8), 623–627 (1935).
15. N. Carrara, "Torque and angular momentum of centimetre electromagnetic waves," *Nature* **164**(4177), 882–884 (1949).
16. G. T. Di Francia, "On a macroscopic measurement of the spin of electromagnetic radiation," *Il Nuovo Cimento* **6**, 150–167 (1957).
17. P. Allen, "A radiation torque experiment," *Am. J. Phys.* **34**(12), 1185–1192 (1966).
18. D. H. Steven and A. L. Cullen, "Angular-momentum wattmeter for the 8 mm waveband," *Proc. Inst. Electr. Eng.* **110**(11), 1968–1974 (1963).
19. A. L. Cullen, "Absolute power measurement at microwave frequencies," *Proc. IEE-Part IV Inst. Monographs* **99**(2), 100–111 (1952).
20. G. D. Bruce, P. Rodríguez-Sevilla, and K. Dholakia, "Initiating revolutions for optical manip-ulation: the origins and applications of rotational dynamics of trapped particles," *Adv. Phys. X* **6**(1), 1838322 (2021).
21. M. Kristensen, M. W. Beijersbergen, and J. P. Woerdman, "Angular momentum and spin-orbit coupling for microwave photons," *Opt. Commun.* **104**(4–6), 229–233 (1994).
22. S. Carusotto, G. Fornaca, and E. Polacco, "Radiation beats and rotating systems," *Il Nuovo Cimento B* **53**(1), 87–97 (1968).
23. O. Emile et al., "Electromagnetically induced torque on a large ring in the microwave range," *Phys. Rev. Lett.* **112**(5), 053902 (2014).
24. Y. Mao, Y. Liu, and H. Lin, "Angular momenta in fields from a rotational mechanical antenna," *J. Phys. Commun.* **5**(12), 125012 (2021).
25. F. S. Chute, "The possibility of using electromagnetic angular momentum to stabilize a space vehicle," PhD dissertation, University of Alberta, Edmonton, Canada (1966).
26. F. Chute, "The reaction torque on an axial multipole radiator," *IEEE Trans. Antenn. Propag.* **15**(4), 585–587 (1967).
27. F. S. Chute and G. B. Walker, "The possibility of stabilizing a space vehicle using electromagnetic angular momentum," *Can. Aero. Space J.* **11**, 219 (1965).
28. H. Barlow, "Measurement of power by absorption of the angular momentum of a circularly polarized wave," *Proc. Inst. Electr. Eng.* **110**(5), 865–868 (1963).
29. G. Delannoy, O. Emile, and A. Le Floch, "Direct observation of a photon spin-induced constant acceleration in macroscopic systems," *Appl. Phys. Lett.* **86**(8), 081109 (2005).
30. R. Yasuda and A. Hatakeyama, "Characterization of a double torsion pendulum used to detect spin-induced torque based on Beth's experiment," *Rev. Sci. Instrum.* **92**(10), 105108 (2021).
31. L. He, H. Li, and M. Li, "Optomechanical measurement of photon spin angular momentum and optical torque in integrated photonic devices," *Sci. Adv.* **2**(9), e1600485 (2016).
32. E. F. Fenton , A. Khan, and P. Solano et al., "Spin-optomechanical coupling between light and a nanofiber torsional mode," *Opt. Lett.* **43**, 1534–1537 (2018).
33. D. Su et al., "Torsional optomechanical cooling of a nanofiber," *Photonics Res.* **10**(2), 601–609 (2022).
34. F. Tebbenjohanns et al., "Feedback-cooling the fundamental torsional mechanical mode of a tapered optical fiber to 30 mK," arXiv:2301.07792 (2023).
35. W. Li et al., "Dynamics of angular momentum-torque conversion in silicon waveguides," *Opt. Express* **27**(7), 10208–10220 (2019).
36. M. W. Beijersbergen and J. Woerdman, "Measuring orbital angular momentum of light with a torsion pendulum," *Proc. SPIE* **5736**, 111–126 (2005).
37. O. Emile and J. Emile, "Energy, linear momentum, and angular momentum of light: what do we measure?" *Ann. der Phys.* **530**, 1800111 (2018).
38. S. Van Enk and G. Nienhuis, "Eigenfunction description of laser beams and orbital angular momentum of light," *Opt. Commun.* **94**(1–3), 147–158 (1992).
39. M. W. Beijersbergen et al., "Astigmatic laser mode converters and transfer of orbital angular momentum," *Opt. Commun.* **96**(1–3), 123–132 (1993).
40. H. Kaviani et al., "Optomechanical detection of light with orbital angular momentum," *Opt. Express* **28**(10), 15482–15496 (2020).
41. M. Bhattacharya and P. Meystre, "Using a Laguerre-Gaussian beam to trap and cool the rotational motion of a mirror," *Phys. Rev. Lett.* **99**, 153603 (2007).
42. M. Bhattacharya, P.-L. Giscard, and P. Meystre, "Entanglement of a Laguerre-Gaussian cavity mode with a rotating mirror," *Phys. Rev. A* **77**(1), 013827 (2008).
43. H.-J. Cheng et al., "Tripartite entanglement in a Laguerre-Gaussian rotational-cavity system with an yttrium iron garnet sphere," *J. Opt. Soc. Am. B* **38**(2), 285–293 (2021).
44. Z. Chen et al., "Entanglement of two rotating mirrors coupled to a single Laguerre-Gaussian cavity mode," *Opt. Express* **27**(21), 29479–29490 (2019).
45. E. Santamato et al., "Collective rotation of molecules driven by the angular momentum of light in a nematic film," *Phys. Rev. Lett.* **57**, 2423–2426 (1986).
46. A. S. Zolot'ko, V. F. Kitaeva, and V. Y. Fedorovich, "Self-effect of a circularly polarized light wave in homeotropically oriented nematic liquid crystal," p. 326, FIAN, Moscow (1986) (in Russian).
47. E. Santamato et al., "Laser-induced nonlinear dynamics in a nematic liquid crystal film," *Phys. Rev. Lett.* **64**, 1377–1380 (1990).
48. B. Piccirillo et al., "Orbital and spin photon angular momentum transfer in liquid crystals," *Phys. Rev. Lett.* **86**, 2285–2288 (2001).
49. D. O. Krimer and E. Brasselet, "Light-driven liquid-crystalline nonlinear oscillator under optical periodic forcing," *Phys. Rev. E* **76**(2), 021705 (2007).
50. K. D. Bonin, B. Kourmanov, and T. G. Walker, "Light torque nanocontrol, nanomotors, and nanorockers," *Opt. Express* **10**(19), 984–989 (2002).
51. T. M. Hoang et al., "Torsional optomechanics of a levitated nonspherical nanoparticle," *Phys. Rev. Lett.* **117**(12), 123604 (2016).
52. J. Ahn et al., "Optically levitated nanodumbbell torsion balance and GHz nanomechanical rotor," *Phys. Rev. Lett.* **121**(3), 033603 (2018).
53. O. Romero-Isart et al., "Toward quantum superposition of living organisms," *New J. Phys.* **12**(3), 033015 (2010).
54. H. Shi and M. Bhattacharya, "Coupling a small torsional oscillator to large optical angular momentum," *J. Mod. Opt.* **60**(5), 382–386 (2013).
55. A. Pontin et al., "Simultaneous cavity cooling of all six degrees of freedom of a levitated nanoparticle," *Nat. Phys.* (2023).
56. H. Magallanes and E. Brasselet, "Macroscopic direct observation of optical spin-dependent lateral forces and left-handed torques," *Nat. Photonics* **12**(8), 461–464 (2018).
57. B. T. Hefner and P. L. Marston, "An acoustical helicoidal wave transducer with applications for the alignment of ultrasonic and underwater systems," *J. Acoust. Soc. Am.* **106**, 3313–3316 (1999).
58. B. Sanchez-Padilla and E. Brasselet, "Torsional mechanical oscillator driven by the orbital angular momentum of sound," *Phys. Rev. Appl.* **13**(6), 064069 (2020).
59. K. Volke-Sepúlveda, A. O. Santillan, and R. R. Boullosa, "Transfer of angular momentum to matter from acoustical vortices in free space," *Phys. Rev. Lett.* **100**, 024302 (2008).
60. K. D. Skeldon et al., "An acoustic spanner and its associated rotational Doppler shift," *New J. Phys.* **10**, 013018 (2008).

61. N. Jiménez, J. M. Benlloch, and F. Camarena, "A new elastographic technique using acoustic vortices," in *IEEE Int. Ultrason. Symp. (IUS)*, IEEE, pp. 1–4 (2020).
62. E. González-Mateo, N. Jiménez, and F. Camarena, "Quasi-omnidirectional shear wave generation using acoustic vortices for elastography," in *IEEE Int. Ultrason. Symp. (IUS)*, IEEE, pp. 1–4 (2022).
63. M. Croquette et al., "Recent advances toward mesoscopic quantum optomechanics," *AVS Quantum Sci.* **5**(1), 014403 (2023).

Etienne Brasselet is research director at CNRS, Laboratoire Ondes et Matière d'Aquitaine, University of Bordeaux, France. His scientific interests include wave-matter interactions in the framework of multidisciplinary environment including nonlinear phenomena, optics and photonics, acoustics, mechanical effects of waves, soft matter systems. His research activities mainly focus on situations where structured fields meet structured matter, which makes singularities, topology and vector fields at play in various circumstances.

Research Article

ADVANCED PHOTONICS

Generation of time-varying orbital angular momentum beams with space-time-coding digital metasurface

Jingxin Zhang,[a] Peixing Li,[b] Ray C. C. Cheung,[b] Alex M. H. Wong,[b,c,*] and Jensen Li[a,*]
[a]The Hong Kong University of Science and Technology, Department of Physics, Hong Kong, China
[b]City University of Hong Kong, Department of Electrical Engineering, Hong Kong, China
[c]City University of Hong Kong, State Key Laboratory of Terahertz and Millimeter Waves, Hong Kong, China

Abstract. The recently proposed extreme-ultraviolet beams with time-varying orbital angular momentum (OAM) realized by high-harmonic generation provide extraordinary tools for quantum excitation control and particle manipulation. However, such an approach is not easily scalable to other frequency regimes. We design a space-time-coding digital metasurface operating in the microwave regime to experimentally generate time-varying OAM beams. Due to the flexible programmability of the metasurface, a higher-order twist in the envelope wavefront structure of time-varying OAM beams can be further designed as an additional degree of freedom. The time-varying OAM field patterns are dynamically mapped by developing a two-probe measurement technique. Our approach in combining the programmability of space-time-coding digital metasurfaces and the two-probe measurement technique provides a versatile platform for generating and observing time-varying OAM and other spatiotemporal excitations in general. The proposed time-varying OAM beams have application potentials in particle manipulation, time-division multiplexing, and information encryption.

Keywords: time-varying orbital angular momentum; digital-coding metasurfaces; wavefront structure.

Received Jan. 31, 2023; revised manuscript received Mar. 6, 2023; accepted for publication Mar. 15, 2023; published online Apr. 17, 2023.

[DOI: 10.1117/1.AP.5.3.036001]

1 Introduction

Electromagnetic waves carry both linear and angular momenta. Specifically, the latter can be decomposed into spin angular momentum (SAM) and orbital angular momentum (OAM).[1] Although SAM is associated with polarization, OAM is associated with the helical wavefront $\exp(-jl\theta)$ in azimuthal angle θ with an integer topological charge l.[2] OAM beams with distinct topological charges are mutually orthogonal, allowing them to carry information and to be multiplexed.[3–7] The increased channel capacity and spectral efficiency with OAM multiplexing can thus be useful in fiber-based and free-space communications, with both prospects and challenges.[8] Moreover, OAM beams with nonzero topological charges have phase singularity with vanished intensity at the beam center, which are useful for optical trapping and lattices.[9–12]

To further unlock the full potential of OAM, there have been persistent efforts in generalization of the concept. Spatiotemporal optical vortex beams[13–19] have been recently demonstrated with phase singularities generally in space-time coordinates, forming higher-order structures, such as a phase-singular ring. Rego et al.[20] proposed a kind of extreme-ultraviolet beam with time-varying OAM arising from high-harmonic generation. The topological charge varies in time periodically, giving a time-dependent phase profile $\exp[-jl(t)\theta]$ and inducing a self-torque of light. It can be potentially applied to various scenarios, including particle manipulation,[21–23] Bose–Einstein condensation,[24,25] and Floquet topological dynamics.[26,27] However, such a high-harmonic approach in generating time-varying OAM is not easily applicable to other frequency regimes, hindering further demonstrations. Alternatively, Sedeh et al.[28] proposed

*Address all correspondence to Alex M. H. Wong, alex.mh.wong@cityu.edu.hk; Jensen Li, jensenli@ust.hk

an optical metasurface with a spiral-staircase profile of modulation frequencies to implement time-varying OAM. In fact, such an approach can be feasible and generalized through a space-time-coding digital metasurface with field-programmable-gate-array (FPGA) technology, particularly in the microwave regime.[29–37] In such a case, different metasurface responses can be digitized by controlling the bias voltages with the adoption of FPGA, which offers the metasurface powerful programmability for space-time modulation.

In this work, we experimentally construct and observe time-varying OAM beams using a space-time-coding digital metasurface in the microwave regime. We also introduce a higher-order twist in the wavefront structure of time-varying OAM beams, enabled by the flexible programmability of the metasurface. To observe the complex field pattern being varied in time, we use a two-probe measurement technique to dynamically map the time-varying OAM field pattern. A space-time-coding digital metasurface together with a two-probe field-mapping technique provides a versatile platform to construct and observe time-varying OAM and spatiotemporal excitations in general. The proposed time-varying OAM beams can be further used in particle manipulation, time-division multiplexing, and information encryption.

2 Materials and Methods

2.1 Theory of Time-Varying OAM Beams Generation

To generate normal OAM beams with phase profile $\exp(-jl\theta)$ by a metasurface [time harmonic convention $\exp(j\omega t)$], the direct way is to create an azimuthal phase gradient of the scattered field with topological charge l, while for the time-varying OAM beams, the phase profile turns to be $\exp[-jl(t)\theta]$ with topological charge $l(t)$ varying linearly with time,[20] manifesting a time-dependent azimuthal phase gradient decided by $l(t)$. To realize such properties, we consider a space-time-coding digital metasurface with active modulation of reflection phase depending on both azimuthal angle θ and time t as

$$\Phi(\theta, t) = -l(t)\theta. \tag{1}$$

When the $l(t) = Nt/T$ is chosen to vary linearly in time with a modulation period T, we obtain N consecutive integer l from 0 to $N-1$ at time instants $t = lT/N$. The metasurface is divided into finite N azimuthal sectors to implement the N different OAM profiles. Due to the discretization of the metasurface, the OAM phase profiles with l and $l \pm N$ are in fact equivalent to each other by assuming each sector can only give a particular reflection phase at a particular time instance, so the value of $l(t)$ cannot increase to infinity but repeats from $-N/2$ to $N/2$ in every period T.[28] Under a monochromatic illumination $E_0 \exp(j\omega t)$ at signal radial frequency ω on the metasurface with spatiotemporal phase modulation $\Phi(\theta, t)$, the reflected field becomes

$$E_r(\rho, \theta, t) = E_0 A(\rho, \theta) \exp(j\omega t) \exp\left(-jN\frac{t}{T}\theta\right), \tag{2}$$

when the modulation frequency is much lower than the signal frequency. The $A(\rho, \theta)$ describes the spatial dependency of the scattered field in cylindrical coordinates (ρ, θ), and the coefficient of θ becomes $l(t)$ as Nt/T, which denotes the time-varying topological charge of the OAM beam.

With the flexible programmability of the metasurface, the envelope wavefront structure of the above-mentioned time-varying OAM beams can be further designed. We modify the spatiotemporal phase modulation in Eq. (1) as

$$\Phi_w(\theta, t) = -l(t)(\theta - \eta(t)), \tag{3}$$

where $l(t) = Nt/T$ and $\eta(t)$ is defined as the time-dependent twisting angle. As an example here, we design $\eta(t)$ as $2\pi wt/T$, a linear function in time, where w is defined as the winding number of the time-varying OAM beam. Then the reflected field can be expressed as

$$E_r(\rho, \theta, t) = E_0 A(\rho, \theta) \exp(j\omega t) \exp\left(-jN\frac{t}{T}\left(\theta - 2\pi w\frac{t}{T}\right)\right). \tag{4}$$

Here we consider the case of $w = -1$, $N = 8$ for illustration purposes. As shown in Fig. 1(a), the envelope wavefront structure of the reflected beam has been plotted, where the constant phase contour is only about the slowly varying modulation phase envelope, and the much faster phase variation at signal frequency is omitted in the drawing for brevity. As can be seen, different time layers at $t = lT/N$ show different OAM phase profiles, taken as $l = 0, 1, 2, 3, 4\ (-4), -3, -2, -1$ periodically. We remark that it is a superposition of two OAM modes: $l = 4$ and $l = -4$ at $t = T/2$. By "geometrically" joining up all the zero phase (cyan color) and π phase (red color) at different time instances, the wavefront structure shows up a higher-order twist for a nonzero w ($w = -1$ in this example) compared with $w = 0$ case (see Fig. S1 in the Supplementary Material). In other words, the envelope wavefront of the time-varying OAM beam ($w = 0$) is further twisted with w round in one period of T. Here we only consider the integer case of $w = -1$ as an example, while the w can be other integers and fractional values (see Sec. 4 for details). The winding number w can be seen as an additional degree of freedom in constructing the time-varying OAM beams. More information can be encoded by designing the w to increase the channel capacity for data transmission. And we provide an example of winding number implementation and measurement with experimental demonstrations, as shown in Sec. 3.2.

In our paper, we generate the time-varying OAM beams with $w = 0$ and $w = -1$, respectively. The case of $w = -1$ is illustrated in the main text, whereas the results of $w = 0$ can be found in Sec. 2 in the Supplementary Material for comparison. To generate the time-varying OAM beam with $w = -1$ by a space-time-coding digital metasurface, as shown in Fig. 1(b), we divide the metasurface into $N = 8$ azimuthal sectors, and each sector is dynamically controlled with 3-bit coding digits "1" to "8," representing the reflection phase from 0 deg to 315 deg in every 45 deg (in addition to reflection from a perfect metal). The space-time-coding scheme is designed according to the phase term $\exp[-j(Nt/T)(\theta - 2\pi wt/T)]$ in Eq. (4), with winding number $w = -1$. For easier implementation, we only adopt eight different time frames with eight coding states in a period of T to generate the integer $l(t)$, whereas the fractional OAM states are not considered for the implementation. The details for the space-time modulation scheme can be found in Tables S1 and S2 in the Supplementary Material. In Fig. 1(b), the corresponding phase states represented by different colors show an l-related distribution at each time layer, and the black

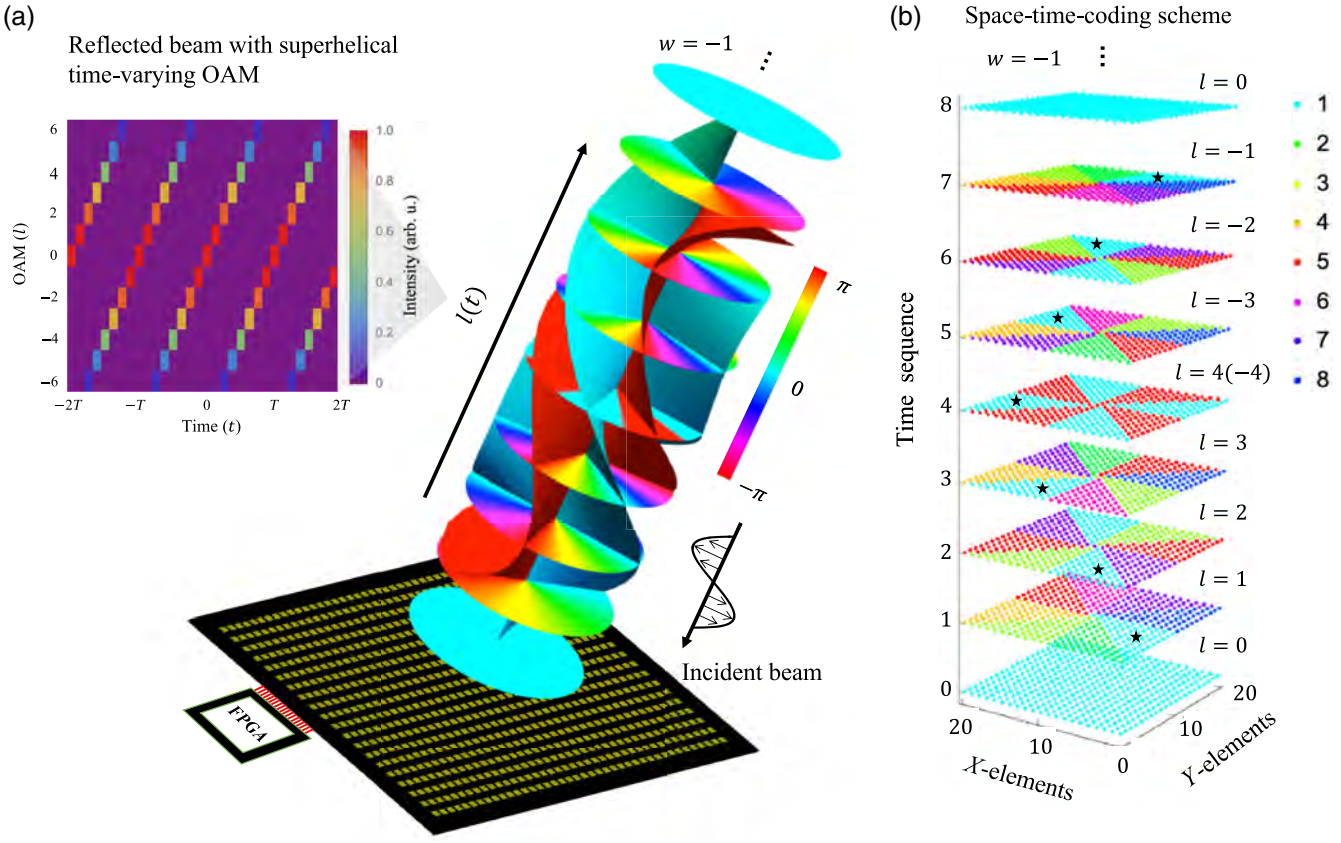

Fig. 1 Time-varying OAM beam generation. (a) Time-varying OAM beam with topological charge $l(t)$ varying from 0, 1, 2, 3, 4 (-4), −3, −2, and −1 periodically in time, with envelope phase profile [omitting $\exp(j\omega t)$ for brevity] shown at different layers in time. The cyan and red curved surfaces geometrically join up the 0 and π phase on different layers, showing a twist completing one cycle in the clockwise direction defined with winding number $w = -1$. The beam is generated by a space-time-coding digital metasurface controlled with FPGA. (b) Digital coding scheme of the metasurface with 3-bit coding digits "1" to "8" representing the 0 deg to 315 deg in every 45 deg for the reflection phase profile (in addition to reflection from a perfect metal) at each time instance. The black stars mark the twisted trajectory of zero phase position with coding digit "1."

stars mark the azimuthal positions of zero phase (coding digit "1") showing the higher-order twist in the envelope wavefront structure of time-varying OAM with $w = -1$. The location of the zero phase takes a time of $T/|w|$ for one revolution. Here we emphasize that the upper limit of the modulation frequency of the space-time-coding digital metasurface is typically within the megahertz range,[29–34] which is much slower than the signal frequency (gigahertz) in the microwave regime. Therefore, the modulation mechanisms and the operation only focus on the modulation envelope rather than the carrier signal. In our current work, the time-varying control is achieved through adiabatic field control at the fundamental frequency. It is also possible to instruct the output beam to another m'th harmonic by adding an additional phase $m2\pi t/T$ to the reflection phase.

2.2 Space-Time-Coding Digital Metasurface

To demonstrate the above-illustrated concept, as shown in Fig. 2(a), we design and fabricate a space-time-coding digital metasurface with $20 \times 20 = 400$ elements operating at 11 GHz. Each element is loaded with a varactor diode, whose capacitance changes with the bias voltage, leading to the frequency shift of the dipole resonance of the metasurface so that the reflection phase can be varied in time. We note that we apply the commonly used element structure embedded with a varactor diode for the realization of digital-coding metasurface as previous work,[30,31,33] but now with a biasing network design appropriate for generating time-varying OAM in Fig. S3 in the Supplementary Material and the digital coding scheme in space-time domain in Fig. 1(b). The 3D structure of each element of the proposed metasurface is illustrated in Fig. 2(b). The geometrical parameters of the element are chosen as $h_1 = 0.813$ mm, $h_2 = 0.1$ mm, $h_3 = 0.305$ mm, $\emptyset_1 = 1.2$ mm, $\emptyset_2 = 0.8$ mm, $s = 0.6$ mm, $a = 10$ mm, $b = 5$ mm, $c = 4$ mm, and $g = 1$ mm. The element is composed of three copper layers printed on two substrate layers (Rogers 4003C, $\varepsilon_r = 3.55$, $\tan\delta = 0.0027$) and a bonding layer (Rogers 4450F, $\varepsilon_r = 3.52$, $\tan\delta = 0.004$). On the top layer, two rectangular metal patches are connected by a varactor diode (MAVR-000120-14110P) soldered on the metasurface by the surface mounting technology (SMT). One patch is connected to the middle layer through metallic via −. Another patch is connected to the bottom layer through via +, which is electrically isolated

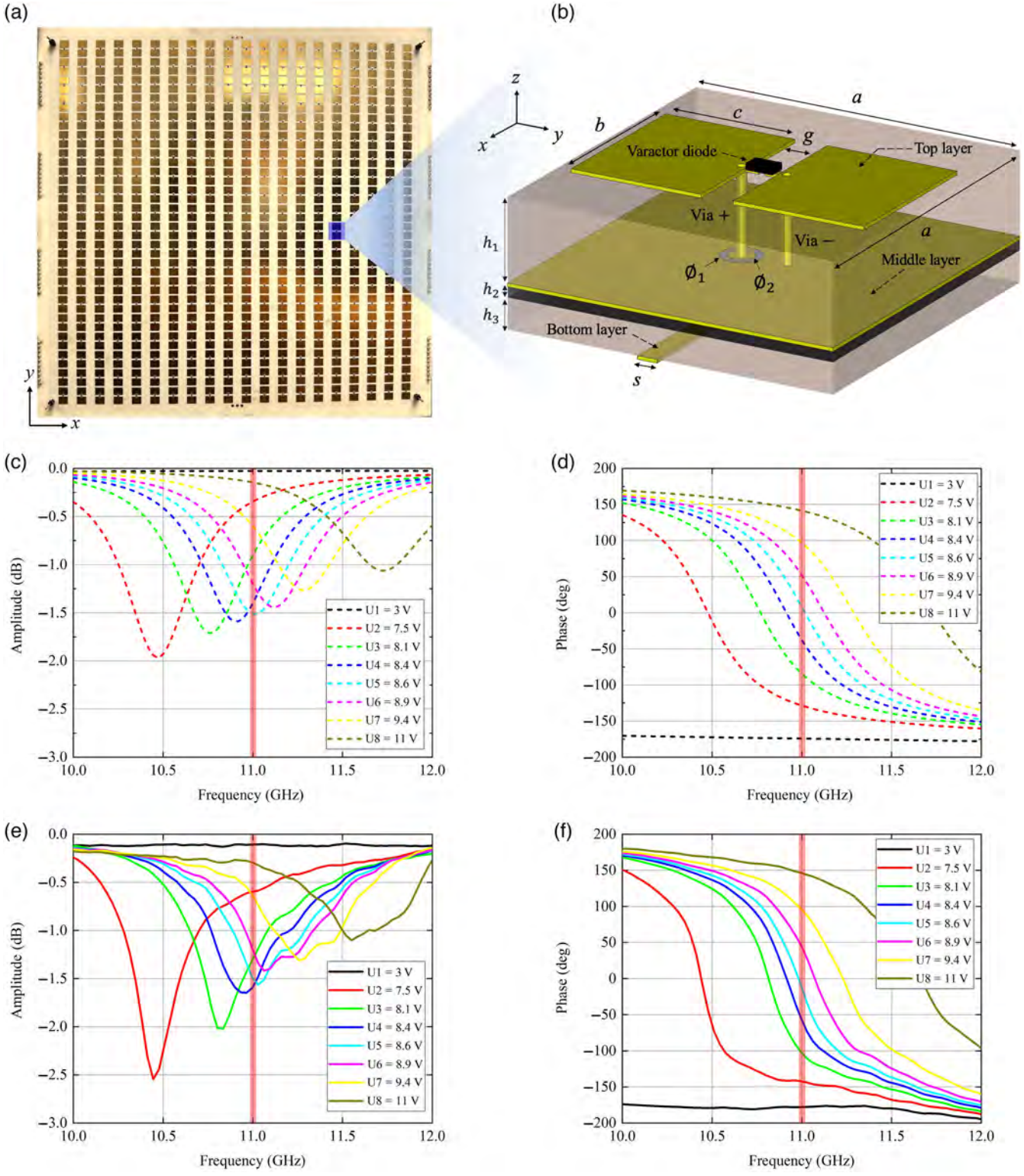

Fig. 2 Metasurface design and reflection responses. (a) Photo of the fabricated space-time-coding digital metasurface. (b) Detailed geometrical parameters of the element structure. (c), (d) Simulated reflection amplitude and phase of the metasurface at different bias voltages, where the vertical orange line indicates the operating frequency at 11 GHz. (e), (f) Measured reflection amplitude and phase of the metasurface at different bias voltages.

from the middle layer by a hollowed ring. The middle layer connects to negative "−" electrode and the bottom layer connects to positive "+" electrode, providing the bias voltage to the varactor diode through the two metallic vias.

To characterize the reflection responses of the metasurface, full-wave simulations are performed (CST Microwave Studio). The simulated reflection amplitude and phase at eight bias voltages from U1 to U8 are shown in Figs. 2(c) and 2(d). As can be seen, we acquire eight different reflection phases at 11 GHz with a 45-deg gradient covering a range of 315 deg, which can be used as 3-bit coding digits from "1" to "8." The corresponding amplitudes at 11 GHz are not uniform, and their differences are controlled within −1.7 dB. The experimental results agree well with the simulation results, as shown in Figs. 2(e) and 2(f), which are obtained by measuring the reflection coefficient of the metasurface in setting the bias voltages for all the elements to be the same one. In addition, we simulate the near-field patterns of the time-varying OAM beam at different time instances, which can be found in Fig. S2 in the Supplementary Material.

3 Results

3.1 Dynamic Field Pattern Measurement of the Time-Varying OAM Beams

For experimental demonstration of the time-varying OAM beams generated by the space-time-coding digital metasurface, we directly measure the time-varying field pattern, including amplitude and phase information at various instants of time. A vector network analyzer can be used in the continuous wave (CW) time sweep mode to measure time-domain S-parameters. However, as the measured S-parameters in the time domain can start at any instant within one modulation cycle, the fields scanned at different positions cannot be compared with each other. Here in addition to the scanning probe S, we add a reference probe R whose position is fixed, and the two probes are measured synchronously. Then the results from the probe R do not vary against different probe S positions except for a time shift, which can now be used to align the S-parameters between signals probed at different positions (see the schematic in Figs. S4 and S5 in the Supplementary Material for more details). In our experiment, as shown in Fig. 3(a), the space-time-coding digital metasurface is applied with 3-bit digital coding sequence [Fig. 1(b)], to generate the time-varying OAM beam with a modulation period around $T = 1$ ms with winding number $w = -1$. The feed horn is placed 0.2 m away from the reflective metasurface to give a monochromatic excitation signal at 11 GHz polarized in the y direction. Note that the feed horn is located at the beam null of the reflected OAM beams to minimize the block effect. Two open-ended waveguide probes (WR-90) are placed 0.44 m away from the metasurface. The stimulus condition of the vector network analyzer (Agilent N5230A) is set as CW time sweep mode at 11 GHz, with a sweep time of 10 ms. Then a time-domain S-parameter waveform (complex value) with a temporal resolution of 12.5 μs can be measured. By simultaneously measuring the probe R and probe S in the scanning range of 0.6 m × 0.6 m, with a step size of 13.6 mm, $45 \times 45 = 2025$ groups of data are obtained. By performing data postprocessing for the received signals at all scanning positions (see details in Sec. 4 in the Supplementary Material), we can map the dynamic amplitude and phase field pattern of the generated time-varying OAM beams at any moment during a modulation cycle.

Figure 3(b) illustrates the measured near-field amplitude and phase patterns of the time-varying OAM beams with $w = -1$ at different instants of time in one period of T, showing the time-varying topological charge l in consecutive integer values. The amplitude patterns with nonzero l show a dark area in the center due to the phase singularity along the OAM beam axis. The nonuniform intensity of the OAM along the azimuthal direction is caused by the differences in reflection amplitude for different coding states at 11 GHz, as shown in Fig. 2(e). In addition, for these phase patterns, a multiannular structure can be observed because the incident beam is seen as a spherical wave when the feed horn is placed not far away enough from the metasurface. The phase pattern of $l = 0$ shows an almost homogeneous phase in the central area and the other patterns with nonzero l show different spiral fringes determined by the value of l. The change of OAM is clearly observable as the spiral fringes vary in time. We observe that these spiral fringes are disconnected from the peripheral phase profile due to the finite size of the fabricated metasurface. Some noise points can be found in the measured field pattern, which is caused by the synchronization error when using two-probe dynamic field mapping.

3.2 OAM Spectrum Analysis and Winding Number Decoding

To further evaluate the OAM mode purity and decode the winding number w of the generated time-varying OAM beams, first we calculate the OAM intensity spectrum $S_{l'}(t)$ by decomposing the field into different angular momenta,[38,39]

$$S_{l'}(t) = \left| \int_{r_1}^{r_2} \int_0^{2\pi} E(\rho, \theta, t) \exp(jl'\theta)\rho \mathrm{d}\theta \, \mathrm{d}\rho \right|^2, \tag{5}$$

where $E(\rho, \theta, t)$ denotes the measured time-varying OAM field in Fig. 3(b), r_1 and r_2 are the radial range of the electric field, and l' is the OAM component to check on the measured field. The OAM intensity spectra for the measured field at different instants of time are shown in Fig. 4(a). Each spectrum contains different l' components, and it is normalized to the maximum component. At each time instant, the OAM field $E(\rho, \theta, t)$ has a topological charge $l(t) = Nt/T$. As can be seen, the OAM intensity spectrum at each time instant is relatively dominated by the component $l' = l(t)$ (marked by a red star), compared with the parasitic ones, showing that the generated beam contains time-varying OAM modes as the theoretical expectation shown in Fig. 1(a). Here we define OAM mode purity as $P(t) = S_{l(t)}/\sum_{l'} S_{l'}$ and obtain the measured mode purity for the dominant topological charges $l(t)$, as shown in the black bar in Fig. 4(b). On the other hand, we can also calculate the theoretical results for the mode purity, as shown in the same figure. We note that the theoretical mode purity is not 100% due to the spatial discretization of the profile $\exp[-jl(t)\theta]$ into eight sectors of constant reflection phases, so that the theoretical mode purity deceases from 100% at $l = 0$ to around 50% at $l = 4$ (-4). Nevertheless, the experimentally extracted mode purity agrees well with the theoretical results. The difference between measured and theoretical results comes from the near-field pattern measurement error, nonuniform azimuthal intensity, and the feed-horn blocking effect. In addition, the insufficient scanning

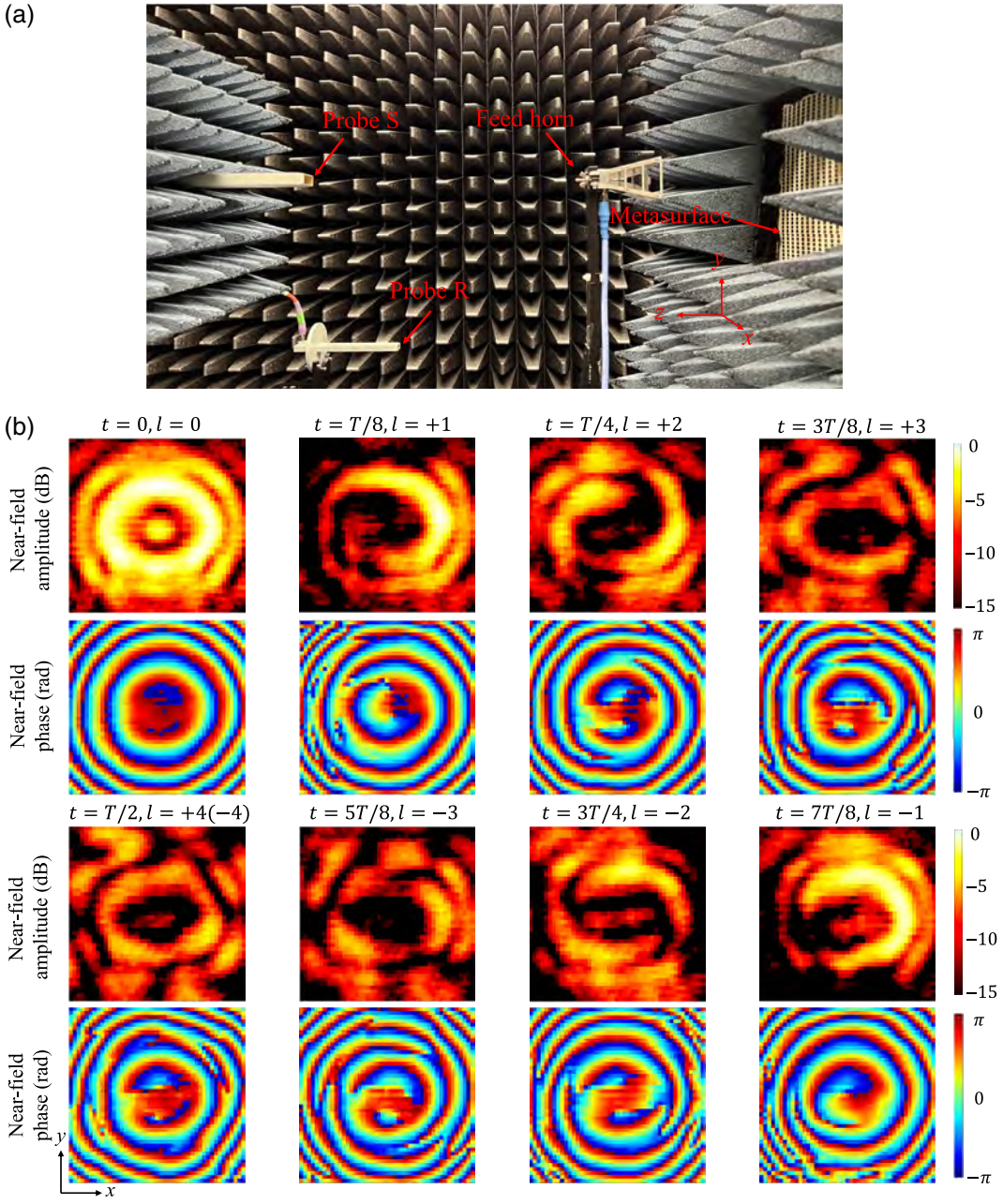

Fig. 3 Dynamic measurement of time-varying OAM field pattern ($w = -1$) using the two-probe technique. (a) Experimental scenario of dynamic electric field pattern measurement of the generated time-varying OAM beams. The probe S is movable to scan the field, and the reference probe R is fixed for synchronization processing. (b) Measured near-field amplitude and phase patterns of the time-varying OAM beams at different time instances in one period of T. The field patterns consisted of $45 \times 45 = 2025$ pixels with a range of 0.6 m × 0.6 m.

range of the field pattern also leads to the lower mode purity, especially for the $l = 4\,(-4)$ case.

Next, we investigate the winding (or twisting) wavefront structure of the time-varying OAM beam. We numerically obtain the field arriving at the measurement plane for a metasurface with zero winding structure using the Fresnel diffraction formula and denote it as $E_b(\rho, \theta, t)$ at different time instants (see Sec. 1 in the Supplementary Material for details). Then the additional phase introduced by the twisting can be obtained from the measured field $E(\rho, \theta, t)$ using

$$\varphi(t) = \arg\left(\int_{r_1}^{r_2}\int_{0}^{2\pi} E(\rho,\theta,t)E_b(\rho,\theta,t)^*\rho \mathrm{d}\theta\,\mathrm{d}\rho\right), \tag{6}$$

which is called twisting phase here; it should be theoretically introduced by Eq. (3), becoming $N2\pi w(t/T)^2 \pmod{2\pi}$. In Fig. 4(c), we plot the twisting phase $\varphi(t)$ at the eight time instances using open circles. They also agree well with the theoretical results (quadratic in time t, with $w = -1$ and $N = 8$), plotted as the red line in the same figure. The results confirm

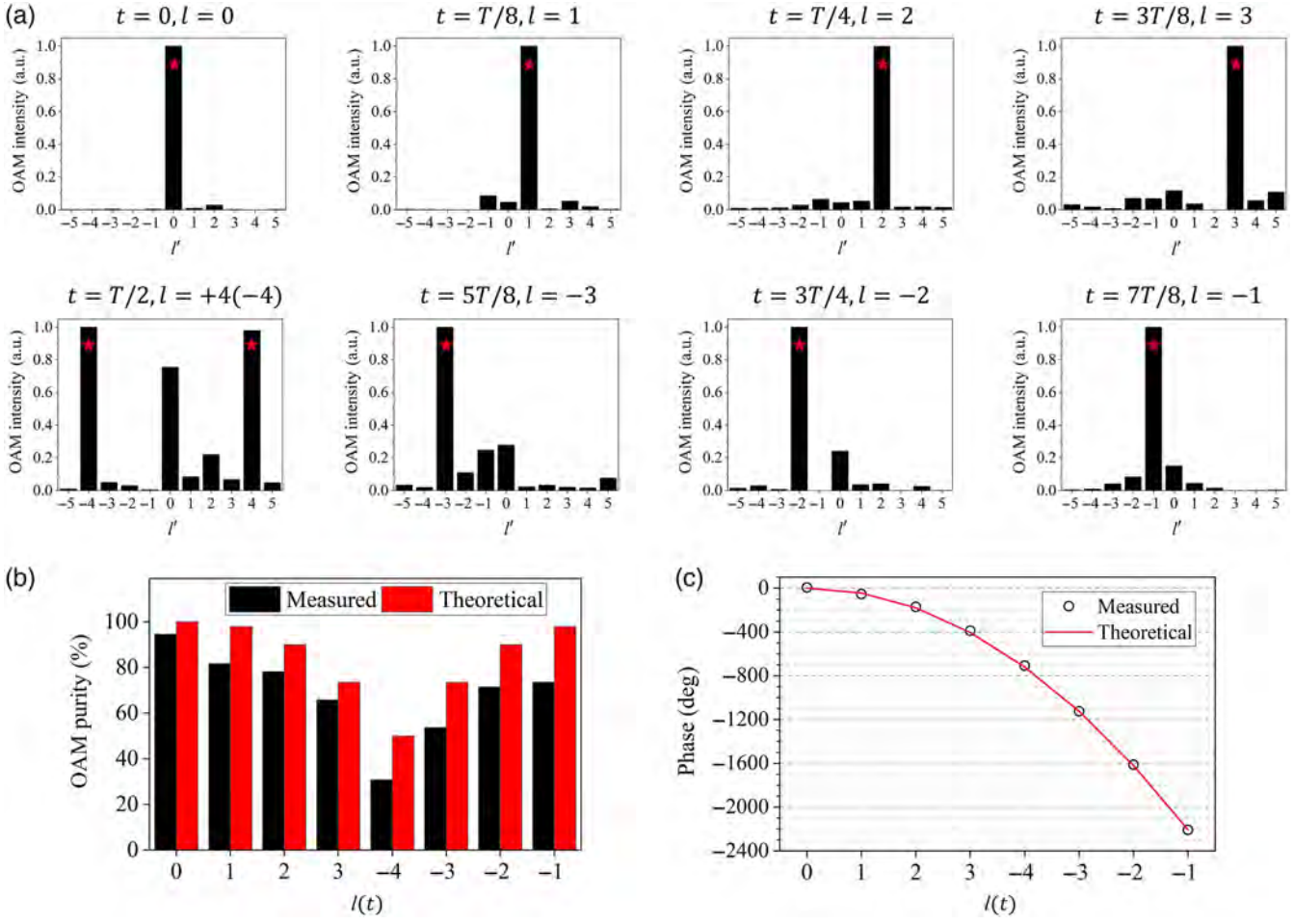

Fig. 4 Spectrum analysis of time-varying OAM. (a) OAM intensity and phase spectrum of the measured time-varying OAM beams at different instants of time. (b) Measured and theoretical OAM mode purity for the dominant $l(t)$. (c) Comparison of measured and theoretical twisting phases for different time instants of dominant $l(t)$.

the realization of the winding number. This also indicates the winding number is a real degree of freedom of time-varying OAM and can be used for information encoding, and it can be decoded from the measured OAM field patterns. This additional degree of freedom is enabled by the flexible programmability of the space-time coding metasurface.

4 Discussion

The space-time-coding digital metasurfaces provide a powerful and flexible platform to manipulate the electromagnetic waves both in the spatial and temporal domains, which contributes to the realization of time-varying OAM beam generation in the current work. In fact, we have only considered the integer case of winding number $w = -1$ as a typical example. The extension to other values, including fractional value, can also be realized with an adjustment of the space-time-coding scheme. For $0 < |w| < 1$, the azimuthal position of zero phase needs to take a time of $T/|w|$ for a full cycle. Then the coding sequence needs to be modified with a longer period of $T/|w|$. For $|w| > 1$, the zero phase rotates around $|w|$ circles in one period of T. The number N of OAM modes varying in one period of T needs to be added to acquire more frames of OAM patterns to characterize the winding number w of time-varying OAM beams.

For experimental verification of the time-varying OAM beam generation, one difficulty is the dynamic measurement of the time-varying amplitude and phase field pattern. The traditional microwave near-field scanning system (which conventionally features one probe) cannot fulfill our demands. The usage of a two-probe measurement technique can observe the OAM amplitude and phase pattern varying in the time domain, which enables the time-varying OAM validation in this work. We note that the S11 signal at the feed horn can also act as the second probe, serving similar purpose of the probe R. Such a two-probe technique might also be applied in other time-varying scenarios to measure other spatiotemporal excitations.

Our proposed metasurface with space-time phase modulation is implemented in the microwave regime. However, it can be extended to other frequency regimes with higher frequencies in terms of principle. From the perspective of implementation, we will need a meta-atom response that can be controlled and tunable in space and time in that frequency regime. For example, in the terahertz regime, by dynamically exciting different metamaterial structures, a reconfigurable wavefront is possible.[40]

In the optical regime, a space-time varying profile of indices can be achieved by the nonlinear Kerr effect.[41] As a brief picture, a micromirror device or an spatial light modulator can be used to excite different locations on metasurface to change the local indices, e.g., using the nonlinear Kerr effect, so that the spatio-temporal profile of the OAM in this work can be achieved based on the elaborated principle. The advantages of introducing time modulation can be twofold. An additional degree of freedom in controlling OAM with a time-varying profile can be used to enhance communication capacity as an immediate application.[42] Moreover, the inhomogeneous OAM profile in both the spatial and temporal domains can also be potentially useful for obtaining unconventional particle trapping, sorting dynamics, and controlling particle trapping stability.[43]

In summary, we have experimentally generated time-varying OAM beams by a space-time-coding digital metasurface in the microwave regime. A higher-order twist described by winding number w in the envelope wavefront structure of time-varying OAM beams is proposed and demonstrated. We develop a two-probe measurement technique to dynamically map the time-varying OAM field patterns and perform the OAM spectrum analysis. The proposed time-varying OAM beams provide new routes in particle manipulation, time-division multiplexing, and information encryption.

Acknowledgment

This work was supported by the Hong Kong Research Grants Council (Project Nos. R6015-18 and C6012-20G).

References

1. R. A. Beth, "Mechanical detection and measurement of the angular momentum of light," *Phys. Rev.* **50**, 115 (1936).
2. L. Allen et al., "Orbital angular momentum of light and the transformation of Laguerre–Gaussian laser modes," *Phys. Rev. A* **45**, 8185 (1992).
3. G. Gibson et al., "Free-space information transfer using light beams carrying orbital angular momentum," *Opt. Express* **12**, 5448–5456 (2004).
4. G. Molina-Terriza, J. P. Torres, and L. Torner, "Twisted photons," *Nat. Phys.* **3**, 305–310 (2007).
5. J. Wang et al., "Terabit free-space data transmission employing orbital angular momentum multiplexing," *Nat. Photonics* **6**, 488–496 (2012).
6. N. Bozinovic et al., "Terabit-scale orbital angular momentum mode division multiplexing in fibers," *Science* **340**, 1545–1548 (2013).
7. Y. Yan et al., "High-capacity millimetre-wave communications with orbital angular momentum multiplexing," *Nat. Commun.* **5**, 4876 (2014).
8. J. Wang et al., "Orbital angular momentum and beyond in free-space optical communications," *Nanophotonics* **11**, 645–680 (2022).
9. D. G. Grier, "A revolution in optical manipulation," *Nature* **424**, 810–816 (2003).
10. M. Padgett and R. Bowman, "Tweezers with a twist," *Nat. Photonics* **5**, 343–348 (2011).
11. Y. Shen et al., "Optical vortices 30 years on: OAM manipulation from topological charge to multiple singularities," *Light Sci. Appl.* **8**, 90 (2019).
12. L. Zhu et al., "Optical vortex lattice: an exploitation of orbital angular momentum," *Nanophotonics* **10**, 2487–2496 (2021).
13. K. Y. Bliokh and F. Nori, "Spatiotemporal vortex beams and angular momentum," *Phys. Rev. A* **86**, 033824 (2012).
14. N. Jhajj et al., "Spatiotemporal optical vortices," *Phys. Rev. X* **6**, 031037 (2016).
15. S. Hancock et al., "Free-space propagation of spatiotemporal optical vortices," *Optica* **6**, 1547–1553 (2019).
16. A. Chong et al., "Generation of spatiotemporal optical vortices with controllable transverse orbital angular momentum," *Nat. Photonics* **14**, 350–354 (2020).
17. S. Hancock, S. Zahedpour, and H. Milchberg, "Mode structure and orbital angular momentum of spatiotemporal optical vortex pulses," *Phys. Rev. Lett.* **127**, 193901 (2021).
18. X. Zhang et al., "Basis function approach for diffractive pattern generation with Dammann vortex metasurfaces," *Sci. Adv.* **8**, eabp8073 (2022).
19. X. Zhang et al., "Multiplexed generation of generalized vortex beams with on-demand intensity profiles based on metasurfaces," *Laser Photonics Rev.* **16**, 2100451 (2022).
20. L. Rego et al., "Generation of extreme-ultraviolet beams with time-varying orbital angular momentum," *Science* **364**, eaaw9486 (2019).
21. A. Picón et al., "Transferring orbital and spin angular momenta of light to atoms," *New J. Phys.* **12**, 083053 (2010).
22. D. Gao et al., "Optical manipulation from the microscale to the nanoscale: fundamentals, advances and prospects," *Light Sci. Appl.* **6**, e17039 (2017).
23. M. Li et al., "Orbital angular momentum in optical manipulations," *J. Opt.* **24**, 114001 (2022).
24. E. Wright, J. Arlt, and K. Dholakia, "Toroidal optical dipole traps for atomic Bose–Einstein condensates using Laguerre–Gaussian beams," *Phys. Rev. A* **63**, 013608 (2000).
25. A. Turpin et al., "Blue-detuned optical ring trap for Bose–Einstein condensates based on conical refraction," *Opt. Express* **23**, 1638–1650 (2015).
26. J. W. McIver et al., "Light-induced anomalous Hall effect in graphene," *Nat. Phys.* **16**, 38–41 (2020).
27. C. Bao et al., "Light-induced emergent phenomena in 2D materials and topological materials," *Nat. Rev. Phys.* **4**, 33–48 (2022).
28. H. B. Sedeh, M. M. Salary, and H. Mosallaei, "Time-varying optical vortices enabled by time-modulated metasurfaces," *Nanophotonics* **9**, 2957–2976 (2020).
29. L. Zhang et al., "Space-time-coding digital metasurfaces," *Nat. Commun.* **9**, 4334 (2018).
30. L. Zhang et al., "Breaking reciprocity with space-time-coding digital metasurfaces," *Adv. Mater.* **31**, 1904069 (2019).
31. J. Y. Dai et al., "High-efficiency synthesizer for spatial waves based on space-time-coding digital metasurface," *Laser Photonics Rev.* **14**, 1900133 (2020).
32. X. Wang et al., "Amplification and manipulation of nonlinear electromagnetic waves and enhanced nonreciprocity using transmissive space-time-coding metasurface," *Adv. Sci.* **9**, 2105960 (2022).
33. J. Zhao et al., "Programmable time-domain digital-coding metasurface for non-linear harmonic manipulation and new wireless communication systems," *Natl. Sci. Rev.* **6**, 231–238 (2019).
34. S. R. Wang et al., "Asynchronous space-time-coding digital metasurface," *Adv. Sci.* **9**, 2200106 (2022).
35. Q. Hu et al., "Arbitrary and dynamic Poincaré sphere polarization converter with a time-varying metasurface," *Adv. Opt. Mater.* **10**, 2101915 (2022).
36. J. C. Ke et al., "Linear and nonlinear polarization syntheses and their programmable controls based on anisotropic time-domain digital coding metasurface," *Small Struct.* **2**, 2000060 (2021).
37. Q. Hu et al., "On-demand dynamic polarization meta-transformer," *Laser Photonics Rev.* **17**, 2200479 (2023).
38. T. Kaiser et al., "Complete modal decomposition for optical fibers using CGH-based correlation filters," *Opt. Express* **17**, 9347–9356 (2009).
39. F. Hosseini et al., "Temporal shaping and time-varying orbital angular momentum of displaced vortices," *Optica* **7**, 1359–1371 (2020).

40. J. Guo et al., "Reconfigurable terahertz metasurface pure phase holograms," *Adv. Opt. Mater.* **7**, 1801696 (2019).
41. X. Guo et al., "Nonreciprocal metasurface with space-time phase modulation," *Light Sci. Appl.* **8**, 123 (2019).
42. Y. Jia et al., "Orbital angular momentum multiplexing in space-time thermoacoustic metasurfaces," *Adv. Mater.* **34**, 2202026 (2022).
43. V. Bobkova et al., "Optical grinder: sorting of trapped particles by orbital angular momentum," *Opt. Express* **29**, 12967–12975 (2021).

Jingxin Zhang received his BS and MS degrees from Beihang University, Beijing, China. He is currently a PhD student, supervised by Prof. Jensen Li, in the Physics Department at the Hong Kong University of Science and Technology, Hong Kong, China. His research interests are focused on programmable digital-coding metasurface, time-varying metamaterials, and machine-learning techniques with the application of beam steering, harmonics manipulation, information encryption, and orbital angular momentum generation.

Peixing Li is currently a final-year undergraduate student in the Department of Electrical Engineering at the City University of Hong Kong. He is conducting research supervised by Dr. Alex M. H. Wong and is a member of the Departmental Undergraduate Research Fellowship. His coursework and research focus on applied electromagnetics, microwave engineering, antenna design, and metamaterials. His research experience includes digital modulation mechanism of time-varying systems, programmable metasurface, and antenna design and measurement.

Ray C. C. Cheung received his BEng (Hons.) and MPhil degrees in computer engineering and computer science and engineering from the Chinese University of Hong Kong and the DIC and PhD degrees in computing from the Imperial College London. He received the Hong Kong Croucher Foundation Fellowship and moved to Los Angeles in Electrical Engineering Department at UCLA. He is an associate professor in the Department of Electrical Engineering at the City University of Hong Kong and at the Digital Systems Laboratory. His current research interests include cryptographic hardware and processor architecture designs.

Alex M. H. Wong obtained his doctoral degree in electrical engineering from the University of Toronto. He is currently an assistant professor in the Department of Electrical Engineering at the City University of Hong Kong. He is also a member of the State Key Laboratory of Terahertz and Millimeter Waves. His research interests lie in metasurfaces from optical to microwave frequencies and applied electromagnetics in general, with societal applications in telecommunication and biomedicine.

Jensen Li is a professor of physics at the Hong Kong University of Science and Technology. His research focuses on optical metasurfaces, non-Hermitian systems, transformation optics, and acoustic metamaterials, resulting in more than 100 peer-reviewed publications. He has led a collaborative research project on "Non-Hermitian Systems in Optics and Acoustics" across several Hong Kong universities. He was elected Croucher senior research fellow in 2022 and is a member of the Hong Kong Young Academy of Sciences.

Research Article

ADVANCED PHOTONICS

Propagation of transverse photonic orbital angular momentum through few-mode fiber

Qian Cao,[a,b,c] Zhuo Chen,[a] Chong Zhang,[a] Andy Chong,[d] and Qiwen Zhan[a,b,c,*]

[a]University of Shanghai for Science and Technology, School of Optical-Electrical and Computer Engineering, Shanghai, China
[b]Zhangjiang Laboratory, Shanghai, China
[c]University of Shanghai for Science and Technology, Shanghai Key Laboratory of Modern Optical System, Shanghai, China
[d]Pusan National University, Department of Physics, Busan, Republic of Korea

Abstract. Spatiotemporal optical vortex (STOV) pulses can carry transverse orbital angular momentum (OAM) that is perpendicular to the direction of pulse propagation. For a STOV pulse, its spatiotemporal profile can be significantly distorted due to unbalanced dispersive and diffractive phases. This may limit its use in many research applications, where a long interaction length and a tight confinement of the pulse are needed. The first demonstration of STOV pulse propagation through a few-mode optical fiber is presented. Both numerical and experimental analysis on the propagation of STOV pulse through a commercially available SMF-28 standard telecommunication fiber is performed. The spatiotemporal phase feature of the pulse can be well kept after the pulse propagates a few-meter length through the fiber even with bending. Further propagation of the pulse will result in a breakup of its spatiotemporal spiral phase structure due to an excessive amount of modal group delay dispersion. The stable and robust transmission of transverse photonic OAM through optical fiber may open new opportunities for transverse photonic OAM studies in telecommunications, OAM lasers, and nonlinear fiber-optical research.

Keywords: photonic orbital angular momentum; spatiotemporal optical vortices; multimode fiber.

Received Feb. 7, 2023; revised manuscript received Mar. 10, 2023; accepted for publication Mar. 27, 2023; published online Apr. 17, 2023.

[DOI: 10.1117/1.AP.5.3.036002]

1 Introduction

Since Allen[1] published his paper on discovering that higher-order Laguerre–Gaussian beam with a spiral phase wavefront $\exp(il\theta_{x-y})$ carries photons with a longitudinal orbital angular momentum (OAM) in 1992, great success has occurred in the past three decades on utilizing optical vortex beam with OAM in research fields such as optical manipulation,[2] optical communication,[3] quantum optics,[4] superresolution microscopy,[5] and many others.[6,7] Very recently, scientists have discovered, both theoretically and experimentally, that photons can also carry a transverse photonic OAM in the form of spatiotemporal optical vortex (STOV) pulses.[8–11] Differing from the vortex beam, the STOV pulse has a spiral phase $\exp(il\theta_{x-t})$ in the spatiotemporal domain ($x-t$ plane). The STOV pulse, therefore, can carry a transverse photonic OAM of $l\hbar$ per photon.[12–14] Since its discovery, much research has been done in studying STOV pulse, including studying its propagation dynamics,[15,16] developing novel characterization approaches,[17–19] utilizing STOV pulse in spatiotemporal imaging,[20] and designing other types of wave packets that also carry transverse photonic OAM.[21–25]

STOV pulse has a spatiotemporally coupled field distribution. Under an unbalanced dispersion and diffraction phase, the STOV pulse can be significantly distorted,[15,16] leading to a breakup of the STOV charge and splitting the STOV pulse into multiple lobes in the spatiotemporal domain. This limits the use of the STOV pulse in many applications where a long interaction length and a tight confinement of the pulse are needed. One solution for overcoming this limitation is to generate a STOV pulse in a Bessel form in the spatiotemporal domain so the STOV charge is confined within a tight space-time cross section and the STOV pulse can be nonspreading when it propagates in a dispersive medium.[26,27] However, this Bessel STOV approach requires the pulse to be engineered to accommodate

*Address all correspondence to Qiwen Zhan, qwzhan@usst.edu.cn

the dispersion relationship of the medium, and the resulting nonspreading propagation distance is still limited by the finite spatial and spectral width of the pulse.

Another approach for achieving a long-distance, stable propagation of the STOV pulse is to use a few-mode optical fiber to guide the STOV pulse. A step-index fiber can support multiple guiding modes if the V-number, defined as $V = k_0 a \cdot \mathrm{NA}$, is larger than 2.405,[28] which forms the fundamental basis for propagating the STOV pulse. Till now, no study on transmitting a STOV pulse through optical fiber or waveguide has been demonstrated. Questions such as how the STOV pulse is going to evolve spatiotemporally after propagating through the fiber, what the maximum transmission length is, and whether it can propagate forever inside the fiber are yet to be explored.

To answer these questions, we present here what we believe is the first demonstration of STOV pulse propagation through a few-mode optical fiber. We choose a commercially available, standard telecommunication fiber, SMF-28, as our platform to perform all the studies. We implement both numerical and experimental analysis on propagating the STOV pulse through the fiber. The spatiotemporal spiral phase structure of STOV pulses can be kept well for a considerable length of a few meters. Further propagating the pulse inside the fiber will result in a breakup of its phase structure due to an excessive amount of group delay difference. Nevertheless, our experiment achieved a long-distance, stable, and robust transmission of transverse photonic OAM through the fiber. This will bring new opportunities in utilizing transverse photonic OAM in optical telecommunication, building novel transverse OAM lasers, and studying nonlinear fiber optical phenomena that involve transverse OAM.

2 Theoretical Analysis and Numerical Simulations

The STOV pulse has an annular intensity profile with a spiral phase of $\exp(il\theta_{x-t})$ in the spatiotemporal $(x-t)$ domain. Figure 1(a) shows the spatiotemporal intensity and phase profile of a STOV pulse with a topological charge of $l = +1$. The analytical expression for the STOV pulse (including chirped STOV pulse) can be found in Eqs. (6) and (7) in Ref. [15]. As the spatiotemporal phase is whirling inside the pulse, the spatial mode of the STOV pulse varies significantly over time.

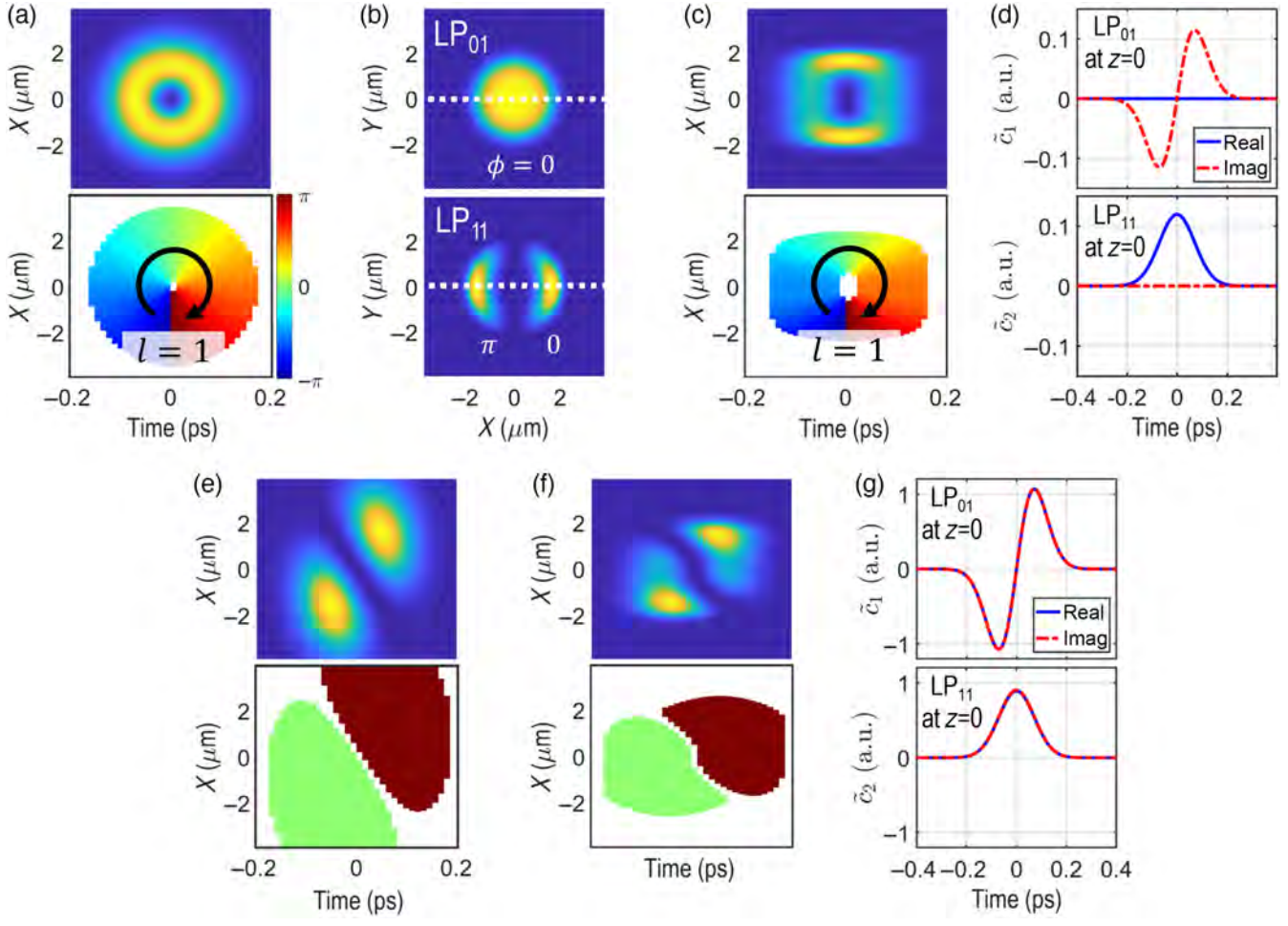

Fig. 1 Modal decomposition of STOV pulse and focused STOV pulse in LP modes. (a) Spatiotemporal intensity and phase profile of a STOV pulse ($l = +1$); (b) spatial intensity profile of LP_{01} and LP_{11} modes in SMF-28; (c) STOV pulse ($l = +1$) synthesized by LP modes; (d) complex coefficient for LP modes for synthesizing a STOV pulse. (e) spatiotemporal intensity and phase profile of a focused STOV pulse ($l = +1$); (f) focused STOV pulse ($l = +1$) synthesized by LP modes; (g) complex coefficient for LP modes for synthesizing a focused STOV pulse.

Table 1 Propagation parameters for LP_{01} and LP_{11} modes of SMF-28.

Parameter	Brief Description	Mode	Value	Unit
n_{eff}	Effective refractive index, $n_{\text{eff}} = \beta/k_0$	LP_{01}	1.446191	
		LP_{11}	1.443798	
n_g	Effective group index, $n_g = c/v_g$, $v_g = (\beta_1)^{-1} = (\partial\beta/\partial\omega)^{-1}$	LP_{01}	1.463457	
		LP_{11}	1.463508	
β_2	GVD coefficient, $\beta_2 = \partial^2\beta/\partial\omega^2$	LP_{01}	18.99	fs^2/mm
		LP_{11}	28.61	
ΔT	Group delay difference between LP_{01} and LP_{11}		−170	fs/m

To transmit it inside the optical fiber, the fiber must support multiple guiding modes. We choose a standard commercially available telecommunication fiber, Corning SMF-28, as our platform to study STOV pulse propagation. SMF-28 has a cutoff wavelength at 1260 nm.[29] Assuming that the input STOV pulse is linearly polarized (LP) with a center wavelength of 1030 nm, under weakly guiding approximation, the STOV pulse can be coupled into two LP modes of SMF-28, LP_{01} and LP_{11} mode. Figure 1(b) plots the spatial intensity profile of LP_{01} and LP_{11} mode with their spatial phase captioned in the figure. To simplify the calculation process, we choose the field along the horizontal dashed line shown in Fig. 1(b) as the eigen function for the LP modes. An LP STOV pulse can be thus decomposed into the combination of LP_{01} and LP_{11} mode, written as

$$E_{\text{STOV}}(x,t;z) = \tilde{c_1}(t;z)E_{01}(x) + \tilde{c_2}(t;z)E_{11}(x), \tag{1}$$

where $\tilde{c_1}(t;z)$ and $\tilde{c_2}(t;z)$ are the complex coefficient for LP_{01} and LP_{11} mode. t is the localized time coordinate for characterizing the STOV pulse and z is the longitudinal coordinate for the fiber length. $E_{01}(x)$ and $E_{11}(x)$ are the normalized eigen function for LP_{01} and LP_{11} mode.

Figure 1(c) shows the spatiotemporal profile of the STOV pulse with a topological charge of $l = +1$ synthesized by LP_{01} and LP_{11} mode. Compared with the STOV pulse in free space [Fig. 1(a)], the STOV pulse in a few-mode fiber is more confined spatially in the x direction due to the waveguide structure. Nevertheless, the spatiotemporal phase feature of the STOV pulse can be kept in this modal decomposition. The complex coefficients $\tilde{c_1}$ and $\tilde{c_2}$ in Eq. (1) are obtained by calculating the overlapping integral between the STOV pulse and the eigen function. Figure 1(d) plots the real part and the imaginary part of $\tilde{c_1}$ and $\tilde{c_2}$ over time, respectively. There is a $\pi/2$ phase difference between $\tilde{c_1}$ and $\tilde{c_2}$.

In the STOV pulses shown in Figs. 1(a) and 1(c), we have assumed that the STOV pulse is already propagating inside the fiber. In practice, a free-space STOV pulse is normally focused into the fiber by an aspherical lens. Figure 1(e) shows the spatiotemporal intensity and phase profile when the STOV pulse is focused. Differing from its free-space form, a focused STOV pulse has two lobes with a π-phase difference between them. Assuming this focused STOV pulse can be perfectly coupled into the fiber, it can be then decomposed into LP modes, as shown in Fig. 1(f). The phase feature is still well kept. Figure 1(g) plots the complex coefficients of the LP modes. Differing from previous modal decomposition, $\tilde{c_1}$ and $\tilde{c_2}$ are now in phase with each other.

To simulate the STOV pulse propagation inside the fiber, we need to make two assumptions: (1) the STOV pulse is propagating linearly inside the fiber without any loss and (2) there is no cross talk between different LP modes. With these assumptions, the evolution of the STOV pulse is dictated by the propagation constant β, including its dispersion relationship. These parameters can be numerically calculated by solving the paraxial Helmholtz equation. [27] Table 1 lists the calculated effective refractive index n_{eff}, effective group index n_g, and the group velocity dispersion (GVD) coefficient β_2 at 1030 nm. ΔT is the group delay difference between the LP_{01} and LP_{11} modes. After propagation, 1 m length inside the fiber, LP_{01}-mode pulse will lead LP_{11}-mode pulse by 170 fs.

We now perform numerical simulation of the focused STOV pulse propagation in SMF-28 by setting the virtual fiber length at 100, 200, and 300 cm. The STOV pulse has a topological charge of $l = +1$. Figure 2(a) shows the results when an unchirped focused STOV pulse is propagating. Due to the GVD and group velocity mismatch (GVM), a focused STOV pulse is distorted during pulse propagations. However, at 100 and 200 cm, the spatiotemporal spiral phase of the STOV pulse is still well preserved, showing a spiral phase with a topological charge of $l = +1$. Further propagating the pulse to 300 cm will merge the spatiotemporal phase singularity with other spatiotemporal phase singularity (note here we plot the phase only for a field whose intensity is >1% of the peak intensity). We consider this as a breakup of the STOV charge. These additional phase singularities are formed by the interference between the LP_{01}-mode pulse and the LP_{11}-mode pulse. To elucidate the cause of this STOV breakup, we perform two more simulations by turning off the GVM and GVD effect separately. The results are shown in Figs. 2(b) and 2(c). When the GVM effect is off [Fig. 2(b)], the pulse will expand symmetrically in space time as it propagates. The spatiotemporal spiral phase is always preserved in the process. When GVD effect is off, the LP_{01}-mode pulse and the LP_{11}-mode pulse propagate in different group velocities. They are temporally walked off for all three propagation distances, and there is no spatiotemporal spiral phase structure anymore. We conclude that the GVM effect is the cause of the STOV charge breakup in the fiber propagation. Changing SMF-28 to an optical fiber with less GVM, for example, a graded-index few-mode fiber, may achieve a longer transmission length for the STOV pulse.

In practice, the input STOV pulse may be chirped. Here, we perform another set of simulations by sending a positively chirped STOV pulse into the fiber. It is positively chirped to have 7 times the pulse duration of its transform-limited form.

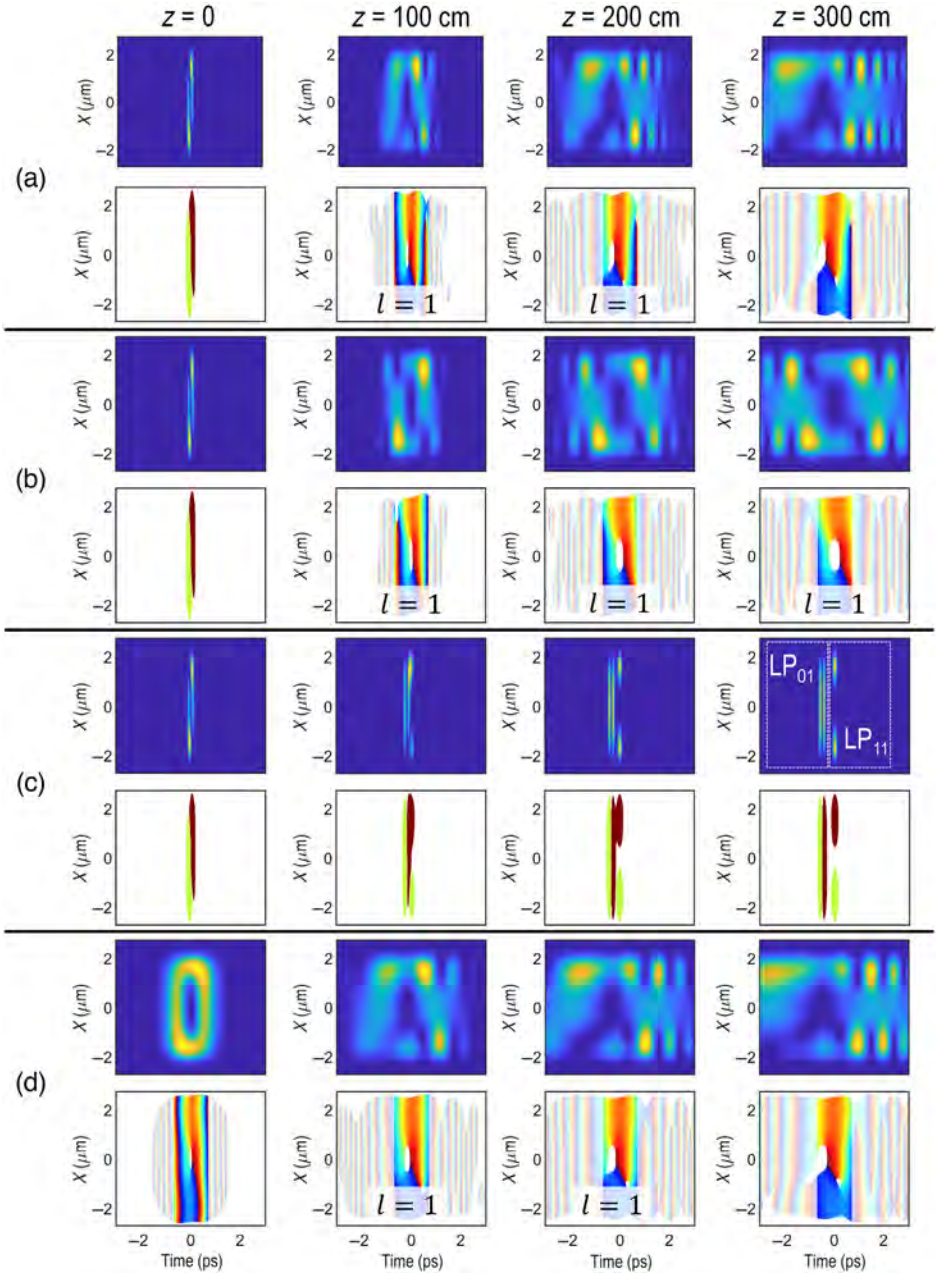

Fig. 2 Numerical propagation of focused STOV pulse in few-mode fiber. (a) Unchirped focused STOV pulse; (b) unchirped focused STOV pulse with GVM between LP modes set at zero; (c) unchirped focused STOV pulse with GVD of each LP mode set at zero; (d) chirped focused STOV pulse.

The results are shown in Fig. 2(d). Similar to the unchirped STOV pulse situation [Fig. 2(a)], an initially chirped STOV pulse can preserve its spatiotemporal spiral phase feature for a propagation distance of 100 and 200 cm. Further propagating, the pulse will cause its phase singularity to merge with other singularities, resulting in the breakup of the STOV charge.

3 Experimental Results and Discussions

In the laboratory, we use a home-built Yb:fiber laser system as our master laser to perform all the experiments. Figure 3 illustrates the schematic of the experimental setup for generating, transmitting, and measuring the STOV pulse through a few-mode optical fiber. The setup has a Mach–Zehnder interferometer configuration. The output of the mode-locked Yb:fiber laser is split into two replicas. (1) One replica that goes in the upper direction in Fig. 3 is phase modulated in its spatial-spectral ($x-\Omega$) domain to form the STOV pulse.[10] The STOV pulse is then coupled into a 100-cm-long few-mode fiber (Corning SMF-28) using an aspherical lens (Thorlabs A280TM-B) mounted on a 3D translation stage (Thorlabs NanoMax 300). It is noteworthy that the fiber is bent 270 deg in the laboratory

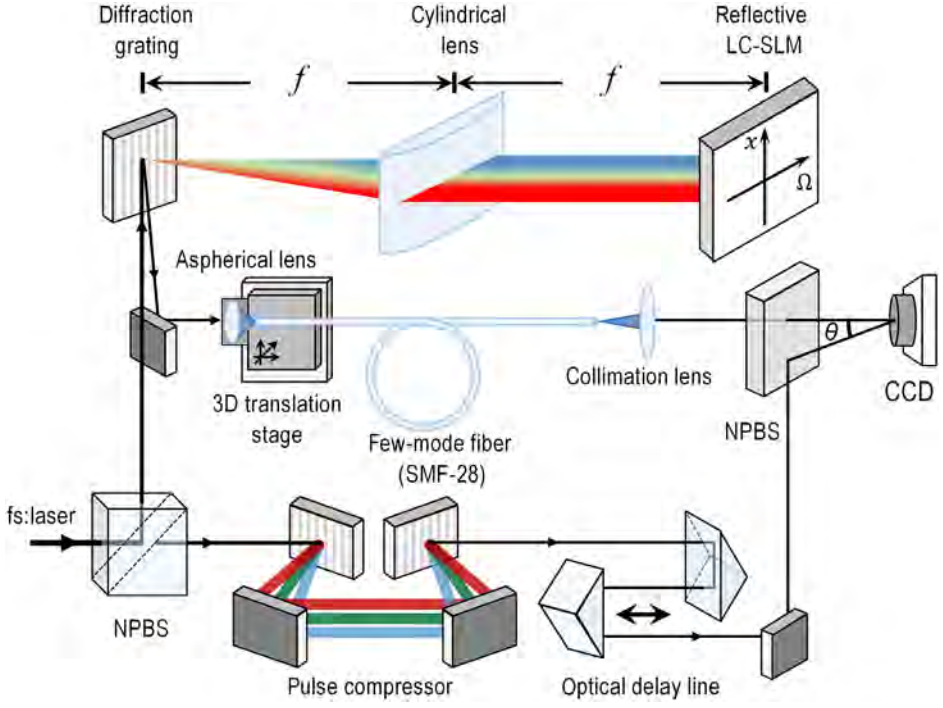

Fig. 3 Schematic for transmitting and measuring STOV pulse through few-mode optical fiber. The system is pumped by a home-built Yb:fiber laser system. One replica of the laser output is spatiotemporally modulated to a STOV pulse. It is then coupled into a few-mode fiber (SMF-28) by a high-NA aspherical lens mounted on a 3D translation stage. Another replica of the laser output is compressed and delay-controlled to serve as a probe pulse to measure the transmitted STOV pulse.

to save lab space. After the fiber, the STOV pulse is collimated and sent into a CCD camera (Ophir SP932U). (2) The other replica of the laser output that goes in the right direction in Fig. 3 is compressed by a grating-pair pulse compressor. The compressed pulse has a pulse duration of 160 fs, and it is close to the transform limit. This pulse serves as the probe pulse for measuring the STOV pulse. The probe pulse is recombined with the transmitted STOV in both the spatial and temporal domains at the CCD. Their relative time delay is controlled by an optical delay line placed in the probe arm. The captured CCD images with interference fringes between the STOV pulse and the probe pulse can be used to reconstruct the 3D intensity and phase profile of the STOV pulse.[10]

The STOV pulse is generated by applying a spatial–spectral spiral phase $\exp(il\theta_{x-\Omega})$. The topological charge l is selected to be $+1$ and -1. For both situations, the STOV pulse is chirped to a group delay dispersion (GDD) of $+36{,}000$ fs^2 before it is coupled into the fiber. The chirp of the STOV pulse is controlled by a quadratic spectral phase using a liquid crystal spatial light modulator (LC-SLM, Holoeye GAEA-2-NIR-069) in our setup. Figure 4 shows the measurement results of the STOV pulse after it propagates through the few-mode optical fiber. The results have confirmed that the STOV pulse's phase singular structure is well kept after the pulse propagates 100 cm through the few-mode fiber. At the tail of the pulse ($t > 0$), the interference pattern caused by GVM between LP modes also is in good agreement with the simulation results. Our current experimental platform achieves transmission of a STOV pulse with a charge of $l = \pm 1$. Achieving the transmission of a STOV pulse with a higher order requires the fiber to support more guiding modes and may also require the STOV pulse to be well engineered, especially in the spatial domain, before it is coupled into the fiber.

4 Conclusions and Outlook

We present the first demonstration of STOV pulse propagation through a step-index, few-mode optical fiber. We perform both numerical and experimental analysis on the propagation dynamics of the STOV pulse inside the fiber. The spatiotemporal spiral phase feature of the pulse can be well kept for a few-meter propagation distance inside the fiber. Further propagating the pulse will break up the STOV phase singularity structure due to an excessive amount of modal group delay difference accumulated from the GVM between LP modes. Changing the fiber to a graded-index fiber with less GVM may extend the maximum transmission length of the STOV pulse. In addition, the interference between LP modes inside the fiber may generate spatiotemporal structures that greatly resemble STOV pulses generated by a partially temporally coherent source,[22] which may be a new approach for producing transverse photonic OAM sources. Further investigation of transmission of transverse photonic OAM through optical fiber may open new avenues for optical telecommunication, building novel transverse OAM lasers, and studying nonlinear fiber optical phenomena that involve transverse OAM.

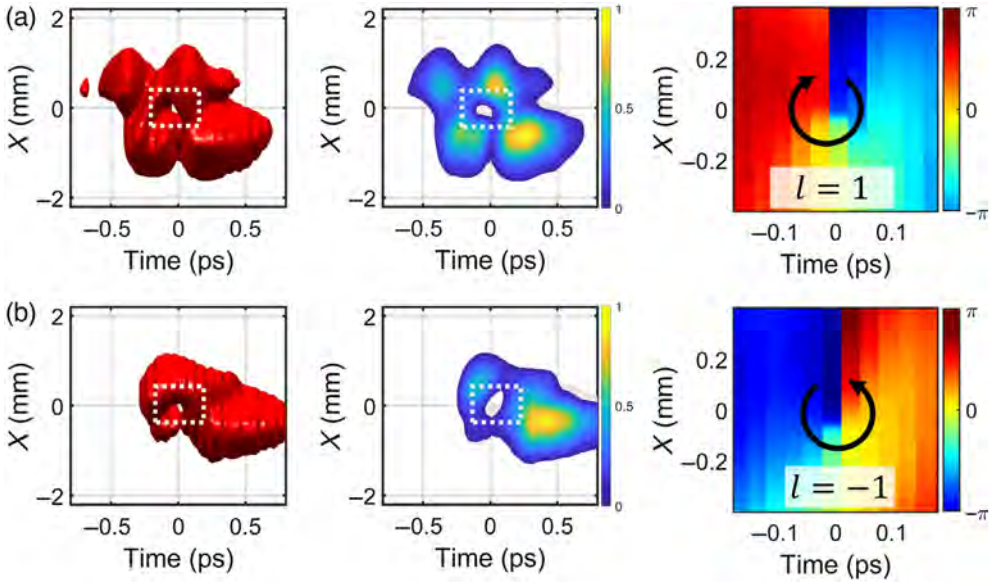

Fig. 4 3D measurement results for positively chirped STOV pulse transmitted by few-mode optical fiber. (a) Topological charge $l = +1$ and (b) topological charge $l = -1$. The STOV pulse has an initial GDD of 36,000 fs^2 before fiber transmission.

Acknowledgments

We acknowledge support from the National Natural Science Foundation of China (NSFC) [Grant Nos. 92050202 (Q.Z.) and 12104309 (Q.C.)], the Shanghai Science and Technology Committee [Grant No. 19060502500 (Q.Z.)], the Shanghai Sailing Program [Grant No. 21YF1431500 (Q.C.)], and the National Research Foundation of Korea (NRF) funded by the Korea government (MSIT) [Grant No. 2022R1A2C1091890 (A.C.)]. The authors have no conflicts to disclose.

Code, Data, and Materials Availability

The data and code for numerical calculation that support the findings of this study are available from the corresponding author upon reasonable request.

References

1. L. Allen et al., "Orbital angular momentum of light and the transformation of Laguerre-Gaussian laser modes," *Phys. Rev. A* **45**, 8185–8189 (1992).
2. M. Padgett and R. Bowman, "Tweezers with a twist," *Nat. Photonics* **5**(6), 343–348 (2011).
3. N. Bozinovic et al., "Terabit-scale orbital angular momentum mode division multiplexing in fibers," *Science* **340**(6140), 1545–1548 (2013).
4. M. Krenn et al., "Orbital angular momentum of photons and the entanglement of Laguerre–Gaussian modes," *Philos. Trans. A Math. Phys. Eng. Sci.* **375**(2087), 20150442 (2017).
5. S. W. Hell, "Far-field optical nanoscopy," *Science* **316**(5828), 1153–1158 (2007).
6. A. M. Yao and M. J. Padgett, "Orbital angular momentum: origins, behavior and applications," *Adv. Opt. Photonics* **3**, 161–204 (2011).
7. M. J. Padgett, "Orbital angular momentum 25 years on [Invited]," *Opt. Express* **25**, 11265–11274 (2017).
8. A. P. Sukhorukov and V. V. Yangirova, "Spatio-temporal vortices: properties, generation and recording," *Proc. SPIE* **5949**, 594906 (2005).
9. K. Y. Bliokh and F. Nori, "Spatiotemporal vortex beams and angular momentum," *Phys. Rev. A* **86**, 033824 (2012).
10. A. Chong et al., "Generation of spatiotemporal optical vortices with controllable transverse orbital angular momentum," *Nat. Photonics* **14**(6), 350–354 (2020).
11. S. W. Hancock et al., "Free-space propagation of spatiotemporal optical vortices," *Optica* **6**, 1547–1553 (2019).
12. G. Gui et al., "Second-harmonic generation and the conservation of spatiotemporal orbital angular momentum of light," *Nat. Photonics* **15**(8), 608–613 (2021).
13. S. W. Hancock, S. Zahedpour, and H. M. Milchberg, "Second-harmonic generation of spatiotemporal optical vortices and conservation of orbital angular momentum," *Optica* **8**, 594–597 (2021).
14. Y. Fang, S. Lu, and Y. Liu, "Controlling photon transverse orbital angular momentum in high harmonic generation," *Phys. Rev. Lett.* **127**(27), 273901 (2021).
15. S. W. Hancock, S. Zahedpour, and H. M. Milchberg, "Mode structure and orbital angular momentum of spatiotemporal optical vortex pulses," *Phys. Rev. Lett.* **127**, 193901 (2021).
16. S. Huang et al., "Properties of the generation and propagation of spatiotemporal optical vortices," *Opt. Express* **29**, 26995–27003 (2021)
17. S. W. Hancock, S. Zahedpour, and H. M. Milchberg, "Transient-grating single-shot supercontinuum spectral interferometry (TG-SSSI)," *Opt. Lett.* **46**, 1013–1016 (2021).
18. S. Huang et al., "Diffraction properties of light with transverse orbital angular momentum," *Optica* **9**, 469–472 (2022).
19. G. Gui et al., "Single-frame characterization of ultrafast pulses with spatiotemporal orbital angular momentum," *ACS Photonics* **9**, 2802–2808 (2022).
20. J. Huang et al., "Spatiotemporal differentiators generating optical vortices with transverse orbital angular momentum and detecting sharp change of pulse envelope," *Laser Photonics Rev.* **16**, 2100357 (2022).
21. C. Wan et al., "Generation of ultrafast spatiotemporal wave packet embedded with time-varying orbital angular momentum," *Sci. Bull.* **65**(16), 1334–1336 (2020).
22. A. Mirando et al., "Generation of spatiotemporal optical vortices with partial temporal coherence," *Opt. Express* **29**, 30426–30435 (2021).

23. Q. Cao et al., "Sculpturing spatiotemporal wavepackets with chirped pulses," *Photonics Res.* **9**, 2261–2264 (2021).
24. C. Wan et al., "Photonic orbital angular momentum with controllable orientation," *Natl. Sci. Rev.* **9**(7), nwab149 (2022).
25. C. Wan et al., "Toroidal vortices of light," *Nat. Photonics* **16**(7), 519–522 (2022).
26. Q. Cao et al., "Non-spreading Bessel spatiotemporal optical vortices," *Sci. Bull.* **67**(2), 133–140 (2022).
27. W. Chen et al., "Time diffraction-free transverse orbital angular momentum beams," *Nat. Commun.* **13**, 4021 (2022).
28. A. W. Snyder and J. D. Love, *Optical Waveguide Theory*, Chapman and Hall, New York (1983).
29. "Corning® SMF-28® ultra optical fibers," https://www.corning.com/optical-communications/worldwide/en/home/products/fiber/optical-fiber-products/smf-28-ultra.html.

Qian Cao received his PhD in physics from the Universität Hamburg. He is currently a postdoctoral researcher at the University of Shanghai for Science and Technology (USST). His research interests include novel spatiotemporal optical fields, ultrafast optics, and nonlinear optics.

Andy Chong received his PhD in applied physics from Cornell University. He is currently an associate professor at Pusan National University (PNU).

Qiwen Zhan received his PhD in electrical and computer engineering from the University of Minnesota. He is currently the principal investigator of Nano-photonics Research Group at USST.

Biographies of other authors are not available.

Research Article

ADVANCED PHOTONICS

Tailoring light on three-dimensional photonic chips: a platform for versatile OAM mode optical interconnects

Jue Wang,[a,b,†] Chengkun Cai,[a,b,†] Feng Cui,[a,b] Min Yang,[a,b] Yize Liang,[a,b] and Jian Wang[a,b,*]

[a]Huazhong University of Science and Technology, Wuhan National Laboratory for Optoelectronics and School of Optical and Electronic Information, Wuhan, China

[b]Optics Valley Laboratory, Wuhan, China

Abstract. Explosive growth in demand for data traffic has prompted exploration of the spatial dimension of light waves, which provides a degree of freedom to expand data transmission capacity. Various techniques based on bulky optical devices have been proposed to tailor light waves in the spatial dimension. However, their inherent large size, extra loss, and precise alignment requirements make these techniques relatively difficult to implement in a compact and flexible way. In contrast, three-dimensional (3D) photonic chips with compact size and low loss provide a promising miniaturized candidate for tailoring light in the spatial dimension. Significantly, they are attractive for chip-assisted short-distance spatial mode optical interconnects that are challenging to bulky optics. Here, we propose and fabricate femtosecond laser-inscribed 3D photonic chips to tailor orbital angular momentum (OAM) modes in the spatial dimension. Various functions on the platform of 3D photonic chips are experimentally demonstrated, including the generation, (de)multiplexing, and exchange of OAM modes. Moreover, chip-chip and chip–fiber–chip short-distance optical interconnects using OAM modes are demonstrated in the experiment with favorable performance. This work paves the way to flexibly tailor light waves on 3D photonic chips and offers a compact solution for versatile optical interconnects and other emerging applications with spatial modes.

Keywords: orbital angular momentum; three-dimensional photonic chips; femtosecond laser writing; spatial modes; chip–chip; chip–fiber–chip; optical interconnects.

Received Feb. 3, 2023; revised manuscript received Mar. 27, 2023; accepted for publication Apr. 13, 2023; published online May 24, 2023.

[DOI: 10.1117/1.AP.5.3.036004]

1 Introduction

Increasing data transmission capacity is a persistent demand for optical interconnects. Recently, different physical dimensions of light waves, including time,[1] amplitude,[2] phase,[3] wavelength,[4] and polarization,[5] have been fully utilized to scale the data traffic. Even though various multiplexing techniques exploiting these physical dimensions have been developed, it is becoming rather difficult to follow the demand of a global network that is growing by 40% annually.[6] To keep pace with the ever-increasing demand, a new physical dimension of light is urgently needed. Fortunately, space-division multiplexing technology that transmits orthogonal spatial modes loaded with different signals in an optical interconnect system has further improved the transmission capacity, providing a new degree of freedom for capacity scaling of optical interconnects[7–9] [Fig. 1(a)]. The utilization of the spatial modes in optical interconnects systems requires the development of key optical devices, including spatial mode generators, (de)multiplexers, and exchangers. Traditional optical devices manipulating the spatial modes rely on bulky optics, such as phase plates[10,11] or spatial light modulators,[12,13] which take up too much space and are unscalable. To meet the requirement of a compact solution, the miniaturization of these key optical devices is of great importance.

*Address all correspondence to Jian Wang, jwang@hust.edu.cn

†These authors contributed equally to this work.

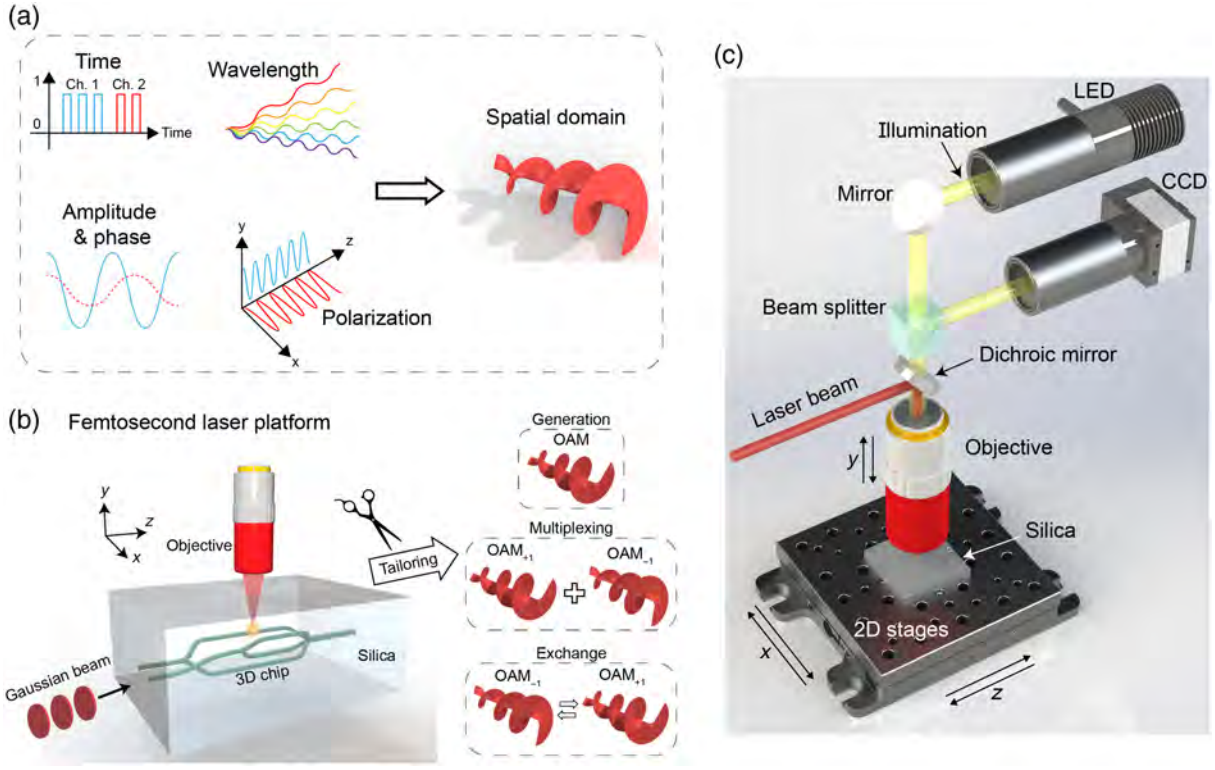

Fig. 1 (a) Multiple physical dimensions of light waves: from traditional ones to the spatial domain (e.g., OAM modes). (b) Concept of 3D photonic chips fabricated by FSLW for tailoring spatial modes (OAM generation/multiplexing/exchange). (c) Fabrication setup for FSLW.

Integrated photonic chips with a small footprint, high efficiency, and low cost are emerging with the rapid development of silicon photonics. Remarkably, most optical devices based on silicon photonics, including lasers,[14–16] modulators,[17,18] switches,[19,20] filters,[21,22] and (de)multiplexers,[23,24] have been widely implemented. Moreover, to further increase the density of integration, three-dimensional (3D) photonic chips have also been demonstrated with the advent of multilayer photonic structures.[25,26] However, these state-of-the-art integration technologies are typically implemented in a modified complementary-metal-oxide-semiconductor process, with the disadvantages of inflexibility and complex process. Thus, flexible fabrication of 3D photonic chips is still a challenge. Fortunately, femtosecond laser writing (FSLW) has been an emerging technique capable of fabricating 3D structures with microscale resolution. The FSLW induces a localized change of the refractive index near the laser foci in the silica substrate (see Appendix). By designing the 3D trajectory of the foci, we can create various photonic devices. Several 3D photonic integrated devices have been demonstrated using the FSLW, such as splitters,[27] mode selective couplers,[28] photonic lanterns,[29–31] and space-division multiplexers.[32–35]

In this work, we propose and demonstrate FSLW-based 3D photonic chips for orbital angular momentum (OAM) mode-[36–40] enabled optical interconnects. Two kinds of 3D photonic chips based on the trench waveguides are designed and fabricated to tailor the spatial modes, realizing the generation, multiplexing, demultiplexing, and exchange of OAM modes [Fig. 1(b)]. We use the setup illustrated in Fig. 1(c) for FSLW to fabricate these 3D photonic chips. We also deploy the fabricated 3D photonic chips in mode-division multiplexing (MDM) systems, characterizing their performance in chip-chip and chip–fiber–chip optical interconnects.

2 Results

2.1 On-Chip OAM Mode Generation

In this work, the first 3D photonic chip for spatial mode tailoring is an on-chip OAM mode generator; its concept and principle are illustrated in Fig. 2(a). The chip is fabricated using the FSLW technique. The detailed fabrication process can be seen in the Appendix. The on-chip OAM mode generator consists of an input waveguide, a Mach–Zehnder interferometer (MZI), and a trench waveguide. The input waveguide and the trench waveguide are designed to support the fundamental and higher-order modes. The principle of the on-chip OAM mode generator is as follows. First, the light launched into the input waveguide excites the fundamental mode. Then the MZI structure (colored by red) that introduces a phase shift in one arm converts the fundamental mode to the first-order quasi-transverse electric mode (TE_{10}) (see Note 1 in the Supplementary Material). The generation of the OAM mode is based on the specially designed trench waveguide. The TE_{10} mode can be considered as the in-phase combination of the diagonally and anti-diagonally distributed linearly polarized (LP)-like modes. When the phase difference between these two LP-like modes is $\pi/2$ or $-\pi/2$, the OAM mode with a topological charge of -1 or $+1$ is generated.

The trench waveguide and its supported eigenmodes are shown in Fig. 2(b). Four parameters define the geometry, which are the waveguide width (W_1), waveguide height (H_1), trench width (w_1), and trench height (h_1). The trench waveguide

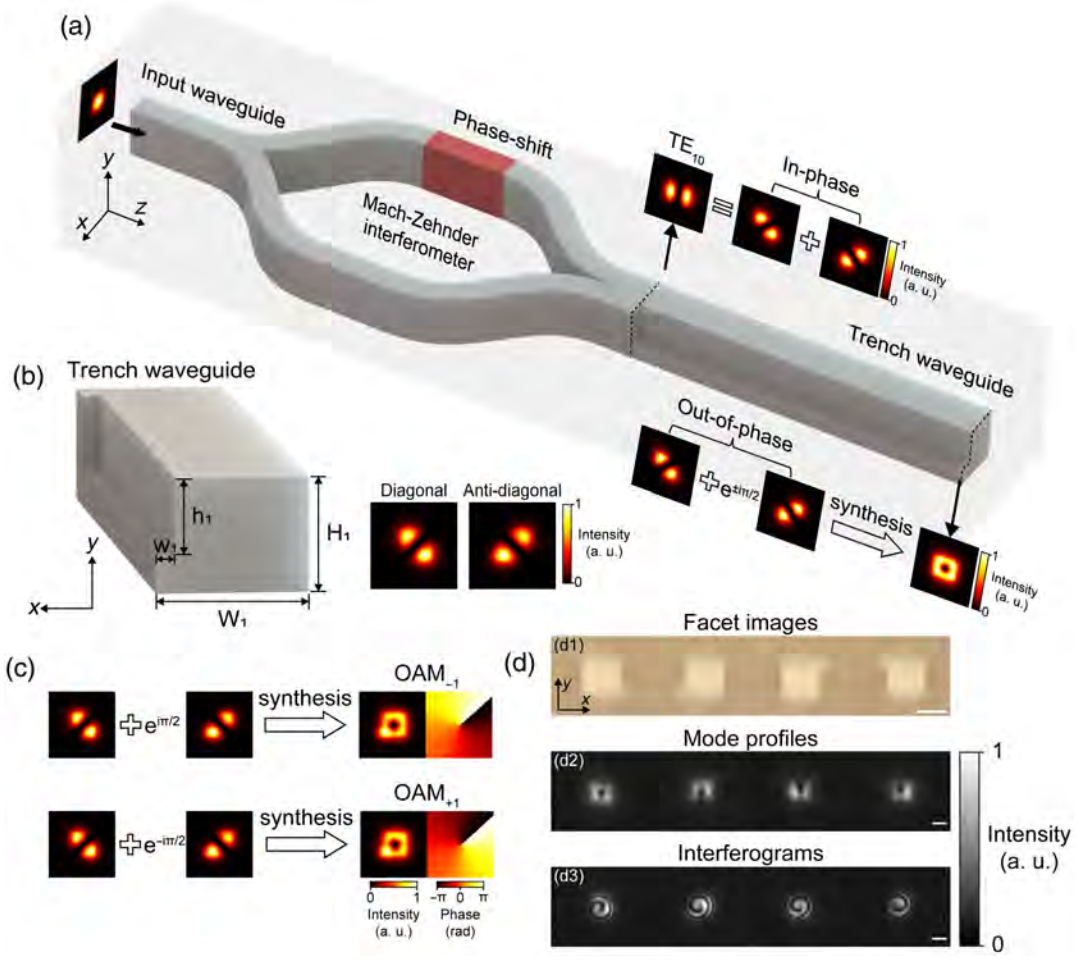

Fig. 2 On-chip OAM mode generator. (a) Concept and principle of the trench-based OAM generator. (b) Structure of trench waveguide and its supporting higher-order modes. (c) Simulated LP-like modes and their synthesized OAM modes. (d) Experimental results of OAM generator with different trench locations: (d1) trench facet images captured by an optical microscope, (d2) measured mode profiles, and (d3) measured interferograms (interference with a reference Gaussian beam). Scale bar, 20 μm.

supports two orthogonal LP-like modes at 1550 nm, which are diagonally and antidiagonally distributed by choosing the proper geometry (see Note 2 in the Supplementary Material). Here, the W_1 and H_1 are set to 17 and 15 μm, respectively. w_1 and h_2 are set to 3 and 9 μm, respectively. These two LP-like modes are nondegenerate due to the asymmetrical structure. Thus, the TE_{10} mode can simultaneously excite two orthogonal LP-like modes with different propagation constants. Further, as depicted in Fig. 2(c), they can be synthesized to OAM modes with topological charges of -1 and $+1$ after propagating through different distances, corresponding to phase differences of $\pi/2$ and $-\pi/2$, respectively. Except for changing the length of the trench waveguide, one can also swap the sign of the topological charge of OAM modes by altering the trench location.

The experimental results for the OAM generation with different trench locations are shown in Fig. 2(d), where $(\mathrm{d1}) \sim (\mathrm{d3})$ are the facet images of the trench waveguides, output mode profiles, and corresponding interferograms (by interference with a reference Gaussian beam), respectively. These four OAM generators are entirely the same, except for the location of the trench structure. We characterize these OAM modes by retrieving their phase profiles and calculating their OAM spectra (see Note 3 in the Supplementary Material). The OAM phase purities for each case are >92%. The details of phase retrieving and mode purity calculation can be found in the Appendix. The measured mode profiles in Fig. 2(d2) show slight defects in the experiment, which are mainly caused by the slight fabrication error of waveguide structures, i.e. inaccurate phase difference (derivation from π) between the two arms of the MZI as well as inaccurate phase difference (derivation from $\pm\pi/2$) between the two eigenmodes of the trench waveguide. However, they still show a high OAM phase purity over 92%. The mode quality might be improved by further reducing the fabrication error with optimized fabrication parameters, such as the laser power, scanning speed, and scanning spacing.

In the experiment, when the polarization state of the input beam changes, the output OAM mode profile keeps almost unchanged, and the polarization state of the output OAM mode almost remains the same as the input beam. That is

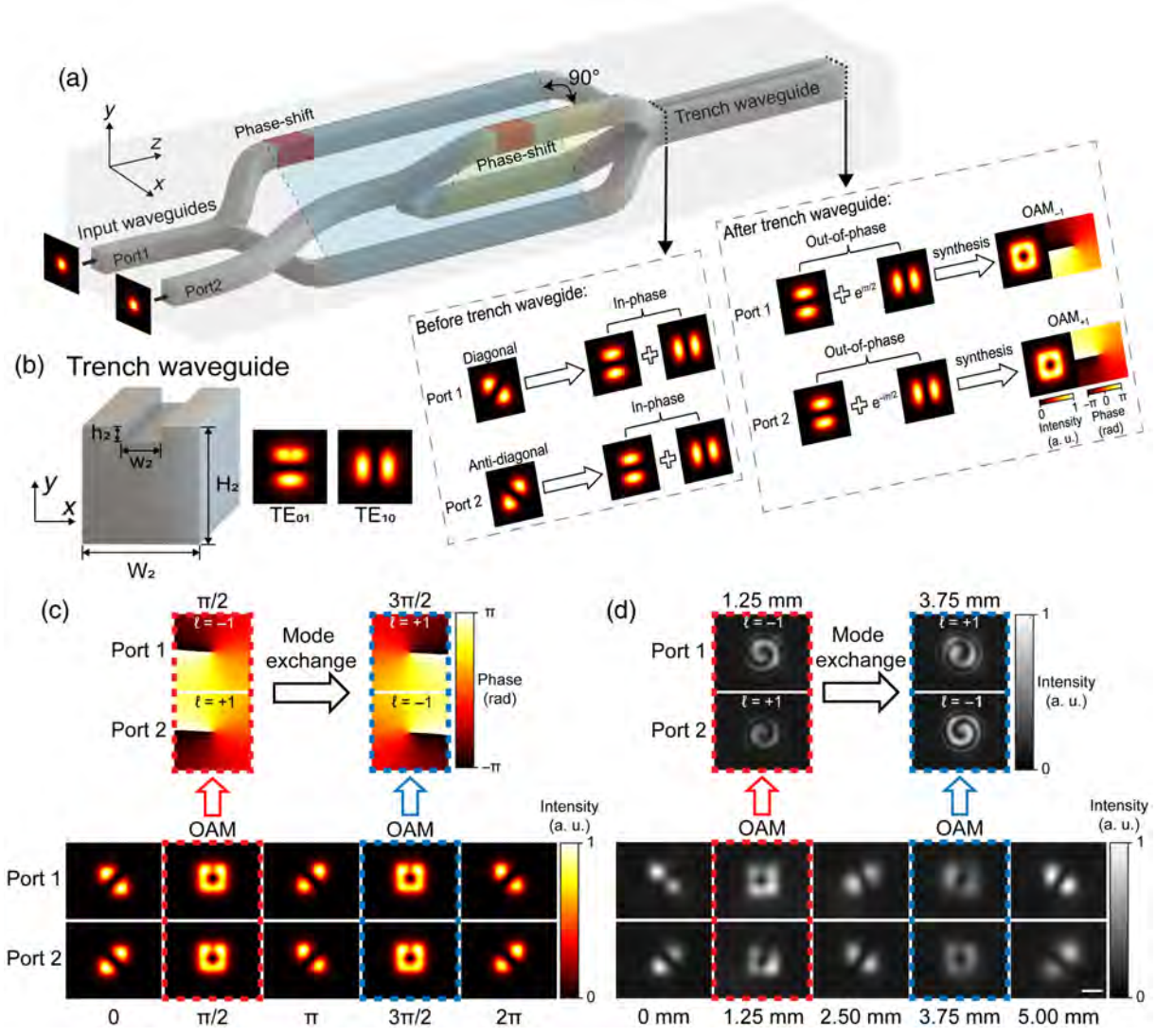

Fig. 3 On-chip OAM mode multiplexer. (a) Concept and principle of the trench-based OAM mode multiplexer. (b) Structure of the trench waveguide and the supported higher-order eigenmodes (TE_{01} and TE_{10}). (c) Simulation results of OAM mode multiplexer and exchanger. (d) Experimental results of OAM mode multiplexer and exchanger. Scale bar, 20 μm.

because, according to our characterization in the experiment, the birefringence induced by FSLW is estimated to be lower than 1×10^{-5}. Meanwhile, the waveguide structures of the 3D photonic chip are relatively symmetrical and short in length.

2.2 On-Chip OAM Mode (De)Multiplexer and Exchanger

Other typical functions for spatial mode tailoring are mode (de)multiplexing and exchange. We propose an on-chip OAM mode multiplexer based on the variation of the trench waveguide; its concept and principle are illustrated in Fig. 3(a). The OAM mode multiplexer consists of two input waveguides, two MZIs, and a specially designed trench waveguide. The angle between the planes (colored cyan and yellow) where the two MZIs are located is 90 deg. At port 1, the fundamental mode is converted to an LP-like mode with the diagonal distribution by the MZI. Before the trench waveguide, the LP-like mode excites two higher-order TE_{01} and TE_{10} modes equal in phase. Then when the phase difference of these two modes is $\pi/2$, the OAM mode with the topological charge of -1 is generated at the output. The same principle is applied to port 2, except for the opposite sign of phase difference ($-\pi/2$) and topological charge number ($+1$) of the OAM mode.

Figure 3(b) shows the detailed structure of the trench waveguide and the higher-order eigenmodes (TE_{01} and TE_{10}) that the waveguide supports. Unlike the former, the trench here is located at the middle top of the waveguide rather than the corners. W_2 and H_2 are the waveguide width and height, respectively. w_2 and h_2 are the trench width and height, respectively. By introducing a small trench structure, the degeneracy of TE_{01} and TE_{10} modes is lifted, which means they have different effective refractive indices. The length of the trench waveguide L can be expressed by

$$L = \frac{\lambda \Delta\varphi}{2\pi \Delta n_{\text{eff}}}, \tag{1}$$

where $\Delta\varphi$ and Δn_{eff} are the phase difference and effective refractive index difference between the two eigenmodes (TE_{01} and TE_{10}), and λ is the wavelength in vacuum. When the trench becomes large, the effective refractive index difference Δn_{eff} between the two eigenmodes also increases [see Fig. S4(b) in the Supplementary Material]. So, according to Eq. (1), a larger Δn_{eff} results in a shorter L for $\Delta\varphi = \pm\pi/2$ (e.g. required phase difference for the synthesis of OAM modes). However, the increasing trench size may degrade the uniformity of the TE_{01} mode, resulting in the reduced mode purity of the output OAM mode [see Fig. S4(a) in the Supplementary Material]. Therefore, an optimized trench size should be considered to achieve high mode quality with a relatively short device. Once the optimized size of the trench structure is chosen, the Δn_{eff} is determined. Thus we can produce OAM modes by propagating through a proper length of the trench waveguide with the accumulated phase difference of $\Delta\varphi = \pm\pi/2$. The detailed analyses on how to balance the length of the trench waveguide and output mode quality can be seen in Note 4 in the Supplementary Material.

Simulation results of the OAM mode multiplexer for input from ports 1 and 2 with phase differences of 0, $\pi/2$, π, $3\pi/2$, and 2π between TE_{01} and TE_{10} modes in the trench waveguide are depicted in Fig. 3(c). When the phase difference is 0 (π), the outputs are diagonally and anti-diagonally (anti-diagonally and diagonally) distributed LP-like modes for input from ports 1 and 2. When the phase difference is $\pi/2$ ($3\pi/2$), the outputs are OAM modes with the topological charge of -1 and $+1$ ($+1$ and -1) for input from ports 1 and 2, verified by their phase profiles. Also, it can be seen that the mode exchange happens when the phase difference changes from $\pi/2$ to $3\pi/2$.

We experimentally demonstrate the OAM mode multiplexing and exchange in our fabricated 3D photonic chip. Figure 3(d) shows a similar mode evolution with our simulation results in Fig. 3(c). When the trench length is 0 or 5.00 mm, corresponding to the phase difference of 0 or 2π, the mode profiles are diagonally and anti-diagonally distributed LP-like modes for input from ports 1 and 2. When the trench length is 2.50 mm, corresponding to the phase difference of π, the mode profiles rotate 90 deg for input from ports 1 and 2, which are anti-diagonally and diagonally distributed LP-like modes. The OAM mode multiplexing happens when the trench length is 1.25 mm. OAM_{-1} and OAM_{+1} modes are generated under this condition; this is verified by their interferograms. By extending the trench length to 3.75 mm, OAM modes swap with each other, where OAM_{-1} is converted to OAM_{+1} for input from port 1, and OAM_{+1} is converted to OAM_{-1} for input from port 2 simultaneously.

Furthermore, we characterize all four OAM modes, retrieving their phase profiles and calculating their OAM spectra (see Note 5 in the Supplementary Material). The OAM phase purities are >92%. The details of phase retrieving and mode purity calculation can be found in the Appendix. Similar to the OAM mode multiplexer, we can also realize the OAM mode demultiplexer simply by using it in an opposite way.

2.3 Chip–Chip Optical Interconnects

Using the designed and fabricated 3D photonic chips for MDM with OAM modes, we demonstrate the chip–chip optical interconnects. The fabricated 3D photonic chips are packaged with single-mode fibers (SMFs) first, as shown in Fig. 4(a). The detailed packaging procedure can be found in Note 6 in the Supplementary Material. The experimental setup for chip–chip optical interconnects is shown in Fig. 4(b). A 1550-nm laser is modulated by an optical I/Q modulator driven by an arbitrary waveform generator (AWG) to generate the 30 Gbit/s 8-ary quadrature amplitude modulation (8-QAM) signal at the transmitter side. A polarization controller (PC) is used to optimize the state of polarization. The amplified optical signal by an erbium-doped fiber amplifier (EDFA) is divided into two channels by an optical coupler (OC), and one of them is transmitted through an additional 1-km SMF for decoherence. Two channel optical signals carried by Gaussian modes are first coupled into an OAM mode multiplexer from inputs 1 and 2, which are transformed into OAM_{-1} and OAM_{+1} modes through the 1.25-mm trench waveguide. These two OAM modes are then coupled into an OAM mode demultiplexer with a trench of the same length and are converted back to Gaussian modes at outputs 1 and 2. The output optical signals are amplified by another EDFA on the receiver side. Then a coherent receiver followed by a local oscillator is used to analyze 8-QAM signals for the performance evaluation. Variable optical attenuators (VOAs) and the following EDFAs are used to adjust the received optical signal-to-noise ratio (OSNR). The measured crosstalk matrix for two inputs and two outputs is plotted in Fig. 4(c), which is < -14.1 dB. The measured bit-error rate (BER) curves for OAM modes transmission are plotted in Fig. 4(d). Compared to the back-to-back case, the measured OSNR penalties at a BER of 3.8×10^{-3} [7% overhead hard-decision forward-error correction (HD-FEC) threshold] for multiplexing transmission of OAM_{-1} and OAM_{+1} modes are less than 1.3 and 3.5 dB, respectively. The insets in Fig. 4(d) are their typical constellations.

2.4 Chip–Fiber–Chip Optical Interconnects

Using the designed and fabricated 3D photonic chips for MDM with OAM modes, we also demonstrate the chip–fiber–chip optical interconnects. Here, we use two individual OAM modes (de)multiplexers interconnected by a 2-km OAM fiber that supports OAM modes. Similarly, the OAM mode (de)multiplexers are packaged first, as shown in Fig. 5(a). The experimental setup for chip–fiber–chip optical interconnects is shown in Fig. 5(b), which is similar to the setup in Fig. 4(b). The difference is that the multiplexed OAM modes are transmitted through an additional 2-km-long OAM fiber. In addition, the transmitted laser is modulated with a 20 Gbit/s quadrature phase-shift keying (QPSK) signal. At the receiver side, the output optical signals are amplified and then a coherent receiver followed by a local oscillator is used to analyze QPSK signals for the performance evaluation. Figure 5(c) shows the measured intensity profiles of the generated OAM_{-1} mode, OAM_{+1} mode, and their multiplexing after propagating through the OAM fiber. The measured crosstalk matrix for two inputs and two outputs is plotted in Fig. 5(d), which is < -10.1 dB. The measured BER curves for OAM multiplexing transmission are plotted in Fig. 5(e). Compared to the back-to-back case, the measured OSNR penalties at a BER of the 7% overhead HD-FEC threshold (3.8×10^{-3}) for multiplexing transmission of OAM_{-1} and OAM_{+1} are less than 4.6 and 5.7 dB, respectively. The insets in Fig. 5(e) are their typical constellations.

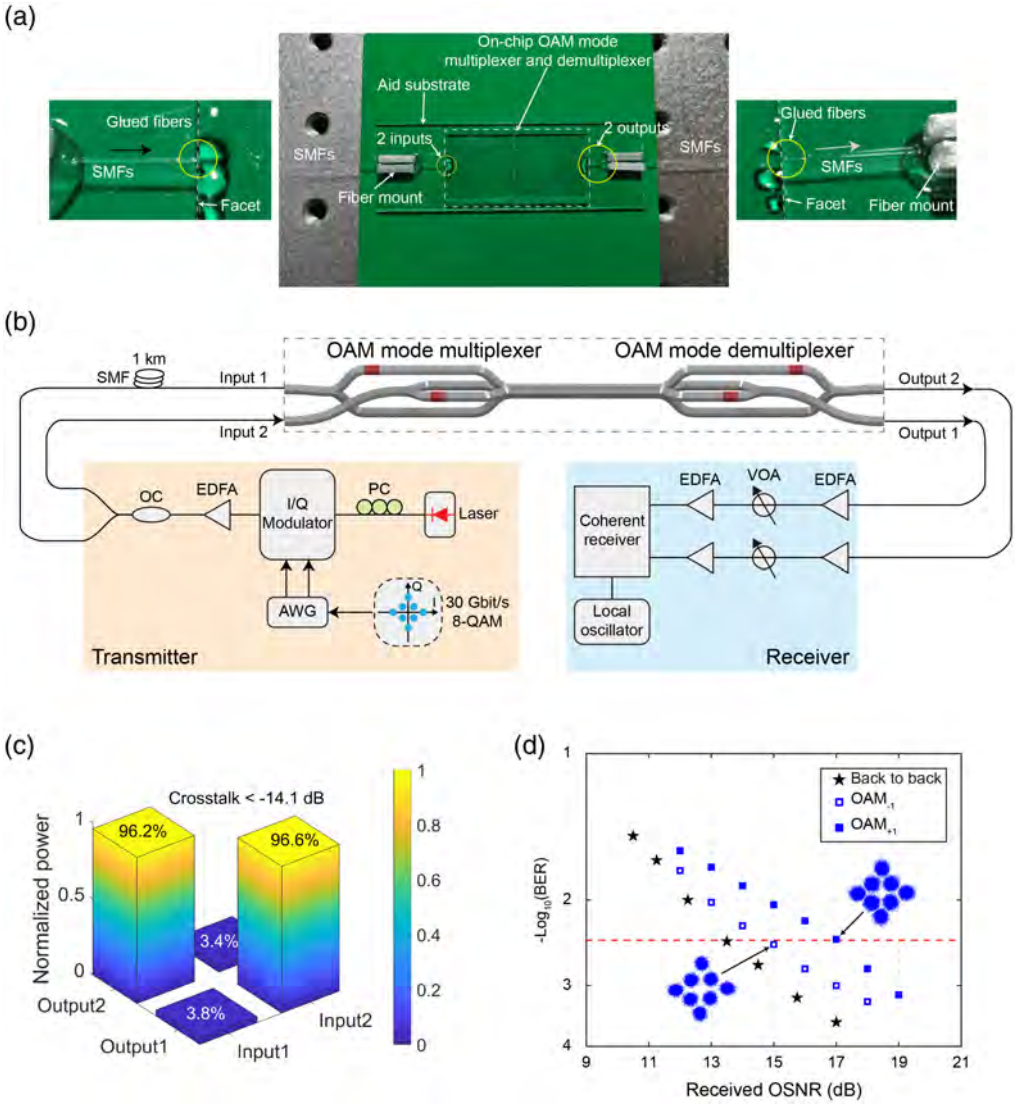

Fig. 4 (a) Middle, photo of the packaged on-chip OAM mode multiplexer and demultiplexer. Left, zoom-in view of the OAM mode multiplexer. Right, zoom-in view of the OAM mode demultiplexer. (b) Experimental setup for chip–chip optical interconnects with OAM modes. PC, polarization controller; EDFA, erbium-doped fiber amplifier; AWG, arbitrary waveform generator; OC, optical coupler; SMF, single-mode fiber; and VOA, variable optical attenuator. (c) Measured crosstalk matrix. (d) Measured BER performance and constellations.

3 Discussion

In summary, we propose and demonstrate a 3D photonic chip platform for versatile spatial mode optical interconnects. Two kinds of 3D photonic chips based on the trench waveguides are designed and fabricated for manipulating the OAM modes, including the OAM mode generation, (de)multiplexing, and exchange. The OAM spectra of the generated OAM modes output from the on-chip multiplexers are analyzed, showing a high mode purity >92%. We also demonstrate chip–chip and chip–fiber–chip optical interconnects with OAM modes using the fabricated 3D photonic chips. OAM modes multiplexing transmission carrying 8-QAM and QPSK signals are successfully demonstrated in the experiment with favorable performance.

Two OAM mode channels are employed in the experiment. There are several potential approaches that might be considered to further increase the number of mode channels. Firstly, reducing the waveguide size and rearranging them in a proper way may provide extra space for more mode channels. Secondly, a photonic lantern structure using special geometrical arrangement might be used for a large number of spatial modes,[41] and OAM modes could be obtained by using a complex trench waveguide structure. Thirdly, a free propagation region employing a Rowland circle might be used, and circular patterned apertures of 3D structures could sample and retrieve spatially overlapped multiple OAM modes.[32]

In the designed and fabricated 3D photonic chip, the bending radii of the bend waveguides are large enough (over 30 mm radius) with negligible bending loss. The propagation loss of single-mode waveguides is about 1 dB/cm. The extra loss caused by the beam splitting and combining is about 0.5 dB. The propagation loss of the trench waveguide is about

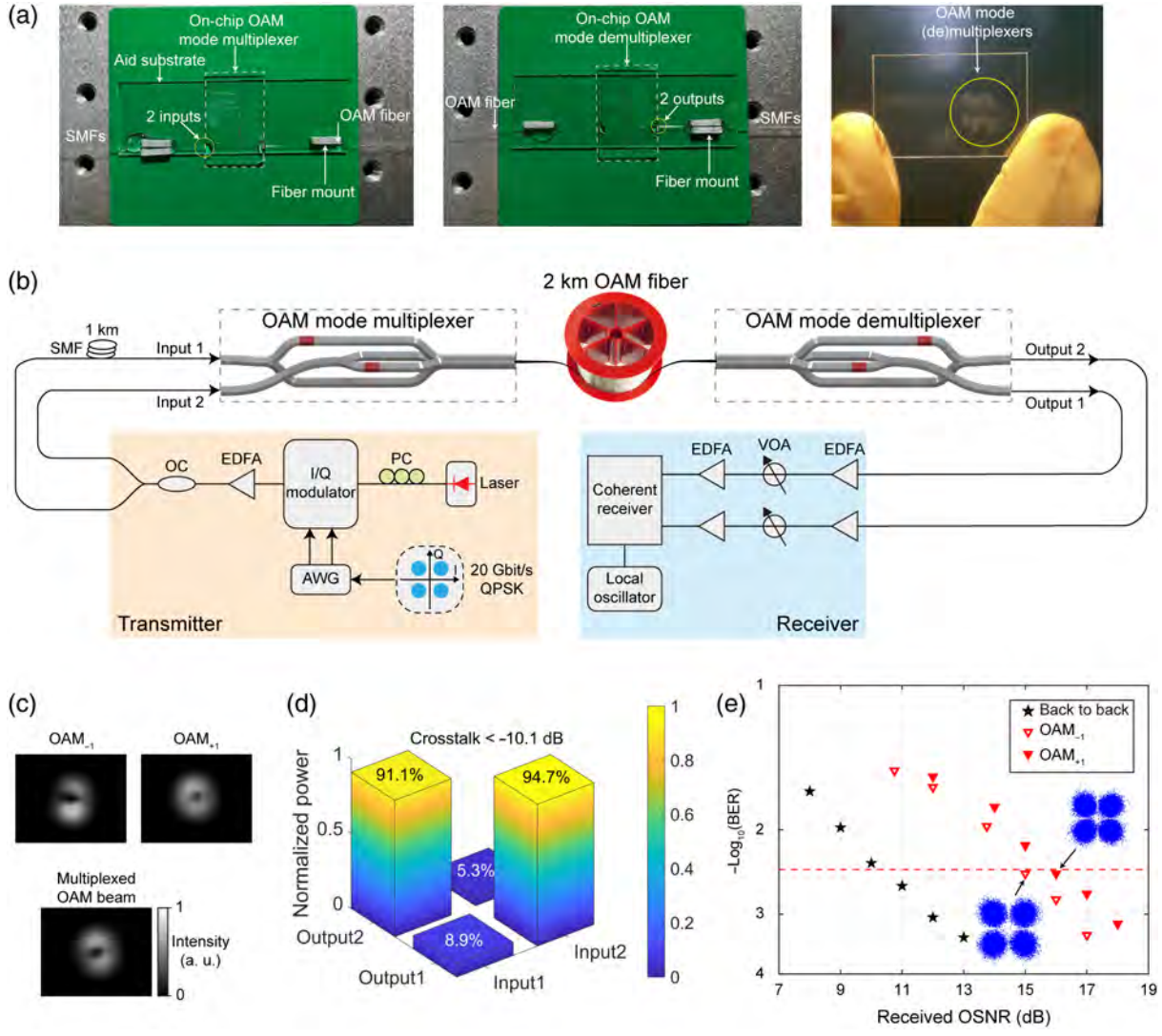

Fig. 5 (a) Photos of the packaged on-chip OAM mode multiplexer (left), OAM mode demultiplexer (middle), and unpackaged OAM mode (de)multiplexers (right) in the silica substrate. (b) Experimental setup for chip–fiber–chip optical interconnects with OAM modes. (c) Measured intensity profiles of OAM modes after propagating through the 2-km OAM fiber. (d) Measured crosstalk matrix. (e) Measured BER performance and constellations.

1.5 dB/cm. The coupling loss between the waveguide and fiber after packaging is about 1 dB/facet. The overall insertion loss of the OAM mode multiplexer is less than 5 dB. With future improvement, the propagation loss and extra loss might be reduced by optimizing the structure design and fabrication parameters. Moreover, the coupling loss might be reduced by matching the mode fields between the 3D photonic chip and fiber.

This work demonstrates a compact, multi-functional and flexible platform for tailoring the spatial structure of lightwaves and enabling chip-assisted spatial mode optical interconnects. The 3D photonic chips fabricated by the FSLW technique may find more and more exciting applications with spatial modes.

4 Appendix: Methods

4.1 3D FSLW Technique

The 3D FSLW technique is based on the laser-induced refractive index change in transparent materials. When a femtosecond laser beam is ultrafocused inside the glass, nonlinear absorption occurs. Under the proper conditions (the pulse duration, pulse energy, and focusing numerical aperture), it will produce a localized refractive index change in the focal volume, which can reach the submicrometer scale.[42]

The setup for FSLW is depicted in Fig. 1(c). A well-polished silica substrate is mounted on the 2D stages (Aerotech), linearly moving along the x and z directions. A femtosecond laser beam reflected by a dichroic mirror propagates through an objective. The objective translating along the y direction controls the depth of the foci in the substrate during fabrication. In addition, an LED illumination propagates through a mirror, beam splitter, dichroic mirror, objective, and lightens the fabricated sample. The sample image is then reflected through the objective, dichroic mirror, beam splitter, and finally captured by a CCD. In this way, we can achieve real-time observation of fabrication. According to the tracks we program, arbitrary structures can be processed.

A femtosecond laser (PHAROS, 200 kHz repetition rate, 515 nm wavelength, and 340 fs pulse width) is focused by a 0.42 NA objective (Mitutoyo long working distance objective) at 0.2 mm below the surface of silica. The cross section of foci perpendicular to the scanning direction (z direction) is elliptical. Therefore, a mechanical slit (along the z direction) is mounted before the objective.[43,44] By adjusting the width of the slit, the Gaussian beam becomes elliptical with an ellipticity of 0.19 (defined by the ratio of the major axis and minor axis). The desired foci with a symmetric cross section can be produced. In the experiment, the pulse energy before the objective with a slit is 355 nJ. The multiscan technique is used with a scanning speed of 10 mm/s. The scanning spacing is 1.0 μm in the x direction and 0.679 μm in the y direction (considering the refractive index). The refractive index contrast is estimated to be about 3×10^{-3} to 5×10^{-3}. Additionally, the birefringence is estimated to be lower than 1×10^{-5}.

4.2 Phase Retrieving and Mode Purity Calculation

We use the off-axis digital holography technology[45,46] to reconstruct the wavefront of generated OAM beams for mode purity characterization. Off-axis digital holography allows a single-exposure acquisition of a beam wavefront by introducing a slight angle between the generated OAM beam and reference beam as they interfere at the digital camera plane. An off-axis hologram containing linear interference fringes is recorded in the experiment. We utilize a two-dimensional Fourier transform to separate the autocorrelation terms and cross-correlation terms of these linear interference fringes in the spatial-frequency domain. Since the cross-correlation terms act as a carrier for the wavefront of the OAM beam, one can retrieve the wavefront of the OAM beam by applying inverse Fourier transform to separated cross-correlation terms. Then the mode purity of the generated OAM beam can be calculated as the normalized power weight coefficient[47] using

$$|C_l| = \left| \iint \exp(i\varphi(x,y)) E_l^*(x,y) \mathrm{d}x\, \mathrm{d}y \right|^2, \tag{2}$$

where $\varphi(x,y)$ is the measured wavefront of the generated OAM beam and $E_l(x,y)$ corresponds to the phase distribution of the conventional lth OAM beam, with the center overlapping with the generated beam. For example, to calculate the mode purity of an OAM beam with a topological charge of $+1$, $E_l(x,y)$ should be $\exp(+i\theta)$, where θ is the azimuthal angle.

Acknowledgments

This work was supported by the National Natural Science Foundation of China (Grant Nos. 62125503 and 62261160388), the Key R&D Program of Hubei Province of China (Grant Nos. 2020BAB001 and 2021BAA024), the Key R&D Program of Guangdong Province (Grant No. 2018B030325002), the Shenzhen Science and Technology Program (Grant No. JCYJ20200109114018750), and the Innovation Project of Optics Valley Laboratory (Grant No. OVL2021BG004). J.W. developed the concept and conceived the experiment. JUE W. and C.C. performed the experiment. JUE W. acquired the experimental data and carried out the data analyses. F.C. provided technical support. All authors contributed to the writing. J.W. finalized the paper. J.W. supervised the project. The authors declare that they have no conflicts of interest.

Data Availability

Data underlying the results presented in this paper are not publicly available at this time but may be obtained from the authors upon reasonable request.

References

1. D. M. Spirit, A. D. Ellis, and P. E. Barnsley, "Optical time division multiplexing: systems and networks," *IEEE Commun. Mag.* **32**(12), 56–62 (1994).
2. M. A. Khalighi, H. Akhouayri, and S. Hranilovic, "Silicon-photomultiplier-based underwater wireless optical communication using pulse-amplitude modulation," *IEEE J. Ocean Eng.* **45**(4), 1611–1621 (2020).
3. L. Tao et al. "Experimental demonstration of 10 Gb/s multi-level carrier-less amplitude and phase modulation for short range optical communication systems," *Opt. Express* **21**(5), 6459–6465 (2013).
4. X.-H. Huang et al., "WDM free-space optical communication system of high-speed hybrid signals," *IEEE Photonics J.* **10**, 7204207 (2018).
5. P. Chvojka et al., "Visible light communications: increasing data rates with polarization division multiplexing," *Opt. Lett.* **45**(11), 2977–2980 (2020).
6. D. J. Richardson, "Filling the light pipe," *Science* **330**(6002), 327–328 (2010).
7. Y. Weng, X. He, and Z. Pan, "Space division multiplexing optical communication using few-mode fibers," *Opt. Fiber Technol.* **36**, 155–180 (2017).
8. T. Mizuno and Y. Miyamoto, "High-capacity dense space division multiplexing transmission," *Opt. Fiber Technol.* **35**, 108–117 (2017).
9. A. Trichili et al., "Communicating using spatial mode multiplexing: potentials, challenges, and perspectives," *IEEE Commun. Surv. Tutor.* **21**(4), 3175–3203 (2019).
10. G. Labroille et al., "Mode selective 10-mode multiplexer based on multi-plane light conversion," in *Opt. Fiber Commun. Conf.*, OSA, Anaheim, California, p. Th3E.5 (2016).
11. S. Bade et al., "Fabrication and characterization of a mode-selective 45-mode spatial multiplexer based on multi-plane light conversion," in *Opt. Fiber Commun. Conf.*, OSA, San Diego, California, p. Th4B.3 (2018).
12. C. Koebele et al., "Two mode transmission at 2×100 Gb/s, over 40 km-long prototype few-mode fiber, using LCOS-based programmable mode multiplexer and demultiplexer," *Opt. Express* **19**(17), 16593–16600 (2011).
13. E. Otte, K. Tekce, and C. Denz, "Spatial multiplexing for tailored fully-structured light," *J. Opt.* **20**(10), 105606 (2018).
14. G. Kurczveil et al., "On-chip hybrid silicon quantum dot comb laser with 14 error-free channels," in *IEEE Int. Semicond. Laser Conf. (ISLC)*, IEEE, Santa Fe, NM, pp. 1–2 (2018).
15. Q. Bao et al., "On-chip single-mode CdS nanowire laser," *Light Sci. Appl.* **9**(1), 42 (2020).
16. K. Shtyrkova et al., "Integrated CMOS-compatible Q-switched mode-locked lasers at 1900 nm with an on-chip artificial saturable absorber," *Opt. Express* **27**(3), 3542–3556 (2019).
17. K. P. Nagarjun et al., "Generation of tunable, high repetition rate optical frequency combs using on-chip silicon modulators," *Opt. Express* **26**(8), 10744–10753 (2018).
18. A. Samani et al., "Silicon photonic Mach–Zehnder modulator architectures for on chip PAM-4 signal generation," *J. Light Technol.* **37**(13), 2989–2999 (2019).
19. Y. Zhang et al., "On-chip silicon photonic 2 × 2 mode- and polarization-selective switch with low inter-modal crosstalk," *Photonics Res.* **5**(5), 521–526 (2017).

20. L. Yang et al., "General architectures for on-chip optical space and mode switching," *Optica* **5**(2), 180–187 (2018).
21. X. Nie et al., "High extinction ratio on-chip pump-rejection filter based on cascaded grating-assisted contra-directional couplers in silicon nitride rib waveguides," *Opt. Lett.* **44**(9), 2310–2313 (2019).
22. W. Zhang and J. Yao, "On-chip silicon photonic integrated frequency-tunable bandpass microwave photonic filter," *Opt. Lett.* **43**(15), 3622–3625 (2018).
23. H. D. T. Linh et al., "Arbitrary $TE_0/TE_1/TE_2/TE_3$ mode converter using 1×4 Y-junction and 4×4 MMI couplers," *IEEE J. Sel. Top Quantum Electron.* **26**(2), 8300708 (2020).
24. Y. Meng et al., "Versatile on-chip light coupling and (de)multiplexing from arbitrary polarizations to controlled waveguide modes using an integrated dielectric metasurface," *Photonics Res.* **8**(4), 564–576 (2020).
25. X. Yu et al., "Monolithically integrated self-rolled-up microtube-based vertical coupler for three-dimensional photonic integration," *Appl. Phys. Lett.* **107**(3), 031102 (2015).
26. N. Nishiyama et al., "Si-photonics-based layer-to-layer coupler toward 3D optical interconnection," *IEICE Trans. Electron.* **E101.C**(7), 501–508 (2018).
27. M. Pospiech et al., "Single-sweep laser writing of 3D-waveguide devices," *Opt. Express* **18**(7), 6994–7001 (2010).
28. S. Gross et al., "Three-dimensional ultra-broadband integrated tapered mode multiplexers: three-dimensional ultra-broadband integrated tapered mode multiplexers," *Laser Photonics Rev.* **8**(5), L81–L85 (2014).
29. R. R. Thomson et al., "Ultrafast laser inscription of an integrated photonic lantern," *Opt. Express* **19**(6), 5698–5705 (2011).
30. H. Chen et al., "Design constraints of photonic-lantern spatial multiplexer based on laser-inscribed 3-D waveguide technology," *J. Light Technol.* **33**(6), 1147–1154 (2015).
31. G. Douglass et al., "Femtosecond laser written arrayed waveguide gratings with integrated photonic lanterns," *Opt. Express* **26**(2), 1497–1505 (2018).
32. B. Guan et al., "Free-space coherent optical communication with orbital angular, momentum multiplexing/demultiplexing using a hybrid 3D photonic integrated circuit," *Opt. Express* **22**(1), 145–156 (2014).
33. P. Mitchell et al., "57 channel (19×3) spatial multiplexer fabricated using direct laser inscription," in *Opt. Fiber Commun. Conf.*, OSA, San Francisco, California, p. M3K.5 (2014).
34. R. G. H. van Uden et al., "Ultra-high-density spatial division multiplexing with a few-mode multicore fibre," *Nat. Photonics* **8**(11), 865–870 (2014).
35. S. Gross et al., "Ultrafast laser-written sub-components for space division multiplexing," in *Opt. Fiber Commun. Conf.*, OSA, San Diego, California, p. W1A.1 (2020).
36. S. Ramachandran and P. Kristensen, "Optical vortices in fiber," *Nanophotonics* **2**(5–6), 455–474 (2013).
37. A. E. Willner et al., "Optical communications using orbital angular momentum beams," *Adv. Opt. Photonics* **7**(1), 66–106 (2015).
38. L. Zhu and J. Wang, "A review of multiple optical vortices generation: methods and applications," *Front. Optoelectron.* **12**(1), 52–68 (2019).
39. X. Wang et al., "Recent advances on optical vortex generation," *Nanophotonics* **7**(9), 1533–1556 (2018).
40. R. Chen et al., "Orbital angular momentum waves: generation, detection and emerging applications," *IEEE Commun. Surv. Tutor.* **22**(2), 840–868 (2020).
41. A. M. Velázquez-Benítez et al., "Scaling photonic lanterns for space-division multiplexing," *Sci. Rep.* **8**(1), 8897 (2018).
42. E. Mazur, "Femtosecond laser micromachining in transparent materials," in *Adv. Photonics Renew. Energy*, OSA, Karlsruhe, Germany, p. BWB4 (2010).
43. M. Ams et al., "Slit beam shaping method for femtosecond laser direct-write fabrication of symmetric waveguides in bulk glasses," *Opt. Express* **13**(15), 5676–5681 (2005).
44. Y. Cheng et al., "Control of the cross-sectional shape of a hollow microchannel embedded in photostructurable glass by use of a femtosecond laser," *Opt. Lett.* **28**(1), 55–57 (2003).
45. N. T. Shaked et al., "Off-axis digital holographic multiplexing for rapid wavefront acquisition and processing," *Adv. Opt. Photonics* **12**(3), 556–611 (2020).
46. M. Mazur et al., "Characterization of long multi-mode fiber links using digital holography," in *Opt. Fiber Commun. Conf.*, OSA, San Diego, California, p. W4C.5 (2019).
47. G. Molina-Terriza, J. P. Torres, and L. Torner, "Management of the angular momentum of light: preparation of photons in multidimensional vector states of angular momentum," *Phys. Rev. Lett.* **88**(1), 013601 (2001).

Jian Wang received his PhD in physical electronics from Wuhan National Laboratory for Optoelectronics, Huazhong University of Science and Technology, China, in 2008. He worked as a postdoctoral research associate in Optical Communications Laboratory at the University of Southern California, United States, from 2009 to 2011. Currently, he is working as a professor at Wuhan National Laboratory for Optoelectronics, Huazhong University of Science and Technology, China. He is vice director of Wuhan National Laboratory for Optoelectronics, Huazhong University of Science and Technology, China. He was elected as an OPTICA fellow (formerly OSA fellow) in 2020 and an SPIE fellow in 2022. He leads the Multi-dimensional Photonics Laboratory. His research interests include optical communications, optical signal processing, silicon photonics, photonic integration, orbital angular momentum, and structured light.

Biographies of the other authors are not available.

Research Article

ADVANCED PHOTONICS

Single-shot Kramers–Kronig complex orbital angular momentum spectrum retrieval

Zhongzheng Lin,[a,†] Jianqi Hu,[b,*,†] Yujie Chen,[a] Camille-Sophie Brès,[b] and Siyuan Yu[a,*]
[a]Sun Yat-sen University, School of Electronics and Information Technology, State Key Laboratory of Optoelectronic Materials and Technologies, Guangzhou, China
[b]École Polytechnique Fédérale de Lausanne, Photonic Systems Laboratory, STI-IEM, Lausanne, Switzerland

Abstract. Orbital angular momentum (OAM) spectrum diagnosis is a fundamental building block for diverse OAM-based systems. Among others, the simple on-axis interferometric measurement can retrieve the amplitude and phase information of complex OAM spectra in a few shots. Yet, its single-shot retrieval remains elusive, due to the signal–signal beat interference inherent in the measurement. Here, we introduce the concept of Kramers–Kronig (KK) receiver in coherent communications to the OAM domain, enabling rigorous, single-shot OAM spectrum measurement. We explain in detail the working principle and the requirement of the KK method and then apply the technique to precisely measure various characteristic OAM states. In addition, we discuss the effects of the carrier-to-signal power ratio and the number of sampling points essential for rigorous retrieval and evaluate the performance on a large set of random OAM spectra and high-dimensional spaces. Single-shot KK interferometry shows enormous potential for characterizing complex OAM states in real time.

Keywords: orbital angular momentum; Kramers–Kronig relations; single-shot measurement; phase retrieval.

Received Mar. 12, 2023; revised manuscript received Apr. 26, 2023; accepted for publication May 19, 2023; published online Jun. 12, 2023.

[DOI: 10.1117/1.AP.5.3.036006]

1 Introduction

Structured light waves with spiral phase fronts carry orbital angular momentum (OAM). Such helical optical beams, either naturally emitted from laser cavities[1] or externally sculpted,[2] have recently attracted significant attention and have been widely used in communication, sensing, imaging, as well as classical and quantum information processing.[3–7] For many of these applications, the ability to diagnose an arbitrary OAM state is essential, so its complex structure can be unveiled and decomposed into an orthogonal OAM basis. Various methods have been explored for the task. Perhaps the most straightforward approach is using vortex phase plates together with a mode filter to obtain the power of each OAM order sequentially.[2,8] The number of measurements required by this approach, however, scales fast with the measurement space. Techniques based on the far-field diffraction patterns through certain types of apertures[9] or gratings[10,11] generally only identify pure OAM orders rather than superimposed states. In that sense, mode sorters are efficient in separating the superposition of OAM modes by mapping different OAM orders into different spatial positions. They have been implemented based on cascaded Mach–Zehnder interferometers with Dove prisms,[12] log-polar transformation,[13,14] and its improvement by means of beam copying,[15] or spiral transformation[16] that increases the mode separation. Moreover, multi-plane light conversion is also employed for sorting OAM modes with enhanced functionalities.[17–19] Yet, mode sorters generally lose the relative phase information among OAM modes, which may be required in many scenarios to unambiguously reconstruct the complex OAM states. For this purpose, the interference measurement techniques are appealing for OAM full-field (amplitude and phase) retrieval.[20–24]

Typical OAM interference measurements are performed by recording the interferograms of a complex signal field and a reference OAM mode (or Gaussian beam) with a camera.[21–23] Since the camera records the light intensity, the complex signal

*Address all correspondence to Jianqi Hu, jianqi.hu@epfl.ch; Siyuan Yu, yusy@mail.sysu.edu.cn

†The authors contributed equally to this work.

field cannot be directly retrieved from the intensity-only measurement. The measured interferogram intensity, however, consists of not only the desired interference between the signal and reference beams but also the self-beating of both of them. While the power of the reference is constant across the azimuthal angle, the existence of the signal–signal beat interference (SSBI) complicates the signal retrieval process. Multiple interferograms are thus required to remove the SSBI by adjusting the power[21,22] and/or phase[23] of the reference light. Single-shot interferometric measurement has been demonstrated in the context of partially coherent fields, but only for symmetric OAM spectra, while two shots are still needed for generalized spectral shapes.[24] Although the SSBI contribution may be omitted when the reference beam is sufficiently strong,[21] rigorous, single-shot retrieval remains elusive for conventional on-axis interferometry.

Notably, the interference measurement of the complex OAM spectrum resembles the detection of complex modulated signals in coherent optical communications, where the reference beam is the counterpart of the local oscillator. A phase-diverse coherent receiver is generally used to retrieve both the amplitude and phase of the modulated signal.[25] In recent years, considerable efforts have been made to reduce the receiver complexity in coherent communication systems, ideally by using only one single-ended photodetector.[26–31] The Kramers–Kronig (KK) receiver is an effective solution for direct detection of complex-valued signals.[28–31] In this case, the receiver works in a heterodyne scheme and requires that the frequency of the local oscillator be outside the signal's spectrum. When the interference waveform satisfies the minimum-phase condition,[31] the signal can be rigorously reconstructed from the intensity measurement via the KK relation. This greatly simplifies the receiver architecture into the straightforward direct detection. In addition, similar KK-based full-field retrieval has also been applied for holographic imaging exploring the space–time duality.[32,33]

In this work, by drawing a close analogy between the time-frequency and azimuth-OAM domains, we extend the KK retrieval concept into the OAM space, for the first time to our knowledge. Such an approach enables the readout of both the amplitude and phase relation of an arbitrary OAM state in a single-shot manner without increasing the system complexity. We describe in detail the retrieval procedure, which is experimentally validated in a high-dimensional OAM space. In particular, we demonstrate the diagnosis of a number of characteristic OAM states,[34–37] including fractional OAM modes[38] that slightly violate the KK retrieval criteria. The typical parameters essential for a KK receiver,[31] i.e., the carrier-to-signal power ratio (CSPR) and the number of sampling points, are discussed in the context of OAM fields. Furthermore, we compare the performance of the proposed KK approach and the conventional Fourier approach for a large set of arbitrary OAM states, where the superiority of the KK approach is clearly shown. The single-shot nature of the KK method may find useful applications for characterizing OAM-based systems in real time.

2 Results

2.1 Principle of Operation

A complex OAM field can be described by the controlled superposition in discrete OAM mode basis:[34]

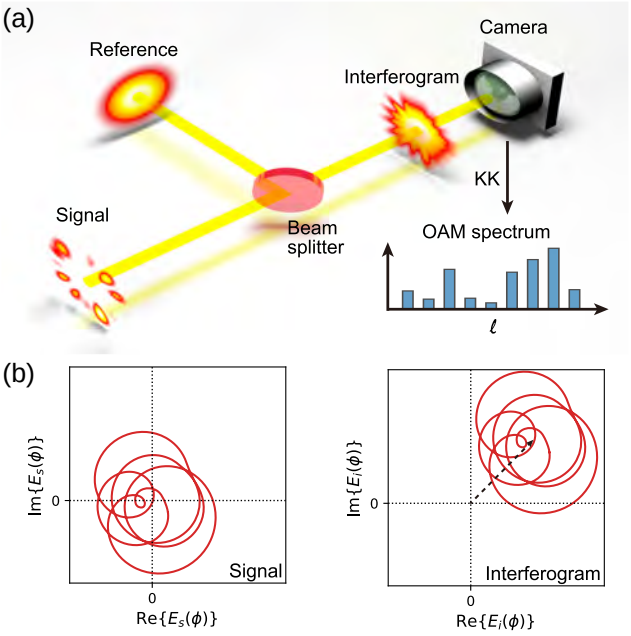

Fig. 1 Conceptual setup and the requirement for the KK retrieval. (a) The signal field with a complex OAM spectrum is co-axially combined with a reference Gaussian beam. The intensity of their interferogram is recorded with a camera and is used for the spectrum retrieval. (b) The azimuthal trajectories of the signal (left) and the interferogram (right) in the complex plane. In order to meet the minimum phase condition, the trajectory must not encircle the origin. With the addition of a sufficiently large reference field (denoted by the dashed arrow), the interferogram satisfies the requirement, and thus the KK method can rigorously reconstruct the complex signal OAM spectrum.

$$E_s(\phi) = \sum_{l=l_0+1}^{l_0+N} a_l e^{il\phi + i\theta_l}, \tag{1}$$

where ϕ is the azimuthal angle; a_l and θ_l are the amplitude and phase of the lth OAM mode, respectively. Here, we consider the modal decomposition of the OAM field in the interval of $[l_0+1, l_0+N]$, spanning an N-dimensional space. Without loss of generality, we assume $l_0 = 0$ hereafter, as we can always use a phase mask with helical phase $e^{-il_0\phi}$ to shift the OAM spectrum entirely above the zeroth order. In this study, the OAM fields are constructed based on perfect vortex modes[39] with identical radial distributions (see Note 1 in the Supplemental Material), such that we are only interested in field extraction in the azimuthal angle. As shown in Fig. 1(a), the complex signal field interferes with a reference beam with plane wave front $E_r(\phi) = Ae^{i\theta_r}$, where A is the amplitude of the reference mode, and θ_r is the relative phase between the reference and signal fields. The CSPR value is defined as the ratio between the power of reference and signal beams averaged in the azimuthal angle, i.e., CSPR $= 10\log\frac{\langle|E_r(\phi)|^2\rangle}{\langle|E_s(\phi)|^2\rangle}$. Similar to the single-sideband modulation for a KK receiver in communications,[28] no guard band is needed in between the reference and the signal OAM spectra. Then, the interferogram is imaged with a camera, and its intensity in the azimuthal angle is proportional to

$$|E_i(\phi)|^2 = |E_s(\phi) + E_r(\phi)|^2$$
$$= A^2 + |E_s(\phi)|^2 + 2A\,\mathrm{Re}\{E_s(\phi)e^{-i\theta_r}\}$$
$$= A^2 + \left|\sum_{l=1}^{N} a_l e^{il\phi + i\theta_l}\right|^2 + 2A\sum_{l=1}^{N} a_l \cos(l\phi + \theta_l - \theta_r). \tag{2}$$

The third term in the last equality of Eq. (2) contains all the Fourier coefficients $a_l e^{i\theta_l}$ required to reconstruct the signal field, apart from scaling and a constant phase shift, while the second term corresponds to the SSBI.

To extract the phase information from a single intensity measurement, the amplitude and phase of the interferogram $E_i(\phi)$ must be uniquely linked. A way to look at this is using the Z-extension as formulated in Ref. 31. By replacing the $e^{i\phi}$ in $E_i(\phi)$ with a variable Z, the interferogram becomes a polynomial function,

$$\mathcal{Z}_{E_i}(Z) = Ae^{i\theta_r} + \sum_{l=1}^{N} a_l e^{i\theta_l} Z^l = \frac{Ae^{i\theta_r}}{\prod_{l=1}^{N}(-z_l)} \prod_{l=1}^{N}(Z - z_l), \tag{3}$$

where z_l $(l = 1, 2, \ldots, N)$ are the roots of $\mathcal{Z}_{E_i}(Z) = 0$, when $a_N \neq 0$. The second equality of Eq. (3) shows that $\mathcal{Z}_{E_i}(Z)$ can be equivalently described by its zeros. Since the interferogram is under square-law detection, the zeros of $|E_i(\phi)|^2$ are found using properties of Z-extension,[31]

$$\mathcal{Z}_{|E_i|^2}(Z) = \mathcal{Z}_{E_i}(Z)\mathcal{Z}_{E_i^*}(Z)$$
$$= \frac{|A|^2}{Z^N \prod_{l=1}^{N}(-z_l)} \prod_{l=1}^{N}(Z - z_l)\left(Z - \frac{1}{z_l^*}\right), \tag{4}$$

where $*$ represents the complex conjugate. In Eq. (4), we obtain the zeros of $\mathcal{Z}_{E_i^*}(Z)$ by conjugating Eq. (3).[31] As such, the zeros of $\mathcal{Z}_{|E_i|^2}(Z)$ are in N pairs, comprising the zeros of $\mathcal{Z}_{E_i}(Z)$ and the inverse of their complex conjugates. It is noted that replacing the zeros of $\mathcal{Z}_{E_i}(Z)$ with their inverse conjugates would not modify the function $\mathcal{Z}_{|E_i|^2}(Z)$. This implies multiple different interferograms are mapped to the same intensity profile, thus causing ambiguity for the retrieval. If the interferogram is constructed such that all its zeros are outside or on the unit circle, also known as the minimum phase waveform,[31] one-to-one mapping between $\mathcal{Z}_{E_i}(Z)$ and $\mathcal{Z}_{|E_i|^2}(Z)$ is established. Evidently, a necessary and sufficient condition to be of a minimum phase waveform is that its trajectory does not encircle the origin of the complex plane.[40] This is visualized in Fig. 1(b). The left panel illustrates the azimuthal trajectory of a general OAM signal field $E_s(\phi)$, which does not meet the minimum phase requirement. With a sufficiently large reference field $Ae^{i\theta_r}$ (indicated by the dashed arrow), the azimuthal trajectory can be translated to match the minimum phase condition, as shown in the right panel of Fig. 1(b). Consequently, the amplitude and phase of the interferogram $E_i(\phi)$ are uniquely related. It is worth mentioning that, for a given signal OAM field, the required reference intensity for the minimum phase condition varies with the relative angle θ_r. Nevertheless, since no prior knowledge of the signal field is known, the reference amplitude needs to be greater than the signal's peak amplitude in the azimuthal angle, i.e., $A > |E_s(\phi)|$ for $\phi \in [0, 2\pi)$, thereby not encircling the origin. With this we can calculate the minimum CSPR required for rigorous retrieval, which is set by the peak-to-average power ratio of the signal field.

Once the minimum phase condition is reached, for an interference field $E_i(\phi) = |E_i(\phi)|e^{i\,\arg(E_i(\phi))}$ (arg denotes the argument), the logarithm of its amplitude $\log(|E_i(\phi)|)$ and phase $\arg(E_i(\phi))$ are related by the Hilbert transform,[31]

$$\arg(E_i(\phi)) = \frac{1}{2\pi}\, p.v. \int_0^{2\pi} \cot\left(\frac{\phi - \phi'}{2}\right) \log(|E_i(\phi')|)\mathrm{d}\phi', \tag{5}$$

where $p.v.$ is the principal value. Note that due to the periodic nature of the azimuthal space, the kernel here in the Hilbert transform is in the cotangent form rather than the inverse, and the integration is over one circle.[41] From Eq. (5), we can reconstruct the full field of the interferogram $E_i(\phi)$, and thus also the signal full field $E_s(\phi)$ by removing the constant reference term. Based on the Fourier relation, this equivalently gives the amplitude and phase of the OAM spectrum of $E_s(\phi)$.

2.2 Experimental KK Retrieval Procedure

In the experiment, the complex signal OAM fields are synthesized using computer-generated holograms and an optical 4-f system.[42] They consist of arbitrary superpositions of ring-shaped OAM modes with topological charges spanning 1 to 20. The OAM fields under test are then co-axially combined with a reference Gaussian beam, and their interferograms are recorded with a camera. The detailed experimental setup is described in the Note S1 in the Supplemental Material. To satisfy the minimum phase condition, we tune the reference light power slightly above the power threshold set by the minimum required CSPR. Due to the signal preparation method we used,[42] the experimental and minimum required CSPR difference is kept constant (~1 dB) for different measurement instances (see Note S2 in the Supplemental Material). In the following, we demonstrate the KK retrieval procedure on a random complex OAM spectrum as an example. The top panel of Fig. 2(a) shows the measured camera images of the reference and the interference beams. Their azimuthal intensity distributions are extracted by sampling around the interfering regions (indicated by the dashed circles) and unwrapped as shown in the bottom panel of Fig. 2(a). It can be seen that the measured reference $|E_r(\phi)|^2$ shows small intensity fluctuations in the azimuthal direction. Such a reference intensity pattern is unchanged while characterizing different signal OAM fields, so only their interferogram $|E_i(\phi)|^2$ needs to be measured each time, suggesting that the retrieval process is a single shot.

Similar to the KK full-field retrieval in space and time,[28,32] digital upsampling may also be required in our case if the number of physical sampling points is not sufficiently large to cover the spectrum expended by the logarithmic operation.[31] The effect of upsampling is discussed in Note S3 in the Supplemental Material. Throughout the paper, we take 71 azimuthal sampling points in the experiment, and then we digitally upsample the normalized interferogram $|E_i(\phi)|^2/|E_r(\phi)|^2$ by 11 times for the subsequent processing. The top panel of the Fig. 2(b) shows the logarithm of the upsampled interferogram $\log(|E_i(\phi)|/|E_r(\phi)|)$ as well as its Hilbert transform $\arg(E_i(\phi)/E_r(\phi))$. Instead of taking the convolution as defined in Eq. (5), the actual implementation of the Hilbert transform is

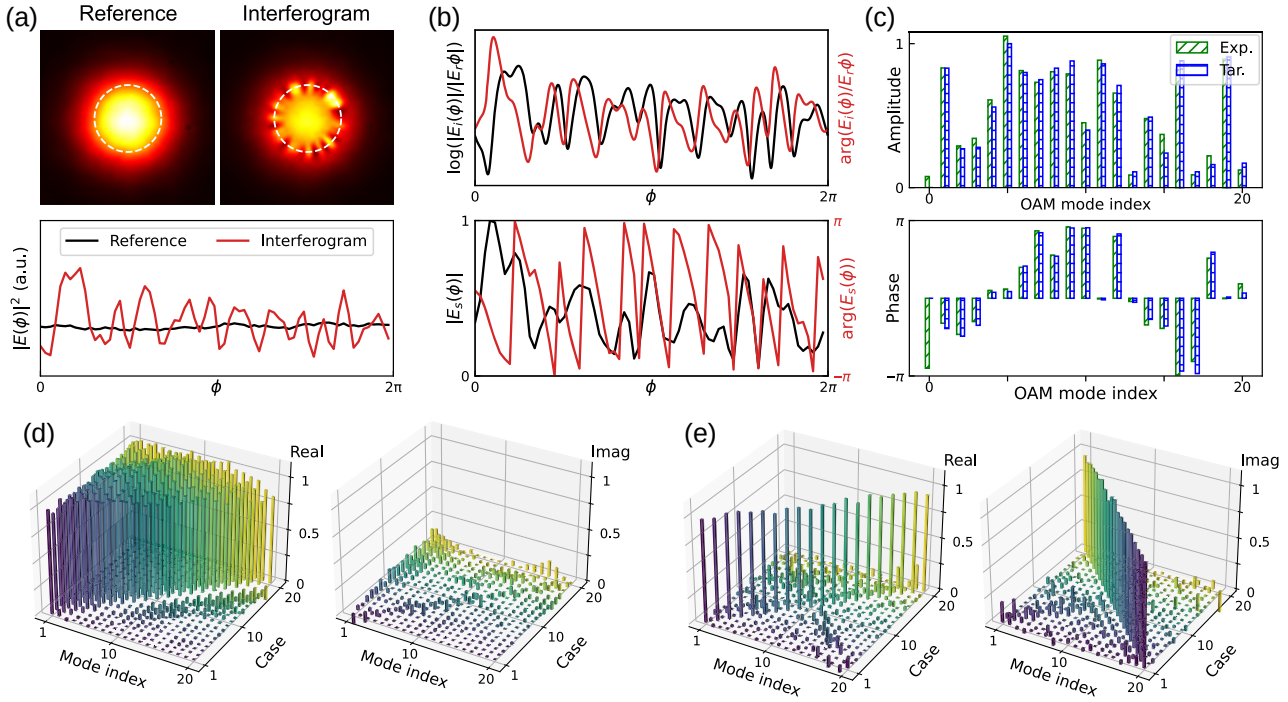

Fig. 2 Experimental single-shot KK retrieval. (a)–(c) Retrieval process of an arbitrary OAM spectrum. (a) The intensity images of the reference (top left) and the interferogram (top right) are captured by a camera. By sampling along the dashed circles in the images, their azimuthal distributions are extracted (bottom). (b) The interferogram is then normalized and digitally upsampled, whose phase is extracted from the Hilbert transform of the logarithm of its amplitude (top). From the full field of the interferogram, the amplitude and phase of the signal are obtained and downsampled to the original sampling points (bottom). (c) Taking the Fourier transform of the signal field derives the normalized amplitude (top) and relative phase relation (bottom) of the OAM spectrum. An accuracy of 97.6% is achieved by comparing the retrieved and the target OAM spectra. (d), (e) Measured 2D bar charts of the OAM states for (d) the superpositions of mode indices from 1 to n ($n = 1, 2, \ldots, 20$) with equal amplitudes and in-phase relations; (e) the superpositions of mode indices n and $21 - n$ ($n = 1, 2, \ldots, 20$) with equal amplitudes and a $\pi/2$ phase shift. The average retrieval accuracies in (d) and (e) are 98.9% and 96.0%, respectively.

realized in the spectral domain using the fast Fourier transform and the sign function.[28] The full field of the interferogram $E_i(\phi)/E_r(\phi)$ is thus derived, from which the full signal field can be easily calculated by $E_s(\phi) \approx |E_r(\phi)|(E_i(\phi)/E_r(\phi) - 1)$. Here, we omit the negligible phase nonuniformity of the experimental reference beam. The retrieved signal field is then downsampled, whose normalized amplitude $|E_s(\phi)|$ and phase $\arg(E_s(\phi))$ are plotted in the bottom panel of Fig. 2(b). Finally, the complex signal OAM spectrum is retrieved by taking the Fourier transform of $E_s(\phi)$. The step-by-step workflow for KK retrieval is described in Note S4 in the Supplemental Material, and the code is also provided therein. Figure 2(c) shows the retrieved amplitude (top) and phase (bottom) profile of the OAM spectrum compared to the ground truth. It can be seen that they are in excellent agreement. To quantitatively assess the performance of the KK retrieval, we introduce the following metric based on the overlap integral of the target and the retrieved OAM spectra,

$$\eta = \frac{\left|\sum_{-\infty}^{\infty} a_l a_l' e^{i\theta_l - i\theta_l'}\right|^2}{\left(\sum_{-\infty}^{\infty} |a_l|^2\right)\left(\sum_{-\infty}^{\infty} |a_l'|^2\right)}, \tag{6}$$

where a_l' and θ_l' are the amplitude and phase of the lth order OAM mode of the retrieved OAM spectrum, respectively. In Fig. 2(c), the retrieval accuracy η is found to be 97.6%.

To further test the validity of the proposed method, we apply the KK retrieval to diagnose a series of OAM spectra shown in Figs. 2(d) and 2(e). The first scenario is the rectangular OAM spectra $E_s(\phi) = \sum_{l=1}^{n} e^{il\phi}$ of different widths ($n = 1, 2, \ldots, 20$), where the constituent OAM modes are of equal amplitudes and in-phase relations. Figure 2(d) shows the real and imaginary parts of the measured OAM spectra for these cases in a complex two-dimensional (2D) bar chart. As expected, the retrieved OAM spectra are approximately of rectangular shapes and are mainly populated in the real part of the bar chart due to their in-phase features. An average accuracy of 98.9% is achieved for these measurements. For the second scenario, the OAM spectra are structured by $E_s(\phi) = e^{in\phi} + ie^{i(21-n)\phi}$, where $n = 1, 2, \ldots, 20$. In this case, the bar chart should be diagonal in its real part but antidiagonal in its imaginary part. This is clearly observed in the measurements shown in Fig. 2(e), with an average retrieval accuracy reaching 96.0%.

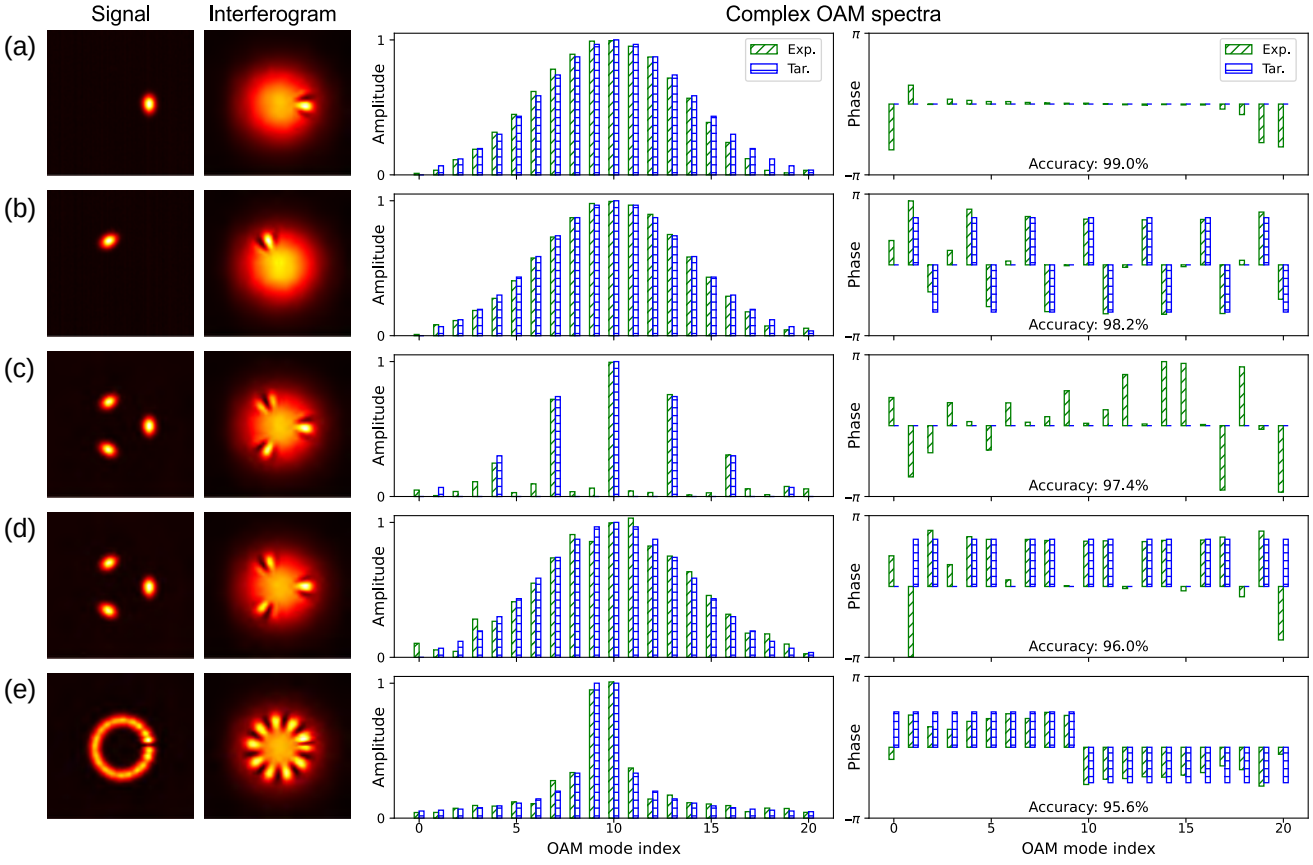

Fig. 3 Measurements of complex OAM spectra. Left, the measured intensity images of the signal and the interferogram; right, the normalized amplitude and relative phase of the target and experimentally retrieved OAM spectrum. (a)–(d) Gaussian-shaped OAM spectra centered at 10th order with versatile OAM mode spacings and relative phase relations. (a) In-phase OAM spectrum with a mode spacing of 1. (b) Linear-phase OAM spectrum with a phase slope of $2\pi/3$ and a mode spacing of 1. (c) In-phase OAM spectrum with a mode spacing of 3. (d) OAM spectrum with periodic Talbot phase $[0, 2\pi/3, 2\pi/3]$ and a mode spacing of 1. (e) Fractional OAM mode with a topological charge of 9.5. The retrieval accuracy is also indicated for each case.

2.3 Measurement of Characteristic OAM States

The single-shot KK full-field retrieval allows for the simple characterization of complex OAM states. In the following, we study various characteristic OAM spectra displayed in Fig. 3. Figure 3(a) demonstrates the measurement of a signal field with a Gaussian-shaped, in-phase OAM spectrum centered at the 10th order, i.e., $E_s(\phi) = \sum_{l=1}^{20} e^{-\frac{(l-10)^2}{30}} e^{il\phi}$, which corresponds to a bright petal horizontally aligned in the azimuthal angle.[34] From only a single interferogram, we can reconstruct the signal's OAM spectrum, which matches the ground truth well. As a single-shot retrieval method, we only use the interferograms to reconstruct the complex OAM fields. Note that all the measured images of the signal beams in Fig. 3 are displayed only as the ground truth and to help visualization of the signal fields, but they are not used for their OAM spectra retrieval. Figure 3(b) shows the condition for the same petal field as in Fig. 3(a) except being rotated by $2\pi/3$ counterclockwise. A linear phase ramp is thus imparted to the OAM spectrum due to the rotation, with a phase slope of $2\pi/3$. This feature is well captured by the KK approach in a single-shot fashion, simplifying the previously used schemes, such as the sequential weak and strong measurements[35] or the phase-shifting holograms.[43]

In addition, it is known that increasing the mode spacing in the OAM spectrum will lead to the multiplication of petals in the azimuthal angle.[34] This is shown in Fig. 3(c), where a three-petal field under test is constructed from in-phase OAM modes with an order spacing of 3 and the same envelope as in Figs. 3(a) and 3(b). The interferogram could accurately retrieve its equidistant OAM structure as well as its in-phase relation. Notice that the large phase error in Fig. 3(c) is only associated with void OAM modes or at small modal amplitudes. Furthermore, we investigate the complex OAM spectrum of the petal field in Fig. 3(c) being subjected to phase modulation. Specifically, when the three petals are modulated with the Talbot phase sequence of $[0, -2\pi/3, -2\pi/3]$, the initial OAM spectrum is self-imaged to create new OAM modes while preserving its overall envelope.[37] The measurement results are shown in Fig. 3(d). Although the signal intensity patterns in Figs. 3(c) and 3(d) are identical, the phenomenon of the OAM spectral self-imaging is clearly observed from the KK retrieval. More interestingly, the approach also provides a direct phase measurement of all

the OAM modes. It can be seen that the relative phases of OAM self-images again follow the Talbot relation of $[0, 2\pi/3, 2\pi/3]$, apart from a constant phase [subtracted thus not shown in Fig. 3(d) for better representability]. Notably, such a phase structure of Talbot self-images has only been recently determined in space[44] and time,[45] while here we measure it for the first time in the OAM basis. The measured quadratic phase relation suggests that the origin of self-imaging here is different from the Gouy-phase-mediated revivals of spatial fields.[46–48]

We also use the KK method to characterize the complex spectra of fractional OAM modes. A fractional OAM order can be viewed as the weighted superposition of integer OAM modes.[49] In Fig. 3(e), we show the measurement of the fractional OAM field with a topological charge of 9.5, i.e., $E_s(\phi) = e^{i9.5\phi}$. The field intrinsically exhibits around 1% power leakage to the negative OAM orders, thus not rigorously satisfying the single-sideband requirement. Nevertheless, since the leakage is small, the KK retrieval still works effectively with an accuracy of 95.6%. We can see that the fractional OAM field in Fig. 3(e) is mainly composed of the 9th and 10th OAM modes, together with the other OAM orders slowly decaying when moving away from the center modes. Moreover, we are able to identify the phase relation of its constituent OAM modes, which is rarely explored for the fractional OAM states. It is found that the orders at the left and right parts of the fractional OAM spectrum are approximately out of phase. The phase deviation between the measured and theoretical fractional OAM spectra may come in part from the finite sampling in the azimuthal angle.

2.4 Effect of CSPR Levels

Figure 4 shows the KK retrieval performance at different CSPR levels. As an example, the same OAM state in Fig. 3(a) is used as the signal field for the study, whose complex amplitude field is displayed in Fig. 4(a). From this we can plot in Fig. 4(b) the trajectory of its azimuthal distribution in the complex plane. As mentioned previously, to guarantee rigorous KK retrieval, the trajectory of the signal field after interfering with the reference light must not encircle the origin of the complex plane. The minimum required reference intensity for such a criterion is highly dependent on the relative angle between the reference and the signal fields. In Fig. 4(b), the minimum required CSPR varies in a range between 5.1 and 11.3 dB, where the lower and upper bounds correspond to the reference field being added in-phase ($\theta_r = 0$) and out-of-phase ($\theta_r = \pi$) with the signal field, respectively. The minimum required CSPR value valid for all these relative angles is thus set by the upper bound, i.e., 11.3 dB.

Figure 4(c) presents the experimental results for the retrieval accuracy at different CSPR levels and various relative phases between the signal and reference fields. In the experiment, the control of the CSPR and its relative phase are realized via the computer-generated holograms. The phases shown in Fig. 4(c) are varied in steps of $\pi/4$. We emphasize here that they do not correspond to the actual θ_r but are offset from a constant unknown phase due to experimental constraints. In Fig. 4(c), when the experimental CSPR is well below the 11.3 dB threshold (marked by the dashed line), the retrieval performance changes significantly with the phase, although for some angles the retrieval accuracy is acceptable. Once the CSPR exceeds the threshold, decent retrieval is achieved for arbitrary relative phases between the reference and signal fields. The experimental

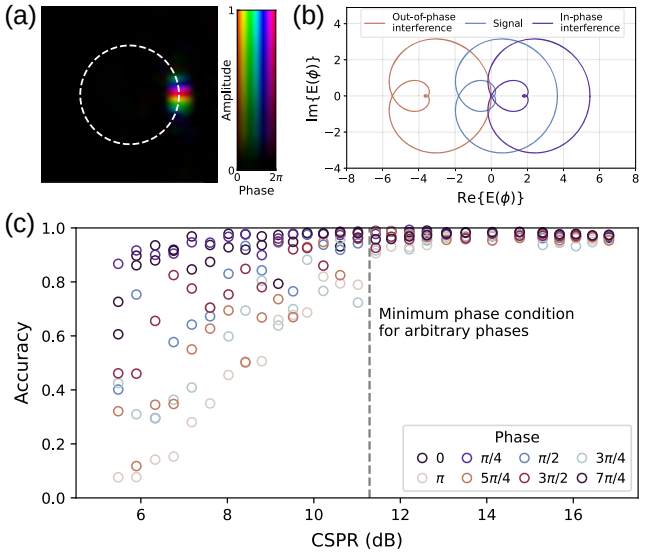

Fig. 4 KK retrieval at different CSPR levels. (a) The complex amplitude field of the signal used for the study [the same as the signal field in Fig. 3(a)]. (b) The azimuthal trajectories of the signal field and interferograms with in-phase and out-of-phase addition of the reference field. The trajectories of interferograms are exactly at the limit of the minimum phase condition, which correspond to the minimum required CSPRs of 5.1 dB (in-phase) and 11.3 dB (out-of-phase), respectively. (c) The accuracy of the KK retrieval at different CSPR levels and varying phases between the signal and reference fields. Below the CSPR threshold for arbitrary phases (11.3 dB, indicated by the dashed line), the retrieval performance varies with the phase, while above, the retrieval accuracy is approximately close to the unity for all the phases.

results in Fig. 4(c) are in accordance with the theoretical analysis carried out above.

2.5 Performance Evaluation

In this part, we evaluate the performance of the KK retrieval on a large set of OAM spectra generated with random complex mode coefficients. As in the previous measurements, the difference between the experimental and minimum required CSPRs is automatically maintained around 1 dB, which is experimentally confirmed in Note S2 in the Supplemental Material for 100 random OAM spectra. Figure 5(a) shows the histogram of the KK retrieval accuracy for 1000 spectrum samples on the same dimensional space as before. An average retrieval accuracy of 95.6% is obtained, with a standard deviation of 1.2%. The performance of the KK retrieval is also compared with the conventional Fourier method,[21,50] computed by the Fourier transform disregarding the SSBI in Eq. (2). A clear advantage of using the KK method is shown in Fig. 5(a), suggesting that the SSBI cannot be neglected under such a CSPR level. Nevertheless, the field retrieved by the Fourier method does gradually approach the ground truth with the increase of CSPR values. The detailed discussion of the Fourier method can be found in Note S5 in the Supplemental Material. Next, we further push the measurement dimensionality up to the 30th OAM order while keeping the azimuthal sampling points and the digital upsampling unchanged. Figure 5(b) shows the

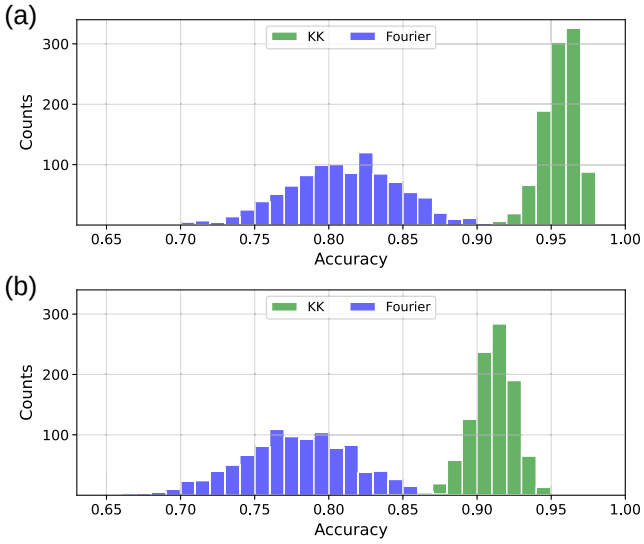

Fig. 5 Performance evaluation of the KK retrieval on random OAM spectra. (a), (b) Histograms of the retrieval accuracy of the KK method and the conventional Fourier method, measured on 1000 OAM spectra with random complex mode coefficients. (a) For an OAM measurement range from 1 to 20, the average and standard deviation of the KK retrieval accuracy are 95.6% and 1.2%, respectively. (b) For an OAM measurement range from 1 to 30, the average and standard deviation of the KK retrieval accuracy are 91.1% and 1.4%, respectively. The KK method shows superiority over the Fourier method in both cases.

corresponding experimental results. The average KK retrieval accuracy in this case still reaches 91.1% with a standard deviation of 1.4%, outperforming the conventional Fourier method by a large margin. Although the performance of the Fourier method may be improved by increasing the reference power, keeping relatively low CSPR values is favored to avoid large DC components in detection, thus maximally utilizing the dynamic range of the camera.

3 Discussion

The experimental setup used in this work is a conventional on-axis interferometer equivalent to the configurations in Refs. 21–23. However, contrary to all the past demonstrations that require a few shots to diagnose a complex OAM spectrum, our method provides single-shot retrieval mediated by the famous KK relation. This greatly accelerates the measurement, as it bypasses the need to adjust the amplitude and/or phase of the reference when characterizing each superimposed state.[21–23] In our system, the speed of the measurement is defined by the frame rate of the camera. On the other hand, off-axis holography is also capable of retrieving full fields in a single shot and has been used to measure OAM beams.[18] While the conventional off-axis method requires separating SSBI and signals in the Fourier space, KK off-axis holography recovers the signal beam with a smaller off-axis angle.[32] In our work, the measurement is on-axis and thus different from KK off-axis holography. Further, the KK conditions in the off-axis method and our approach are also different, with the former in the wave vector space and the latter in the OAM space (see Note S6 in the Supplemental Material). To visualize the difference, we present in Note S6 in the Supplemental Material an example that can be rigorously retrieved by our OAM KK method, using a reference beam whose wave vector component lies within the signal field in the wave vector space, while violating the condition for spatial KK retrieval. In addition, our approach demonstrates advantages when characterizing perfect vortex fields of narrow ring widths, as these beams take up a large space in the wave vector domain that requires high sampling resolution in off-axis holography. In addition, we discuss the choice of the sampling radius for retrieval in Note S7 in the Supplemental Material. Recently, complex OAM spectrum analyzers have also been demonstrated using machine learning but require either dense layers of deep neural network[51] or a multitude of diffractive phase masks in cascade,[52] as well as being sensitive to the parameters of input fields, while our method can be easily extended to measuring multiple concentric OAM states as well as the superposition of Laguerre–Gaussian modes (see Note S8 in the Supplemental Material). Since in this study we are mainly dealing with only the azimuthal field distribution, the detection can be seamlessly connected to the rotational Doppler effect.[53] In this scenario, the camera is replaced by a fast photodetector with a spinning phase mask performing the azimuth-to-time mapping.[21]

To sum up this work, we propose and experimentally demonstrate a high-dimensional OAM analyzer that can measure complex OAM states in one single shot. The idea is inspired by the KK receiver in optical communications, while here we introduce the same concept to the OAM spectrum analysis and represent a new application scenario of KK phase retrieval. As demonstrated here, the proposed single-shot KK interferometry can be readily employed for state measurements in OAM-based information processing, sensing, and communication systems. This work also implies the general duality between azimuth-OAM and time-frequency, suggesting that their processing techniques may be borrowed interchangeably.

Data, Materials, and Code Availability

Data underlying the results presented in this paper are not publicly available at this time but may be obtained from the authors upon reasonable request. A sample code for KK retrieval of OAM fields is provided at https://github.com/GeorgeCravis/OAM-KK.

Acknowledgments

This work was supported by the National Key Research and Development Program of China (2018YFB1801803, 2019YFA0706302), the Basic and Applied Basic Research Foundation of Guangdong Province (2021B1515020093, 2021B1515120057), the Local Innovative and Research Teams Project of Guangdong Pearl River Talents Program (2017BT01X121), and the Swiss National Science Foundation (P2ELP2_199825). The authors declare no conflicts of interest.

References

1. D. Naidoo et al., "Controlled generation of higher-order Poincaré sphere beams from a laser," *Nat. Photonics* **10**(5), 327–332 (2016).
2. A. Forbes, A. Dudley, and M. McLaren, "Creation and detection of optical modes with spatial light modulators," *Adv. Opt. Photonics* **8**(2), 200–227 (2016).

3. A. E. Willner et al., "Optical communications using orbital angular momentum beams," *Adv. Opt. Photonics* **7**(1), 66–106 (2015).
4. H. Rubinsztein-Dunlop et al., "Roadmap on structured light," *J. Opt.* **19**(1), 013001 (2016).
5. M. J. Padgett, "Orbital angular momentum 25 years on," *Opt. Express* **25**(10), 11265–11274 (2017).
6. M. Erhard et al., "Twisted photons: new quantum perspectives in high dimensions," *Light Sci. Appl.* **7**(3), 17146 (2018).
7. Y. Shen et al., "Optical vortices 30 years on: OAM manipulation from topological charge to multiple singularities," *Light. Sci. Appl.* **8**(1), 90 (2019).
8. C. Schulze et al., "Measurement of the orbital angular momentum density of light by modal decomposition," *New J. Phys.* **15**(7), 073025 (2013).
9. J. Hickmann et al., "Unveiling a truncated optical lattice associated with a triangular aperture using light's orbital angular momentum," *Phys. Rev. Lett.* **105**(5), 053904 (2010).
10. K. Dai et al., "Measuring OAM states of light beams with gradually-changing-period gratings," *Opt. Lett.* **40**(4), 562–565 (2015).
11. S. Zheng and J. Wang, "Measuring orbital angular momentum (OAM) states of vortex beams with annular gratings," *Sci. Rep.* **7**(1), 40781 (2017).
12. J. Leach et al., "Measuring the orbital angular momentum of a single photon," *Phys. Rev. Lett.* **88**(25), 257901 (2002).
13. G. C. Berkhout et al., "Efficient sorting of orbital angular momentum states of light," *Phys. Rev. Lett.* **105**(15), 153601 (2010).
14. M. P. Lavery et al., "Refractive elements for the measurement of the orbital angular momentum of a single photon," *Opt. Express* **20**(3), 2110–2115 (2012).
15. M. Mirhosseini et al., "Efficient separation of the orbital angular momentum eigenstates of light," *Nat. Commun.* **4**(1), 2741 (2013).
16. Y. Wen et al., "Spiral transformation for high-resolution and efficient sorting of optical vortex modes," *Phys. Rev. Lett.* **120**(19), 193904 (2018).
17. G. Labroille et al., "Efficient and mode selective spatial mode multiplexer based on multi-plane light conversion," *Opt. Express* **22**(13), 15599–15607 (2014).
18. N. K. Fontaine et al., "Laguerre-Gaussian mode sorter," *Nat. Commun.* **10**(1), 1865 (2019).
19. Y. Zhang et al., "Simultaneous sorting of wavelengths and spatial modes using multi-plane light conversion," arXiv:2010.04859 (2020).
20. H. Huang et al., "Phase-shift interference-based wavefront characterization for orbital angular momentum modes," *Opt. Lett.* **38**(13), 2348–2350 (2013).
21. H.-L. Zhou et al., "Orbital angular momentum complex spectrum analyzer for vortex light based on the rotational Doppler effect," *Light Sci. Appl.* **6**(4), e16251 (2017).
22. A. D'Errico et al., "Measuring the complex orbital angular momentum spectrum and spatial mode decomposition of structured light beams," *Optica* **4**(11), 1350–1357 (2017).
23. S. Fu et al., "Universal orbital angular momentum spectrum analyzer for beams," *PhotoniX* **1**(1), 19 (2020).
24. G. Kulkarni et al., "Single-shot measurement of the orbital-angular-momentum spectrum of light," *Nat. Commun.* **8**(1), 1054 (2017).
25. E. Ip et al., "Coherent detection in optical fiber systems," *Opt. Express* **16**(2), 753–791 (2008).
26. W.-R. Peng et al., "Spectrally efficient direct-detected OFDM transmission employing an iterative estimation and cancellation technique," *Opt. Express* **17**(11), 9099–9111 (2009).
27. S. Randel et al., "100-Gb/s discrete-multitone transmission over 80-km SSMF using single-sideband modulation with novel interference-cancellation scheme," in *Eur. Conf. Opt. Commun. (ECOC)*, IEEE, pp. 1–3 (2015).
28. A. Mecozzi, C. Antonelli, and M. Shtaif, "Kramers–Kronig coherent receiver," *Optica* **3**(11), 1220–1227 (2016).
29. Z. Li et al., "SSBI mitigation and the Kramers–Kronig scheme in single-sideband direct-detection transmission with receiver-based electronic dispersion compensation," *J. Lightwave Technol.* **35**(10), 1887–1893 (2017).
30. T. Bo and H. Kim, "Kramers–Kronig receiver operable without digital upsampling," *Opt. Express* **26**(11), 13810–13818 (2018).
31. A. Mecozzi, C. Antonelli, and M. Shtaif, "Kramers–Kronig receivers," *Adv. Opt. Photonics* **11**(3), 480–517 (2019).
32. Y. Baek et al., "Kramers–Kronig holographic imaging for high-space-bandwidth product," *Optica* **6**(1), 45–51 (2019).
33. Y. Baek and Y. Park, "Intensity-based holographic imaging via space-domain Kramers–Kronig relations," *Nat. Photonics* **15**(5), 354–360 (2021).
34. G. Xie et al., "Spatial light structuring using a combination of multiple orthogonal orbital angular momentum beams with complex coefficients," *Opt. Lett.* **42**(5), 991–994 (2017).
35. M. Malik et al., "Direct measurement of a 27-dimensional orbital-angular-momentum state vector," *Nat. Commun.* **5**(1), 3115 (2014).
36. J. Hu, C.-S. Brès, and C.-B. Huang, "Talbot effect on orbital angular momentum beams: azimuthal intensity repetition-rate multiplication," *Opt. Lett.* **43**(16), 4033–4036 (2018).
37. Z. Lin et al., "Spectral self-imaging of optical orbital angular momentum modes," *APL Photonics* **6**(11), 111302 (2021).
38. J. B. Götte et al., "Light beams with fractional orbital angular momentum and their vortex structure," *Opt. Express* **16**(2), 993–1006 (2008).
39. P. Vaity and L. Rusch, "Perfect vortex beam: Fourier transformation of a Bessel beam," *Opt. Lett.* **40**(4), 597–600 (2015).
40. A. Mecozzi, "A necessary and sufficient condition for minimum phase and implications for phase retrieval," arXiv:1606.04861 (2016).
41. V. Cizek, "Discrete Hilbert transform," *IEEE Trans. Audio Electroacoust.* **18**(4), 340–343 (1970).
42. V. Arrizón et al., "Pixelated phase computer holograms for the accurate encoding of scalar complex fields," *J. Opt. Soc. Am. A* **24**(11), 3500–3507 (2007).
43. G. Xie et al., "Using a complex optical orbital-angular-momentum spectrum to measure object parameters," *Opt. Lett.* **42**(21), 4482–4485 (2017).
44. H. G. De Chatellus et al., "Phases of Talbot patterns in angular self-imaging," *J. Opt. Soc. Am. A* **32**(6), 1132–1139 (2015).
45. J. Clement, H. G. de Chatellus, and C. R. Fernández-Pousa, "Far-field Talbot waveforms generated by acousto-optic frequency shifting loops," *Opt. Express* **28**(9), 12977–12997 (2020).
46. B. P. da Silva et al., "Pattern revivals from fractional Gouy phases in structured light," *Phys. Rev. Lett.* **124**(3), 033902 (2020).
47. R.-Y. Zhong et al., "Gouy-phase-mediated propagation variations and revivals of transverse structure in vectorially structured light," *Phys. Rev. A* **103**(5), 053520 (2021).
48. H.-J. Wu et al., "Conformal frequency conversion for arbitrary vectorial structured light," *Optica* **9**(2), 187–196 (2022).
49. H. Zhang et al., "Review on fractional vortex beam," *Nanophotonics* **11**(2), 241–273 (2022).
50. N. Bozinovic et al., "Control of orbital angular momentum of light with optical fibers," *Opt. Lett.* **37**(13), 2451–2453 (2012).
51. H. Guo, X. Qiu, and L. Chen, "Simple-diffraction-based deep learning to reconstruct a high-dimensional orbital-angular-momentum spectrum via single-shot measurement," *Phys. Rev. Appl.* **17**(5), 054019 (2022).
52. H. Wang et al., "Intelligent optoelectronic processor for orbital angular momentum spectrum measurement," *PhotoniX* **4**(1), 9 (2023).
53. J. Courtial et al., "Measurement of the rotational frequency shift imparted to a rotating light beam possessing orbital angular momentum," *Phys. Rev. Lett.* **80**(15), 3217–3219 (1998).

Zhongzheng Lin received his BS degree in physics from Dalian University of Technology, Dalian, China, in 2018. He is currently a PhD candidate in the School of Electronics and Information Technology at Sun Yat-sen University, Guangzhou, China. His research mainly focuses on the manipulation and detection of the structured light, especially optical vortices.

Jianqi Hu received his BE degree from the University of Electronic Science and Technology of China, in 2016, and his PhD in photonics from École Polytechnique Fédérale de Lausanne (EPFL), Switzerland, in 2021. He continued his research as a postdoc at EPFL from 2021 to 2022. Currently, he is an SNF postdoc fellow in Laboratoire Kastler Brossel, École Normale Supérieure, France. His research interests include integrated nonlinear photonics, frequency combs, orbital angular momentum, and optical computing.

Yujie Chen received his PhD in physics (photonics) from the Institute of Photonics, University of Strathclyde, Glasgow, United Kingdom, in 2012. He is currently a professor in the School of Electronics and Information Technology, Sun Yat-sen University, Guangzhou, China. His research interests include micro/nano-structured photonic devices for manipulating light fields, as well as their applications in optical information processing and optical communications.

Camille-Sophie Brès received her bachelor's degree in electrical engineering from McGill University, Canada, in 2002, and her PhD in electrical engineering from Princeton University, USA, in 2007. After a postdoc at UCSD, she joined the Institute of Electrical Engineering at EPFL, Switzerland, where she is currently an associate professor. Her work focusses on leveraging and enhancing nonlinear processes in optical waveguides for the optimization of light conversion, signal processing, and sensing. She was elected fellow of Optica in 2019.

Siyuan Yu received his PhD in photonics from the University of Glasgow, United Kingdom, in 1997. He is currently a professor with Sun Yat-sen University, Guangzhou, China. He has helped in pioneering areas, such as high-speed integrated optical switches, microring lasers, integrated quantum photonics, and more recently, mode-division multiplexing devices and systems based on orbital angular momentum modes of light. He has published over 200 papers, including two cover features on science, and has been granted several international patents.

Research Article

ADVANCED PHOTONICS

Orbital angular momentum based intra- and interparticle entangled states generated via a quantum dot source

Alessia Suprano,[a] Danilo Zia,[a] Mathias Pont,[b] Taira Giordani,[a] Giovanni Rodari,[a] Mauro Valeri,[a] Bruno Piccirillo,[c,d] Gonzalo Carvacho,[a] Nicolò Spagnolo,[a] Pascale Senellart,[b] Lorenzo Marrucci,[c] and Fabio Sciarrino[a,*]

[a]Sapienza Università di Roma, Dipartimento di Fisica, Roma, Italy
[b]Université Paris-Saclay, UMR 9001, Centre for Nanosciences and Nanotechnology, CNRS, Palaiseau, France
[c]Università di Napoli Federico II, Complesso Universitario di Monte Sant'Angelo, Dipartimento di Fisica "Ettore Pancini", Napoli, Italy
[d]INFN - Sezione di Napoli, Napoli, Italy

Abstract. Engineering single-photon states endowed with orbital angular momentum (OAM) is a powerful tool for quantum information photonic implementations. Indeed, due to its unbounded nature, OAM is suitable for encoding qudits, allowing a single carrier to transport a large amount of information. Most of the experimental platforms employ spontaneous parametric down-conversion processes to generate single photons, even if this approach is intrinsically probabilistic, leading to scalability issues for an increasing number of qudits. Semiconductor quantum dots (QDs) have been used to get over these limitations by producing on-demand pure and indistinguishable single-photon states, although only recently they have been exploited to create OAM modes. Our work employs a bright QD single-photon source to generate a complete set of quantum states for information processing with OAM-endowed photons. We first study hybrid intraparticle entanglement between OAM and polarization degrees of freedom of a single photon whose preparation was certified by means of Hong–Ou–Mandel visibility. Then, we investigate hybrid interparticle OAM-based entanglement by exploiting a probabilistic entangling gate. The performance of our approach is assessed by performing quantum state tomography and violating Bell inequalities. Our results pave the way for the use of deterministic sources for the on-demand generation of photonic high-dimensional quantum states.

Keywords: orbital angular momentum; quantum dot; intraparticle entanglement; interparticle entanglement; Bell violation.

Received Feb. 8, 2023; revised manuscript received Jun. 2, 2023; accepted for publication Jul. 31, 2023; published online Aug. 30, 2023.

[DOI: 10.1117/1.AP.5.4.046008]

1 Introduction

In the last few decades, structured light states characterized by an on-demand distribution for both field amplitude and phase have gained great interest.[1] Among them, twisted beams carrying orbital angular momentum (OAM) have been the focus of several studies, due to their wide range of applications. As pointed out by Allen et al.,[2] OAM is carried by all the beams that present a phase term of the form $e^{i\ell\phi}$, where ϕ is the azimuthal angle in cylindrical coordinates and ℓ is an unbounded integer. This phase term is responsible for the typical helicoidal wavefront, and each photon shows an OAM equal to $\ell\hbar$.

In the classical domain, the nontrivial phase structure of OAM states is used in several protocols covering a wide number of fields, such as metrology,[3] imaging,[4–6] particle trapping,[7] and communication.[8–14] The unbounded nature of the OAM is instead the basis of its employment in quantum information. Therefore, OAM modes are used in quantum communication,[15–20] cryptography,[21–23] simulation,[24–26] computation, and information processing.[27–29] In particular, OAM-based encoding enlarges the amount of information that a single photon can support, leading to increased security in the communication protocols.[30,31] When

*Address all correspondence to Fabio Sciarrino, fabio.sciarrino@uniroma1.it

the helicoidal wavefront is coupled with a nontrivial distribution of the spin angular momentum (SAM), also known as polarization, a new class of states called vector vortices (VVs) are introduced. Given this peculiar coupling, VV beams turn out to be intrasystem maximally entangled in the OAM and polarization degrees of freedom.[32] As for the OAM modes, VV beams are applied in several areas, both in the classical and quantum regime, such as optical trapping,[33,34] communication,[35,36] computing,[37–45] sensing, and metrology.[46–50] Moreover, knowing the importance of the Hong–Ou–Mandel (HOM) effect[51] and its applicability in quantum information science,[52] the interference behavior between structured photons has also been studied in order to perform increasingly complex tasks.[53–55]

Despite the large number of applications, sources that produce single photons carrying OAM deterministically and with high brightness are still under development.[56] In fact, most of the experimental implementations leverage the production of single photons through spontaneous parametric down-conversion (SPDC) in nonlinear crystals and modulating their states using bulk systems, such as spatial light modulators[57,58] and q-plates,[22,59,60] employing metasurfaces also for generating entangled states in the OAM and polarization degrees of freedom.[61] However, SPDC is intrinsically probabilistic and suffers from a trade-off between the brightness and the purity of the produced single photons. Moreover, since in each process, it is always possible to generate more than one photon, these kinds of sources undermine the security of quantum cryptography schemes.[62] Semiconductor quantum dots (QDs) have emerged as a platform to overcome these limitations. Acting as artificial atoms when resonantly pumped with pulsed lasers, QDs are capable of generating indistinguishable single photons with high brightness in a nearly deterministic fashion.[63–66] However, most of the efforts have been concentrated on the generation of single or entangled states encoding the information in the photons polarization[67–72] or in the temporal domain.[73] Only recently, works exploiting QDs to engineer OAM modes[56] within a prepare-and-measure framework have appeared. In particular, integrated sources based on microring resonators embedded with QDs[56] have been implemented, in which the OAM states encoded in the generated single photons could not be easily manipulated.

At variance with Ref. 56, we exploit commercial QD-based single-photon sources and focus on the development of quantum information processing protocols with VV beams. Specifically, well-known OAM manipulation technologies have been extensively used to develop high-dimensional quantum communication protocols,[18,22] to reach a high flexibility in engineering arbitrary qudit states,[74,75] and to develop simulated processes based on the quantum walk dynamics.[24,25] Here, we combine these technologies with an innovative and nearly deterministic single-photon source, opening the way for further developments of quantum information protocols that take advantage of high-dimensional resources and of the benefits introduced by using QDs. In particular, besides focusing on interfacing between these two kinds of technologies, we go a step forward and study the hybrid entanglement in high-dimensional Hilbert spaces implementing a quantum gate both in the intra- and interparticle regime (Fig. 1). Previously, states characterized by hybrid intraphoton entanglement between the OAM and polarization degree of freedom have been generated via SPDC processes.[18,38,76,77] However, since this kind of source is probabilistic, the state is certified in a heralded configuration that drastically decreases

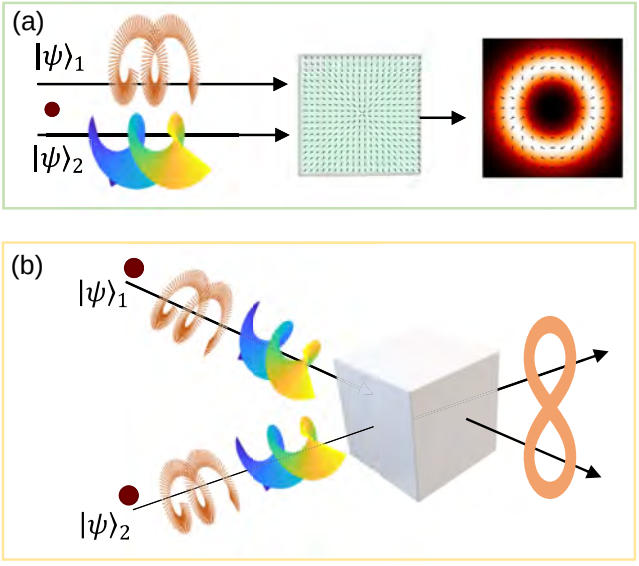

Fig. 1 Entanglement generation. (a) In the intraparticle entanglement, the polarization and OAM subsystems are made to interact using a q-plate. The two-dimensional state $|\psi\rangle_1$ is initialized with the right polarization $|R\rangle = |0\rangle$, while the qudit $|\psi\rangle_2$ is prepared with a null OAM value $|0\rangle$. The action of the unitary operator consists of increasing or decreasing the OAM value in a polarization-dependent way. (b) In the interparticle regime, two photons characterized by defined states in the hybrid space composed of polarization and OAM interfere using a beam splitter. Fixing the elements of the computational basis as $|0\rangle = |L,-2\rangle$ and $|1\rangle = |R,2\rangle$, both $|\psi\rangle_1$ and $|\psi\rangle_2$ are initialized with the qubit state $|0\rangle$, and after postselecting on the coincidence counts a probabilistic entangling quantum gate is implemented. It is worth noting that considering separately the polarization and OAM Hilbert spaces of both photons, the proposed apparatus implements a four-qubit gate.

the generation rate. On the contrary, the employment of a deterministic single-photon source allows us to certify the state directly on the single counts, increasing the generation rate. Moving toward the interparticle regime, QD sources have been proved capable of generating on-demand photons pair entangled in polarization encoding.[78] However, the production of entangled states in different degrees of freedom, such as OAM and radial structure, easily obtained with SPDC sources,[79–81] is still under development. Here, we show a probabilistic approach implementing a gate for an engineer-entangled state in the OAM space. The versatility and flexibility in the generation and manipulation of indistinguishable photons are crucial features for gate implementation. We then move a step forward with respect to Ref. 56 by investigating the indistinguishability of the generated photons and employing a versatile approach. In our platform, the combination of QD-based single-photon sources and well-known OAM manipulation devices allows us to satisfy the aforementioned requirements.

This work is organized as follows. We start by studying the single-photon intraparticle entanglement generation in VV states. By means of q-plate devices,[59,60] we couple the two components of the angular momentum degree of freedom and generate VV beams [Fig. 1(a)]. Then, we move to the multi-photon scenario. Preliminarily, we certify the efficiency of encoding

OAM states on single photons emitted by the QD in different pulses of the pump beam through the evaluation of HOM interference visibility. Thus, we implement a two-photon probabilistic quantum gate, first introduced in Ref. 82, that is able to generate OAM-based entangled photon pairs involving up to four subsystems [Fig. 1(b)]. We verify both the single-photon intraparticle and the two-photon entanglement by performing quantum state tomography and evaluating the Bell inequality in the Clauser–Horne–Shimony–Holt (CHSH) fashion.

2 Experimental Platform

In this section, we preliminarily describe the employed quasi-deterministic single-photon source, by evaluating the intensity autocorrelation and indistinguishability of the generated photons. Subsequently, we present the implemented scalable platform in which, by interfacing well-known OAM manipulation devices with the QD source, entangled intra- and interparticle states are generated in the hybrid Hilbert space composed of OAM and polarization.

2.1 Single-Photon Source

The single-photon source is a quantum-dot-based emitter embedded in an electrically controlled cavity on a commercially available Quandela e-Delight-LA photonic chip. A single self-assembled InGaAs QD is surrounded by a two Bragg reflectors made of GaAs/$Al_{0.95}Ga_{0.05}As$ $\lambda/4$ layers with 36 (16) pairs for the bottom (top) and positioned in the center of a micropillar.[63] The micropillar is connected to a larger circular structure that is electrically contacted, enabling the tuning of the emission frequency of the QD via the Stark effect. The sample is kept at 4 K in a low-vibration closed-cycle He cryostat Attocube - Attodry800. The QD source is pumped with a 79 MHz-pulsed laser shaped with a QShaper (Quandela) 4f pulse shaper to select a specific wavelength and achieve a bandwidth of ∼100 pm. The optical excitation of the QD is achieved in an LA phonon-assisted configuration with a laser at 927.2 nm blue-detuned from the transition,[83] which enables single-photon generation by exciton emission at (927.8 ± 0.2) nm [Fig. 2(a)]. The emitted photons are directly coupled in single-mode fiber (SMF) and spectrally separated from the residual pumping laser with bandpass filters. At the output of the e-Delight-LA system, we measure a single-photon count rate of $R_{\mathrm{det}} = 4$ MHz. The fibered brightness of the single-photon source depends mainly on the coupling efficiency into the SMF, the spectral separation transmission of the single-photon stream from the pump laser—whose effects we estimate in an overall efficiency of $\eta_{\mathrm{setup}} \sim 52\%$—and the detector efficiency, estimated to be around $\eta_{\mathrm{det}} \sim 38\%$. Using these figures, we estimate a first lens brightness of $B = \frac{R_{\mathrm{det}}}{R_{\mathrm{exc}}\eta_{\mathrm{det}}\eta_{\mathrm{setup}}} \sim 26\%$, where R_{exc} is the pump frequency. The overall quality of the single-photon generation can be characterized by measuring the multi-photon emission and indistinguishability. Using a standard Hanbury Brown and Twiss setup, we measured a second-order autocorrelation of $g^{(2)}(0) = (1.26 \pm 0.05)\%$. Such a figure is computed by normalizing the zero-time delay coincidences to the side peaks coincidences between two consecutive near-resonant excitations [Fig. 2(b)]. We also measured the indistinguishability between photons successively emitted by the QD, through an HOM interference experiment.[51] Two consecutively emitted photons are split by a beam splitter (BS) and coupled in SMFs, whose length

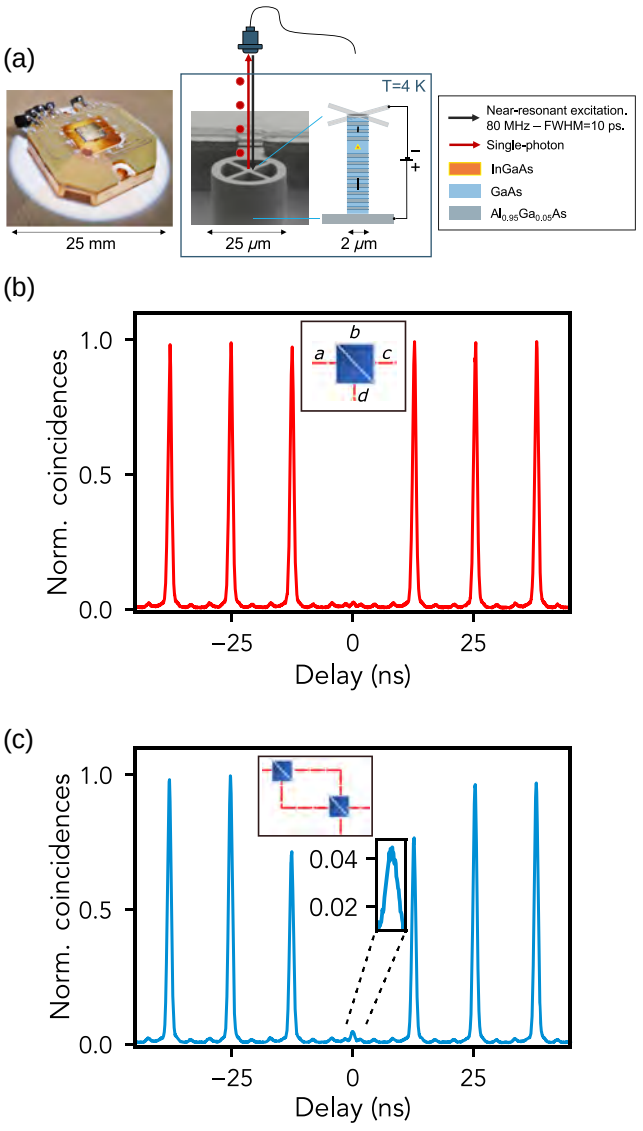

Fig. 2 Source HOM interference and second-order correlation function. (a) (Left) The single-photon source is a commercial device (Quandela): InGaAs quantum-dot based bright emitters are embedded in (right) electrically contacted micropillars. The source is pumped with a near-resonant ($\Delta\lambda = -0.6$ nm) FWHM 10 ps 79 MHz-pulsed laser (red arrow). The single photons (red dots) are emitted at a wavelength of 927.8 nm and are directly coupled to an SMF. (b) Through a standard Hanbury Brown and Twiss setup, we measure the second-order autocorrelation histogram of our QD-based source as a function of the delay. We obtain a single-photon purity of $g^{(2)}(0) = (1.26 \pm 0.05)\%$. (c) Normalized correlation histogram, obtained via an HOM interference experiment, through which we measure a two-photon interference fringe visibility between subsequent single photons emitted by the QD source of $V_{\mathrm{HOM}} = (93.05 \pm 0.06)\%$. Moreover, following Ref. 84, we obtain an indistinguishability value of $M_s = (95.5 \pm 0.1)\%$.

is chosen to delay one of them by ≈12.5 ns to ensure temporal overlap on a second BS. At its outputs, photons are collected in avalanche photodiode detectors (APDs) to record photon coincidence counts. Therefore, we evaluate a two-photon interference

visibility derived from the correlation histogram [Fig. 2(c)] as $V_{\mathrm{HOM}} = 1 - 2\frac{C_0}{\langle C\rangle_{t\to\infty}}$, where C_0 is the counts when the two photons are synchronized and $\langle C\rangle_{t\to\infty}$ is the average peak counts for relative temporal delays larger than one repetition rate of the laser. We measure an interference visibility $V_{\mathrm{HOM}} = (93.05 \pm 0.06)\%$, which can be corrected to account for unwanted multi-photon components,[84] resulting in a photon indistinguishability equal to $M_s = (95.5 \pm 0.1)\%$.

2.2 Experimental Implementation of OAM-Based Platform

We experimentally implemented a flexible platform for the study of single and multi-photon properties capable of implementing a probabilistic entangling quantum gate. A visual scheme of the setup is shown in Fig. 3.

For this purpose, the stream of single photons generated by the QD is preliminarily split through a fiber BS, and OAM encoding is performed separately on the two outputs. In particular, the input state, $|H,0\rangle$, having horizontal polarization and null OAM value, is selected through single mode fibers and polarizing beam splitters (PBSs). In the engineering stage, by placing a set of wave plates together with a q-plate on each arm, we are able to independently generate two distinct OAM-encoded single-photon states. In particular, a q-plate is a thin film of birefringent material (in our case, nematic liquid crystals) characterized by a nonuniform distribution of the optic axis across the plane transverse to the light propagation direction. The angle between the optic axis and the horizontal axis x of the device follows the relation $\alpha(\phi) = \alpha_0 + q\phi$, where ϕ is the azimuthal angle in the transverse plane, α_0 is the optic axis orientation for $\phi = 0$, and q is the topological charge, i.e., the winding number of the optic axis for $\phi \in [0,2\pi]$. Owing to the inhomogeneity of its optic axis distribution and to the resulting Pancharatnam–Berry geometric phases, the q-plate develops on the OAM degree of freedom of single photons an action that depends on their polarization, according to the following expression:[59,60]

$$\hat{Q} = \sum_m e^{-i2\alpha_0}|m-2q\rangle\langle m| \otimes |L\rangle\langle R| + e^{i2\alpha_0}|m+2q\rangle\langle m| \otimes |R\rangle\langle L|, \tag{1}$$

where $|R\rangle$ and $|L\rangle$ indicate right and left circular polarization states, respectively, and $|m\rangle$ represents the OAM value. The q-plates employed in the experiment are electrically tunable, i.e., they implement the operation $\hat{Q}_{\mathrm{exp}}(\delta) = \sin\frac{\delta}{2}\hat{Q} + \cos\frac{\delta}{2}\hat{\mathbb{I}}$, where $\hat{\mathbb{I}}$ is the identity operator and δ is the plate retardance that is controlled by applying an external voltage to the device. In the experiment, all the q-plates have $\delta = \pi$ in order to maximize the OAM-SAM conversion.

Therefore, an optical setup consisting of a quarter-wave plate (QWP), a half-wave plate (HWP), and a q-plate with $q = 1$, acting on the input state $|H,0\rangle$, is able to engineer arbitrary superpositions of $|L,-2\rangle$ and $|R,2\rangle$ as given by

$$|\Phi\rangle = \cos(\theta/2)|L,-2\rangle + e^{i\psi}\sin(\theta/2)|R,2\rangle, \tag{2}$$

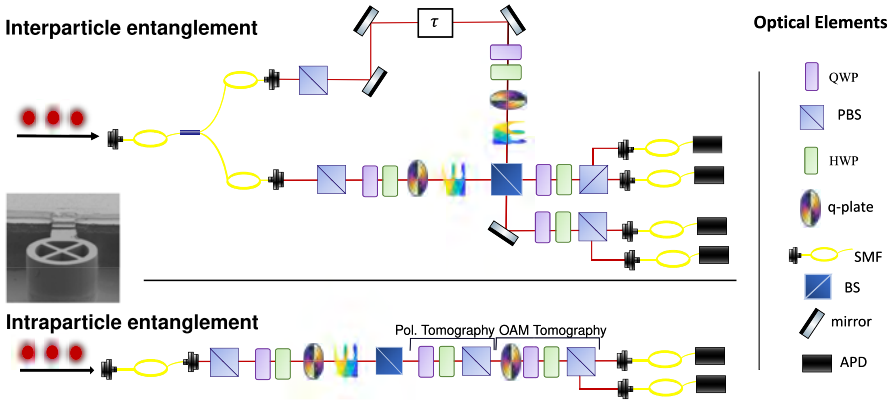

Fig. 3 Experimental setup. Single-photon states at a wavelength of 927.8 ± 0.2 nm are generated using a QD source pumped with a shaped 79 MHz-pulsed laser at 927.2 nm. Then, a fiber BS splits the photons between the two arms of the setup, and after passing through a PBS, the input states have horizontal polarization and OAM eigenvalue $m = 0$. In both paths, a series of QWP, HWP, and q-plate are used to produce OAM modes of the form reported in Eq. (2), while in one of the arms, a delay line (τ) is inserted in order to synchronize on the BS the photons emitted in different pulses of the pump beam. The intraparticle regime is investigated removing the fiber BS and performing all the experiment on a single line, involving the first input and output of the BS, as shown in the below panel. On the other hand, in the interparticle experiment, the photons are sent to the fiber BS, and the gate is implemented interfering on the second BS. After passing through the BS, the state of the photons is analyzed, coupled to SMFs and detected by APDs. The measurement setup consists in two different stages, a series of q-plate, QWP, HWP, and PBS are used to study the OAM states of the photons coupled with the polarization, while a QWP, an HWP, and a PBS compose the polarization analysis setup. In the interparticle regime, only OAM analysis is performed on the photon pairs, while in the intraparticle regime both analysis setups are used to separately investigate the polarization and OAM content of single photons, as shown in the lower panel.

where $\theta \in [0, \pi]$ and $\psi \in [0, 2\pi]$ can be set by properly orienting the optic axes of QWP and HWP. In this way, intrasystem entanglement between OAM and SAM degrees of freedom of single photons can be easily achieved. In particular, for $\theta = \pi/2$, the superpositions given in Eq. (2) correspond to the above mentioned VV states.

Subsequently, the two arms are synchronized by introducing a fixed delay in fiber and a tunable delay in air and then sent to a bulk BS used to probabilistically generate an entangled state between the two photons in the hybrid space of OAM and SAM by a postselection on the measured events.

Finally, in both single- and two-photon experiment, the state reconstruction is performed by using q-plates and polarization tomography setups comprising a QWP and an HWP followed by a PBS. In fact, the OAM tomography setup is implemented by adding a q-plate in front of the polarization tomography setup to convert the correlations present in the OAM degree of freedom on the polarization space [Eq. (1)]. The efficacy of this approach was demonstrated in Ref. 85 by exploiting pure-phase holograms displayed on photographic plates. In particular, in the intraparticle regime, the fiber BS is removed, and the entangled state is generated along the lower arm of the interferometer. Both the polarization and OAM analysis of such states is performed along one BS output by inserting the polarization tomography setups followed by the OAM tomography one. Instead, the analysis of the interparticle entangled state is performed by placing only the OAM tomography setups on each BS output. After the projection, the photons are collected in SMFs and detected using APDs. This scheme is used both to study the entanglement content of the states through Bell inequalities violation and to perform quantum state tomographies.

3 Entanglement Certification

In this section, we provide the theoretical description and report the results obtained studying the intraparticle and interparticle hybrid entanglement generated with the experimentally implemented platform. In all cases of interest, entanglement is certified through a violation of a CHSH Bell inequality and complete state tomography.

3.1 Vector Vortex Beam: Intrasystem Entanglement

The first investigation regards the generation of VV beams encoded into the single-photon states generated by the QD source. The VV beams are superpositions of two different OAM beams associated with orthogonal circular polarizations [see, for example, Eq. (2)]. Here, the two systems individuated by the OAM eigenstates $\{|-2\rangle, |2\rangle\}$ and the polarization states $\{|R\rangle, |L\rangle\}$ can be exploited for encoding two qubits. In this way, it is possible to define a complete basis of maximally entangled states between these two degrees of freedom. The set of Bell-like states is reported in Fig. 4, in which the nonuniform polarization distribution in the transverse plane is highlighted.

In our setup, to increase the generation rate, the signal is sent only in one of the two arms of the interferometer by removing the first fiber BS (see Fig. 3). The VV beams are prepared by making horizontally polarized photons passing subsequently through a QWP, an HWP, and a q-plate with $q = 1$. In this way, the state produced by the device is described by $\theta = \pi/2$ in Eq. (2) and a value of ψ which depends on the α_0 of the q-plate optic axis. This additional phase term is compensated by a further HWP (not shown in Fig. 3) in order to have $\psi = 0$. The final entangled state between OAM and polarization will be

$$|\Phi^+\rangle = \frac{1}{\sqrt{2}}(|L,-2\rangle + |R,2\rangle). \tag{3}$$

Although such an entanglement structure is not associated with nonlocal properties (since it is encoded in a single carrier), these correlations can be detected using Bell-like inequalities. We refer to such type of quantum correlations as intraparticle entanglement.

The adoption of a nearly deterministic single-photon source allows us to perform the intraparticle analysis without the need of heralding measurements or postselection. The latter are

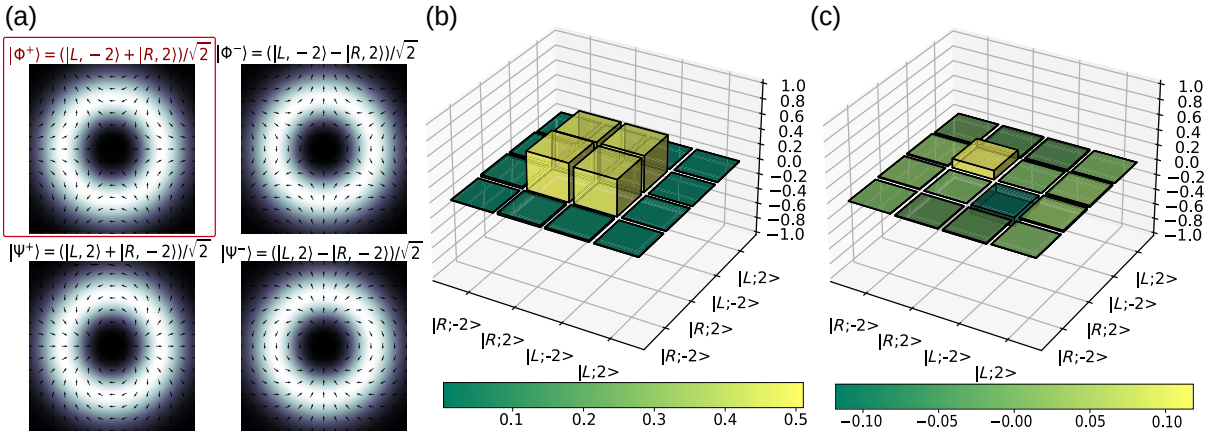

Fig. 4 Intraparticle entangled state: (a) intensity and polarization patterns of the Bell states basis in the combined OAM and polarization space. As highlighted by the red box, we focused our attention on the $|\Phi^+\rangle$ state. (b) Real and (c) imaginary parts of the measured density matrix for the $|\Phi^+\rangle$ state reconstructed via quantum state tomography. The fidelity between the reconstructed state and the theoretical one is equal to $\mathcal{F} = 0.9714 \pm 0.0007$, where the standard deviations are estimated through a Monte Carlo approach assuming a Poissonian statistics.

Table 1 Experimental results. The results are obtained both for the intraparticle and interparticle regimes. The measurement acquisition time T, the generation rate, the values for the Bell parameter (S), and the fidelity are reported. In particular, the violation $S^{(\text{raw})}$ is computed using raw data, while the parameter S is obtained by subtracting the background signal or the accidental coincidence. The fidelity value is computed by comparing the reconstructed density matrix with the triplet Bell state.

State	T (s)	Rate (Hz)	$S^{(\text{raw})}$	S	$\mathcal{F}$
Intra	20	99,000	2.736(8)	2.792(8)	0.9714(7)
Inter	400	146	2.516(6)	2.779(6)	0.935(2)

unavoidable procedures for generating single-photon states with high purity via probabilistic sources. This reduces drastically the losses allowing to reach a rate of ≃99 kHz of VV states generation (see the Supplementary Material for further details). The quality of the state and of its entanglement structure has been certified by the measurement stage setup shown and described in Sec. 2. In particular, we performed a quantum state tomography by analyzing the OAM and the polarization independently via cascaded measurement stages as in the lower panel of Fig. 3. The resulting density matrix is reported in Fig. 4, and the relative fidelity, computed by subtracting for dark counts, is $\mathcal{F} = 0.9714 \pm 0.0007$. Moreover, we also certified the intraparticle entanglement by evaluating a CHSH-like inequality. Collecting data for 20 s, we obtained a raw violation of $S^{(\text{raw})} = 2.736 \pm 0.008$, which exceeds the separable bound by 92 standard deviations, while the value obtained by subtracting the background signal is $S = 2.792 \pm 0.008$, which exceeds the classical bound by 99 standard deviations. The results are summarized in Table 1.

3.2 Certification of Photon States Generation

In quantum information processes, an important computational resource relies on the capability of manipulating multiple photons and making them interact. Therefore, in this section, we assess the capacity of codifying specific OAM states on photons generated by subsequent pulsed pumping of the QD. This is performed by evaluating the visibility of HOM interference in a BS, which is equivalent to a pairwise overlap estimation in a SWAP test.[86] There are some previous examples of HOM experiments with single-photon states carrying OAM,[39,87] but our tests are among the first to be applied to vector beams generated by a deterministic single-photon source.

Let us first briefly review the effect of an unbiased BS on the field annihilation and creation operators, $\hat{a}, \hat{a}^\dagger$ and $\hat{b}, \hat{b}^\dagger$. The relation between input modes $\{a, b\}$ and output modes $\{c, d\}$ can be expressed as (Fig. 2)

$$\hat{a}^\dagger \mapsto \frac{1}{\sqrt{2}}(\hat{c}^\dagger - \hat{d}^\dagger), \hat{b}^\dagger \mapsto \frac{1}{\sqrt{2}}(\hat{c}^\dagger + \hat{d}^\dagger). \tag{4}$$

By considering two photons at the two inputs of the BS, the signature of the interference is a change in the probability to detect photons in different outputs (see the Supplementary Material). In particular, two photons are indistinguishable if their states, associated with each degree of freedom, are the same from the point of view of the observer. To approach this condition in our setup, a delay line is used to synchronize the photons in the temporal domain. This is mandatory because the two single photons are emitted by the QD at different times. However, when the photons are characterized by an OAM value different from zero and superposed polarizations, it is necessary to take into account the effect of reflections. Indeed, in a physical BS, the semireflective mirror flips the elicity of both OAM and polarization. In other words, after one reflection, we have $\{|R\rangle, |L\rangle\} \rightarrow \{|L\rangle, |R\rangle\}$ and $|\pm 2\rangle \rightarrow |\mp 2\rangle$, while horizontal and vertical polarizations are eigenstates of this operation with eigenvalues of opposite signs. Then, we have that the creation operators are changed as follows:

$$\begin{aligned}
&\hat{a}_R^\dagger, \hat{b}_R^\dagger \mapsto \frac{1}{\sqrt{2}}(\hat{c}_R^\dagger - \hat{d}_L^\dagger), \quad \frac{1}{\sqrt{2}}(\hat{c}_L^\dagger + \hat{d}_R^\dagger),\\
&\hat{a}_L^\dagger, \hat{b}_L^\dagger \mapsto \frac{1}{\sqrt{2}}(\hat{c}_L^\dagger - \hat{d}_R^\dagger), \quad \frac{1}{\sqrt{2}}(\hat{c}_R^\dagger + \hat{d}_L^\dagger),\\
&\hat{a}_m^\dagger, \hat{b}_m^\dagger \mapsto \frac{1}{\sqrt{2}}(\hat{c}_m^\dagger - \hat{d}_{-m}^\dagger), \quad \frac{1}{\sqrt{2}}(\hat{c}_{-m}^\dagger + \hat{d}_m^\dagger).
\end{aligned} \tag{5}$$

Since the indistinguishability of photons generated by the source has already been checked in Sec. 2.1, here we are interested in computing the overlap between VV states encoded in different photons. As for the previous analysis, the OAM and polarization degrees of freedom are controlled through a series of QWP, HWP, and q-plate placed in each arm of the interferometer. This allows us to prepare the desired state for each photon.

Considering the BS action in Eq. (5), we expect no interference when the two photons are prepared as $|R, 2\rangle_a |R, 2\rangle_b$, since the reflected beam and the transmitted one in the outputs c and d will display orthogonal states. Conversely, the HOM effect occurs when the initial state is $|R, 2\rangle_a |L, -2\rangle_b$. The correlation histograms, obtained via an HOM interference experiment, for both input states $|R, 2\rangle_a |R, 2\rangle_b$ and $|R, 2\rangle_a |L, -2\rangle_b$ are reported in Figs. 5(a) and 5(b). The visibility of such HOM experiments quantifies the variation, from the maximum to minimum overlapping between the wave functions, of the probability of detecting photons in different outputs. The obtained visibilities are $V_{|R,2\rangle,|R,2\rangle} = -4\% \pm 1\%$ and $V_{|R,2\rangle,|L,-2\rangle} = 90.1\% \pm 0.3\%$, respectively. We repeat the same interference scheme with VV states, such as $|\Phi^+\rangle$ and $|\Phi^-\rangle$ (see Fig. 4). For these classes of states, we note that they are symmetric with respect to the BS operation. This means that the reflected photon and the transmitted one always display the same state if they are indistinguishable at the input faces of the BS (see the Supplementary Material). The resulting HOM correlations for the input state $|\Phi^+\rangle_a |\Phi^-\rangle_b$ are reported in Fig. 5(c) and the achieved visibility is equal to $V_{|\Phi^+\rangle,|\Phi^-\rangle} = 0.70\% \pm 0.10\%$, as expected. On the contrary, when the two photons are prepared in the same VV states such as $|\Phi^+\rangle_a |\Phi^+\rangle_b$, the theoretical HOM visibility is 1. We measured $V_{|\Phi^+\rangle,|\Phi^+\rangle} = 88.2\% \pm 0.3\%$, as reported in Fig. 5(d).

A further peculiar configuration is when the interfering input states are neither equal nor orthogonal, for which we expect a $V = \frac{1}{2}$. This is the case of two photons prepared in the input ports as $|\Phi^+\rangle_a |R, 2\rangle_b$. The measured visibility is $V_{|\Phi^+\rangle,|R,2\rangle} = 44.5\% \pm 0.6\%$ [Fig. 5(e)].

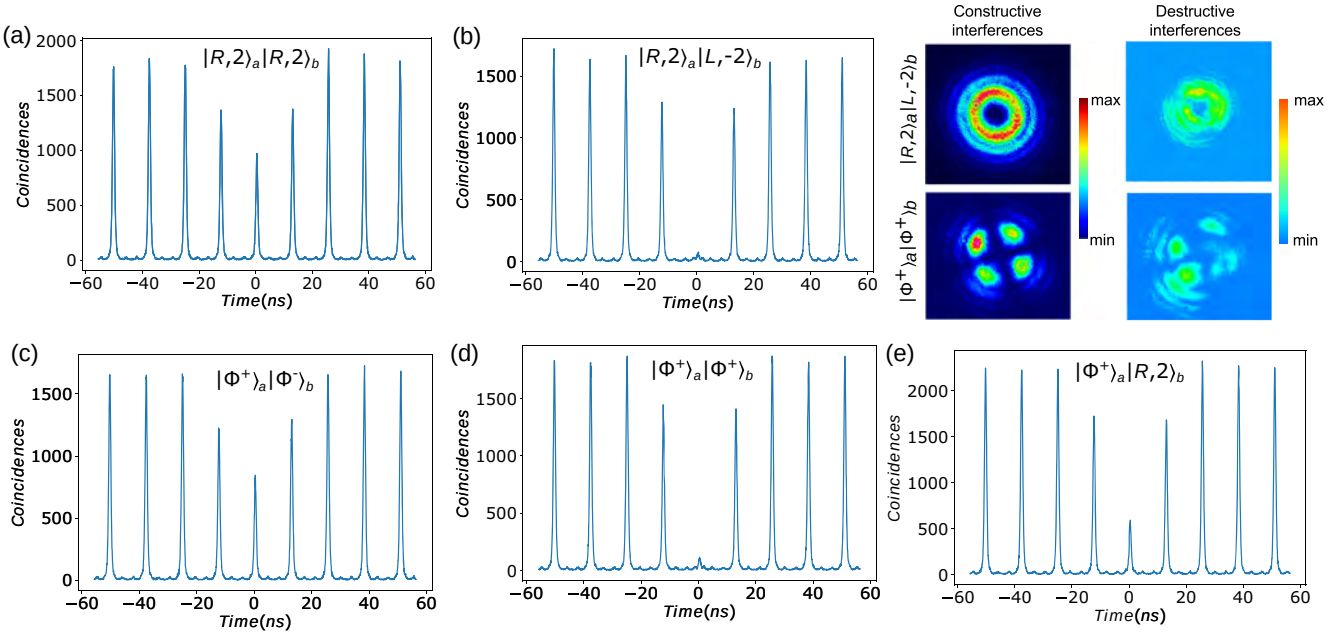

Fig. 5 HOM interference for OAM states: measured coincidences at the output of the final BS, see Fig. 3, for different input states in the hybrid space of OAM and polarization. A perfect HOM interference can be obtained only when the photon states are indistinguishable from the point of view of the observer. By knowing the BS action on circular polarization and OAM (see the Supplementary Material), we observe a near-unitary visibility when the photons are prepared in the same eigenstate of the BS reflection operation $|\Phi^+\rangle_a|\Phi^+\rangle_b$ (panel d), or when the initial states have opposite circular polarization and OAM value [panel (b)]; while near-zero visibility is reported in panels (a) and (c) for initial states $|R,2\rangle_a|R,2\rangle_b$ and $|\Phi^+\rangle_a|\Phi^-\rangle_b$, respectively. Moreover, we also analyze the hybrid configuration in which one photon is prepared in the state $|R,2\rangle$ and the other in the VV state $|\Phi^+\rangle$. In the latter case, the expected number of coincidences is half of the one obtained for distinguishable photons [panel (e)]. The reported intensity patterns are associated to constructive and destructive interference for both initial states $|R,2\rangle_a|L,-2\rangle_b$ and $|\Phi^+\rangle_a|\Phi^+\rangle_b$.

3.3 Two-Photon Quantum Gate: Intersystem Entanglement

The configuration described in the previous section can be exploited to implement a multi-qubit probabilistic quantum gate able to generate an entangled state in the hybrid space composed by OAM and polarization. In particular, by postselecting on the two-photon coincidence events resulting from the preparation $|R,2\rangle_a|R,2\rangle_b$, and noticing that one of the outputs is affected by a further reflection that introduces a phase π between horizontal and vertical polarization, and inverts the OAM value, the following state is generated:

$$|\Phi\rangle = \frac{|L,-2\rangle_c|R,2\rangle_d + |R,2\rangle_c|L,-2\rangle_d}{\sqrt{2}} = \frac{|1,0\rangle|0,1\rangle + |0,1\rangle|1,0\rangle}{\sqrt{2}}, \tag{6}$$

where we took off the direction subscript $\{c,d\}$ and we identified $|L,-2\rangle = |1,0\rangle$ and $|R,2\rangle = |0,1\rangle$. Therefore, the generated state is entangled in the space spanned by the tensor product of the four-dimensional (4D) qudits encoded in the combined OAM and polarization degrees of freedom for each photon. However, in the hybrid OAM-SAM space, this state can also be considered equivalent to a two-dimensional (2D) maximally entangled state. Indeed, relabeling the state $|L,-2\rangle$ as qubit $|0\rangle$ and the state $|R,2\rangle$ as qubit $|1\rangle$, the state in Eq. (6) turns out to be equivalent to a triplet Bell state,

$$|\Phi\rangle = \frac{|L,-2\rangle_c|R,2\rangle_d + |R,2\rangle_c|L,-2\rangle_d}{\sqrt{2}} = \frac{|0\rangle|1\rangle + |1\rangle|0\rangle}{\sqrt{2}}. \tag{7}$$

Therefore, this state exhibits quantum correlations that could be detected by performing a Bell-like test that is used as an entanglement witness. In particular, we evaluated a CHSH-like inequality performing the projective measurements placing the OAM measurement stage, shown in Fig. 3, on both BS outputs. Collecting data for 400 s and with a coincidence rate of 146 Hz, we obtained a raw violation of $S^{(\mathrm{raw})} = 2.516 \pm 0.006$, which exceeds the classical bound by 86 standard deviations. The value obtained by subtracting the accidental coincidences, mainly due to background noise and quantified measuring coincidences between signals in the region between two consecutive peaks (with a relative delay of ~6 ns), is $S = 2.779 \pm 0.006$, which exceeds the separable bound by 130 standard deviations.

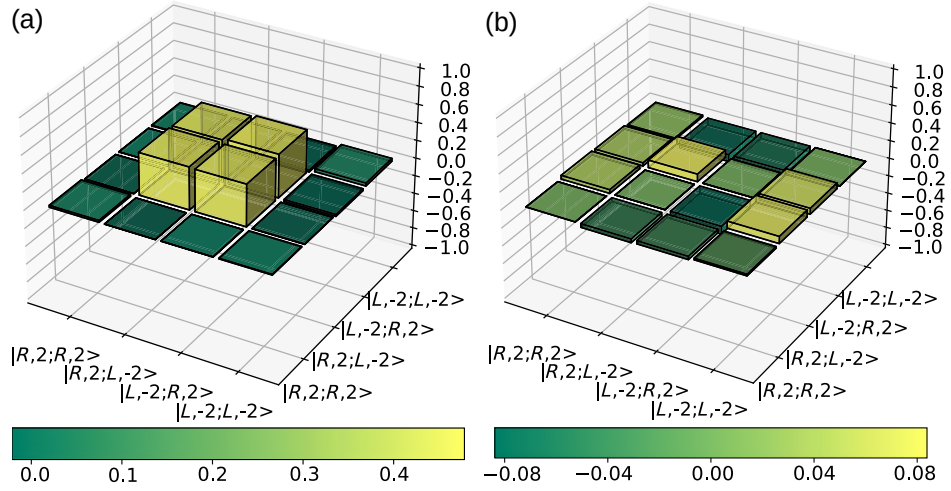

Fig. 6 Interparticle entangled state. (a) Real and (b) imaginary parts of the measured density matrix for the two-photon state in the hybrid OAM-polarization space reported in Eq. (7), these are reconstructed via quantum state tomography. The fidelity between the reconstructed state and the theoretical one is equal to $\mathcal{F} = 0.935 \pm 0.002$, where the standard deviation is estimated through a Monte Carlo approach assuming a Poissonian statistics.

Moreover, we also performed a quantum state tomography of the state using the same experimental configuration. The measurement apparatus selects on the 4D subspace $\{|R,2\rangle_1, |L,-2\rangle_1\} \otimes \{|R,2\rangle_2, |L,-2\rangle_2\}$ in which the interparticle entangled state lives. In fact, it contains the significantly nonzero elements of the whole density matrix of the states. Other terms outside such a subspace come from the imperfect conversion of the OAM by the q-plates. The probability of such components in the state can be kept very low, and thus can be neglected, by tuning the δ parameters of the q-plates toward the π value. Subtracting for accidental coincidences, the estimated fidelity changes from $\mathcal{F}^{(\mathrm{raw})} = 0.869 \pm 0.002$ to $\mathcal{F} = 0.935 \pm 0.002$. The retrieved density matrix is shown in Fig. 6. The results are summarized in Table 1. It is worth noting that the decrease in the coincidence rate is mainly due to the coupling efficiency into SMFs in the detection stage of about 45% (see the Supplementary Material for further details). This lower value depends on both the limited conversion efficiency of the QPs and on the higher divergence to which beams endowed with OAM are subjected. Other loss effects that need to be included are the q-plate transmission of about 75% acting on each photon. Therefore, looking toward gates with more than two photons, where the weight of the losses increases exponentially in the number of photons, the rate could be improved by compensating for losses due to the divergence and adopting experimental devices with limited losses.

4 Conclusions

In this paper, we experimentally implemented a platform capable of generating on-demand photonic quantum states in high-dimensional Hilbert spaces. This was achieved by combining a bright QD source with q-plates, devices capable of coupling OAM and polarization of single photons, placed in an interferometric configuration. After assessing the properties of the source, such as the multi-photon component, and the indistinguishability of the emitted photons, we focused on the generation and analysis of entangled states in the hybrid space composed of OAM and polarization. The setup allows us to study both the intra- and interparticle entanglement. For the former, we generated a VV state using only the engineering stage placed in one arm of the interferometer, while for the latter we exploited the interference between modulated single photons generated by the QD in two consecutive excitations to implement a probabilistic quantum gate capable of producing entangled two-photon states. The characterization of the interferometer scheme was preliminarily performed by evaluating the overlap between quantum states of single photons encoded in the hybrid Hilbert space. In particular, we observed high HOM visibilities for single photons that turn out to be indistinguishable in the detection stage, while very low visibility was observed for orthogonal quantum states. The qualities of both intra- and interparticle hybrid entangled states were evaluated by performing quantum state tomography and using Bell tests to estimate the CHSH inequality. The high values of fidelities and inequality violations highlight the performance of the proposed setup for the engineering of high-dimensional entangled states.

In summary, we proposed and implemented experimentally a flexible platform able to generate both nearly deterministic single-photon states that exhibit entanglement between OAM and SAM degrees of freedom and two-photon entangled states. The employed simple and effective scheme could be extended to the multi-photon regime, opening the way to high-dimensional multi-photon experiments, whose scalability is extremely demanding for platforms based on probabilistic sources. In conclusion, the results demonstrated in the present paper can provide advances both for fundamental investigations and quantum photonic applications.

Code, Data, and Materials Availability

Data underlying the results presented in this paper may be obtained from the authors upon reasonable request.

Acknowledgments

This work was supported by the European Union's Horizon 2020 Research and Innovation Programme under the PHOQUSING Project GA No. 899544, and the European Union's Horizon 2020 Research and Innovation Programme QUDOT-TECH under the Marie Sklodowska-Curie Grant Agreement No. 86109. The authors declare no conflicts of interest.

References

1. H. Rubinsztein-Dunlop et al., "Roadmap on structured light," *J. Opt.* **19**, 013001 (2016).
2. L. Allen et al., "Orbital angular momentum of light and the transformation of Laguerre-Gaussian laser modes," *Phys. Rev. A* **45**, 8185–8189 (1992).
3. M. P. Lavery et al., "Detection of a spinning object using light's orbital angular momentum," *Science* **341**(6145), 537–540 (2013).
4. L. Torner, J. P. Torres, and S. Carrasco, "Digital spiral imaging," *Opt. Express* **13**, 873–881 (2005).
5. D. S. Simon and A. V. Sergienko, "Two-photon spiral imaging with correlated orbital angular momentum states," *Phys. Rev. A* **85**, 043825 (2012).
6. N. Uribe-Patarroyo et al., "Object identification using correlated orbital angular momentum states," *Phys. Rev. Lett.* **110**, 043601 (2013).
7. Q. Zhan, "Trapping metallic Rayleigh particles with radial polarization," *Opt. Express* **12**, 3377–3382 (2004).
8. A. E. Willner et al., "Optical communications using orbital angular momentum beams," *Adv. Opt. Photonics* **7**, 66 (2015).
9. M. Malik et al., "Influence of atmospheric turbulence on optical communications using orbital angular momentum for encoding," *Opt. Express* **20**(12), 13195–13200 (2012).
10. J. Wang et al., "Terabit free-space data transmission employing orbital angular momentum multiplexing," *Nat. Photonics* **6**, 488–496 (2012).
11. J. Baghdady et al., "Multi-gigabit/s underwater optical communication link using orbital angular momentum multiplexing," *Opt. Express* **24**(9), 9794–9805 (2016).
12. N. Bozinovic et al., "Terabit-scale orbital angular momentum mode division multiplexing in fibers," *Science* **340**, 1545–1548 (2013).
13. G. Gibson et al., "Free-space information transfer using light beams carrying orbital angular momentum," *Opt. Express* **12**(22), 5448–5456 (2004).
14. M. Krenn et al., "Twisted light transmission over 143 km," *Proc. Natl. Acad. Sci. U. S. A.* **113**, 13648–13653 (2016).
15. D. Cozzolino et al., "High-dimensional quantum communication: benefits, progress, and future challenges," *Adv. Quantum Technol.* **2**(12), 1900038 (2019).
16. M. Krenn et al., "Twisted photon entanglement through turbulent air across Vienna," *Proc. Natl. Acad. Sci. U. S. A.* **112**(46), 14197–14201 (2015).
17. M. Malik et al., "Multi-photon entanglement in high dimensions," *Nat. Photonics* **10**, 248–252 (2016).
18. D. Cozzolino et al., "Air-core fiber distribution of hybrid vector vortex-polarization entangled states," *Adv. Photonics* **1**(4), 046005 (2019).
19. Y. Zhou et al., "Using all transverse degrees of freedom in quantum communications based on a generic mode sorter," *Opt. Express* **27**(7), 10383–10394 (2019).
20. X.-L. Wang et al., "Quantum teleportation of multiple degrees of freedom of a single photon," *Nature* **518**, 516–519 (2015).
21. M. Mirhosseini et al., "High-dimensional quantum cryptography with twisted light," *New J. Phys.* **17**, 033033 (2015).
22. A. Sit et al., "High-dimensional intracity quantum cryptography with structured photons," *Optica* **4**, 1006–1010 (2017).
23. F. Bouchard et al., "Quantum cryptography with twisted photons through an outdoor underwater channel," *Opt. Express* **26**, 22563–22573 (2018).
24. F. Cardano et al., "Statistical moments of quantum-walk dynamics reveal topological quantum transitions," *Nat. Commun.* **7**, 11439 (2016).
25. F. Cardano et al., "Detection of Zak phases and topological invariants in a chiral quantum walk of twisted photons," *Nat. Commun.* **8**, 15516 (2017).
26. I. Buluta and F. Nori, "Quantum simulators," *Science* **326**(5949), 108–111 (2009).
27. B. P. Lanyon et al., "Simplifying quantum logic using higher-dimensional Hilbert spaces," *Nat. Phys.* **5**, 134–140 (2009).
28. T. C. Ralph, K. J. Resch, and A. Gilchrist, "Efficient Toffoli gates using qudits," *Phys. Rev. A* **75**, 022313 (2007).
29. B. Hiesmayr, M. De Dood, and W. Löffler, "Observation of four-photon orbital angular momentum entanglement," *Phys. Rev. Lett.* **116**(7), 073601 (2016).
30. H. Bechmann-Pasquinucci and A. Peres, "Quantum cryptography with 3-state systems," *Phys. Rev. Lett.* **85**(15), 3313–3316 (2000).
31. L. Sheridan and V. Scarani, "Security proof for quantum key distribution using qudit systems," *Phys. Rev. A* **82**(3), 030301 (2010).
32. A. Aiello et al., "Quantumlike nonseparable structures in optical beams," *New J. Phys.* **17**, 043024 (2015).
33. M. Li et al., "Transverse spinning of particles in highly focused vector vortex beams," *Phys. Rev. A* **95**(5), 053802 (2017).
34. F. Cardano and L. Marrucci, "Spin-orbit photonics," *Nat. Photonics* **9**, 776–778 (2015).
35. G. Vallone et al., "Free-space quantum key distribution by rotation-invariant twisted photons," *Phys. Rev. Lett.* **113**(6), 060503 (2014).
36. V. D'Ambrosio et al., "Complete experimental toolbox for alignment-free quantum communication," *Nat. Commun.* **3**, 961 (2012).
37. S. Slussarenko et al., "Universal unitary gate for single-photon spin-orbit four-dimensional states," *Phys. Rev. A* **80**, 022326 (2009).
38. E. Nagali et al., "Polarization control of single photon quantum orbital angular momentum states," *Opt. Express* **17**, 18745–18759 (2009).
39. E. Nagali et al., "Optimal quantum cloning of orbital angular momentum photon qubits through Hong–Ou–Mandel coalescence," *Nat. Photonics* **3**, 720–723 (2009).
40. L.-P. Deng, H. Wang, and K. Wang, "Quantum CNOT gates with orbital angular momentum and polarization of single-photon quantum logic," *J. Opt. Soc. Am. B* **24**, 2517–2520 (2007).
41. Y. Chen et al., "Mapping twisted light into and out of a photonic chip," *Phys. Rev. Lett.* **121**(23), 233602 (2018).
42. B. P. da Silva et al., "Spin–orbit laser mode transfer via a classical analogue of quantum teleportation," *J. Phys. B Atomic Mol. Opt. Phys.* **49**, 055501 (2016).
43. V. Parigi et al., "Storage and retrieval of vector beams of light in a multiple-degree-of-freedom quantum memory," *Nat. Commun.* **6**(1), 7706 (2015).
44. T. Giordani et al., "Machine learning-based classification of vector vortex beams," *Phys. Rev. Lett.* **124**(16), 160401 (2020).
45. A. R. C. Pinheiro et al., "Vector vortex implementation of a quantum game," *J. Opt. Soc. Am. B* **30**, 3210–3214 (2013).
46. Y. Kozawa, D. Matsunaga, and S. Sato, "Superresolution imaging via superoscillation focusing of a radially polarized beam," *Optica* **5**(2), 86–92 (2018).
47. A. Suprano et al., "Propagation of structured light through tissue-mimicking phantoms," *Opt. Express* **28**(24), 35427–35437 (2020).
48. E. Polino et al., "Photonic quantum metrology," *AVS Quantum Sci.* **2**(2), 024703 (2020).
49. R. Fickler et al., "Quantum entanglement of high angular momenta," *Science* **338**(6107), 640–643 (2012).

50. S. Berg-Johansen et al., "Classically entangled optical beams for high-speed kinematic sensing," *Optica* **2**(10), 864–868 (2015).
51. C. K. Hong, Z. Y. Ou, and L. Mandel, "Measurement of subpicosecond time intervals between two photons by interference," *Phys. Rev. Lett.* **59**(18), 2044–2046 (1987).
52. F. Bouchard et al., "Two-photon interference: the Hong–Ou–Mandel effect," *Rep. Progr. Phys.* **84**, 012402 (2020).
53. E. Karimi et al., "Exploring the quantum nature of the radial degree of freedom of a photon via Hong-Ou-Mandel interference," *Phys. Rev. A* **89**, 013829 (2014).
54. Y. Zhang et al., "Hong-Ou-Mandel interference of entangled hermite-Gauss modes," *Phys. Rev. A* **94**, 033855 (2016).
55. M. Hiekkamäki and R. Fickler, "High-dimensional two-photon interference effects in spatial modes," *Phys. Rev. Lett.* **126**(12), 123601 (2021).
56. B. Chen et al., "Bright solid-state sources for single photons with orbital angular momentum," *Nat. Nanotechnol.* **16**(3), 302–307 (2021).
57. R. Fickler et al., "Real-time imaging of quantum entanglement," *Sci. Rep.* **3**(1), 1914 (2013).
58. E. Yao et al., "Observation of quantum entanglement using spatial light modulators," *Opt. Express* **14**, 13089–13094 (2006).
59. L. Marrucci, C. Manzo, and D. Paparo, "Optical spin-to-orbital angular momentum conversion in inhomogeneous anisotropic media," *Phys. Rev. Lett.* **96**(16), 163905 (2006).
60. L. Marrucci et al., "Spin-to-orbital conversion of the angular momentum of light and its classical and quantum applications," *J. Opt.* **13**, 064001 (2011).
61. T. Stav et al., "Quantum entanglement of the spin and orbital angular momentum of photons using metamaterials," *Science* **361**(6407), 1101–1104 (2018).
62. G. Brassard et al., "Limitations on practical quantum cryptography," *Phys. Rev. Lett.* **85**(6), 1330–1333 (2000).
63. N. Somaschi et al., "Near-optimal single-photon sources in the solid state," *Nat. Photonics* **10**, 340–345 (2016).
64. H. Wang et al., "Towards optimal single-photon sources from polarized microcavities," *Nat. Photonics* **13**, 770–775 (2019).
65. R. Uppu et al., "Scalable integrated single-photon source," *Sci. Adv.* **6**(50), eabc8268 (2020).
66. N. Tomm et al., "A bright and fast source of coherent single photons," *Nat. Nanotechnol.* **16**(4), 399–403 (2021).
67. E. Waks et al., "Quantum cryptography with a photon turnstile," *Nature* **420**(6917), 762 (2002).
68. R. Collins et al., "Quantum key distribution system in standard telecommunications fiber using a short wavelength single photon source," *J. Appl. Phys.* **107**(7), 073102 (2010).
69. J.-P. Li et al., "Multiphoton graph states from a solid-state single-photon source," *ACS Photonics* **7**(7), 1603–1610 (2020).
70. D. Istrati et al., "Sequential generation of linear cluster states from a single photon emitter," *Nat. Commun.* **11**(1), 5501 (2020).
71. J.-P. Li et al., "Heralded nondestructive quantum entangling gate with single-photon sources," *Phys. Rev. Lett.* **126**(14), 140501
(2021).
72. A. Dousse et al., "Ultrabright source of entangled photon pairs," *Nature* **466**(7303), 217–220 (2010).
73. K. Takemoto et al., "Quantum key distribution over 120 km using ultrahigh purity single-photon source and superconducting single-photon detectors," *Sci. Rep.* **5**(1), 14383 (2015).
74. T. Giordani et al., "Experimental engineering of arbitrary qudit states with discrete-time quantum walks," *Phys. Rev. Lett.* **122**(2), 020503 (2019).
75. A. Suprano et al., "Dynamical learning of a photonics quantum-state engineering process," *Adv. Photonics* **3**(6), 066002 (2021).
76. V. D'Ambrosio et al., "Entangled vector vortex beams," *Phys. Rev. A* **94**, 030304 (2016).
77. E. Karimi et al., "Spin-orbit hybrid entanglement of photons and quantum contextuality," *Phys. Rev. A* **82**, 022115 (2010).
78. D. Huber et al., "Strain-tunable GAAS quantum dot: a nearly dephasing-free source of entangled photon pairs on demand," *Phys. Rev. Lett.* **121**(3), 033902 (2018).
79. J. Torres, A. Alexandrescu, and L. Torner, "Quantum spiral bandwidth of entangled two-photon states," *Phys. Rev. A* **68**(5), 050301 (2003).
80. S. P. Walborn et al., "Spatial correlations in parametric down-conversion," *Phys. Rep.* **495**, 87–139 (2010).
81. N. H. Valencia et al., "Entangled ripples and twists of light: radial and azimuthal Laguerre–Gaussian mode entanglement," *J. Opt.* **23**(10), 104001 (2021).
82. Y. H. Shih and C. O. Alley, "New type of Einstein–Podolsky–Rosen–Bohm experiment using pairs of light quanta produced by optical parametric down conversion," *Phys. Rev. Lett.* **61**(26), 2921–2924 (1988).
83. S. E. Thomas et al., "Bright polarized single-photon source based on a linear dipole," *Phys. Rev. Lett.* **126**(23), 233601 (2021).
84. H. Ollivier et al., "Hong-Ou-Mandel interference with imperfect single photon sources," *Phys. Rev. Lett.* **126**(6), 063602 (2021).
85. E. Nagali et al., "Quantum information transfer from spin to orbital angular momentum of photons," *Phys. Rev. Lett.* **103**(1), 013601 (2009).
86. J. C. Garcia-Escartin and P. Chamorro-Posada, "Swap test and Hong-Ou-Mandel effect are equivalent," *Phys. Rev. A* **87**, 052330 (2013).
87. B. Ndagano and A. Forbes, "Entanglement distillation by Hong-Ou-Mandel interference with orbital angular momentum states," *APL Photonics* **4**(1), 016103 (2019).

Alessia Suprano received her PhD in physics in 2022. She is currently a post doc in the Physics Department at Sapienza University of Rome. Her current interests are focused on high-dimensional quantum information protocols in particular, for the implementation and exploitation of quantum walks in the orbital angular momentum degree of freedom of photons and for the study of nonlocality in networks.

Danilo Zia is a PhD student in the Quantum Information Laboratory of Pr. Fabio Sciarrino. Currently, he is investigating the applications of quantum walk dynamics in the orbital angular momentum degree of freedom of the photons using machine learning techniques. He graduated in October 2020 from Sapienza Università di Roma.

Mathias Pont studied theoretical physics and applied mathematics at Ecole Polytechnique in Paris. He joined Pr. S. Francoeur's research group at Polytechnique Montreal to work on the resonant excitation of Te isoelectronic centers in ZnSe for quantum information applications. He then pursued a doctoral degree in P. Senellart's group at C2N in Paris to work on interfacing bright QD single-photon source with integrated photonic circuits. He is now working at Quandela as a research information scientist.

Taira Giordani received her PhD in physics in 2020. She is currently a researcher in the Physics Department at Sapienza University of Rome. Her research focuses on the experimental implementation of quantum walks in integrated photonic devices and the angular momentum of light. In this context, her efforts aim to develop machine learning and optimization methods for the certification and engineering of photonic quantum walks platforms.

Giovanni Rodari is a PhD student in the Quantum Information Laboratory of Pr. Fabio Sciarrino. His main research interests are related to foundational themes—nonclassicality, causality—together with the investigation and implementation of quantum information protocols on photonis-based platforms. He graduated in October 2021 from Sapienza Università di Roma.

Mauro Valeri received his PhD in 2021 with a thesis entitled "Photonics technologies for quantum communication and metrology." The research activity of Mauro Valeri involved the study of quantum technology for quantum communication and metrology. During his PhD, he developed integrated and bulk sources of entangled photons to be distributed in quantum networks and exploited for quantum information protocols.

Bruno Piccirillo is professor of physics at the University of Naples "Federico II." His expertise ranges from nonlinear optics to microfluidics, optical interferometry, angular momentum of light, quantum optics, etc. He is currently interested in shaping and sensing wavefront and polarization of electromagnetic radiation. His main achievements include the first demonstration of photon OAM transfer from light to transparent media without topological defects (2001), the first electrically driven q-plate, the first geometric phase-based shearing interferometer.

Gonzalo Carvacho obtained his PhD from the University of Rome in 2018 with a thesis entitled "Multiphoton hybrid systems and their applications in quantum information and quantum communication." He is currently a lecturer in the Physics Department at Sapienza University of Rome and his research activities are focused on quantum causality, quantum communication and multiphoton dynamics by exploiting bulk optics, photonic integrated devices and G/Q-plates for structured light.

Nicolò Spagnolo received his PhD in 2012 in physical sciences of matter with a thesis on experimental multiphoton quantum optical states. He is currently a tenure-track assistant professor in the Physics Department of Sapienza Università di Roma. His research interests are focused on quantum information protocols employing different photonic platforms. These research activities include the implementation of boson sampling instances and of validation protocols with integrated photonics, quantum phase estimation experiments, and optical quantum communications.

Pascale Senellart obtained her PhD from University Paris 6 in 2001 for her studies on microcavity polaritons. After two postdoctoral positions in industrial laboratories, she joined the CNRS at the end of 2002 at the Laboratoire de Photonique et de Nanostructures where she started a research line on cavity quantum electrodynamics with semiconductor quantum dots. Her main field of research is solid-state quantum physics.

Lorenzo Marrucci is professor of physics at the University of Naples. He has coauthored over 200 scientific articles and 5 patents in optics and photonics. He is well known for his invention of the "q-plate," a device that allows generating orbital angular momentum from polarization manipulations. He has coordinated several international research projects, including an ERC Advanced Grant. He has also held various academic-management positions; currently he is vice rector for research at the University of Naples.

Fabio Sciarrino received his PhD in 2004 with a thesis in experimental quantum optics. He is a full professor and head of the Quantum Information Lab in the Department of Physics of Sapienza Università di Roma. Since 2013, he has been a fellow of the Sapienza School for Advanced Studies. His main field of research is quantum information and quantum optics, with works on quantum teleportation, optimal quantum machines, fundamental tests, quantum communication, and orbital angular momentum.

Research Article

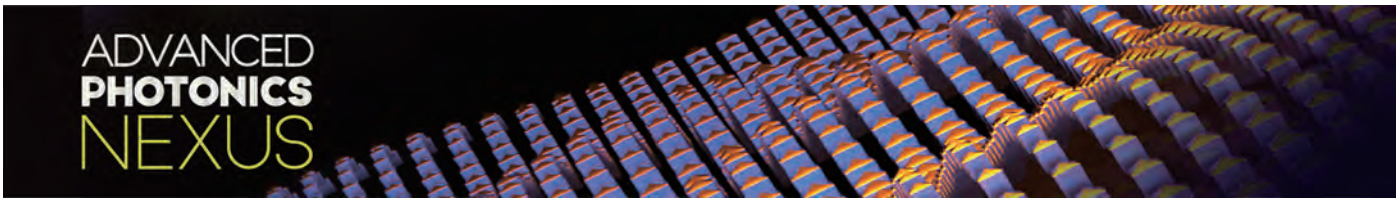

Self-seeded free-electron lasers with orbital angular momentum

Jiawei Yan* **and Gianluca Geloni***
European XFEL, Schenefeld, Germany

Abstract. X-ray beams carrying orbital angular momentum (OAM) are an emerging tool for probing matter. Optical elements, such as spiral phase plates and zone plates, have been widely used to generate OAM light. However, due to the high impinging intensities, these optics are challenging to use at X-ray free-electron lasers (XFELs). Here, we propose a self-seeded free-electron laser (FEL) method to produce intense X-ray vortices. Unlike passive filtering after amplification, an optical element will be used to introduce the helical phase to the radiation pulse in the linear regime, significantly reducing thermal load on the optical element. The generated OAM pulse is then used as a seed and significantly amplified. Theoretical analysis and numerical simulations demonstrate that the power of the OAM seed pulse can be amplified by more than two orders of magnitude, reaching peak powers of several tens of gigawatts. The proposed method paves the way for high-power and high-repetition-rate OAM pulses of XFEL light.

Keywords: free-electron laser; orbital angular momentum; self-seeded FEL.

Received Dec. 28, 2022; revised manuscript received Feb. 9, 2023; accepted for publication Feb. 28, 2023; published online Mar. 30, 2023.

[DOI: 10.1117/1.APN.2.3.036001]

1 Introduction

Structured light could provide new perspectives on numerous physical phenomena. In particular, optical vortices carrying orbital angular momentum (OAM),[1] characterized by a helical phase-front $\exp(il\phi)$, where ϕ is the azimuthal coordinate and l is the topological charge, are intensively studied. OAM light at visible and infrared wavelengths has been used in a wide range of fields.[2–7] In the short wavelength range, optical vortices are promising means to trigger new phenomena through light–matter interaction.[8–10] X-ray beams carrying OAM have been proposed for research in quadrupolar X-ray dichroism experiments,[11] photoionization experiments,[12] resonant inelastic X-ray scattering,[13] and magnetic helicoidal dichroism.[14,15] Most recently, a new type of phase dichroism has been demonstrated to probe the real-space configuration of the antiferromagnetic ground state with X-ray beams carrying OAM.[16] Moreover, the hard X-ray helical dichroism of disordered molecular media has been demonstrated.[17] At present, X-ray OAM light is provided by synchrotron radiation facilities. The generation of high-intensity X-ray OAM beams by X-ray free-electron lasers (XFELs) could open new possibilities for studies requiring well-defined spatial intensity and phase variations.

Modern XFELs deliver high-brightness pulses with durations spanning from tens of femtoseconds down to the attosecond range, enabling new research in a variety of scientific fields.[18,19] The majority of XFEL facilities worldwide[20–24] employ the mechanism of self-amplified spontaneous emission (SASE).[25] The SASE process starts from the initial electron-beam shot noise and allows operation over a wide spectral range, reaching sub-angstrom wavelengths. Self-seeding schemes[26,27] are used at several facilities to enhance the temporal coherence of free-electron laser (FEL) pulses while increasing their spectral density. However, the transverse radiation profile of FELs operating at saturation is restricted to the fundamental FEL mode, which can usually be approximated by a Gaussian mode with no azimuthal phase dependence.

The generation of OAM light at XFELs can be realized by using helical undulators or forming electron bunches with helical shapes. In the first case, the harmonic radiation in helical undulators has long been theoretically shown to carry a helical phase,[28–30] but which was experimentally demonstrated only recently.[31–33] However, the intensity of the harmonic emission

*Address all correspondence to Jiawei Yan, jiawei.yan@xfel.eu; Gianluca Geloni, gianluca.aldo.geloni@xfel.eu

is much weaker than that of the fundamental.[29] In order to deal with this issue, harmonic interaction between a seed laser and an electron beam in a helical undulator[34,35] was further proposed to generate OAM radiation at the fundamental wavelength. In addition, schemes to generate OAM radiation by using an external seed laser with a proper transverse phase structure to form the electron bunches into a helical pattern[36,37] have been proposed. However, these methods are limited by the availability of external seed lasers, or by the harmonic conversion number, especially at the shortest wavelengths. Also, a transverse-mode selection method using Bragg reflectors and longitudinal transverse-mode coupling[38] has been proposed, but it requires an XFEL oscillator configuration.

A more straightforward approach to generate X-ray OAM light is to employ optical elements, such as spiral phase plates (SPPs),[39,40] spiral Fresnel zone plates (SZPs),[41,42] and other diffractive optics[43] behind an undulator. In recent years, these optical elements have been well developed and have been experimentally demonstrated to produce soft and hard X-ray OAM light at synchrotron light sources. The design of an SPP typically features a rotating step with increasing thickness in the azimuthal direction. As the light beam passes through the SPP, it collects an azimuthally varying phase, transforming it into a beam with a helical phase.[44] Recently, SPPs made from fused silica[40] have been successfully used to shape synchrotron radiation at photon energies of 8.2 keV, and are considered for potential use at XFELs. In addition, the SZP is a unique class of diffractive optics that not only imparts a spiral phase to the incoming beam but also exhibits focusing properties. SZPs with silicon membranes have been successfully used at an FEL in the extreme-ultraviolet wavelength range with an efficiency of 17% and a pulse energy of around 10 μJ.[33] However, for obtaining X-ray OAM radiation with high pulse energies, the efficiency and thermal loading of these optics can constitute a significant challenge, especially considering the development of high-repetition-rate XFELs based on superconducting accelerators.

In this work, we propose a new scheme to generate intense X-ray vortices that is free from the previous issues. The method is based on the widely used SASE mode of operation and does not require helical undulators or external seed laser systems; thus it can in principle be applied to all existing XFEL user facilities with minimal hardware additions, especially when in synergy with self-seeding setups.

2 Principles and Methods

The schematic layout of the proposed method, referred to as self-seeded FEL with OAM (SSOAM), is shown in Fig. 1. Several undulator segments are employed as the first stage to generate an SASE FEL pulse in the linear regime. Then, an optical element, such as an SPP or SZP, is used to imprint the helical phase of a low-order OAM mode onto the FEL beam, generating an OAM seed pulse. Finally, the OAM seed pulse is significantly amplified in the second-stage undulator. A small magnetic chicane located between the first stage and the second stage is needed to detour the electron bunch, removing the microbunching introduced in the first stage, and resulting in a small delay below ten femtoseconds between the OAM seed and the electron bunch. Therefore, a relatively long electron bunch is requested in this scheme to ensure the amplification of the OAM seed in the second stage. In addition, fresh slice[45] or twin bunch operation[46] can also be employed to obtain better performance. The drift section between the first stage and the optical element can be increased to make the transverse size of the FEL pulses hitting the optics larger, which further reduces the impinging intensity and therefore minimizes heat-loading effects. In this case, utilizing an SZP or additional focusing optics may be necessary before entering the second stage.

Previous theoretical analyses indicated that an OAM seed can be amplified by the FEL process.[47,48] In the SSOAM scheme, however, the SASE pulse filtered by the optical element is not a pure OAM pulse. We can theoretically analyze how FEL modes evolve in this scheme. First, we expand the slowly varying envelope of the electric field in the frequency domain into a Fourier series in the azimuthal angle ϕ according to Ref. 49,

$$\tilde{E}(z,r,\phi)=\sum_{n=-\infty}^{\infty}\tilde{E}^{(n)}(z,r)\exp(-in\phi), \tag{1}$$

Where z and r are the longitudinal and transverse coordinates with respect to the undulator axis. $-n$ indicates the topological charge. Each of the azimuthal harmonics is then decomposed into "self-reproducing" modes,

$$\tilde{E}^{(n)}(\hat{z},\hat{r})=\sum_{j}a_j^{(n)}\Phi_{nj}(\hat{r})\exp(\lambda_j^{(n)}\hat{z}), \tag{2}$$

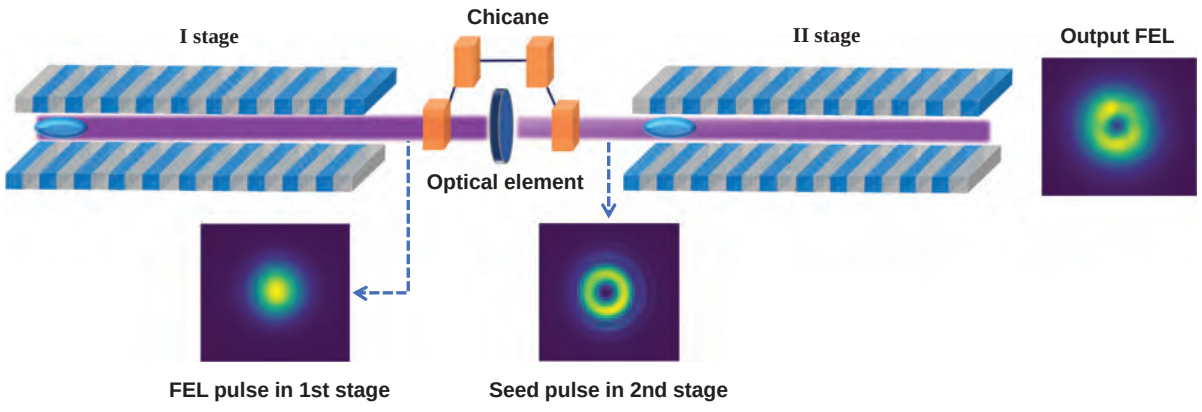

Fig. 1 Schematic layout of the self-seeded FEL with OAM.

with $\hat{r} = r/r_0$ and $\hat{z} = \Gamma z$. $\hat{r}$ and $\hat{z}$ are normalized versions of r and z according to the definition in Ref. 49, where Γ is the gain parameter. $\lambda_j^{(n)}$ and $\Phi_{nj}(\hat{r})$ are eigenvalues and eigenfunctions of the guiding modes, respectively. Assuming no changes in the transverse profile and typical dimension r_0 of the electron beam, and the same gain parameter during the entire process, the normalization parameters will remain constant during all the steps, and the FEL eigenmodes obey the eigenvalue equation [49],

$$[\Delta_n + g(\hat{r}, \lambda_j^{(n)})]\Phi_{nj}(\hat{r}) + 2iB\lambda_j^{(n)}\Phi_{nj}(\hat{r}) = 0, \tag{3}$$

where we recognize that

$$\Delta_n \equiv \left[\frac{\partial^2}{\partial\hat{r}^2} + \frac{1}{\hat{r}}\frac{\partial}{\partial\hat{r}} - \frac{n^2}{\hat{r}^2}\right], \tag{4}$$

is the Bessel differential operator. Here, g is a function of $\hat{r}$ and $\lambda_j^{(n)}$ defined in Ref. 49 and $B = r_0^2\Gamma\omega/c$.

Instead, during free-space propagation, the azimuthal harmonics of the electric field do not evolve in self-reproducing modes. Since

$$\left[\nabla^2 + \frac{2i\omega}{c}\frac{\partial}{\partial z}\right]\tilde{E} = 0, \tag{5}$$

after expansion in azimuthal harmonics, we have

$$\left[\Delta_n + 2iB\frac{\partial}{\partial\hat{z}}\right]\Phi_{nj}(\hat{r}, \hat{z}) = 0. \tag{6}$$

In the first stage, we have a first azimuthal series of FEL modes $\Phi_{nj}^{(I)}$ satisfying Eq. (3). The modes evolve in free space before filtering. For simplicity, here we assume that filtering happens directly at the exit of the first undulator. The filtering amounts to a change in the phase. A phase of $\exp(il\phi)$ is introduced to the radiation field, which is a reasonable assumption when using a finely stepped phase plate. We can therefore write the filtered self-reproducing modes as $\Phi_{n-l,j}^{(Ib)}(\hat{r}) = \Phi_{nj}^{(I)}$.

The modes $\Phi_{n-l,j}^{(Ib)}$ need now to be propagated in free space for a distance $\delta\hat{z}$. We call with $\Phi_{n-l,j}^{(Ic)}(\hat{z}, \hat{r})$ the free-space propagated version of $\Phi_{n-l,j}^{(Ib)}$, which obeys

$$\left[\Delta_{n-l} + 2iB\frac{\partial}{\partial\hat{z}}\right]\Phi_{n-l,j}^{(Ic)}(\hat{r}, \hat{z}) = 0. \tag{7}$$

Solving this equation for a propagation distance $\delta\hat{z}$, we obtain

$$\Phi_{n-l,j}^{(Ic)}(\hat{r}, \delta\hat{z}) = \frac{iB}{2\pi\delta\hat{z}}\int_0^\infty \mathrm{d}\hat{r}'\hat{r}'\int_0^{2\pi}\mathrm{d}\delta\phi' \exp\left\{\frac{iB}{2\delta\hat{z}}[\hat{r}^2 - 2\hat{r}\hat{r}'\cos(\delta\phi') + \hat{r}'^2]\right\} \times \Phi_{nj}^{(I)}(\hat{r}')\exp[-i(n-l)\delta\phi']. \tag{8}$$

Performing first the integral over the phase, we find

$$\Phi_{n-l,j}^{(Ic)}(\hat{r}, \delta\hat{z}) = \frac{i^{n-l+1}B}{\delta\hat{z}}\exp\left(\frac{iB\hat{r}^2}{2\delta\hat{z}}\right)\int_0^\infty \mathrm{d}\hat{r}'\hat{r}' \exp\left(\frac{iB\hat{r}'^2}{2\delta\hat{z}}\right)\Phi_{nj}^{(I)}(\hat{r}')J_{n-l}\left(-\frac{\hat{r}\hat{r}'B}{\delta\hat{z}}\right). \tag{9}$$

To summarize, the field at the entrance of the second stage amounts to

$$\tilde{E}(\hat{r}, \phi) = \sum_{n=-\infty}^{\infty}\sum_j a_j^{(n)}\exp(\lambda_j^{(n)}\hat{z}_1)\Phi_{n-l,j}^{(Ic)}(\hat{r})\exp[-i(n-l)\phi], \tag{10}$$

where $\hat{z}_1$ indicates the normalized position in the first stage. One may approximate $j = 1$ as fixed because we assume good mode selection in the first stage. Then, the contribution to the field at the entrance of the second stage can be approximated to

$$\tilde{E}(\hat{r}, \phi) = \sum_{n=-\infty}^{\infty} a_1^{(n)}\exp(\lambda_1^{(n)}\hat{z}_1)\Phi_{n-l,1}^{(Ic)}(\hat{r})\exp[-i(n-l)\phi] \equiv \sum_{n=-\infty}^{\infty} A^{(n)}\Phi_{n-l,1}^{(Ic)}(\hat{r})\exp[-i(n-l)\phi]. \tag{11}$$

All the contributions for all values of n will enter the second stage with a topological charge $h = -(n-l)$.

Now, the FEL eigenmodes in the second stage obey

$$[\Delta_m + g(\hat{r}, \lambda_k^{(II,m)})]\Phi_{m,k}^{(II)}(\hat{r}) + 2iB\lambda_k^{(II,m)}\Phi_{m,k}^{(II)}(\hat{r}) = 0, \tag{12}$$

and we can decompose

$$\Phi_{n-l,1}^{(Ic)}(\hat{r}, \delta\hat{z}) = \sum_k \alpha_k\Phi_{n-l,k}^{(II)}. \tag{13}$$

Since the orbital momentum should be conserved, each of the components $\Phi_{n-l,k}^{(II)}$ carries a fraction of the total OAM with topological charge $-(n-l)$. Each mode will be amplified at different rates for different values of k. Assuming good mode selection, the mode for $k = 1$ will be dominant for the topological charge $-(n-l)$. However, all the FEL modes with fixed $-(n-l)$ and different k will contribute to an OAM field distribution with the same topological charge given as

$$\tilde{E}^{(n-l)}(\hat{r}, \phi) = A^{(n)}\sum_k \alpha_k\Phi_{n-l,k}^{(II)}\exp[-i(n-l)\phi] \exp(\lambda_k^{(II,n-l)}\hat{z}_2), \tag{14}$$

where $\hat{z}_2$ indicates the normalized position in the second stage. In this sense, these modes will not be in competition. The competition will come from modes with different topological charges.

The contribution for $n = 0$ corresponds to the fundamental FEL mode and will be dominant in the first stage. As a result, the seed pulse in the second stage is mainly composed of the $h = l$ mode. In particular, the component of the $h = 0$ mode of the seed pulse is transformed from the $-l$ mode in the first

stage. Therefore, it is important for the proposed method to properly optimize the undulator settings of both stages to ensure a good amplification of the $h = l$ mode at the second stage.

3 Results

To further illustrate the proposed scheme, a detailed example based on the parameters of European XFEL[23] is studied with GENESIS[50] simulations. A 14 GeV electron beam with a normalized emittance of 0.5 mm.mrad, a bunch length of 20 fs, and a current flattop profile of 5000 A is assumed here to produce nine keV FEL pulses. The electron beam is sent to the first stage and generates SASE pulses with energies of a few microjoules or less. Then, an SPP is used to impart a helical phase of $\exp(i\phi)$, corresponding to $l = 1$, on the SASE pulse. We assume the intensity of the pulse is unchanged by the SPP. The distance between the SPP and both undulator sections is set to 2 m. For simplicity, the SASE pulse interacts with a fresh electron beam with an unchanged bunch length in the second stage.

As indicated by the theoretical analysis, the $h = 0$ mode of the SASE pulse is transformed to the $h = 1$ OAM mode while the the $h = -1$ mode is transformed to the $h = 0$ mode after the filtering. Therefore, the resonance and taper of the first stage undulator need to be optimized to achieve the largest possible ratio of the $h = 0$ mode while keeping the pulse energy small. Meanwhile, the undulator of the second stage needs to be optimized to achieve the strongest possible amplification of the $h = 1$ mode.

In the simulation, nine undulator segments with a length of 5 m and a 40 mm period are employed as the first stage. The optimization of the first-stage undulator suggests a slight reverse taper with $\Delta K/K = -0.18\%$. In this case, an SASE pulse with a pulse energy of 9.58 μJ is obtained at the end of the first stage. The mode decomposition of the pulse shows that the relative weight of the $h = 0$, $h = -1$, and $h = 1$ modes are 91%, 3%, and 3%, respectively. The temporal power profile and transverse profile of the pulse are shown in Figs. 2(a) and 2(b), respectively. The FEL pulse is then propagated sequentially through the free-space section, the SPP, and the second free-space section, before being amplified as a seed in the second stage. As shown in Figs. 2(c) and 2(d), the seed pulse mainly consists of the $h = 1$ mode, with a ratio of 91%. The ratio of the $h = 0$ mode of the seed pulse is 3%.

The OAM seed pulse is amplified in the second stage, which consists of seven undulator segments. To ensure optimal gain for the $h = 1$ mode, the undulator taper is optimized to a strength of $\Delta K/K = -0.06\%$. The gain curves of pulse and different OAM modes are shown in Fig. 3. The pulse energy reaches 430.17 μJ at the end of the undulator. The modes $h = 0$ and $h = 2$, which transform from $h = -1$ and $h = 1$ in the first stage, respectively, have similar initial components in the second stage but grow at very different rates. At the exit of the second stage, the $h = 1$ mode is amplified 43.5-fold and approaches saturation. The ratio of the $h = 1$ mode is first increased to 95% and then slowly decreased to 88%. The ratio of the $h = 0$ mode reaches 9% at the end of the second stage. Figures 4(a) and 4(b) show the transverse profiles of the pulse at the exit of the fifth undulator cell, where the pulse energy is 184.44 μJ and the ratio of the $h = 1$ mode is 93%, and the end of the seventh cell, respectively. Figure 4(c) presents the transverse phase distribution at the position in the pulse with a peak power of 92 GW, located at 1.58 μm in Fig. 4(d).

Figure 5(a) presents the variation of the different OAM modes contained in the FEL pulse at the exit of the fifth

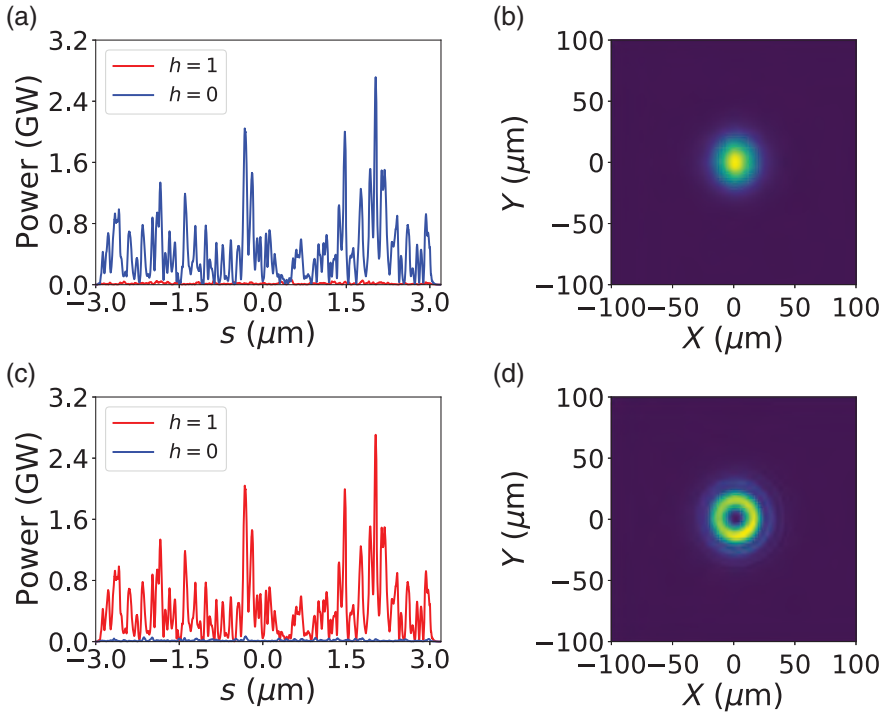

Fig. 2 Temporal power of the FEL pulse at (a) the end of the first stage and (c) the entrance of the second stage decomposed into OAM modes. The corresponding transverse profiles of the pulse at these two positions are shown in (b) and (d), respectively.

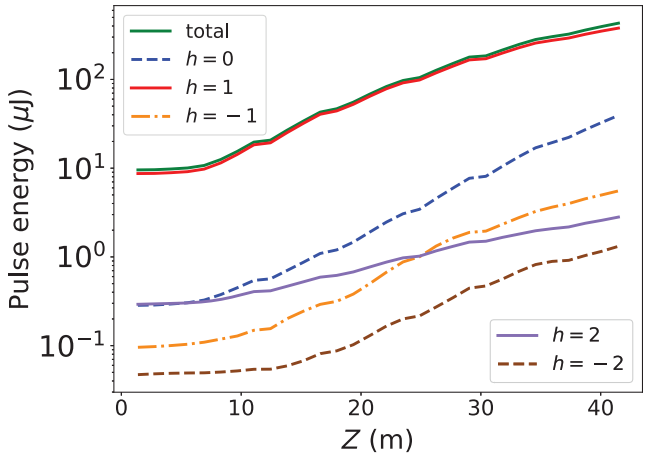

Fig. 3 Gain curves of different OAM modes along the second stage.

undulator cell of the second stage as the total phase shift, i.e. $2\pi l$, imprinted by the SPP changes. The results show that the proposed scheme can tolerate relatively large phase shift variations due to imperfections in optical element fabrication or changes in photon energy. With the introduction of phase shifts from 1.7π to 2.4π, corresponding to $l = 0.85$ to $l = 1.2$, pulses with $h = 1$ mode ratio exceeding 80% can be obtained. Moreover, the results also indicate that the proposed method can be used to effectively amplify the $h = 2$ mode. FEL pulses with 84% of $h = 2$ mode and pulse energy of 52 μJ can be obtained when the introduced phase shift is 4π. High-order OAM modes with topological charge larger than 2 cannot be well amplified due to stronger diffraction.[36,47]

To simulate the effects of a weaker seed power, we assume that the use of an optical element still introduces $\exp(i\phi)$ into the SASE pulse but with an efficiency of only 10%, while the undulator settings remain unchanged. In comparison to Fig. 2(c), the pulse energy of this seed pulse is reduced to

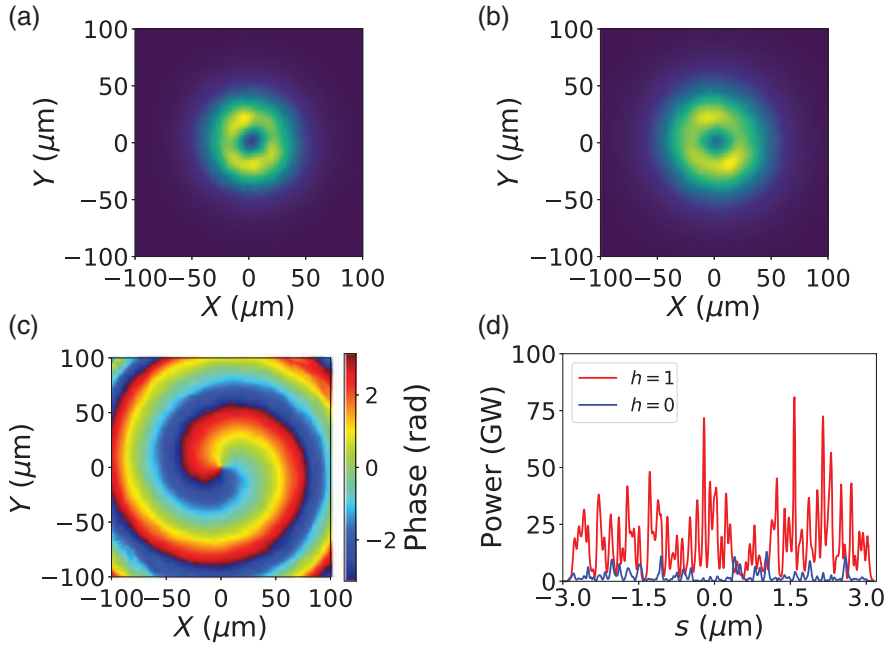

Fig. 4 Transverse profile of the FEL pulse at the end of (a) the fifth cell and (b) the second stage. (c) Transverse phase distribution at the position of maximum power in the pulse. (d) Temporal power profile of the pulse at the end of the second stage.

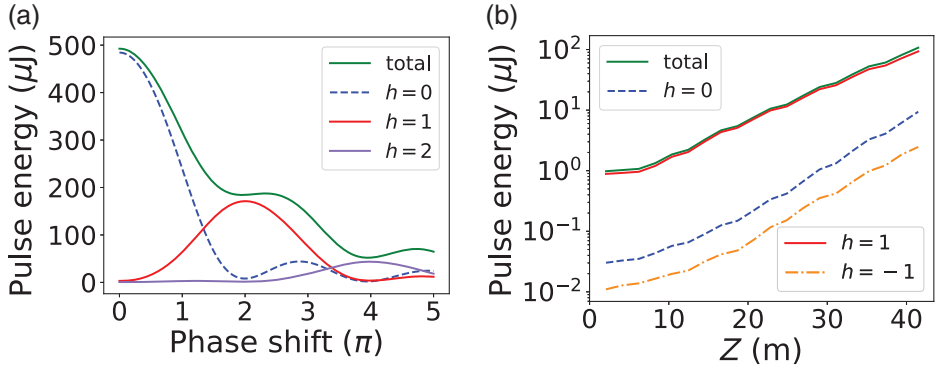

Fig. 5 (a) Variation of the different OAM modes with the change of the imprinted total phase shift. (b) Gain curves of different OAM modes at the second stage starting from a weaker seed pulse.

0.96 μJ. As shown in Fig. 5(b), the $h = 1$ mode can be amplified 107-fold in the second stage even if it starts with a much weaker seed pulse. At the exit of the seventh undulator cell, the pulse energy reaches 107.16 μJ, where the ratios of the $h = 1$ and $h = 0$ modes are 87% and 9%, respectively. The FEL pulse can be further amplified to 307.94 μJ when nine undulator cells are employed. In this case, the ratios of the $h = 1$ and $h = 0$ modes are 78% and 17%, respectively.

4 Conclusion

We proposed a scheme to produce high-intensity short-wavelength vortices. Theoretical analysis and simulations demonstrate that the introduction of an OAM mode to an FEL beam using an optical element leads to changes in multiple transverse modes of the FEL beam, where the dominant OAM mode can be amplified by more than two orders of magnitude. Since the SSOAM scheme is based on the SASE operation, it can be enabled in a wide range of wavelengths, including extreme ultraviolet, soft, and hard X-rays. In combination with the self-seeding scheme, introducing OAM to a weak and monochromatic seed pulse and further amplifying it, narrow bandwidth X-ray vortices can be generated. The proposed method paves the way for the realization of high-power and high-repetition-rate X-ray vortices and promises to open up new ways for probing matter with such light, such as time-resolved twisted X-ray diffraction techniques.[51]

Acknowledgments

We thank Serguei Molodtsov, Svitozar Serkez, Weilun Qin, and Tianyun Long for useful discussions and for their interest in this work.

Data Availability

The data that support the findings of this study are available from the corresponding author upon reasonable request.

References

1. L. Allen et al., "Orbital angular momentum of light and the transformation of laguerre-gaussian laser modes," *Phys. Rev. A* **45**(11), 8185 (1992).
2. Y. Shen et al., "Optical vortices 30 years on: OAM manipulation from topological charge to multiple singularities," *Light: Sci. Appl.* **8**(1), 1–29 (2019).
3. H. He et al., "Direct observation of transfer of angular momentum to absorptive particles from a laser beam with a phase singularity," *Phys. Rev. Lett.* **75**(5), 826 (1995).
4. D. G. Grier, "A revolution in optical manipulation," *Nature* **424**(6950), 810–816 (2003).
5. A. Sit et al., "High-dimensional intracity quantum cryptography with structured photons," *Optica* **4**(9), 1006–1010 (2017).
6. D.-S. Ding et al., "Quantum storage of orbital angular momentum entanglement in an atomic ensemble," *Phys. Rev. Lett.* **114**(5), 050502 (2015).
7. S. Fürhapter et al., "Spiral phase contrast imaging in microscopy," *Opt. Express* **13**(3), 689–694 (2005).
8. A. Picón et al., "Transferring orbital and spin angular momenta of light to atoms," *New J. Phys.* **12**(8), 083053 (2010).
9. G. De Ninno et al., "Photoelectric effect with a twist," *Nat. Photonics* **14**(9), 554–558 (2020).
10. I. P. Ivanov, "Promises and challenges of high-energy vortex states collisions," *Progr. Particle Nucl. Phys.* **127**, 103987 (2022).
11. M. van Veenendaal and I. McNulty, "Prediction of strong dichroism induced by x rays carrying orbital momentum," *Phys. Rev. Lett.* **98**(15), 157401 (2007).
12. A. Picón et al., "Photoionization with orbital angular momentum beams," *Opt. Express* **18**(4), 3660–3671 (2010).
13. A. S. Rury, "Examining resonant inelastic spontaneous scattering of classical Laguerre-Gauss beams from molecules," *Phys. Rev. A* **87**(4), 043408 (2013).
14. M. Fanciulli et al., "Electromagnetic theory of helicoidal dichroism in reflection from magnetic structures," *Phys. Rev. A* **103**(1), 013501 (2021).
15. M. Fanciulli et al., "Observation of magnetic helicoidal dichroism with extreme ultraviolet light vortices," *Phys. Rev. Lett.* **128**(7), 077401 (2022).
16. M. R. McCarter et al., "Antiferromagnetic real-space configuration probed by x-ray orbital angular momentum phase dichroism," arXiv:2205.03475 (2022).
17. J. R. Rouxel et al., "Hard x-ray helical dichroism of disordered molecular media," *Nat. Photonics* **16**, 570–574 (2022).
18. C. Pellegrini, A. Marinelli, and S. Reiche, "The physics of x-ray free-electron lasers," *Rev. Mod. Phys.* **88**(1), 015006 (2016).
19. N. Huang et al., "Features and futures of x-ray free-electron lasers," *Innovation* **2**(2), 100097 (2021).
20. P. Emma et al., "First lasing and operation of an Ångstrom-wavelength free-electron laser," *Nat. Photonics* **4**(9), 641–647 (2010).
21. D. Pile, "X-rays: first light from SACLA," *Nat. Photonics* **5**(8), 456–457 (2011).
22. H.-S. Kang et al., "Hard x-ray free-electron laser with femtosecond-scale timing jitter," *Nat. Photonics* **11**(11), 708–713 (2017).
23. W. Decking et al., "A MHz-repetition-rate hard x-ray free-electron laser driven by a superconducting linear accelerator," *Nat. Photonics* **14**, 391–397 (2020).
24. E. Prat et al., "A compact and cost-effective hard x-ray free-electron laser driven by a high-brightness and low-energy electron beam," *Nat. Photonics* **14**(12), 748–754 (2020).
25. A. Kondratenko and E. Saldin, "Generating of coherent radiation by a relativistic electron beam in an ondulator," *Part. Accel.* **10**, 207–216 (1980).
26. J. Feldhaus et al., "Possible application of x-ray optical elements for reducing the spectral bandwidth of an x-ray SASE FEL," *Opt. Commun.* **140**(4–6), 341–352 (1997).
27. G. Geloni, V. Kocharyan, and E. Saldin, "A novel self-seeding scheme for hard x-ray FELs," *J. Mod. Opt.* **58**(16), 1391–1403 (2011).
28. W. Colson, "The nonlinear wave equation for higher harmonics in free-electron lasers," *IEEE J. Quantum Electron.* **17**(8), 1417–1427 (1981).
29. G. Geloni et al., "Theory of nonlinear harmonic generation in free-electron lasers with helical wigglers," *Nucl. Instrum. Methods Phys. Res. Sec. A Accel. Spectrom. Detect. Assoc. Equip.* **581**(3), 856–865 (2007).
30. E. Hemsing, "Coherent photons with angular momentum in a helical afterburner," *Phys. Rev. Accel. Beams* **23**(2), 020703 (2020).
31. J. Bahrdt et al., "First observation of photons carrying orbital angular momentum in undulator radiation," *Phys. Rev. Lett.* **111**(3), 034801 (2013).
32. E. Hemsing et al., "First characterization of coherent optical vortices from harmonic undulator radiation," *Phys. Rev. Lett.* **113**(13), 134803 (2014).
33. P. R. Ribič et al., "Extreme-ultraviolet vortices from a free-electron laser," *Phys. Rev. X* **7**(3), 031036 (2017).
34. E. Hemsing, A. Marinelli, and J. Rosenzweig, "Generating optical orbital angular momentum in a high-gain free-electron laser at the first harmonic," *Phys. Rev. Lett.* **106**(16), 164803 (2011).
35. E. Hemsing et al., "Coherent optical vortices from relativistic electron beams," *Nat. Phys.* **9**(9), 549–553 (2013).

36. E. Hemsing and A. Marinelli, "Echo-enabled x-ray vortex generation," *Phys. Rev. Lett.* **109**(22), 224801 (2012).
37. P. R. Ribič, D. Gauthier, and G. De Ninno, "Generation of coherent extreme-ultraviolet radiation carrying orbital angular momentum," *Phys. Rev. Lett.* **112**(20), 203602 (2014).
38. N. Huang and H. Deng, "Generating x-rays with orbital angular momentum in a free-electron laser oscillator," *Optica* **8**(7), 1020–1023 (2021).
39. A. G. Peele et al., "Observation of an x-ray vortex," *Opt. Lett.* **27**(20), 1752–1754 (2002).
40. F. Seiboth et al., "Refractive hard x-ray vortex phase plates," *Opt. Lett.* **44**(18), 4622–4625 (2019).
41. A. Sakdinawat and Y. Liu, "Soft-x-ray microscopy using spiral zone plates," *Opt. Lett.* **32**(18), 2635–2637 (2007).
42. J. Vila-Comamala, A. Sakdinawat, and M. Guizar-Sicairos, "Characterization of x-ray phase vortices by ptychographic coherent diffractive imaging," *Opt. Lett.* **39**(18), 5281–5284 (2014).
43. J. T. Lee et al., "Laguerre–Gauss and Hermite–Gauss soft x-ray states generated using diffractive optics," *Nat. Photonics* **13**(3), 205–209 (2019).
44. R. Chen et al., "Orbital angular momentum waves: generation, detection, and emerging applications," *IEEE Commun. Surv. Tutor.* **22**(2), 840–868 (2019).
45. A. A. Lutman et al., "Fresh-slice multicolour x-ray free-electron lasers," *Nat. Photonics* **10**(11), 745–750 (2016).
46. A. Marinelli et al., "High-intensity double-pulse x-ray free-electron laser," *Nat. Commun.* **6**(1), 1–6 (2015).
47. E. Hemsing et al., "Longitudinal dispersion of orbital angular momentum modes in high-gain free-electron lasers," *Phys. Rev. Spl. Top.-Accel. Beams* **11**(7), 070704 (2008).
48. E. Hemsing, A. Gover, and J. Rosenzweig, "Virtual dielectric waveguide mode description of a high-gain free-electron laser. ii. modeling and numerical simulations," *Phys. Rev. A* **77**(6), 063831 (2008).
49. E. Saldin, E. Schneidmiller, and M. Yurkov, "Diffraction effects in the self-amplified spontaneous emission fel," *Opt. Commun.* **186**(1–3), 185–209 (2000).
50. S. Reiche, "Genesis 1.3: a fully 3D time-dependent FEL simulation code," *Nucl. Instrum. Methods Phys. Res. Sect. A: Accel. Spectrom. Detect. Assoc. Equip.* **429**(1–3), 243–248 (1999).
51. H. Yong et al., "Direct monitoring of conical intersection passage via electronic coherences in twisted x-ray diffraction," *Phys. Rev. Lett.* **129**(10), 103001 (2022).

Jiawei Yan is a physicist at the European XFEL. He received his PhD from the Shanghai Institute of Applied Physics of the Chinese Academy of Sciences in 2021. His current research interests include free-electron laser physics, accelerator physics, and machine learning. His research work was awarded as one of China's Top 10 Optical Breakthroughs (2021). He won the Excellent Doctoral Dissertation Award from the Chinese Academy of Sciences and the Young Investigator FEL Prize.

Gianluca Geloni is a physicist at the European XFEL. His interests are at the interface between electron accelerators and radiation generation by ultrarelativistic beams. He studied at Università di Genova (Italy) and he received his doctorate in physics from the Technische Universiteit Eindhoven (The Netherlands) in 2003. He spent the following years working at DESY, HASYLAB (Germany), and in 2010 he joined the European XFEL (Germany), where he became leader of the FEL Physics group and co-coordinator of the FEL R&D group. He currently focuses his research activity on the inception, assessment, and development of advanced FEL schemes.

Research Article

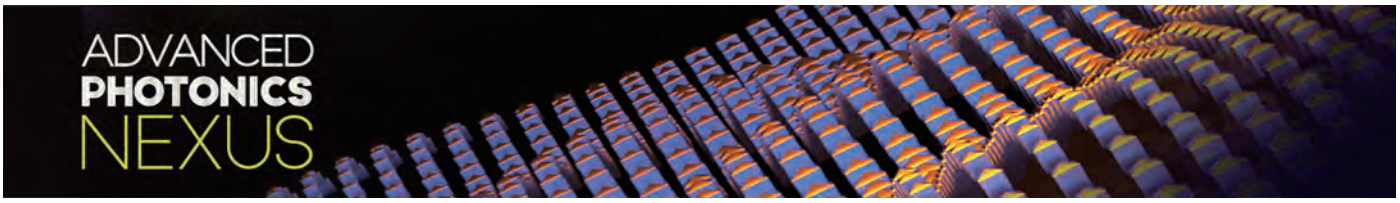

Generation of high-efficiency, high-purity, and broadband Laguerre-Gaussian modes from a Janus optical parametric oscillator

Dunzhao Wei,[a,b,†] Pengcheng Chen,[a,†] Yipeng Zhang,[a,†] Wenzhe Yao,[a] Rui Ni,[a] Xiaopeng Hu,[a,c] Xinjie Lv,[a,c] Shining Zhu,[a,c] Min Xiao,[a,c,d] and Yong Zhang[a,c,*]

[a]Nanjing University, College of Engineering and Applied Sciences, School of Physics, National Laboratory of Solid State Microstructures, Nanjing, China
[b]Sun Yat-Sen University, School of Physics, State Key Laboratory of Optoelectronic Materials and Technologies, Guangzhou, China
[c]Nanjing University, Collaborative Innovation Center of Advanced Microstructures, Nanjing, China
[d]University of Arkansas, Department of Physics, Fayetteville, Arkansas, United States

Abstract. Laguerre-Gaussian (LG) modes, carrying the orbital angular momentum of light, are critical for important applications, such as high-capacity optical communications, superresolution imaging, and multidimensional quantum entanglement. Advanced developments in these applications demand reliable and tunable LG mode laser sources, which, however, do not yet exist. Here, we experimentally demonstrate highly efficient, highly pure, broadly tunable, and topological-charge-controllable LG modes from a Janus optical parametric oscillator (OPO). The Janus OPO featuring a two-faced cavity mode is designed to guarantee an efficient evolution from a Gaussian-shaped fundamental pump mode to a desired LG parametric mode. The output LG mode has a tunable wavelength between 1.5 and 1.6 μm with a conversion efficiency >15%, a controllable topological charge up to 4, and a mode purity as high as 97%, which provides a high-performance solid-state light source for high-end demands in multidimensional multiplexing/demultiplexing, control of spin-orbital coupling between light and atoms, and so on.

Keywords: orbital angular momentum; Laguerre-Gaussian mode; optical parametric oscillator.

Received Dec. 28, 2022; revised manuscript received Mar. 7, 2023; accepted for publication Apr. 3, 2023; published online Apr. 21, 2023.

[DOI: 10.1117/1.APN.2.3.036007]

1 Introduction

Laguerre-Gaussian (LG) modes with unique spiral wavefronts are the paraxial solutions of the scalar Helmholtz equation in cylindrical coordinates, which can be distinguished by an azimuthal index l and a radial index p, i.e., LG(l, p). In 1992, Allen et al. demonstrated that an LG mode carries an orbital angular momentum (OAM) of $l\hbar$ per photon,[1] where l is called the topological charge (TC). Their pioneering work has significantly boosted the applications of LG modes from optical trapping and optical tweezer to optical communications, superresolution imaging, precision measurement, quantum information processing, and so on.[2–9] In turn, these high-end demands have triggered the developments of LG-mode laser sources in recent years.[10–17] Almost all the applications benefit from the high purity of an LG laser source, such as improved signal-to-noise ratio in rotation measurement, enhanced resolution in fluorescence imaging, and optimized coupling with an OAM photonic chip.[18–20] High-power laser output of LG mode could provide an effective way to decrease thermal noises in gravitational-wave detection.[21] In particular, LG laser sources are expected to be wavelength-tunable for wavelength division multiplexing in OAM-based high-capacity optical communication, investigation of spin-orbital coupling with various atoms in quantum storage and isolation, and excitations of versatile fluorescence in superresolution imaging.[19,22–25] However, these advanced applications are severely hampered by the limited wavelength bandwidth and mode purity in previous LG mode lasers. A reliable and broadband-tunable LG mode laser source does not yet exist.

*Address all correspondence to Yong Zhang, zhangyong@nju.edu.cn
†These authors contribute equally to this work.

The optical parametric oscillator (OPO) has been recognized as one of the most popular tunable sources.[26–29] A pump wave with frequency of ω_p generates two parametric waves,[30] i.e., signal and idler waves at the frequencies of ω_s and ω_i, respectively, through the second-order nonlinear downconversion process. It satisfies the energy conservation of $\omega_p = \omega_i + \omega_s$. By controlling the phase-matching condition for momentum conservation, one can obtain wavelength-tunable output of the generated parametric waves.[31] An OPO system is capable of outputting broad wavelengths covering ultraviolet (UV), visible, and infrared bands, which makes it an excellent candidate for broadband output of high-quality LG modes. There are two reported configurations. One is to build a traditional OPO outputting a Gaussian mode, and then convert it to an LG mode using a spiral phase plate, a fork grating, a Q-plate, a vector vortex waveplate (VVW), or a spatial light modulator [Fig. 1(a)].[6,32–35] Because these devices only introduce a spatial phase modulation, the generated beam is actually a superposition of various higher-order LG modes with the same azimuthal index l but a different radial index p, i.e., $\sum_p \mathrm{LG}(l, p)$. Although the conversion efficiency of a commercial device reaches 95%, it suffers from poor mode purity,[36,37] and generally, the higher the TC is, the lower mode purity becomes (typically 80% and 60% for LG(1, 0) and LG(2, 0) modes, respectively). See Note 1 in the Supplementary Material for details. The other approach is to oscillate an LG mode inside the OPO cavity [Fig. 1(b)] by utilizing the fact that

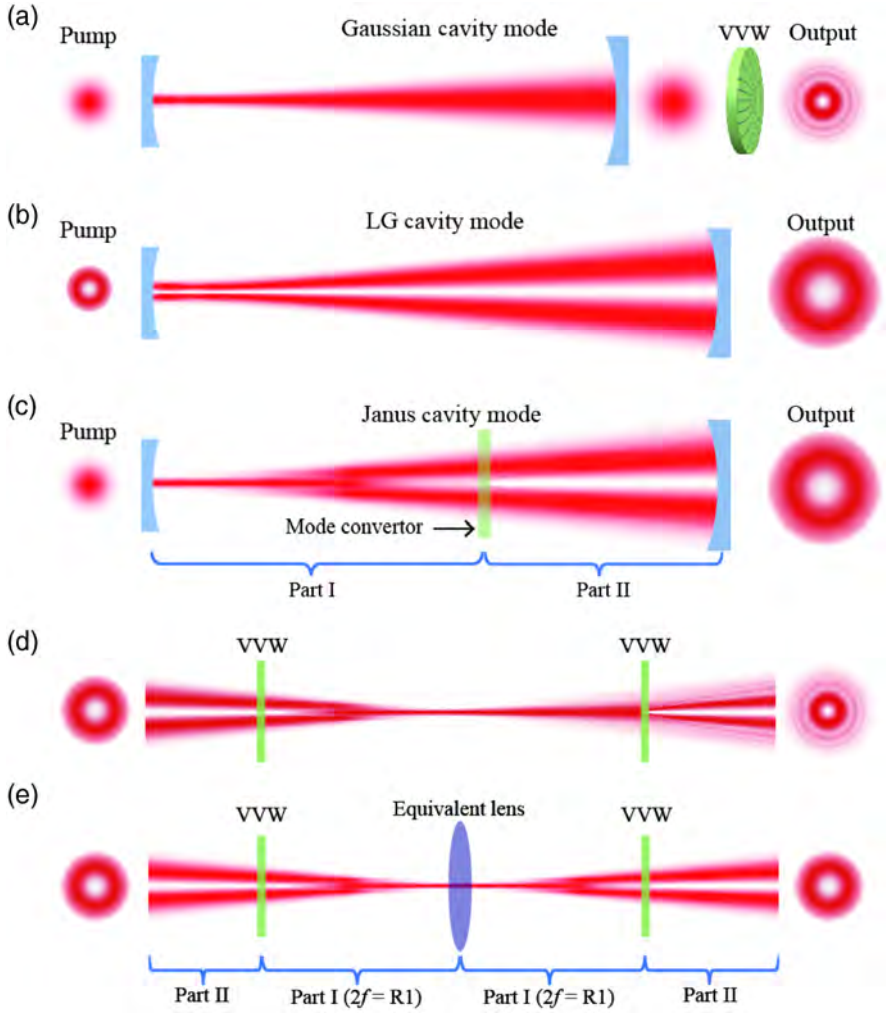

Fig. 1 Different cavity modes in OPO and Janus OPO designs. (a) A Gaussian-pumped OPO oscillating in a fundamental Gaussian mode. (b) An LG-pumped OPO with an LG cavity mode and an LG output mode. (c) A specially designed Janus OPO that is pumped by a Gaussian mode but outputs an LG mode. (d) A one-round-trip mode conversion without an imaging system. An LG mode passing through a VVW produces a hollow Gaussian beam, which evolves into a Gaussian-like mode after a certain propagation. However, the hollow Gaussian beam cannot recover itself without the equivalent lens as in panel (e) and neither can the LG mode. (e) A one-round-trip mode conversion inside a Janus OPO. The input coupler with a radius curvature of R1 can be seen as an equivalent lens with a focusing length of $2f = \mathrm{R1}$. Therefore, the light field after the VVW, which is set at the curvature center, will recover itself at the same position after being reflected by the input coupler.

LG modes are Eigen cavity modes,[38,39] which could also extend the output wavelength.[40] In comparison to a Gaussian-mode OPO system, the frequency conversion of an LG mode is less efficient because its donut-shaped profile has a much lower power density. In addition, the output mode quality is not as good as had been hoped. The fiber laser is another potential platform for broadband output of LG mode, but it suffers from low mode purity as well.[41,42]

Here, we propose and experimentally demonstrate a Janus OPO based on quasi-phase-matching (QPM) configuration[43–47] for highly efficient output of highly pure, broadly tunable, and TC-controllable LG modes [Fig. 1(c)]. The Janus cavity that we have previously studied features two-faced transverse-mode structures (like the god Janus in ancient Roman mythology), which combines the advantages of both Gaussian and LG cavity modes.[48] The nonlinear crystal, i.e., a periodically poled lithium niobate (PPLN) crystal, is set next to the front mirror to fully utilize the Gaussian-like front face of Janus cavity mode for high conversion efficiency. Most importantly, due to the introduction of an intracavity imaging system, the generated parametric light is naturally converted into a designed LG mode at the output port of the cavity. The cavity loss is significantly reduced because no additional spatial mode filter is used inside the cavity. The experimental results present a high-performance LG mode source beyond the existing methods. For the generated signal LG beam, the wavelength is tunable between 1.5 and 1.6 μm, the conversion efficiency is $>15\%$, the TC is controllable up to 4, and most importantly, the mode purity can reach 97%.

2 Janus Cavity Theory

As shown in Fig. 1(c), the Janus cavity has a two-faced cavity mode, distinguishing itself from the traditional cavity mode configuration [Figs. 1(a) and 1(b)]. The front face at the input mirror has a Gaussian profile to achieve a better conversion efficiency because of its higher power density relative to the LG mode. The back face at the end mirror is a donut-shaped LG profile, which guarantees the direct output of a high-purity LG mode. The key question is how to smoothly evolve the cavity mode from a Gaussian profile to an LG profile, and vice versa, without breaking the cavity mode reversibility. The general idea is to directly put a spatial phase modulator, such as a VVW, into the cavity to complete the mode conversion.[14,49] However, phase modulation alone is not sufficient to perform a perfect spatial mode conversion due to lack of necessary amplitude modulation. Let us consider an ideal LG mode at the output mirror. As shown in Fig. 1(d), it propagates through the VVW, which produces a beam superimposed by multiple modes in Part I of the Janus OPO rather than a single mode, as in a traditional cavity.[50] This superimposed beam of multiple spatial modes hardly keeps its profile during free propagation. Therefore, the VVW alone cannot convert it back into the same LG mode as the initial one [Fig. 1(d)], which breaks the spatial mode reversibility inside the cavity. Under this situation, previous reports used an iris to filter out the unwanted high-order mode, which introduces a substantial cavity loss and severely limits laser performance.[14,49]

To realize an ideal Janus OPO [Fig. 1(c)], the mode reversibility has to be simultaneously satisfied for multiple modes in Part I of the cavity.[48] The key is to introduce an imaging system into the cavity. In our experiment, we use a concave front (input) mirror as an equivalent imaging lens for the compact Janus OPO design [Fig. 1(c)]. Figure 1(e) shows the transformation of Janus cavity mode in a round trip. When the imaging system works properly, the multiple spatial modes will repeat themselves after passing through the equivalent lens (i.e., being reflected back at the concave front mirror). Then, the VVW can convert them back into an ideal LG mode in Part II of the Janus OPO, and the reversibility condition inside the cavity can therefore be perfectly fulfilled in principle. In addition, the cavity mode profile near the front mirror is required to match the pump Gaussian mode. In our Janus cavity design, the multiple modes after an LG mode passing through the VVW compose a so-called hollow-Gaussian beam,[50] which naturally evolves into a spatial profile very close to a Gaussian mode after a certain propagation distance [Fig. 1(d)]. See Note 3 in the Supplementary Material for the detailed mathematics in designing a Janus cavity. In comparison to previous designs, all the spatial modes during mode conversion are fully utilized in such a Janus cavity. Therefore, the cavity loss greatly decreased and the output performance significantly improved.

3 Results

3.1 Experimental Setup of the Janus OPO

Figure 2(a) shows the experimental setup of a Janus OPO for generation of an LG-mode signal beam. Its output wavelength is designed to be tunable within the optical communication band. Two concave mirrors form the input and output couplers, which are coated for high reflectivity at the signal wavelength. A PPLN crystal serves as the nonlinear medium, which has multiple channels to extend the QPM bandwidth. The pump beam is generated by a 1064-nm pulsed nanosecond laser and focused into the crystal with a spot size of 200 μm in diameter, which matches the size of signal Gaussian-like face inside the crystal (see Note 4 in the Supplementary Material). Besides the Janus cavity mode as discussed above, the polarization of the field in the cavity is also precisely controlled to facilitate the parametric downconversion and mode conversion. In the PPLN crystal, both the pump and signal waves polarize vertically to utilize the biggest nonlinear coefficient d_{33} of the PPLN crystal for high conversion efficiency. By changing the temperature and selecting a channel of the PPLN crystal, the output wavelength of signal wave can range from 1480 to 1650 nm (see Note 2 in the Supplementary Material for the details). The next mode conversion subsystem includes a Faraday rotator (FR), a quarter-wave plate (QWP), and a VVW (the system has a work bandwidth of 1550 nm $\pm$ 50 nm). The VVW has a distinct q factor, with its value being a positive multiple of 1/2. In the forward propagation direction, a TC of $l = \pm 2q$ is loaded onto the signal wave, which will be canceled when it passes through the VVW again on its way back. To generate a high-purity LG mode at the output, the cavity mode in Part I should be reconfigured to form a superposition of multiple spatial modes, which is automatically achieved by the Janus cavity design. Here, we use a concave input coupler and set the VVW at its curvature center, which composes a symmetric imaging system to satisfy the condition of multimode reversibility in Part I of the Janus OPO [Fig. 1(e)]. In principle, an ideal LG mode propagates in Part II of the cavity. Such a stable Janus cavity mode is confirmed by numerical calculations based on the Fox–Li simulating process [Fig. 2(b)]. The cross sections of the Janus modes for different TCs show how a Gaussian-like mode is naturally transformed to a desired LG mode (See Appendix A and Note 4 in the Supplementary Material for the details). It should be noted that the mode

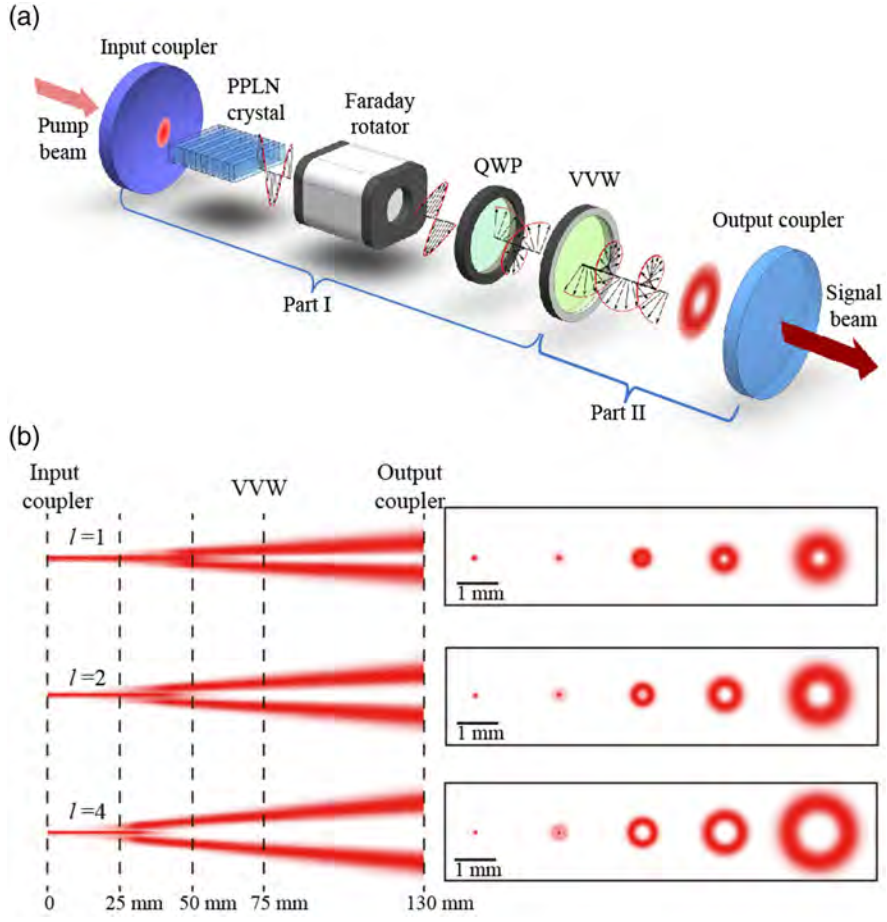

Fig. 2 Experimental setup and Janus mode simulation. (a) The PPLN crystal, as the nonlinear medium, transforms one pump photon into a signal photon and an idle photon through the QPM parametric downconversion process. The input/output couplers are coated for high reflectivity at the signal wavelength. The FR, QWP, and VVW form a mode conversion setup inside the cavity. The QWP alters the vertical polarization of the signal beam to circular polarization so that the spin-OAM conversion can happen on the VVW to achieve the desired Gaussian-to-LG mode conversion. The output LG mode can be changed by rotating the QWP or replacing the VVW. FR is used to keep the signal wave to be vertically polarized inside the PPLN crystal. (b) Janus cavity modes for $l = 1$, 2, and 4 and their cross sections at different distances of 0, 25, 50, 75, and 130 mm away from the input coupler.

conversion process requires a circularly polarized signal wave on the VVW. To fulfill the polarization reversibility in the cavity, we add an FR and a QWP to accomplish the polarization control (see Note 5 in the Supplementary Material for the details).

3.2 Performance of the Janus OPO

First, we demonstrate the generation of high-purity LG(1, 0) and LG(−1,0) modes. A VVW with $q = 1/2$ is used to introduce a TC of $l = \pm 1$. The sign is controlled by the orientation of the QWP. Under QPM configuration, the vertically polarized pump beam produces a vertically polarized signal beam in the PPLN crystal. After passing through the FR, the signal beam has a 45 deg linear polarization. When the fast axis of the QWP orients vertically (or horizontally), the signal polarization is further changed to a left- (or right-) circularly polarized one, resulting in $l = 1$ (or -1) after the VVW (Fig. 2) (see Note 5 in the Supplementary Material). The intensity patterns of the output LG(1, 0) and LG(−1,0) modes at 1550 nm showed in Figs. 3(a) and 3(b) exhibit high-quality donut intensity distribution without observable sidelobes. Clearly, the undesired higher-order LG modes ($p > 0$) are significantly suppressed by the Janus OPO cavity. Further modal analyses in Figs. 3(a) and 3(b) show that the generated LG(1, 0) and LG(−1,0) modes have mode purities of 96.6% and 97.0%, respectively (see Note 6 in the Supplementary Material for the modal analysis process). The mode purity is greatly enhanced in comparison to the typical value of ~80% using a VVW outside the cavity.[37] Our specially designed Janus OPO is also suitable for generating high-order, high-purity LG modes [Fig. 2(b)]. As a demonstration, VVWs of $q = 1$ and $q = 2$ are used to generate LG($\pm$2,0) and LG($\pm$4,0) modes. Since LG($\pm l$, 0) modes experience the similar transverse-mode evolution in the OPO, we only show the results of LG(2, 0) and LG(4, 0) modes [Figs. 3(c) and 3(d)]. The mode purities of 95.2% for the output LG(2, 0) mode and 93.7% for the LG(4, 0) mode are much superior to the 60% and 50% values

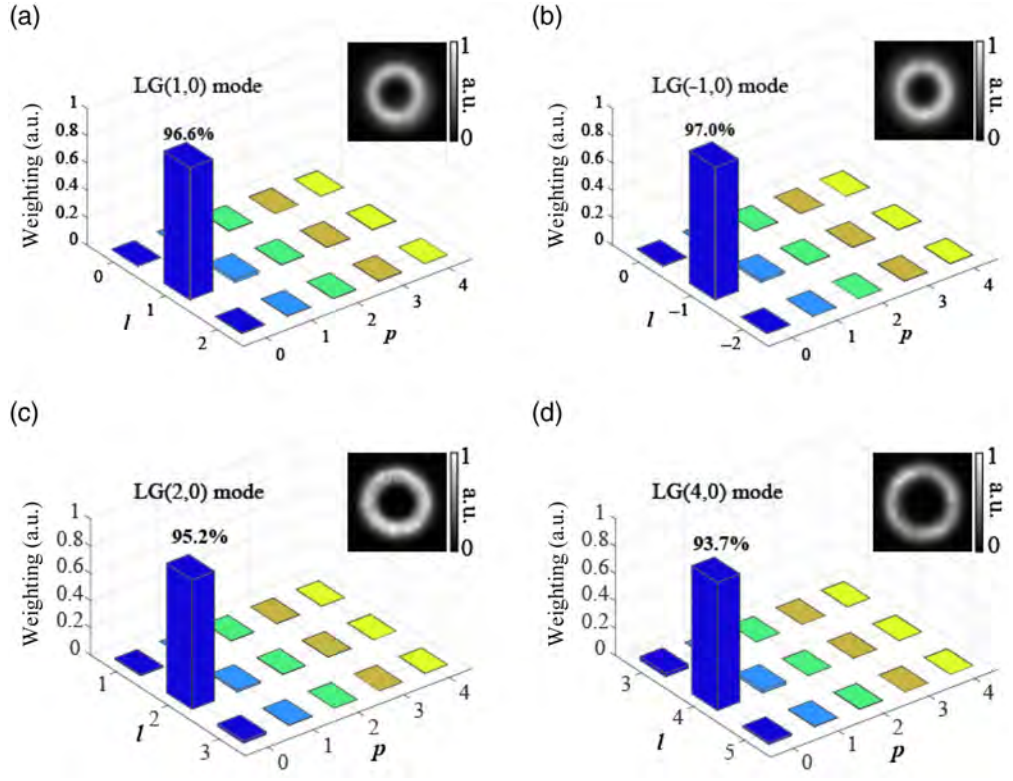

Fig. 3 TC-controllable generation of high-purity LG(l, 0) modes at the wavelength of 1550 nm. Modal analyses show high mode purities of 96.6%, 97.0%, 95.2%, and 93.7% for (a) LG(1, 0), (b) LG(–1, 0), (c) LG(2, 0), and (d) LG(4, 0) modes, respectively. The insets are the intensity patterns of the corresponding LG modes.

using VVWs outside the cavity.[37] It should be noted that the VVWs should be precisely collimated with the optical axis of the cavity to realize a high-purity output of LG modes. See Note 7 in the Supplementary Material for details.

In our experiment, the output wavelength of the Janus OPO can be tuned by changing the QPM channel and the temperature of the PPLN crystal. The Janus OPO shows excellent performance within the designed wavelengths ranging from 1500 to 1600 nm. As shown in Fig. 4(a), the conversion efficiency of the signal LG mode surpasses 10% in most of the working wavelengths. Under a pump power of 4.2 W, the conversion efficiencies for LG(1,0), LG(2, 0), and LG(4, 0) modes at 1550 nm reach 15.3%, 15.8%, and 15.6%, respectively. Notably, the Janus OPO maintains a high conversion efficiency for high-order LG modes. In comparison to the output performance of the signal Gaussian mode in a traditional OPO system [Fig. 4(a)], the slightly decreasing conversion efficiencies for the outputs of LG modes can be mainly attributed to the limited mode conversion efficiency of VVWs shown in Table S1 in the Supplementary Material and the reflection losses from the FR and QWP. Figure 4(b) compares the power dependence of the output LG(1,0) mode on the pump power at 1525, 1550, 1575, and 1600 nm, respectively, whose thresholds are 1.6, 1.1, 1.2, and 1.5 W, respectively. The differences in the threshold and conversion efficiency for different wavelengths can be attributed to the fact that the intracavity optical components are not uniformly optimized at all the wavelengths. Figure 4(c) depicts the modal analysis results of the output LG(1, 0) mode at the wavelengths of 1525 and 1575 nm, which show high mode purities of 97.1% and 95.9%, respectively. The bandwidth of this Janus OPO can be further extended using ultrawideband optical components as intracavity elements.

4 Discussion

We have proposed and experimentally demonstrated a Janus OPO system for generating highly efficient, highly pure, broadly tunable, and TC-controllable LG modes. Such a Janus OPO distinguishes itself by possessing a two-faced cavity mode, which makes use of the distinct advantages of both the Gaussian and LG cavity modes. The front (input) face has a Gaussian profile to achieve the high-efficiency nonlinear frequency conversion, while its back (output) face is a donut-shaped LG profile that guarantees the direct output of a desired high-purity LG mode from the cavity. The key to realizing such a Janus OPO is the introduction of an imaging system to facilitate the perfect intracavity mode conversion. In this work, the Janus OPO is designed for the Gaussian-to-LG mode conversion of the signal light, which can be easily adjusted to output an LG mode at the idler wavelength. The conversion efficiency of the Janus OPO could be further enhanced by use of a double-pass pump configuration.[47] In addition, by selecting proper optical components, our experimental configuration can be readily extended to visible and UV wavelength bands, as well as to generate tunable vector beams and multidimensional quantum entangled sources. The excellent features of the LG modes from our Janus OPO (e.g., wavelength tunable between

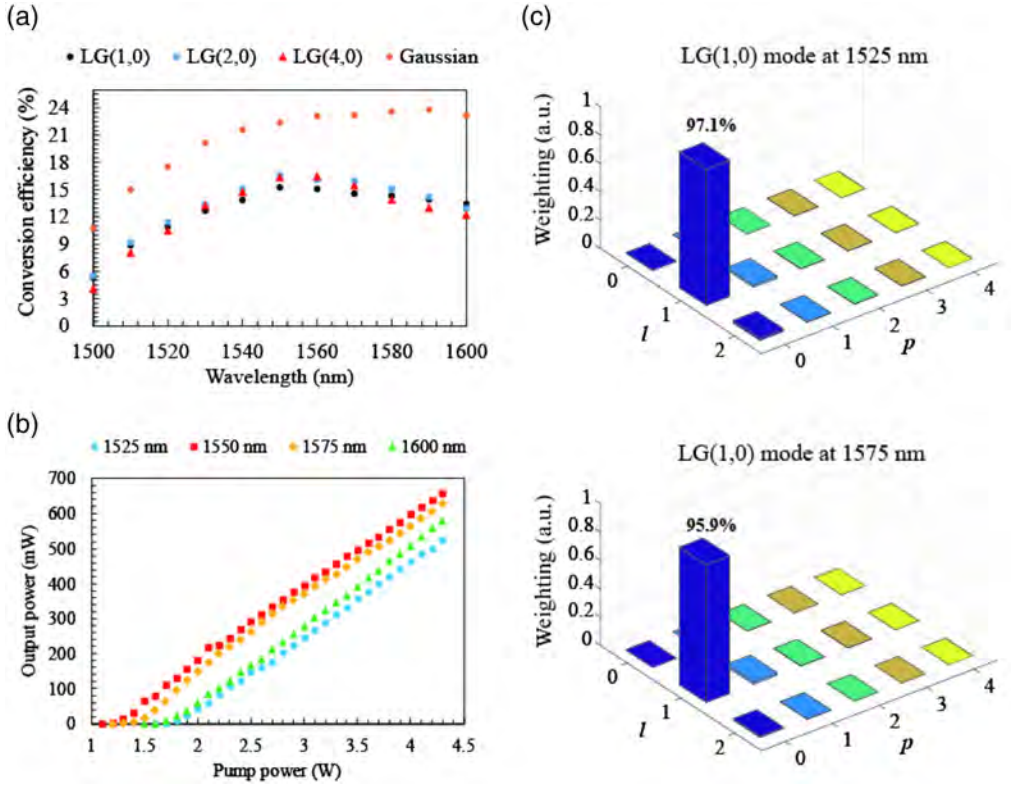

Fig. 4 Wavelength tunable high-purity LG modes. (a) Dependence of the conversion efficiencies of LG modes ($l = 1, 2, 4$) on the wavelength ranging from 1500 to 1600 nm at a pump power of 4.2 W, showing high conversion efficiencies at the designed bandwidth. (b) Dependences of output powers of LG(1, 0) mode on the pump power at 1525, 1550, 1575, and 1600 nm, respectively, showing high-quality OPO output performances. (c) Modal analysis for the output LG(1, 0) mode at the wavelengths of 1525 and 1575 nm, showing the mode purity up to 97.1%.

1.5 and 1.6 μm, conversion efficiency >15%, and mode purity >97%) can meet the critical requirements of high-level applications such as high-capacity optical communications, high-precision sensing and measurements, and superresolution imaging. In addition, the linewidth of LG modes could be narrowed using a continuous wave (CW) pump laser, enabling potential investigation of spin-orbital coupling with various atoms in quantum applications.

5 Appendix A: Experimental Setup

As shown in Fig. 2(a), a PPLN crystal with dimensions of $25(x) \times 12.3(y) \times 1(z)$ mm^3 serves as the nonlinear medium. Both of its end faces have a transmittance >99% in the 1380- to 1800-nm wavelength range. It is mounted inside an oven with the temperature tunability up to 150°C. The input coupler (with a radius of curvature of 75 mm) is coated with a high transmittance (>99%) at 1064 nm and a high reflectivity (>99%) at 1450 to 1650 nm, while the output coupler (with a radius of curvature of 125 mm) is coated with a transmittance of 30% at 1450 to 1650 nm. The cavity length is 140 mm, satisfying the stability condition of a resonator. A pump beam (wavelength of 1064 nm, repetition rate of 22 kHz, pulse width of 45 ns, linewidth of 5 nm) is generated by a nanosecond-pulsed fiber laser (YDFLP-M7-3-PM, JPT Co.). It is focused by a lens into a 200-μm-in-diameter spot inside the crystal. The PPLN crystal has 10 channels. In the experiment, we use four channels with periods of 31.02, 30.49, 29.98, and 29.52 μm, respectively. Under the pumping wavelength of 1064 nm, the output signal wave with a wavelength bandwidth of 1.4 nm (see Notes 2 and 8 in the Supplementary Material for details) can be tuned from 1480 to 1650 nm in the temperature range from 25°C to 138°C. An FR, a QWP, and a VVW are inserted into the cavity to achieve the reversible mode conversion inside the cavity. VVW is a spatially variant half-wave plate whose optical axis rotates continuously around a singularity point. All their working wavelength bandwidths are from 1500 to 1600 nm. The VVW is placed at a distance of 90 mm away from the input coupler, where the curvature center of the input coupler is, considering the effective length due to the high refractive index of the PPLN crystal. VVWs of $q = 0.5$, 1, 2 have been used to generate LG$(l, 0)$ modes with different TCs. The output intensity patterns are recorded by a laser beam profiler (LBP, Newport Corp.).

6 Appendix B: Cavity Mode Simulations

The numerical simulations have been carried out based on the Fox–Li method. A one-round-trip transition of the cavity mode can be described in what follows. A parametric wave starting from the input coupler travels a distance of L_A and passes through the VVW with a TC of l (or $-l$). After traveling a distance of L_B, the parametric wave is reflected by the output coupler and propagates backward. The TC is canceled when the

parametric wave passes through the VVW along the opposite direction. Finally, the parametric wave reaches the input mirror to finish its one-round-trip transition. The parametric wave repeats the cycle until a stable cavity mode is formed. Base on angular spectrum theory, the iterative procedure described above is calculated step by step using MATLAB programming.

Acknowledgments

This work was supported by the National Key R&D Program of China (Grant No. 2021YFA1400803), the National Natural Science Foundation of China (Grant Nos. 91950206, 11874213, and 11674171), the Key Research Program of Jiangsu Province (Grant No. BE2015003-2), and the Guangdong Natural Science Funds for Distinguished Young Scholars (Grant No. 2022B1515020067).

Data Availability

The data that support the results within this paper and other findings of the study are available from the corresponding authors upon reasonable request.

Code Availability

The custom code and mathematical algorithm used to obtain the results within this paper are available from the corresponding authors upon reasonable request.

References

1. L. Allen et al., "Orbital angular momentum of light and the transformation of Laguerre-Gaussian laser modes," *Phys. Rev. A* **45**, 8185–8189 (1992).
2. Y. Shen et al., "Optical vortices 30 years on: OAM manipulation from topological charge to multiple singularities," *Light Sci. Appl.* **8**, 90 (2019).
3. Y. Yang et al., "Optical trapping with structured light: a review," *Adv. Photonics* **3**, 034001 (2021).
4. N. Bozinovic et al., "Terabit-scale orbital angular momentum mode division multiplexing in fibers," *Science* **340**, 1545–1548 (2013).
5. S. W. Hell, "Far-field optical nanoscopy," *Science* **316**, 1153–1158 (2007).
6. A. Mair et al., "Entanglement of the orbital angular momentum states of photons," *Nature* **412**, 313–316 (2001).
7. M. Erhard, M. Krenn, and A. Zeilinger, "Advances in high-dimensional quantum entanglement," *Nat. Rev. Phys.* **2**, 365–381 (2020).
8. Q. Jia et al., "Transferring linear motion of an optical wedge to rotational frequency shift in an orbital angular momentum interferometer," *Appl. Phys. Lett.* **111**, 091102 (2017).
9. V. D. Salakhutdinov, E. R. Eliel, and W. Loffler, "Full-field quantum correlations of spatially entangled photons," *Phys. Rev. Lett.* **108**, 173604 (2012).
10. M. Piccardo et al., "Vortex laser arrays with topological charge control and self-healing of defects," *Nat. Photonics* **16**, 359 (2022).
11. A. Forbes, "Structured light from lasers," *Laser Photonics Rev.* **13**, 1900140 (2019).
12. H. Sroor et al., "High-purity orbital angular momentum states from a visible metasurface laser," *Nat. Photonics* **14**, 498–503 (2020).
13. J. Fan et al., "Two-channel, dual-beam-mode, wavelength-tunable femtosecond optical parametric oscillator," *Adv. Photonics* **2**, 1 (2020).
14. D. Naidoo et al., "Controlled generation of higher-order Poincaré sphere beams from a laser," *Nat. Photonics* **10**, 327–332 (2016).
15. Z. Zhang et al., "Tunable topological charge vortex microlaser," *Science* **368**, 760–763 (2020).
16. X. Cai et al., "Integrated compact optical vortex beam emitters," *Science* **338**, 363–366 (2012).
17. P. Miao et al., "Orbital angular momentum microlaser," *Science* **353**, 464–467 (2016).
18. M. P. J. Lavery et al., "Detection of a spinning object using light's orbital angular momentum," *Science* **341**, 537–540 (2013).
19. B. Neupane, F. S. Ligler, and G. Wang, "Review of recent developments in stimulated emission depletion microscopy: applications on cell imaging," *J. Biomed. Opt.* **19**, 080901 (2014).
20. Y. Chen et al., "Mapping twisted light into and out of a photonic chip," *Phys. Rev. Lett.* **121**, 233602 (2018).
21. L. Carbone et al., "Generation of high-purity higher-order Laguerre-Gauss beams at high laser power," *Phys. Rev. Lett.* **110**, 251101 (2013).
22. A. Alexandrescu, D. Cojoc, and E. Di Fabrizio, "Mechanism of angular momentum exchange between molecules and Laguerre-Gaussian beams," *Phys. Rev. Lett.* **96**, 243001 (2006).
23. A. E. Willner et al., "Recent advances in high-capacity free-space optical and radio-frequency communications using orbital angular momentum multiplexing," *Phil. Trans. R. Soc. A* **375**, 20150439 (2017).
24. M. S. Kwon et al., "Direct transfer of light's orbital angular momentum onto a nonresonantly excited polariton superfluid," *Phys. Rev. Lett.* **122**, 045302 (2019).
25. N. Carlon Zambon et al., "Optically controlling the emission chirality of microlasers," *Nat. Photonics* **13**, 283–288 (2019).
26. N. E. Yu et al., "Efficient optical parametric oscillation based on periodically poled 1.0 mol% MgO-doped stoichiometric $LiTaO_3$," *Appl. Phys. Lett.* **85**, 5134–5136 (2004).
27. C. Canalias and V. Pasiskevicius, "Mirrorless optical parametric oscillator," *Nat. Photonics* **1**, 459–462 (2007).
28. F. Kienle et al., "High-power, high repetition-rate, green-pumped, picosecond LBO optical parametric oscillator," *Opt. Express* **20**, 7008–7014 (2012).
29. A. Marandi et al., "Network of time-multiplexed optical parametric oscillators as a coherent Ising machine," *Nat. Photonics* **8**, 937–942 (2014).
30. R. W. Boyd, *Nonlinear Optics*, 3rd ed., Academic Press (2008).
31. O. Gayer et al., "Temperature and wavelength dependent refractive index equations for MgO-doped congruent and stoichiometric $LiNbO_3$," *Appl. Phys. B* **91**, 343–348 (2008).
32. S. S. Oemrawsingh et al., "Production and characterization of spiral phase plates for optical wavelengths," *Appl. Opt.* **43**, 688–694 (2004).
33. M. Rafayelyan and E. Brasselet, "Spin-to-orbital angular momentum mapping of polychromatic light," *Phys. Rev. Lett.* **120**, 213903 (2018).
34. B. Y. Wei et al., "Generating switchable and reconfigurable optical vortices via photopatterning of liquid crystals," *Adv. Mater.* **26**, 1590–1595 (2014).
35. X. W. Wang et al., "Recent advances on optical vortex generation," *Nanophotonics* **7**, 1533–1556 (2018).
36. E. Karimi et al., "Hypergeometric-Gaussian modes," *Opt. Lett.* **32**, 3053–3055 (2007).
37. B. Sephton, A. Dudley, and A. Forbes, "Revealing the radial modes in vortex beams," *Appl. Opt.* **55**, 7830–7835 (2016).
38. K. Miyamoto et al., "Optical vortex pumped mid-infrared optical parametric oscillator," *Opt. Express* **19**, 12220–12226 (2011).
39. A. Aadhi et al., "Controlled switching of orbital angular momentum in an optical parametric oscillator," *Optica* **4**, 349 (2017).
40. T. Omatsu, K. Miyamoto, and A. J. Lee, "Wavelength-versatile optical vortex lasers," *J. Opt.* **19**, 123002 (2017).
41. N. Zhou, J. Liu, and J. Wang, "Reconfigurable and tunable twisted light laser," *Sci. Rep.* **8**, 11394 (2018).
42. J. Zou et al., "Green/red pulsed vortex-beam oscillations in all-fiber lasers with visible-resonance gold nanorods," *Nanoscale* **11**, 15991–16000 (2019).

43. C.-S. Yu and A. H. Kung, "Grazing-incidence periodically poled $LiNbO_3$ optical parametric oscillator," *J. Opt. Soc. Am. B* **16**, 2233–2238 (1999).
44. M. Lazoul et al., "Multi-resonant optical parametric oscillator based on 2D-PPLT nonlinear photonic crystal," *Opt. Lett.* **40**, 1861–1864 (2015).
45. U. Bäder et al., "Nanosecond periodically poled lithium niobate optical parametric generator pumped at 532 nm by a single-frequency passively Q-switched Nd:YAG laser," *Opt. Lett.* **24**, 1608–1610 (1999).
46. H. C. Guo et al., "Multiple-channel mid-infrared optical parametric oscillator in periodically poled MgO: $LiNbO_3$," *J. Appl. Phys.* **101**, 113112 (2007).
47. S. T. Yang, R. C. Eckardt, and R. L. Byer, "Continuous-wave singly resonant optical parametric oscillator pumped by a single-frequency resonantly doubled Nd:YAG laser," *Opt. Lett.* **18**, 971–973 (1993).
48. P. C. Chen et al., "Self-consistent transverse modes in a geometric-phase-plate-assisted optical resonator," *Phys. Rev. A* **105**, 033525 (2022).
49. D. Wei et al., "Generating controllable Laguerre-Gaussian laser modes through intracavity spin-orbital angular momentum conversion of light," *Phys. Rev. Appl.* **11**, 014038 (2019).
50. Y. J. Cai, X. H. Lu, and Q. Lin, "Hollow Gaussian beams and their propagation properties," *Opt. Lett.* **28**, 1084–1086 (2003).
51. A. M. Yao and M. J. Padgett, "Orbital angular momentum: origins, behavior and applications," *Adv. Opt. Photonics* **3**, 161–204 (2011).
52. M. W. Beijersbergen et al., "Helical-wavefront laser beams produced with a spiral phaseplate," *Opt. Commun.* **112**, 321–327 (1994).
53. K. Sueda et al., "Laguerre-Gaussian beam generated with a multilevel spiral phase plate for high intensity laser pulses," *Opt. Express* **12**, 3548–3553 (2004).
54. L. E. Myers et al., "Quasi-phase-matched optical parametric oscillators in bulk periodically poled $LiNbO_3$," *J. Opt. Soc. Am. B* **12**, 2102–2116 (1995).
55. O. Svelto, *Principles of Lasers*, 5th ed., Springer Science +Business Media (2010).
56. J. W. Goodman, *Introduction to Fourier Optics*, 2nd ed., McGraw-Hill Companies (1996).
57. L. Marrucci, C. Manzo, and D. Paparo, "Optical spin-to-orbital angular momentum conversion in inhomogeneous anisotropic media," *Phys. Rev. Lett.* **96**, 163905 (2006).
58. V. Arrizón et al., "Pixelated phase computer holograms for the accurate encoding of scalar complex fields," *J. Opt. Soc. Am. A* **24**, 3500–3507 (2007).

Dunzhao Wei received his PhD in physics from Nanjing University in 2018 and engaged as a researcher in the College of Engineering and Applied Science at Nanjing University. Currently, he has been working as an associate professor in the School of Physics at Sun Yat-sen University since 2019. His research interests include the nonlinear optical effects of micro-nano structured materials and their applications in laser frequency conversion, light field manipulation, and quantum frequency conversion.

Yong Zhang received his PhD from the Department of Physics of Nanjing University in 2007 and engaged in postdoctoral research at Arkansas University in 2008 and 2009. Currently, he is working as a professor at Nanjing University, doctoral supervisor, and head of the Department of Optical Engineering since 2010. His research interests include the new nonlinear and quantum optical effects in micro-nanostructured lithium niobate and other materials, and their applications in laser, imaging, sensing, and precision measurement.

Biographies of the other authors are not available.

Research Article

ADVANCED PHOTONICS NEXUS

Characteristics of a Gaussian focus embedded within spiral patterns in common-path interferometry with phase apertures

Yizhou Tan[a,b] and Ying Gu[a,b,*]

[a]Chinese PLA General Hospital, the First Medical Center, Department of Laser Medicine, Beijing, China
[b]Hainan Hospital, Chinese PLA General Hospital, Laser Medicine Center, Sanya, China

Abstract. A phase-only method is proposed to transform an optical vortex field into desired spiral diffraction–interference patterns. Double-ring phase apertures are designed to produce a concentric high-order vortex beam and a zeroth-order vortex beam, and the diffracted intensity ratio of two beams is adjustable between 0 and 1. The coherent superposition of the two diffracted beams generates a brighter Airy spot (or Poisson spot) in the middle of the spiral pattern, where the singularity for typical vortex beam is located. Experiments employing circular, triangular, and rectangular phase apertures with topological charges from 3 to 16 demonstrate a stable, compact, and flexible apparatus for vortex beam conversion. By adjusting the parameters of the phase aperture, the proposed method can realize the optical Gaussian tweezer function and the optical vortex tweezer function simultaneously along the same axis or switch the experimental setup between the two functions. It also has potential applications in light communication through turbulent air by transmitting an orbital angular momentum-coded signal with a concentric beacon laser.

Keywords: finite aperture diffraction; phase-only beam transformation; orbital angular momentum; common-path interferometry; optical manipulation; light transmission through turbulent air.

Received Jan. 20, 2023; revised manuscript received Feb. 19, 2023; accepted for publication Mar. 8, 2023; published online Apr. 24, 2023.

[DOI: 10.1117/1.APN.2.3.036008]

1 Introduction

Optical waves carrying orbital angular momentums (OAMs) have been applied in optical manipulation, microscopy, quantum optics, and information encoding[1] since its first discovery by Allen et al. 30 years ago.[2] To expand the controllability of optical vortices, efforts have been made to modify the doughnut-shaped intensity distribution of the vortex beams, such as using the interference of Laguerre–Gaussian (LG) beams in a Mach–Zehnder interferometer to rotate optically trapped particles,[3] generating tiny dark spot diffraction of nonzero LG laser beams by an opaque disk,[4] generating continuously adjustable vortex beams by coaxial or small-angle interference,[5] using laser beams of different wavelengths incoherently overlaid to produce a sub-diffraction dark spot,[6] or generating concentric multirings by compound spiral phase plates.[7]

An important feature of the optical vortex beams is that the beam axis marks a singularity in the optical phase, and the amplitude of light becomes zero. Therefore, generating a bright Gaussian focus embedded with a spiral pattern remains challenging. Existing technology, such as computer-generated holograms, can generate a vortex beam of arbitrary patterns, including the diffraction–interference patterns studied in this work.[8,9] However, optical elements have to be carefully aligned in the holographic off-axis optical system, which makes it infeasible in long-term optical trapping with high positioning accuracy. Meanwhile, although a metasurface plate allows conversion of a polarized input beam into an arbitrary vortex mode, it is not possible to modify the operating parameters dynamically in a prefabricated metasurface.[10,11]

The generalized phase contrast (GPC) method converts a pattern of phase modulation into the corresponding intensity distribution.[12,13] Inspired by GPC, we propose a method for transforming an optical vortex field into the desired spiral

*Address all correspondence to Ying Gu, guyinglaser@sina.com

interferograms. Amplitude aperture is referred to as the hole on an optically opaque screen, and its diameter determines the diameter of the bundle of rays traversing through. Different from a triangular amplitude aperture, which produces a triangular lattice correlated with the topological charge of the vortex beam in the far-field plane,[14,15] we designed double-ring phase apertures to generate a concentric diffraction field. Based on the interference of the two diffraction fields, a sharp focus laser spot can be embedded into the middle of the spiral fringes.

Our experimental results have potential applications for micromanipulation: the measurements of torque, angle, and displacement of small objects such as enzymes link, protein binding, and DNA molecules require central trapping with rotation controls.[11,16] Verification of quantum entanglement needs the petal-like fringes containing a brighter reference point for the rotation angle identification, and twisted light transmission at long distances will need a concentric brighter beacon laser inside the encoded vortex beams to resolve the atmospheric turbulence problems.[17,18]

2 Principle

In this work, the experimental principle includes three main issues: the design of the double-ring phase-aperture, the diffraction theory for phase element, and the coherent combination between the vortex beam and Gaussian beam.[19–21]

2.1 Phase Only Transform

The double-ring phase-aperture is made of a transparent element which is divided into two parts: the inner circle zone of radius r_1 and the ring zone between r_1 and out radius r_2 , as shown in Fig. 1.

The double-ring phase-aperture is specially designed to realize three functions: (1) The element splits incident light at a designated ratio into two separate subbeams with phase difference. (2) The helical phase modulation profile, covered on the local zone, is able to generate a subbeam carrying OAM. (3) Diffraction patterns in the far-field are created by finite aperture diffraction. In the rest of this work, the double-ring phase-aperture element is frequently referred to as "phase aperture" for short.

The beam conversion process is shown in Fig. 1. In the far-field, the diffracted intensity distribution $I_p(x,y) = |E_p(x,y)|^2$. The diffracted electric field distributions $E_p(x,y)$ for the circular aperture (annular and polygon aperture) are expressed by Eqs. (S1)–(S4) in the Supplemental Material. Full details of the diffraction-interference calculation for vortex beams are given in the Supplemental Material.

2.2 Common-Path Interference Scheme

In our experiments, one zone of the double-ring phase-aperture element is covered with the helical phase modulated profile $\exp(il\theta)$ with the topological charge l and the azimuthal angle θ, and the other zone has a uniform phase profile.

When a plane wave beam passes through the double-ring phase apertures, the incident beam is split into high-order vortex beam A and zeroth-order vortex beam B. A simple and compact optical interference setup is shown in Fig. 1 and Fig. S1 in the Supplemental Material, in which the subbeam A and concentric subbeam B travel along essentially the same path.[20,22,23]

2.3 Interference between Two Diffraction Fields

The compound patterns, such as the Gaussian laser focus embedded with spiral petal-like fringes, are observed. We explain the physical reasons behind this result based on the theoretical model: (1) Both the vortex beam and the plane wave (or Gaussian laser) beam are converted into Fraunhofer diffraction fields through a finite aperture. (2) The coherent superposition of two diffraction fields generates interference fringes in the far-field.

Case I: The inner circle zone outputs a vortex beam, and the circular phase aperture generates the diffraction electric distribution $E_{\text{circular}}(x,y)$ in the far-field. The ring zone without phase modulation outputs a Gaussian beam. The annular phase aperture generates the diffraction electric field $E_{\text{annular}}(x,y)$ in the far-field, which creates the Poisson diffraction spot on the optic axis, as shown in Fig. S1(e) in the Supplemental Material.[4,24] In Fig. 1(a), when the coherent superposition between $E_{\text{circular}}(x,y)$ and $E_{\text{annular}}(x,y)$ occurs in the far-field, the resulting compound pattern is a spiral petal-like fringe with the brighter Poisson spot in the middle.

Case II: The circular inner zone outputs a Gaussian beam, which generates the diffraction electric distribution $E_{\text{circular}}(x,y)$ with a brighter spot on the optic axis, called an Airy spot

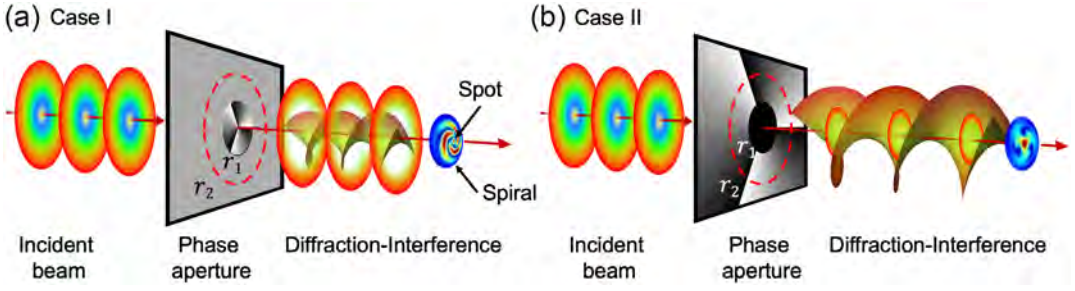

Fig. 1 Interference between diffracted vortex beam and diffracted plane wave beam through a phase aperture in common-path interferometry. (a) Case I: the inner circle zone ($\leq r_1$) is covered with the helical phase-modulated profile $\exp(il\theta)$ with the topological charge $l = 3$. The ring zone ($\geq r_1, \leq r_2$) is without phase modulation and outputs a Gaussian beam. (b) Case II: the circle zone ($\leq r_1$) is without phase modulation. The ring zone ($\geq r_1, \leq r_2$) is covered with the helical phase-modulated profile $\exp(il\theta)$ with the topological charge $l = 3$.

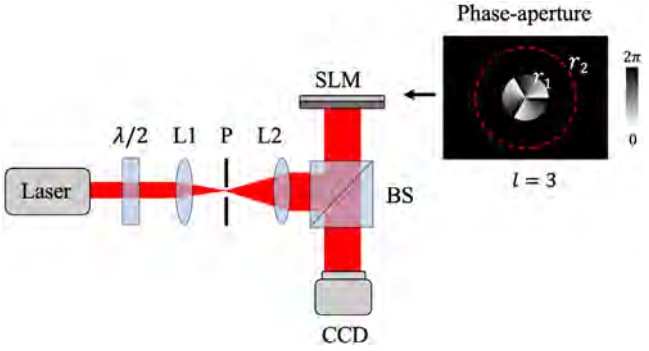

Fig. 2 Experimental setup of common-path interferometry with a phase aperture. $\lambda/2$, half-wavelength plate; L1, L2, lens; P, pinhole; BS, beam splitter; SLM, spatial light modulator; CCD, charge-coupled device. r_1 is the inner radius of the phase aperture, r_2 is the outer radius of the phase aperture indicated by red dashed line.

in Fig. S1(i) in the Supplemental Material. The ring zone outputs a vortex beam, which generates the diffraction electric field $E_{\text{annular}}(x, y)$ in the far-field. The coherent superposition between $E_{\text{circular}}(x, y)$ and $E_{\text{annular}}(x, y)$ results in a compound pattern in the far-field, which has propeller-like fringes with the brighter Airy spot in the middle in Fig. 1(b).[20,21,25]

A noticeable feature in our method is that a brighter Airy spot (Poisson spot) can automatically align with the center of the vortex beam all the time, which is attributed to the coherent combination of the vortex beam and the concentric Gaussian beam.

In this section, we analyze the theory and method for shaping the light optical wavefront by employing a transmissive spatial light modulator (SLM). The transmission-mode SLM is a necessary condition for realization of common-path interference in Fig. 1 and Fig. S1 in the Supplemental Material.

In following experimental study, we employ the reflection-mode SLM to demonstrate the diffraction-interference theory for vortex beams.

3 Experimental Setup

The experimental arrangement is shown in Fig. 2. The light beam from an He–Ne laser ($\lambda = 632.8$ nm) passes through a $\lambda/2$ plate that changes its polarization direction. The beam is then expanded by lenses L1 and L2 to fulfill the reflection area of the SLM (resolution, 1920×1080; effective area, 15.36 mm $\times$ 8.86 mm). A pinhole (P) is inserted to remove any other higher-order diffracted term. The incident light is redirected to illuminate the SLM vertically. The designed circular phase aperture is loaded onto the SLM. The modulated beam is recorded by a CCD camera, which is placed on the image plane.

4 Results

4.1 Beam Transformation through a Circular Phase Aperture in Common-Path Interferometry

To verify the feasibility of generating spiral petal-like fringes with a Gaussian focus in the middle, two experiments have been carried out. The experimental conditions correspond to Case I and Case II in Sec. 2.

In Experiment I, a transparent phase-aperture element is designed. The internal circle zone has an $\exp(il\theta)$-modulated phase profile of $l = 3$, and the ring zone has a uniform phase profile. The combination of the two profiles, which is loaded onto the SLM, is shown in Fig. 3(a).

The phase-modulated SLM produces a concentric beam in the Fresnel region: the inner is a vortex beam with a circular cross section, and the outer beam is a plane-wave beam with an annular cross section.

The interference between the diffraction fields of the vortex beam and the plane wave occurs in the far-field. Numerical calculations of the interference fringe are performed according to the theoretical model in Sec. 2 and Eqs. (A1)–(A4) in the Supplemental Material. The simulated intensity two-dimensional (2D)-distribution is shown in Fig. 3(b). A three-lobe spiral pattern with a brighter spot in the middle was observed in Fig. 3(c). The experimentally recorded interference fringe is in agreement with the numerical calculation result.

In Experiment II, a transparent phase-aperture element is designed. The internal circle zone has a uniform phase profile, and the ring zone has an $\exp(il\theta)$-modulated phase profile of $l = 3$. The combination of the two profiles is shown in Fig. 3(d). In the Fresnel region, the inner plane-wave beam has a circular cross section, and the outer vortex beam has an annular cross section. The diffraction–interference pattern is shown in Fig. 3(e) for the calculation result, and in Fig. 3(f) for the experimental result. We observed a three-arm propeller-like pattern with a strong light focus in the middle.

4.2 Beam Transformation through a Triangular Phase Aperture in Common-Path Interferometry

To verify the diffraction–interference effect of the triangular phase aperture, two experiments have been carried out.

In Experiment I, a transparent phase-aperture element is designed: the inner triangle zone has an $\exp(il\theta)$-modulated phase profile of $l = 3$, and the zone between the inner triangle and the outer ring has a uniform phase profile. The combination of two profiles, which is loaded onto the SLM, is shown in Fig. 4(a). The phase-modulated SLM produces a concentric beam in the Fresnel region: the inner is a vortex beam with a triangular cross section, and the outer is a dark hollow plane-wave beam. The interference between the diffraction fields of the vortex beam and the plane wave occurs in the far-field. The 2D distributions of the diffraction–interference pattern is numerically simulated; the result is shown in Fig. 4(b). The experimental result is shown in Fig. 4(c). A three-lobe spiral pattern with a brighter spot in the middle was observed.

In Experiment II, a transparent phase-aperture element is designed: the inner circle zone has a uniform phase profile, and the zone between the inner triangle and the outer ring has an $\exp(il\theta)$-modulated phase profile of $l = 3$. The combination of the two profiles is shown in Fig. 4(d).

In the Fresnel region, the inner plane-wave beam has a triangular cross section, and the outer beam is dark hollow vortex beam. Numerically simulated 2D distributions of the diffraction–interference pattern is shown in Fig. 4(e) and the experimentally recorded intensity distribution is shown in Fig. 4(f). A three-arm Y-shaped pattern with a brighter spot in the center of the interference fringe was observed.

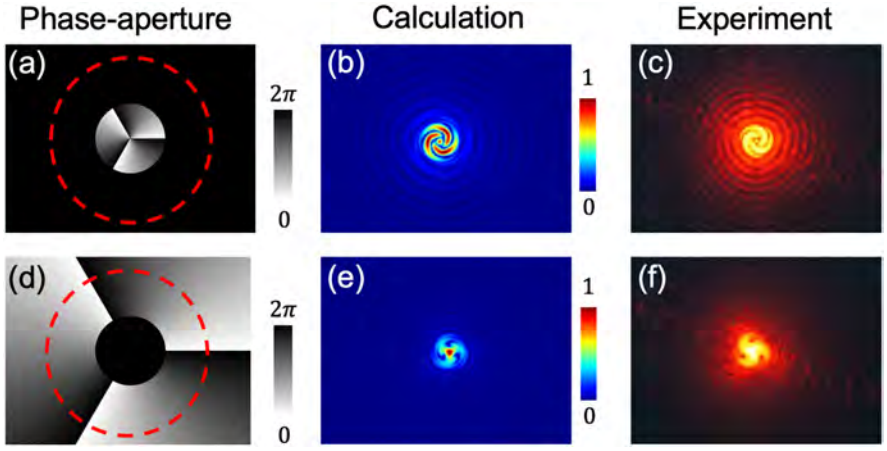

Fig. 3 (a) Circular phase-aperture element with a helical phase-modulated profile in the inner circle zone. (b) Numerically simulated light intensity distribution modulated by (a). (c) Experimentally recorded intensity distribution modulated by (a). (d) Circular phase-aperture element with a helical phase-modulated profile in the ring zone. (e) Numerically simulated light intensity distribution modulated by (d). (f) Experimentally recorded intensity distribution modulated by (d). The red dashed circle indicates the outer radius r_2 of the phase aperture.

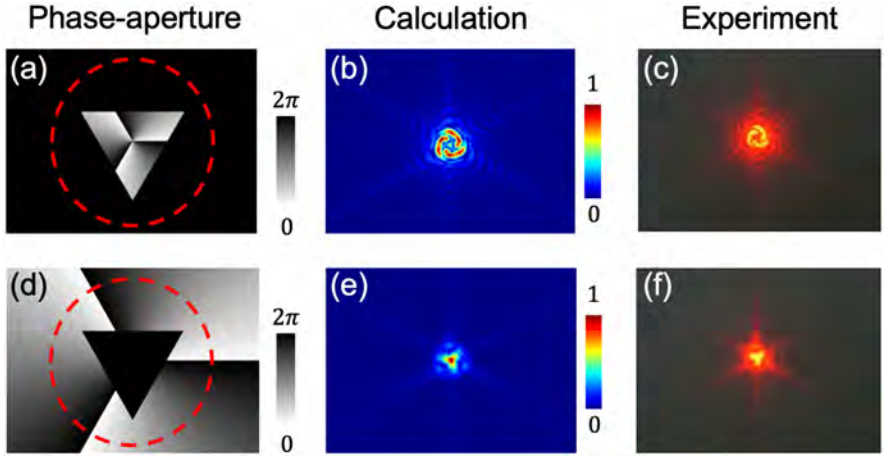

Fig. 4 (a) Triangular phase-aperture element with a helical phase-modulated profile in the inner zone. The inner equilateral triangle has the side length d. (b) Numerically simulated intensity distribution modulated by (a). (c) Experimentally recorded intensity distribution modulated by (a). (d) Circular phase-aperture element with a helical phase-modulated profile in the zone between the inner triangle and outer ring. (e) Numerically simulated intensity distribution modulated by (d). (f) Experimentally recorded intensity distribution modulated by (d). The red-dashed circle indicates the outer radius r_2 of the phase aperture.

4.3 Effect of Phase Aperture Size on the Diffraction–Interference Pattern

Next, we study the effect of the size of the phase aperture on the diffraction–interference pattern. The side length d of the triangular phase aperture is set to 100, 300, 600, and 900 pixels (the SLM width is 1080 pixels in our experiment). By adjusting the side length d, we observed the revolving of the diffraction–interference patterns from a Gaussian spot to a doughnut-shaped intensity pattern; results are shown in Fig. 5.

The effect of the size of the circular and rectangular phase apertures on the diffraction–interference pattern is plotted in Fig. S2 in the Supplemental Material.

4.4 Rotating the Diffraction–Interference Pattern

The orientation of diffraction–interference pattern is turned by the following methods.

In the first experiment, the helically modulated phase profile stays constant. Meanwhile, the direction of the triangular phase

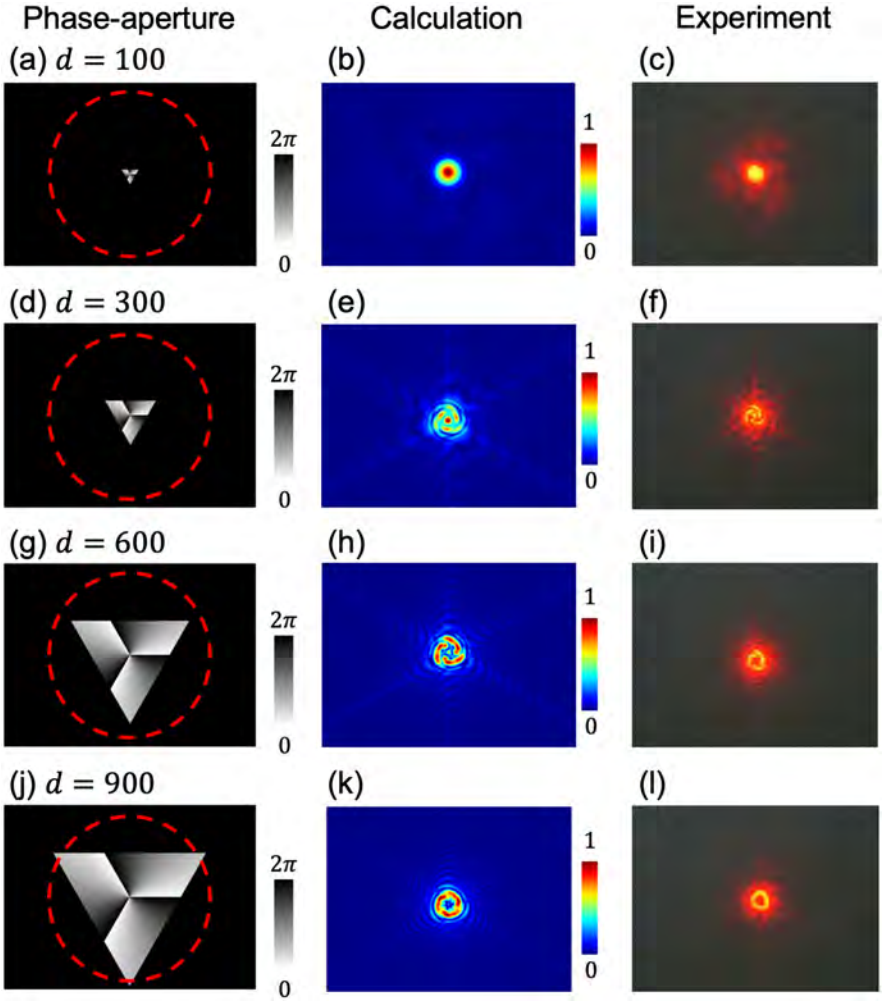

Fig. 5 (a), (d), (g), (j) Triangular phase-aperture element with a helical phase-modulated profile in the inner zone. The triangular phase aperture has a different side length, d. (b), (e), (h), (k) Numerically simulated intensity distribution and (c), (f), (i), (l) experimental intensity distribution in the far-field. The red dashed circle indicates the outer radius r_2 of the phase aperture.

aperture is rotated around the optical axis of the phase-aperture element, as shown in Figs. 6(a), 6(d), 6(g), and 6(j). The numerically simulated intensity 2D distribution and recorded intensity distribution demonstrated that the diffraction–interference pattern rotates in a clockwise direction. Results are shown in Fig. 6.

In the previous experiment, the phase shift in the outer zone of the phase aperture is set to 2π. In the following experiments, the phase shift of the outer area of the triangular phase aperture equals 0, as shown in Fig. 7(a). The interference fringe is shown in Fig. 7(b) for calculation and in Fig. 7(c) for the experiment. To test the effect of the phase shift on the orientation of the diffraction–interference pattern, the phase shift is set to π in the outer zone, represented by the gray area in Fig. 7(d). We found that the orientation of interference fringe tilted 60 deg. The calculation and experimental results are shown in Figs. 7(e) and 7(f), respectively.

4.5 *Effect of Phase Aperture Shape and Topological Charge on the Diffraction–Interference Pattern*

The relationship between the shape of the phase aperture and the topological charge l is studied. A phase aperture with an inner triangular zone containing $l = 4$ and $l = 8$ is loaded onto the SLM, as shown in Figs. 8(a1) and 8(b1). Spiral petal-like diffraction shapes with four and eight lobes were observed with asymmetric energy distribution; the results are shown in Figs. 8(a2) and 8(a3) and Figs. 8(b2) and 8(b3), and the Gaussian spot was not observed in the middle of the pattern. A phase aperture with an inner rectangular zone containing $l = 4, 8, 16$ is loaded onto the SLM separately. Spiral petal-like diffraction–interference patterns of 4, 8, and 16 lobes with a bright spot in the center were observed and are shown in Figs. 8(c), 8(d), and 8(e), respectively.

5 Discussion

5.1 *Integration of Optical Trapping Function and Controllable Rotation Function*

In optical Gaussian tweezers, a tightly focused Gaussian laser beam generates a trapping force that can capture and move small particles under a microscope.[26,27] In an optical tweezers employed vortex beam, micrometer particles can be rotated by the twisting force originating from OAM.[3,28,29]

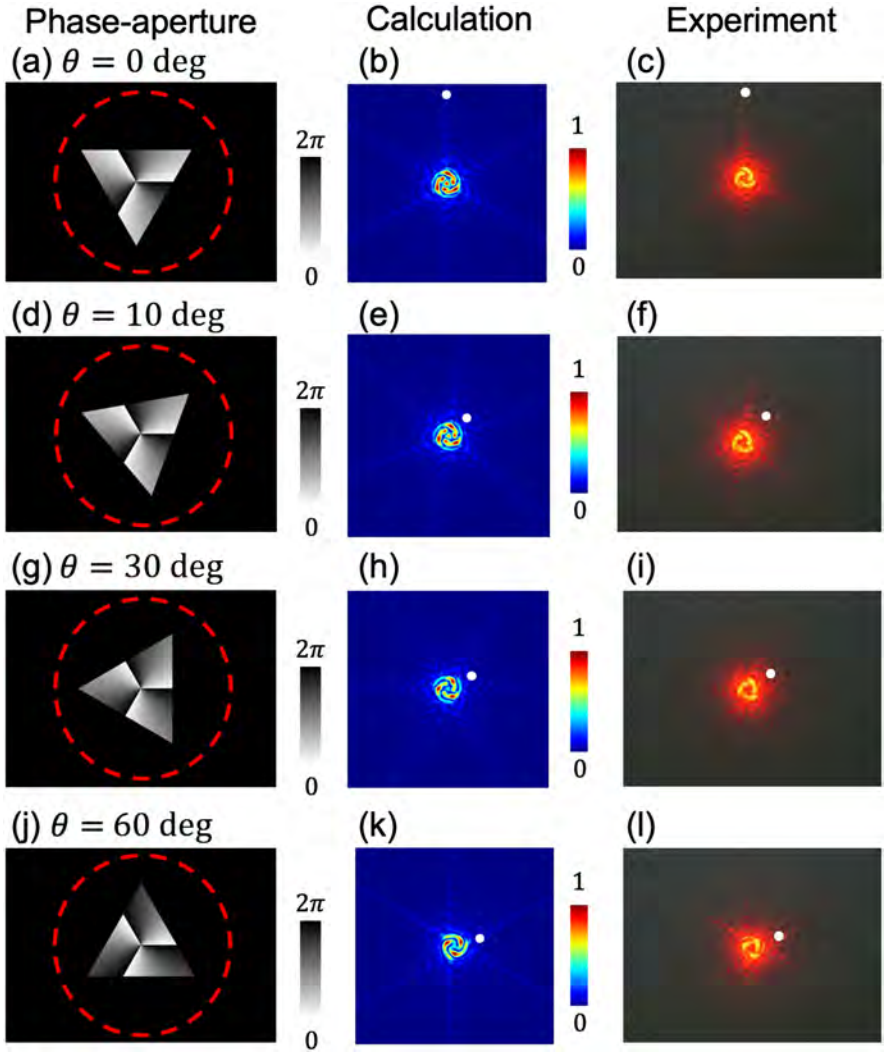

Fig. 6 (a), (d), (g), (j) Triangular phase-aperture element with a helical phase-modulated profile inside. The orientation of the triangular phase aperture tilts with different angle θ; the angle $\theta = 10$ deg, 30 deg, 60 deg. (b), (e), (h), (k) Numerically simulated intensity distribution and (c), (f), (i), (l) experimentally generated intensity pattern. *The white dots indicate the changed direction of the interference fringes. The red dashed circle indicates the outer radius r_2 of the phase aperture.

Owing to the different roles of optical Gaussian tweezers and optical vortex tweezers, each of them could not be replaced by another.[3,30] To investigate and control rotational motion of small particles, it is necessary to develop a compact device that combines an optical trapping function with a controllable rotation function.[30–32]

We demonstrated that our experimental setup is able to generate three kinds of light intensity distributions: a tightly focused spot, a spiral petal-like fringe, and a doughnut-shaped fringe, which stay at the same center line. The phase-only transform method in our work supports a concept of optical tweezers that integrates the optical Gaussian tweezers and optical vortex tweezers in a single optical system.

By adjusting the inner size of the phase aperture, the light intensity distributions gradually evolve from a tightly focused spot to a doughnut-shaped fringe, as shown in Fig. 5 and Fig. S2 in the Supplemental Material. The experimental results are in good agreement with the theoretical calculation results.

For the side length of a triangular phase aperture $d = 100$ pixel, the helical phase-modulated pattern occupies about 10% of the effective modulation area, and the intensity distribution at the far-field is closed to a Gaussian focal spot, as shown in Figs. 5(b) and 5(c). While the side length d increases, more light carries OAM information and a three-armed spiral fringe appears, as shown in Figs. 5(e) and 5(f) and Figs. 5(h) and 5(i). When $d = 900$ pixel, which occupies nearly 90% of the phase modulation area due to the dominant contribution of the vortex beam, the light intensity distribution is expanded to a doughnut-shaped pattern, as shown in Figs. 5(k) and 5(l).

To achieve symmetric energy distribution with a bright center, a triangular phase aperture with even topological charges

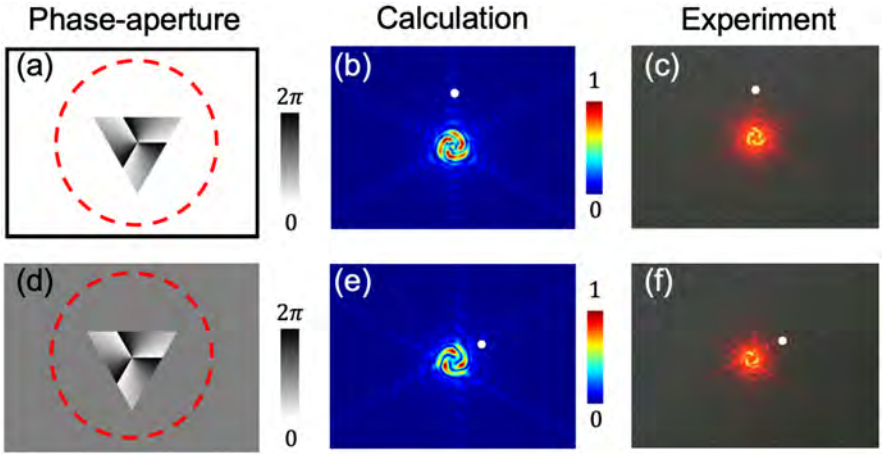

Fig. 7 (a) Triangular phase-aperture element with a helical phase-modulated profile inside. The outer zone of the phase aperture has 0 phase shift. (b) Numerically simulated intensity distribution. (c) Experimental recording. (d) The outer zone of the phase aperture has π phase shift. (e) Numerically simulated intensity distribution. (f) Experimental recording. The white dots indicate the changed direction of the interference fringes. The red dashed circle indicates the outer radius r_2 of the phase aperture.

or a rectangular phase aperture with odd topological charges is necessary.[14,15] When an even topological charges phase-modulated profile is loaded inside a triangular phase aperture, the interference fringe is asymmetric, and the central bright spot is either missing or weak, as shown in Figs. 8(a) and 8(b).[33] While the circular phase aperture generates symmetric energy distribution in every lobe, it is difficult to distinguish the rotation, which will be discussed in the following section.

5.2 Rotate the Orientation of Diffraction–Interference Pattern by Adjusting the Phase Aperture

This work studies two strategies to rotate the orientation of diffraction–interference pattern. First, we explore the possibility of controlling rotation by turning the orientation of the triangular phase aperture. As shown in Fig. 6, the orientation of the triangular phase aperture is rotated by steps, with the orientation of the diffraction–interference pattern rotated accordingly.

The existing method rotates the orientation of the pattern by changing the optical path.[3,16] By comparison, our approach realized concentric rotation of the diffraction–interference pattern of the optical vortex by adjusting the geometric variable only.[3,16]

Second, we show that the phase shift of a triangular phase aperture affects the orientation of the diffraction-interference pattern. By comparison, the phase shift of 0 [Figs. 4(b) and 4(c)] and 2π [Figs. 7(b) and 7(c)] generates exactly same light intensity distributions. However, the phase shift π rotates the direction of the diffraction-interference pattern around the optic axis in Figs. 7(e) and 7(f). A φ phase change in the wavefront will cause the diffraction–interference pattern to rotate by φ/l, which is 60 deg in Figs. 7(e) and 7(f). The effect is similar to a Guoy phase shift observed in a Mach–Zehnder interferometer (MZI).[1,16,34]

5.3 Potential Application in Optical Communication

To compensate for small perturbations in optical communication, a vortex beam carrying encoded OAM has been transformed into a 3×3 grid with $l = 0$ component in the center as the measurement.[35] We demonstrates optical transmission with a topological charge values $l = 4, 8, 16$ using a rectangular phase aperture, which automatically embedded the diffraction fringe with a Gaussian spot for reference in Figs. 8(c)–8(e).

Long-distance twisted light transmission experiments have been realized, and the transmission quality of the OAM modes was primarily reduced due to atmospheric turbulence near the sender.[17,18] The literature[18] proposed employing a second laser beam to create a guide star.[18] Our method is able to generate a Gaussian spot that can be used as the beacon laser with OAM-encoded information simultaneously in a simple optical setting.

5.4 Comparison between Optical Conversion Methods

Both computer-generated holograms and conventional MZIs are able to generate spiral petal-like patterns, which are similar to the patterns reported in this work.[3,8,9,34] A holographic system is able to generate arbitrary patterns, but the zero-order diffracted beam is not used, which inevitably wastes incident optical power. Meanwhile, the holographic optical elements need to be carefully aligned due to the shortcomings of the off-axis optical system, making it unfeasible in long-time stable optical trapping.[8,9]

The MZI is the most common way to modulate intensity patterns of an optical vortex field. However, misalignment during interference may cause unsatisfactory interference fringes. And 50:50 splitting incident beam decreases its light conversion efficiency.[3,20,21,34]

In terms of fulfilling the special requirement, such as new concepts of optical tweezers and laser beacon in turbulent air (or as a reference point for OAM-coded pattern recognition), the common-path interferometer with a double ring phase aperture has advantages in various applications. For instance, it can work in a vibrating or noisy environment with relatively simple and compact optical setups. The transmissive phase-only element has high conversion efficiency. The double ring phase-aperture

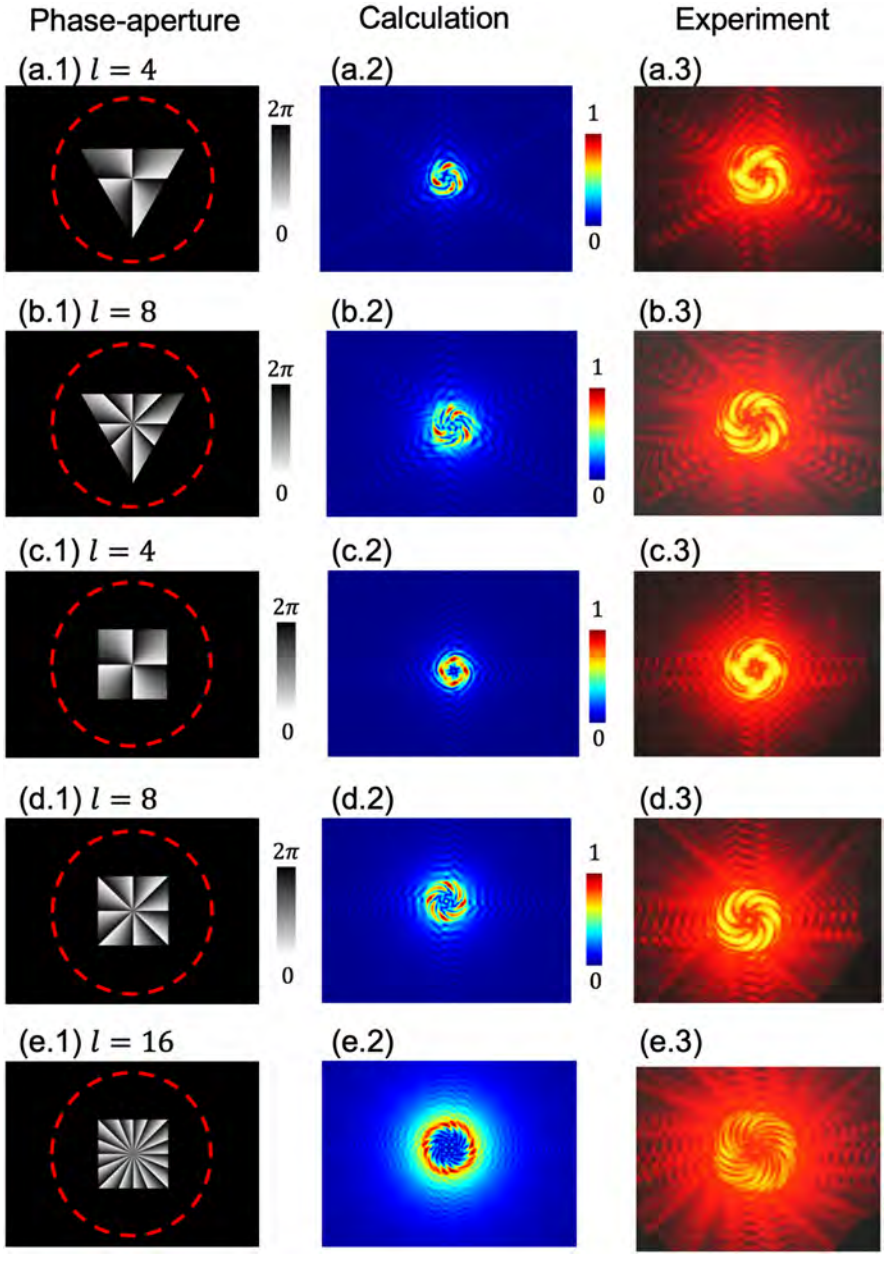

Fig. 8 (a), (b) Triangular phase aperture with a helical phase-modulated profile inside ($l = 4$ and $l = 8$). (c)–(e) Rectangular phase aperture with a helical phase-modulated profile inside ($l = 4, 8, 16$). The red dashed circle indicates the outer radius r_2 of the phase aperture. The first column illustrates the phase modulation profile; the second column shows the calculated light intensity distribution, and the third column shows the experimental results.

element produces concentric beams, which allow dynamical parameter adjustment of optical vortex fringes along the same axis; details are given in Sec. 4.[36–38]

6 Conclusion

This work proposes a phase-only method for transforming an optical vortex field into a desired spiral interference fringe. By employing double ring phase-aperture elements to realize common-path interference, a brighter spot is embedded with the optical vortex fringe. The embedded spot is located the singularity of the typical vortex beam is. In theory, this type of brighter spot originates from an Airy spot (or Poisson spot) due to the zeroth-order vortex beam diffracted at the phase aperture. A noticeable feature is that the brighter spot is automatically aligned with the central axis of the vortex beam because it is attributed to the coherent combination of vortex beam and concentric Gaussian beam. The theoretical calculated patterns are in excellent agreement with diffraction–interference fringes in experiment. Our experimental setup offers a method to implement optical tweezers that can trap and twist a particle (or biological sample) spatially and angularly. By controlling the phase

shift and the size of the circular or polygonal phase aperture, the intensity distributions in the far field are able to evolve from a doughnut shape to a Gaussian focus, and the orientation of the diffraction–interference pattern can be rotated and controlled.

Acknowledgments

This work was supported by the National Natural Science Foundation of China (Grant Nos. T2293753 and T2293750) and the Major Science and Technology Project in Hainan Province of China (Grant No. ZDKJ2019012).

References

1. M. Padgett and R. Bowman, "Tweezers with a twist," *Nat. Photonics* **5**, 343–348 (2011).
2. L. Allen et al., "Orbital angular momentum of light and the transformation of Laguerre-Gaussian laser modes," *Phys. Rev. A* **45**, 8185–8189 (1992).
3. L. Paterson et al., "Controlled rotation of optically trapped microscopic particles," *Science* **292**, 912–914 (2001).
4. O. Emile et al., "Dark zone in the centre of the Arago-Poisson diffraction spot of a helical laser beam," *Europhys. Lett.* **101**, 54005 (2013).
5. J. Qi et al., "Continuously adjustable cylindrical vector and vortex beams by programming vortex half-wave plates and detection based on coaxial or small-angle interference," *Phys. Rev. Appl.* **18**, 034086 (2022).
6. C. Li et al., "Analytical description of sub-diffraction dark spot," *Opt. Commun.* **499**, 127295 (2021).
7. X. Liu et al., "Coaxial multi-ring optical vortex generation based on compound spiral phase plates," *Laser Phys.* **32**, 035402 (2022).
8. J. E. Curtis, B. A. Koss, and D. G. Grier, "Dynamic holographic optical tweezers," *Opt. Commun.* **207**, 169–175 (2002).
9. J. E. Curtis and D. G. Grier, "Modulated optical vortices," *Opt. Lett.* **28**, 872–874 (2003).
10. M. Piccardo and A. Ambrosio, "Arbitrary polarization conversion for pure vortex generation with a single metasurface," *Nanophotonics* **10**, 727–732 (2020).
11. T. Li et al., "Multidimensional light field manipulation and applications based on optical metasurface," *Proc. SPIE* **11850**, 1185004 (2021).
12. D. J. Lee and A. M. Weiner, "Optical phase imaging using a synthetic aperture phase retrieval technique," *Opt. Express* **22**, 9380–9394 (2014).
13. W. Chi and N. George, "Phase-coded aperture for optical imaging," *Opt. Commun.* **282**, 2110–2117 (2009).
14. J. M. Hickmann et al., "Unveiling a truncated optical lattice associated with a triangular aperture using light's orbital angular momentum," *Phys. Rev. Lett.* **105**, 053904 (2010).
15. L. E. de Araujo and M. E. Anderson, "Measuring vortex charge with a triangular aperture," *Opt. Lett.* **36**, 787–789 (2011).
16. M. P. MacDonald et al., "Revolving interference patterns for the rotation of optically trapped particles," *Opt. Commun.* **201**, 21–28 (2002).
17. M. Krenn et al., "Communication with spatially modulated light through turbulent air across Vienna," *New J. Phys.* **16**, 113028 (2014).
18. M. Krenn et al., "Twisted light transmission over 143 km," *Proc. Natl. Acad. Sci. U. S. A.* **113**, 13648–13653 (2016).
19. F. Kenny et al., "Adaptive optimisation of a generalised phase contrast beam shaping system," *Opt. Commun.* **342**, 109–114 (2015).
20. J. Glückstad and P. C. Mogensen, "Optimal phase contrast in common-path interferometry," *Appl. Opt.* **40**, 268–282 (2001).
21. A. Ustinov et al., "Focal-plane field when lighting double-ring phase elements," *Comput. Opt.* **41**, 515–520 (2017).
22. A. Bañas and J. Glückstad, "Light shaping with holography, GPC and holo-GPC," *Opt. Data Process. Storage* **3**, 20–40 (2017).
23. D. Palima and J. Glückstad, "Generalised phase contrast: microscopy, manipulation and more," *Contemp. Phys.* **51**, 249–265 (2010).
24. P. Fischer et al., "The dark spots of Arago," *Opt. Express* **15**, 11860–11873 (2007).
25. C. Jun, K. Deng-Feng, and F. Zhi-Liang, "Properties of Fraunhofer diffraction by an annular spiral phase plate for sidelobe suppression," *Chin. Phys. Lett.* **26**, 094210 (2009).
26. A. Ashkin, J. M. Dziedzic, and T. Yamane, "Optical trapping and manipulation of single cells using infrared laser beams," *Nature* **330**, 769–771 (1987).
27. A. Ashkin and J. M. Dziedzic, "Optical trapping and manipulation of viruses and bacteria," *Science* **235**, 1517–1520 (1987).
28. V. Shahabadi and E. Madadi, "Effective multiple optical trapping of sub-micrometer particles with petal beams," *J. Opt. Soc. Am. B* **37**, 3665 (2020).
29. S. P. Kotova et al., "Manipulation of microscopic objects with two-lobe light fields," *Bull. Lebedev Phys. Inst.* **49**, 362–365 (2022).
30. F. Pedaci et al., "Excitable particles in an optical torque wrench," *Nat. Phys.* **7**, 259–264 (2011).
31. A. La Porta and M. D. Wang, "Optical torque wrench: angular trapping, rotation, and torque detection of quartz microparticles," *Phys. Rev. Lett.* **92**, 190801 (2004).
32. C. Deufel et al., "Nanofabricated quartz cylinders for angular trapping: DNA supercoiling torque detection," *Nat. Methods* **4**, 223–225 (2007).
33. A. Ambuj et al., "Symmetry in the diffraction of beams carrying orbital angular momentum," *Phys. Rev. A* **99**, 013846 (2019).
34. H. Huang et al., "Phase-shift interference-based wavefront characterization for orbital angular momentum modes," *Opt. Lett.* **38**, 2348–2350 (2013).
35. G. Gibson et al., "Free-space information transfer using light beams carrying orbital angular momentum," *Opt. Express* **12**, 5448–5456 (2004).
36. S. W. Hell and J. Wichmann, "Breaking the diffraction resolution limit by stimulated emission: stimulated-emission-depletion fluorescence microscopy," *Opt. Lett.* **19**, 780–782 (1994).
37. G. Vicidomini, P. Bianchini, and A. Diaspro, "STED super-resolved microscopy," *Nat. Methods* **15**, 173–182 (2018).
38. M. J. Villangca et al., "Dark GPC: extended nodal beam areas from binary-only phase," *Opt. Eng.* **55**, 125102 (2016).
39. A. Ambuj, R. Vyas, and S. Singh, "Diffraction of orbital angular momentum carrying optical beams by a circular aperture," *Opt. Lett.* **39**, 5475 (2014).
40. R. Vasilyeu et al., "Generating superpositions of higher-order Bessel beams," *Opt. Express* **17**, 23389–23395 (2009).

Yizhou Tan is an assistant researcher at Chinese PLA General Hospital. He received his BS and MS degrees from the National University of Defense Technology in 2011 and 2013, respectively, and his PhD in physics from Cavendish Laboratory, Cambridge University, in 2018. His current research focuses on laser medicine and its clinical application.

Ying Gu: Biography is not available.

Research Article

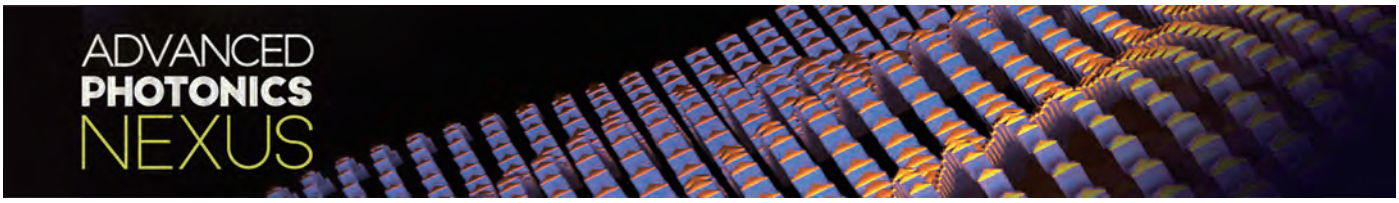

Multiparameter encrypted orbital angular momentum multiplexed holography based on multiramp helicoconical beams

Nian Zhang,[a,b,c,d] Baoxing Xiong,[a,b,c,d] Xiang Zhang,[a,b,c,d] and Xiao Yuan[a,b,c,d,*]
[a]Soochow University, School of Optoelectronic Science and Engineering, Suzhou, China
[b]Soochow University, Collaborative Innovation Center of Suzhou Nano Science and Technology, Suzhou, China
[c]Soochow University, Key Lab of Advanced Optical Manufacturing Technologies of Jiangsu Province, Suzhou, China
[d]Soochow University, Key Lab of Modern Optical Technologies of Education Ministry of China, Suzhou, China

Abstract. Optical orbital angular momentum (OAM) multiplexed holography has been implemented as an effective method for information encryption and storage. Multiramp helicoconical-OAM multiplexed holography is proposed and experimentally implemented. The mode selectivity of the multiramp mixed screw-edge dislocations, constant parameter K, and normalized factor are investigated, respectively, which demonstrates that those parameters can be used as additional coding degrees of freedom for holographic multiplexing. The combination of the topological charge and the other three parameters can provide a four-dimensional multiplexed holography and can enhance information capacity.

Keywords: orbital angular momentum multiplexed holography; multiramp helicoconical beams; multiple-dimensional multiplexing; information encryption.

Received Feb. 22, 2023; revised manuscript received Mar. 29, 2023; accepted for publication May 5, 2023; published online Jun. 5, 2023.

[DOI: 10.1117/1.APN.2.3.036013]

1 Introduction

Optical holography is one of the promising technologies for information encryption and storage.[1] In traditional holography, the different physical dimensions of light, such as phase, polarization, and wavelength, have been implemented for multiplexing multiple data in a single multiplexed hologram to improve the capability of security encryption.[2–5] However, the multiplexing capability is still limited, and the decoding process is complicated. The orbital angular momentum (OAM) carried by the vortex beam has been investigated due to its unique spiral phase structure and physically unconstrained orthogonal mode, which is an approach to enhancing classical and quantum communications.[6–8] OAM is represented as a spiral phase $\exp(il\varphi)$, where l and φ are the topological charge (TC) and the azimuthal angle, respectively.[9] In the past three decades, different types of OAM beams, such as the Airy vortex beam, the Bessel vortex beam, and Pearcy vortex beam, have had vast applications in optical tweezers, optical images, and so on.[10–12] In addition, the OAM can be used as an additional degree of freedom to improve the information capacity due to the orthogonality of OAM modes.[13,14]

Recently, OAM multiplexed holography has been demonstrated and experimentally implemented as an independent information channel that can preserve the OAM property and achieve the OAM selectivity in the reconstructed images.[15–17] After that, different OAM holography has been developed rapidly. The polarization-encrypted OAM holography was implemented based on a birefringent metasurface, which can obtain the reconstruction information in both TC and polarization channels.[18] The ultradense perfect OAM multiplexed holography with integer and fractional TCs was investigated, which can achieve two-dimensional spatial division multiplexing in both radial and angular dimensions.[19] Partial OAM holography was proposed in the angular space by dividing an integer OAM mode into several partial phase modes, which can enhance information capacity.[20] The modulated OAM holography was investigated based on the cosine-modulated OAM beams.[21] The multiple-image and multiple-dimensional encrypted OAM multiplexed holography based on the OAM beam with phase

*Address all correspondence to Xiao Yuan, xyuan@suda.edu.cn

jump factor and the modulated chiro-optical beams were implemented.[22,23] By introducing the multiple parameters into the OAM holography, a four-dimensional spatial multiplexing can be achieved. In the ellipticity-encrypted OAM holography, the multiple images can be encoded into the ellipticity channel.[24] However, the encoded information capacity is still limited. The additional degree of freedom is needed to improve information security and capacity. A new kind of vortex beam has been studied, namely, the helicoconical beam (HCB), which has both helical and conical phases.[25–27] Note that the HCBs have the additional conical phase modulation compared to the conventional OAM beam, which can provide a new way to boost information capacity. In addition, the multiramp helical-conical (MHC) beam was proposed by Wen et al.[28] and its focusing properties were investigated. However, to the best of our knowledge, the MHC beams have not been implemented to enhance the holographic information capacity. We find that the phase modulated by the conical parameter and the number of multiramp mixed screw-edge dislocations of the MHC beam also have similar holographic preservation and selectivity like the helical phase. In holography, the use of an MHC beam not only increases the degree of coding freedom, but also improves the security of the information.

In this work, multiramp helical-conical orbital angular momentum (MHC-OAM) multiplexed holography is proposed and implemented. The four parameters of the MHC beam can be independently modulated, namely, TC, the number of multiramp mixed screw-edge dislocations m, the constant K, and the normalized factor r_0. The MHC-OAM mode selectivity has been investigated based on the number of multiramp mixed screw-edge dislocations m, the constant K, and the normalized factor r_0. According to these parameters, the multidimensional multiplexed holography can be obtained. The feasibility of the MHC-OAM multiplexed holography in different dimensions is verified in experiments. This method shows the huge application possibilities in information encryption and storage.

2 Principle and Methods

2.1 Principle of MHC-OAM Multiplexed Holography

The phase function of the MHC beams is written as[28]

$$E(x,y)=\exp\left[i\alpha\left(\frac{\sqrt{x^2+y^2}}{r_0}-K\right)\left(\theta-\frac{2\pi n}{m}\right)\right], \tag{1}$$

where (x,y) represents the Cartesian coordinates in the holographic plane, α is the TC of the MHC beams, and $\theta=\tan^{-1}(y/x)$ is the azimuthal angle. m represents the number of multiramp mixed screw-edge dislocations, which is an integer. Here $n=[m\theta/(2\pi)]$ and $[\cdot]$ denotes the floor function. K is a constant that takes the values of 1 or 0, and r_0 represents the normalized factor of the radial coordinate $r^2=x^2+y^2$.

The spatial frequency distribution of the MHC beams based on the Fourier integral theorem is expressed as[29]

$$E_1(X,Y)=\frac{k}{i2\pi f}\iint_{-\infty}^{+\infty}E(x,y)\exp\left(-i\frac{k}{f}(Xx+Yy)\right)\mathrm{d}x\,\mathrm{d}y, \tag{2}$$

where (X,Y) indicates the Cartesian coordinates in the image plane, $k=2\pi/\lambda$ is the wavenumber, λ is the wavelength, and f is the focal length. Figures 1(a1)–1(a3) show the phase distribution with $\alpha=6$ and $r_0=1$ mm, and different values of K and m. The simulation of the spatial frequency distribution of the MHC beam is shown in Figs. 1(b1)–1(b3). When $m=1$, it is a traditional HCB, as shown in Figs. 1(a1) and 1(b1). However, when $m=3$, the phase distribution of the MHC beam is divided into three parts, as shown in Figs. 1(a2) and 1(a3), and each part can be used to generate HCBs [Figs. 1(b2) and 1(b3)]. Notice that the distance between the three subbeams will get closer because $K=1$. It can be explained that for $K=1$, the phase in Eq. (1) introduces an azimuthally varying phase shift, resulting in a beam with a greater degree of spiral, which is not present in $K=0$.

In a computer-generated hologram (CGH), a Fourier pair is formed between the electric field of the image plane and holographic plane, so the electric field of the reconstructed image is[16]

$$\begin{aligned}E^{\mathrm{OAM}}(X,Y)&=\Im[E_h^{\mathrm{OAM}}(x,y)]=\Im[E_h(x,y)\cdot E^{\mathrm{OAM}}(x,y)]\\&=\Im[E_h(x,y)]*\Im[E^{\mathrm{OAM}}(x,y)],\end{aligned} \tag{3}$$

where $E_h(\cdot)$ and $E^{\mathrm{OAM}}(\cdot)$ are the complex amplitudes of the hologram and the MHC beam, respectively. The operators $\Im$ and * are the Fourier transform and convolution, respectively. If the sampling array of the target image is correlated with the spatial frequency of the MHC-OAM beam, the OAM properties will be preserved in the reconstructed image. Therefore, the sampling constant d of sampling array is a key issue. The sampling constant as a function of TC is shown in Fig. 1(c). It can be seen that the constant d increases linearly with the increase of TC, and the larger value of m is, the smaller the value of d under the same TC is. Note that the sampling constant d is also related to the normalized factor r_0 (Note S1 and Fig. S1 in the Supplementary Material).

The design principle of the MHC-OAM holography is shown in Fig. 1(d). According to the adaptive weighted Gerchberg–Saxton (AWGS) algorithm, an OAM-preserved hologram is obtained, as depicted in the middle part of Fig. 1(d). Notice that the MHC beam is preserved in each pixel of the reconstructed image. From the right part in Fig. 1(d), the phase function $\phi(\alpha,m,K,r_0)$ of an MHC beam is superimposed into the OAM-preserved hologram, resulting in the generation of an OAM-selective hologram. Due to OAM conservation, the Gaussian spots with a stronger intensity distribution in the desired holographic image are obtained only for a given incident MHC phase mode with $\phi(-\alpha,m,K,r_0)$. Finally, the multiplexed hologram can be obtained from the superposition of multiple selective holograms.

2.2 MHC-OAM Mode Selectivity

The mode selectivity of MHC beams with the constant K, the number of multiramp mixed screw-edge dislocations m, and the normalized factor r_0 in image reconstruction are illustrated in Fig. 2. The encoded phase parameters of the hologram are fixed as $\alpha=6$, $m=3$, $K=0$, and $r_0=1$ mm. First, we demonstrate the MHC mode selectivity under the constant K, as shown in Fig. 2(a). When the decoded phase mode with $\alpha=-6$, $m=3$, $K=0$, $r_0=1$ mm illuminates the hologram, the Gaussian spot with stronger intensity is obtained. However, the reconstructed light field with lower intensity is formed when the incident decoded MHC beam with $K=1$, which can be regarded as

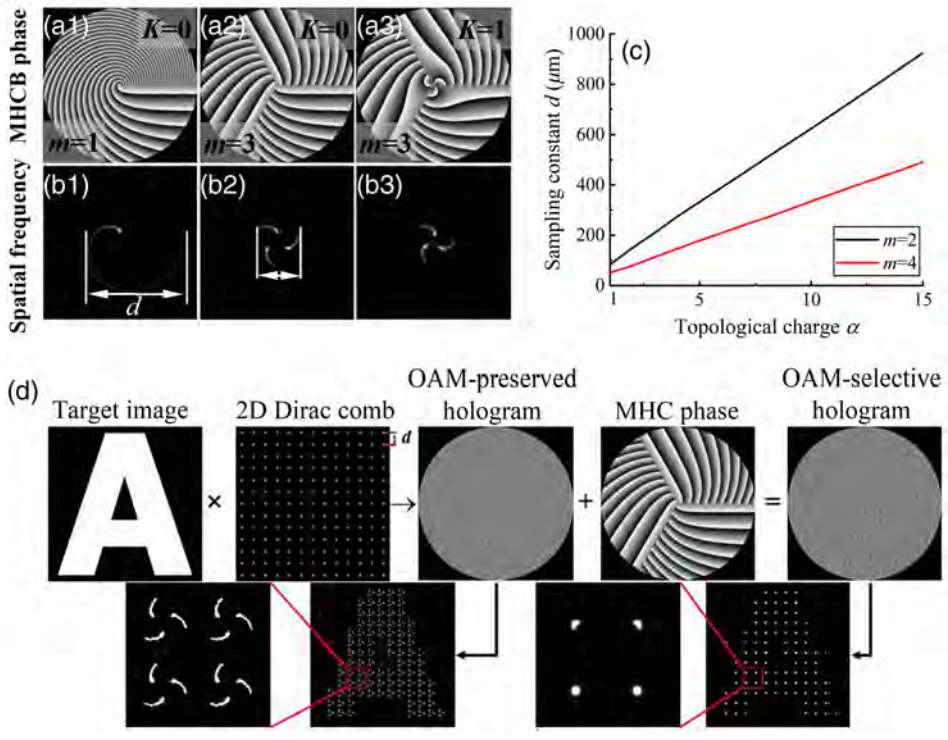

Fig. 1 (a1)–(a3) Phase distributions of the MHC beams. (b1)–(b3) Simulation of the spatial frequency distributions of the MHC beams. (c) Relationship between the TC and sampling constant d. (d) Principle of the MHC-OAM holography.

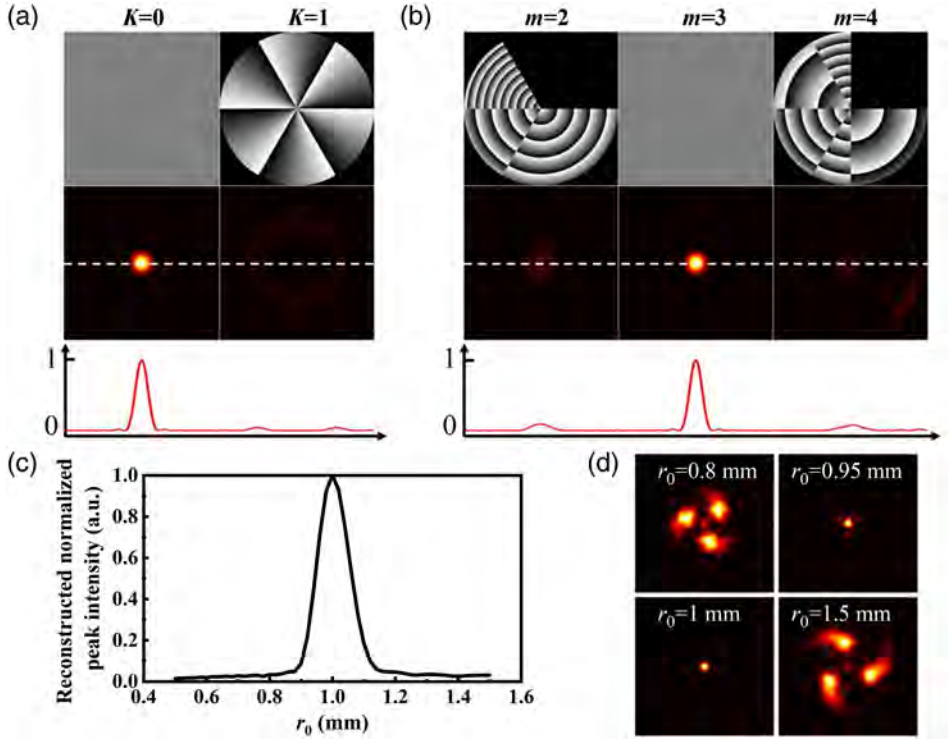

Fig. 2 MHC-OAM mode selectivity. (a) Mode selectivity of the constant K. (b) Mode selectivity of the multiramp mixed screw-edge dislocations. (c) Relationship between the reconstructed normalized peak intensity and normalized factor r_0. (d) Interference field distribution of the encoded MHC beam with $r_0 = 1$ mm and decoded MHC beams with $r_0 = 0.8$ mm, $r_0 = 0.95$ mm, $r_0 = 1$ mm, and $r_0 = 1.5$ mm, respectively.

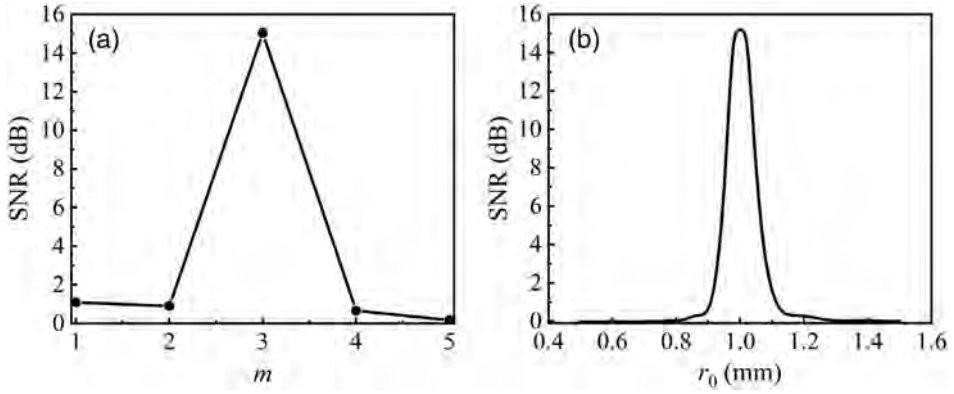

Fig. 3 (a) SNR as a function of the number of multiramp mixed screw-edge dislocations. (b) SNR as a function of the normalized factor.

background intensity and ignored. Figure 2(b) shows the effect of the number of multiramp mixed screw-edge dislocations m on the mode selectivity. Similarly, when the hologram is illuminated by the decoded phase mode with $\phi(-6, 3, 0, 1\ \text{mm})$, the desired Gaussian spot is obtained. Otherwise, the peak intensity of the mode with $m = 2$ or 4 is lower than that of the mode with $m = 3$. The relationship between the reconstructed peak intensity and the normalized factor is shown in Fig. 2(c). It can be seen that the peak intensity is influenced by the decoded phase with different normalized factors r_0. If the difference between decoding $r_{0\text{-de}}$ and encoding $r_{0\text{-encod}}$ is more than 0.1 mm, the reconstructed peak intensity can be neglected. In this case, the multiplexing interval of r_0 can be set to $\Delta r_0 \geq 0.1$ mm. The reconstructed intensity distributions with different r_0 are shown in Fig. 2(d).

In order to select the appropriate parameters m and r_0 for the multiplexed holograms and to ensure that the multiplexed results have a good signal-to-noise ratio (SNR), the corresponding OAM-selective holograms are designed using OAM selectivity. The effect of the number of multiramp mixed screw-edge dislocations m on the SNR is shown in Fig. 3(a). The MHC phase with $m_{\text{encode}} = 3$ is superposed on the MHC-OAM-preserved hologram, resulting in the generation of an MHC-OAM-selective hologram, and $m_{\text{decode}} = 1, 2, 3, 4, 5$ are the decoding phase parameters of incident MHC beams. When the incident MHC beam with parameter $m_{\text{decode}} = 3$ illuminates the hologram, we can decode the target image with a relatively high SNR, as the parameter m_{decode} of the incident MHC beam can match better with the design value of m_{encode}. On the contrary, we get the reconstructed image with poor SNR, and the reconstructed image will be hidden. Under the promise of obtaining a high SNR, the difference of m in holographic multiplexing can be chosen as 1. The SNR as a continuous function of the decoded normalized factor is depicted in Fig. 3(b). When the decoded normalized factor is close to the encoded normalized factor, the reconstructed result with a relatively high SNR is obtained. Under the promise of a high SNR, the difference between the normalized factors of the encoded and the decoded MHC phase modes is required to exceed 0.1 mm.

3 Results and Discussion

The schematic diagram of the experimental setup of MHC-OAM holography is shown in Fig. 4. An He–Ne laser

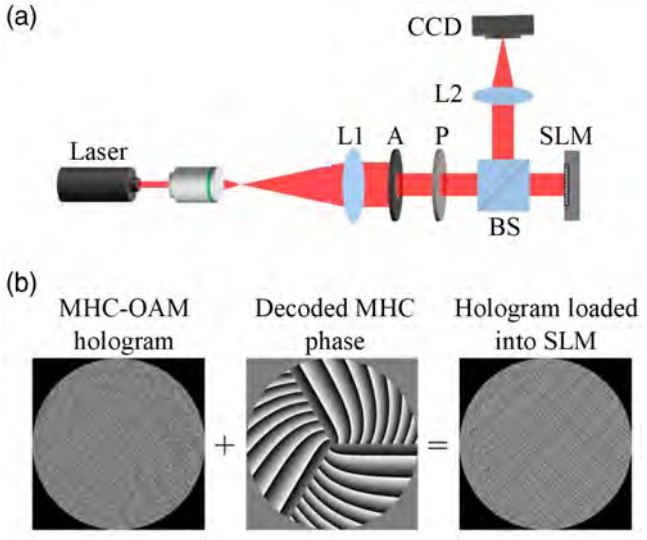

Fig. 4 (a) Schematic diagram of the experimental setup of MHC-OAM holography. L1 and L2, lens; A, aperture; P, polarizer; BS, beam splitter; and SLM, spatial light modulator. (b) The hologram loaded into the SLM contains the decoded phase and OAM hologram.

(Research Electro-Optics, R-31007) with a wavelength of 633 nm and a power of 0.8 mW is used as the light source. The laser beam is expanded and collimated by a 20× objective and a lens L1 with a focal length of 400 mm. An aperture is used to adjust the size of the incident beam matching the phase-only spatial light modulator (SLM, Hamamatsu-X13138 series-07, 1272 pixels × 1024 pixels, pixel pitch of 12.5 μm). Since the SLM is only sensitive to the horizontal polarized component of the incident beam, a polarizer is inserted between the aperture and the SLM to generate a horizontal polarized beam. The beam is modulated by the SLM and passes through a lens L2 with the focal length of 100 mm to a CCD (GS3-PGE-91S6M-C, 3376 pixels × 2704 pixels, pixel pitch of 3.69 μm) used to capture the reconstructed holographic image. In this work, the experimental system is simplified, since we have only one SLM. The hologram pattern is not directly illuminated by an MHC beam. Alternatively, the decoded MHC phase distribution is

superimposed into the hologram, which is illuminated by a planar beam, as shown in Fig. 4(a). In the decrypted process, the hologram used is represented as the superposition of the decoded MHC phase and the MHC-OAM hologram, so the mathematical phase-only hologram can be described as

$$P = \arg\left[\sum_{i=1}^{N} \exp(i\phi_i)\exp(i\psi_{i\text{-de}})\right], \tag{4}$$

where ϕ_i, $\psi_{i\text{-de}}$, and N represent the phase information of each image channel, the decoded MHC phase distribution, and the number of multiplexing channels, respectively. The design principle of the hologram loaded into the SLM is shown in Fig. 4(b).

3.1 *m*- or r_0-Encrypted MHC-OAM Multiplexed Holography

According to the results in Sec. 2, the number of multiramp mixed screw-edge dislocations m and the normalized factor r_0 can be used as independent channels for multiplexed holography. The MHC-OAM multiplexed holography with m- and r_0-encryption is implemented in the experiment. Figure 5 shows the schematic diagram of the m-encrypted MHC-OAM multiplexed holography. The four Arabic numbers "1," "2," "3," and "4" are set as target images and encoded into four OAM preserved holograms using the AWGS algorithm, respectively. Then the four MHC phase modes with the TC of 8, the constant $K = 0$, the normalized factor of 1 mm, and the number of multiramp mixed screw-edge dislocations of 4, 5, 6, and 7 are superimposed into the OAM-preserved hologram, leading to the four OAM selective holograms, respectively. These four OAM selective holograms can be superimposed into one OAM-multiplexed hologram, as shown in Fig. 5(a). The feasibility of the m-multiplexed holography is numerically simulated (Note S2 and Fig. S2 in the Supplementary Material). The experimental results are shown in Figs. 5(b)–5(e). When the MHC-OAM multiplexed hologram with the key m is illuminated by the different incident MHC beams with $\phi(-8, 4, 0, 1\text{ mm})$, $\phi(-8, 5, 0, 1\text{ mm})$, $\phi(-8, 6, 0, 1\text{ mm})$, and $\phi(-8, 7, 0, 1\text{ mm})$, four distinct images are reconstructed, respectively. The pixel intensity fluctuations in the reconstructed images may originate from three factors: inadequate phase modulation of the SLM, the uniformity of the incident beam, and nonuniform photon sensitivity of the pixelated CCD camera. When the multiplexed hologram is illuminated by a planar beam, four images appear simultaneously and are indistinguishable from each other, as shown in Fig. 5(f). The results exhibit that four images can be encrypted and decrypted from one multiplexed hologram under the same TC of the MHC beams.

In order to enhance the capacity of holographic multiplexation, the normalized factor r_0 is used in OAM-multiplexed holography. The design process of the r_0-encrypted MHC-OAM-multiplexed holography is shown in Fig. 6(a). Four images with the letters "C," "O," "P," and "E" are encrypted into a single MHC-OAM-multiplexed hologram, where the normalized factors of $r_0 = 0.5$, 0.6, 0.7, and 0.8 mm are adopted to decrypt each image, respectively. The other coding parameters are fixed as $\alpha = 5$, $m = 3$, and $K = 0$. In the decryption process, each image can be reconstructed when the incident MHC beam with $\phi(-\alpha, m, K, r_0)$. The influence of parameter

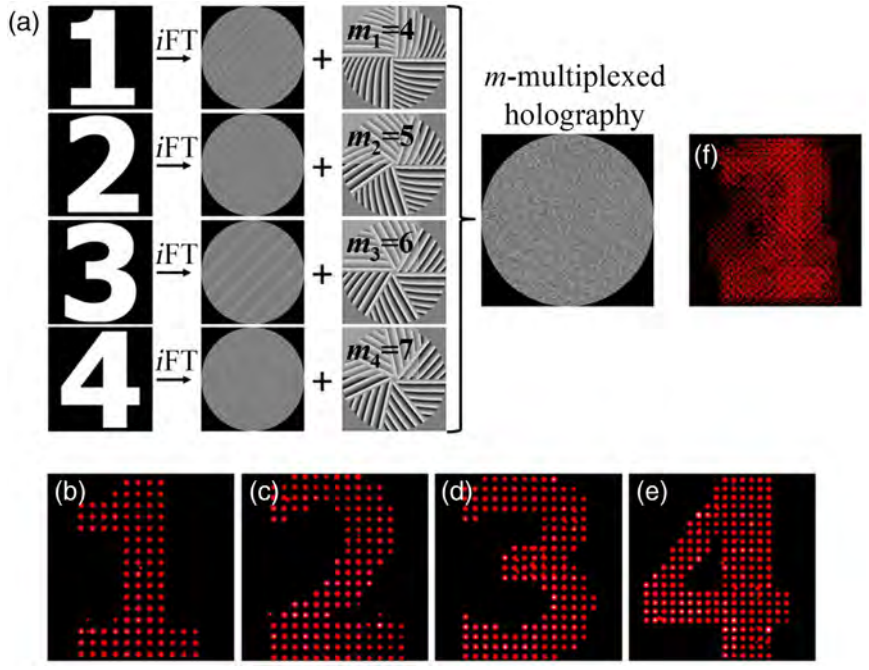

Fig. 5 Schematic diagram of MHC-OAM-multiplexed holography designed with key m. (a) Design process. (b)–(e) Experimental reconstruction results based on the m-dependence of the incident MHC beams with $m = 4$, 5, 6, and 7, respectively. (f) Reconstruction holographic image by a planar wave.

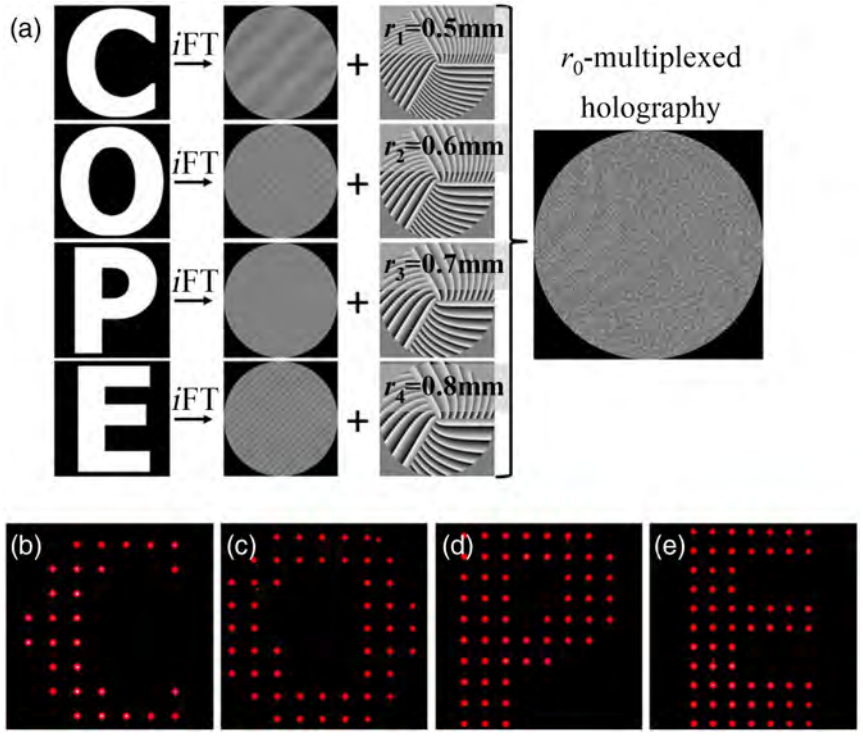

Fig. 6 Schematic diagram of MHC-OAM-multiplexed holography designed with key r_0. (a) Design process. (b)–(e) Experimental reconstruction results based on the r_0-dependence of the incident MHC beams with $r_0 = 0.5$, 0.6, 0.7, and 0.8 mm, respectively.

r_0 on MHC-OAM-multiplexed holography is numerically investigated (Note S3 and Fig. S3 in the Supplementary Material). It is clear to see that the reconstructed target images have a relatively low SNR due to the spatial overlap of MHC modes (Table S1 in the Supplementary Material). In order to reduce the overlap between MHC modes, the target images with larger sampling constants are numerically simulated (Table S2 and Fig. S4 in the Supplementary Material). The experimental results are shown in Figs. 6(b)–6(e). In this case, the MHC-OAM-multiplexed holography with the r_0-encryption is implemented, demonstrating that the normalized factor can be used as an independent information channel. The multiplexing crosstalk is analyzed in the holographic reconstruction (Note S4 and Fig. S5 in the Supplementary Material). In addition, the crosstalk can have originated from the noise of the CCD, the uniformity of the incident beam, or the limitation of the sampling point. In CGH, the MHC-OAM hologram and target image are discretely sampled, which is limited by the pixel pitch of the SLM and the spatial frequency of the MHC beam. Although the iteration algorithm can optimize the intensity value of each sampling point, the area between the sampling points is completely unrestricted. If the phase difference between the adjacent sampling points is chose to π, the noise may appear.

On the other hand, the impact of TC α on the MHC-OAM-multiplexed holography is numerically characterized (Note S5 and Fig. S6 in the Supplementary Material). Our numerical results show that the use of MHC beams with a larger TC difference in the holographic multiplexing can yield a lower crosstalk. Moreover, it should be mentioned that the effect of constant K on the reconstruction of MHC-OAM-multiplexed holography exhibits a good SNR (Note S6 and Fig. S7 in the Supplementary Material). The above results show that using MHC modes with a smaller TC difference or a smaller normalized factor difference produces a higher crosstalk. Therefore, the selection of TC and the normalized factor needs special consideration in the design of holographic multiplexing. Meanwhile, our results suggest that the selection of larger sampling constants is beneficial to improve the SNR.

3.2 X-K-Encrypted MHC-OAM-Multiplexed Holography

In this section, the combination of the parameter X and the constant K will be demonstrated in different multiplexing channels. Three modulation parameters of the MHC beams, namely, TC, m, and r_0 can be used as independent degrees of freedom, so the parameter X is chosen as any one of the above three parameters.

The α-K-encrypted MHC-OAM-multiplexed holography is shown in Fig. 7. Two different TCs ($\alpha = -5$ and 5) and two different constants K ($K = 0$ and 1) are used to encode the four images with the letters "D," "A," "T," and "E." One α-K-encrypted MHC-OAM-multiplexed hologram can be obtained by superimposing the four OAM selective holograms generated from the OAM-preserved holograms and four MHC phase modes with $\phi(-5, 3, 0, 1\ \text{mm})$, $\phi(-5, 3, 1, 1\ \text{mm})$, $\phi(5, 3, 0, 1\ \text{mm})$, and $\phi(5, 3, 1, 1\ \text{mm})$. Here the TC and the constant K together determine the encrypted and decrypted images. The four images can be reconstructed when the multiplexed hologram is illuminated by different MHC beams with $\phi(5, 3, 0, 1\ \text{mm})$, $\phi(5, 3, 1, 1\ \text{mm})$, $\phi(-5, 3, 0, 1\ \text{mm})$, and $\phi(-5, 3, 1, 1\ \text{mm})$, respectively, as shown in Figs. 7(b)–7(e).

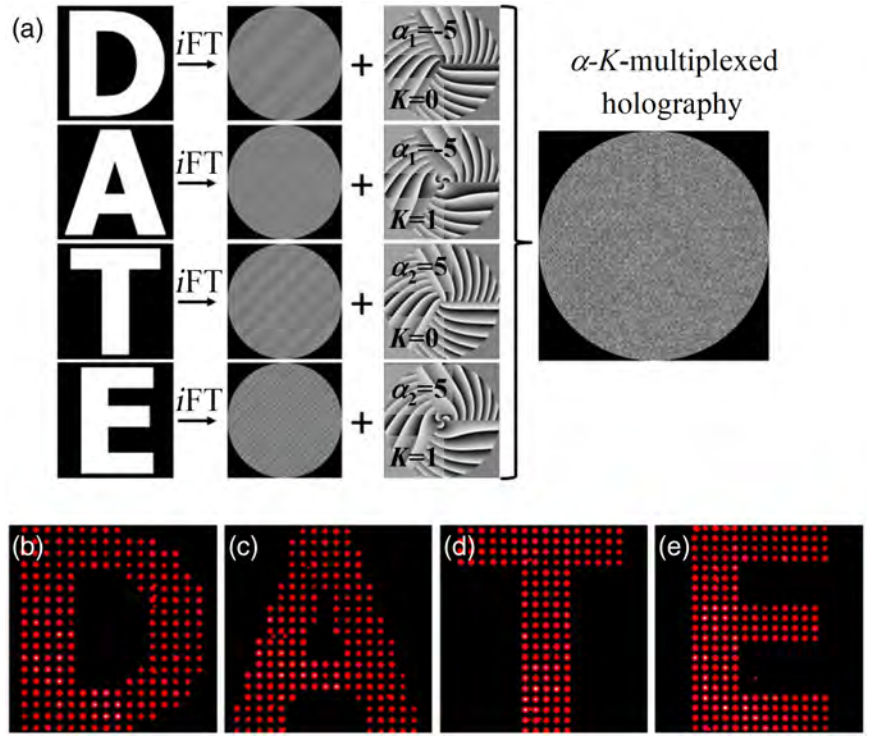

Fig. 7 Experimental reconstruction results of the α-K-encrypted MHC-OAM multiplexed holography. (a) The design process and (b)–(e) experimental reconstruction results.

The MHC-OAM-multiplexed holography based on the number of multiramp mixed screw-edge dislocations m and the constant K is implemented under the same TC and the same normalized factor. The design process is shown in Fig. 8(a). The four images with the letters "W," "O," "R," and "D" are encrypted by the different number of multiramp mixed screw-edge dislocations m ($m = 3$ and 5) and the different constants K ($K = 0$ and 1). The reconstructed results are shown in Figs. 8(b)–8(e). The encoded images can be reconstructed when the incident MHC beams with inverse TC, and the specific number of multiramp mixed screw-edge dislocations, the constant, and the normalized factor are used. Furthermore, the r_0-K-encrypted MHC-OAM-multiplexed hologram is designed, as shown in Fig. 9(a). The four letters "L," "I," "F," and "E" are encoded by the four different MHC phase modes with the same TC ($\alpha = 5$), the same number of multiramp mixed screw-edge dislocations m ($m = 3$), two different normalized factors r_0 ($r_0 = 0.5$ and 1 mm), and two different constants K ($K = 0$ and 1). The experimental results are shown in Figs. 9(b)–9(e), where each image is reconstructed from the suitable incident MHC beam.

In addition, the m-α-encrypted MHC-OAM-multiplexed holography is further investigated. Four images with Arabic numbers "5," "6," "7," and "8" are used and encrypted into four OAM holograms. The four MHC phase modes with $\phi(2, 3, 0, 1\ \text{mm})$, $\phi(3, 4, 0, 1\ \text{mm})$, $\phi(4, 5, 0, 1\ \text{mm})$, and $\phi(5, 6, 0, 1\ \text{mm})$ are superimposed into the above four OAM holograms, resulting in four OAM selective holograms. The MHC-OAM-multiplexed hologram with the m-α-encryption is designed in Fig. 10(a). Each image can only be reconstructed by the incident MHC beam with $\phi(-\alpha, m, K, r_0)$, as shown in Figs. 10(b)–10(e).

3.3 α-m-Y-Encrypted MHC-OAM-Multiplexed Holography

Here the parameter Y is chosen as the normalized factor r_0 and the constant K. First, the principle of α-m-r_0-encrypted OAM-multiplexed holography is illustrated in Fig. 11(a). The nine images with Arabic numbers 1 to 9 are encoded into nine holograms, then nine different MHC phase modes with the constant $K = 0$, TC values of -6, 6, and 12, m values from 3 to 5 with the interval of 1, and r_0 values from 0.5 to 0.7 mm with the interval of 0.1 mm are added to the above nine holograms, resulting in the nine OAM selective holograms. The α-m-r_0-encrypted MHC-OAM-multiplexed hologram is obtained by superimposing all selective holograms. In the decryption process, the encrypted images can be reconstructed by the suitable incident MHC beams with $\phi(-\alpha, m, K, r_0)$, as shown in Fig. 11(b). Thus the combination of these parameters provides a high level of information security.

The TC α, the number of multiramp mixed screw-edge dislocations m, and the constant K are used to increase the number of multiplexed channels. The 12 images from 1 to 6 and A to F are encrypted into different OAM-preserved holograms. Four different TCs ($\alpha = -12, -6, 6, 12$), three multiramp mixed screw-edge dislocations ($m = 3, 4, 5$) and two constants ($K = 1, 0$) are used to encrypt the above 12 images. The encoded phase mode of each image is shown in Fig. 12(a), and the experimental reconstruction results are shown in Fig. 12(b).

3.4 α-m-r_0-K-Encrypted MHC-OAM-Multiplexed Holography

The four parameters of the MHC beam are independent of each other and can potentially be used for holographic

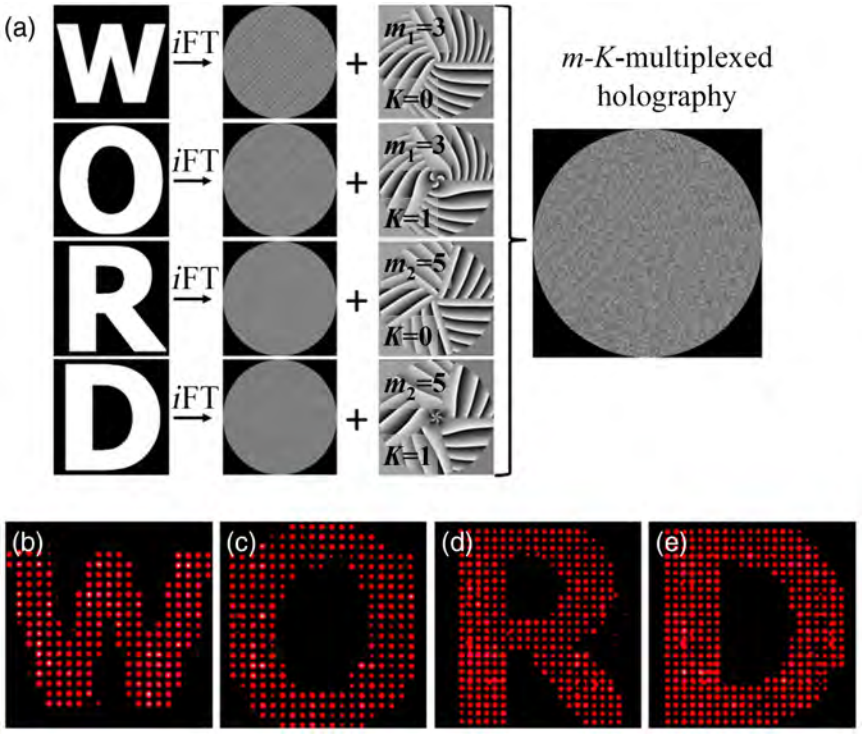

Fig. 8 The experimental reconstruction results of the *m*-*K*-encrypted MHC-OAM-multiplexed holography. (a) Design process and (b)–(e) experimental reconstruction results.

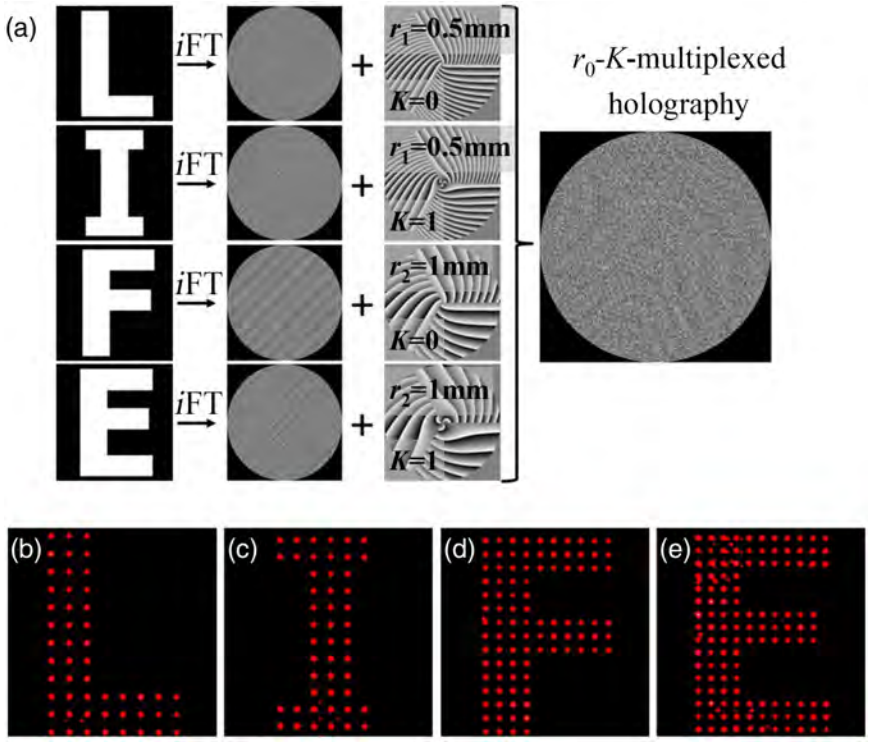

Fig. 9 Experimental reconstruction results of the r_0-*K*-encrypted MHC-OAM-multiplexed holography. (a) Design process and (b)–(e) experimental reconstruction results.

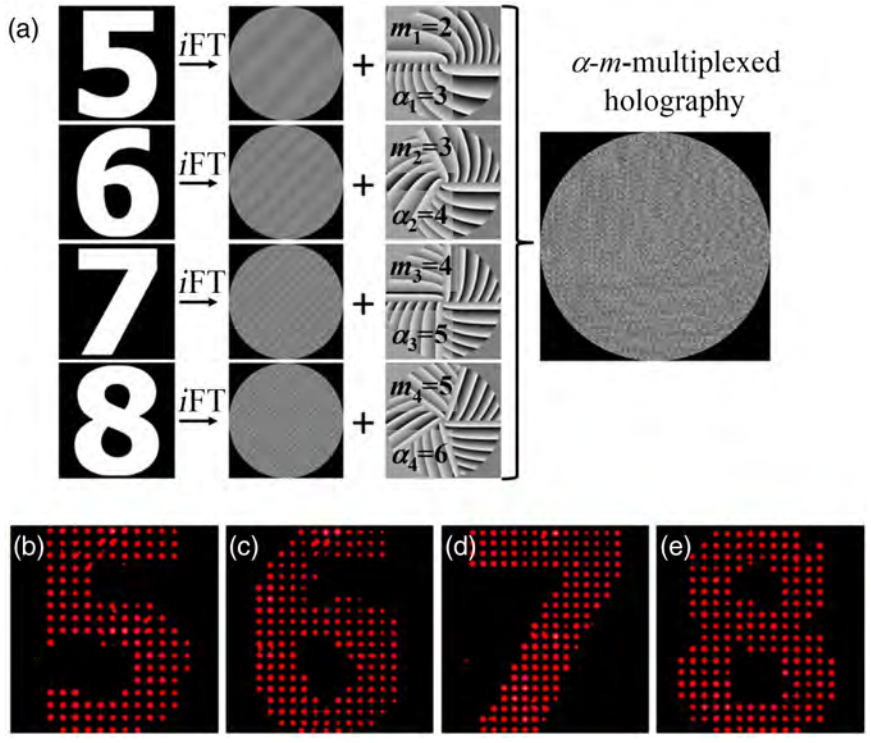

Fig. 10 Experimental reconstruction results of the α-m-encrypted MHC-OAM-multiplexed holography. (a) Design process and (b)–(e) experimental reconstruction results.

multiplexing in four dimensions. A four-parameter dimensional multiplexed holography can be achieved by encrypting 16 images in different channels with these parameters. Four different TCs ($\alpha = -12, -8, 8, 12$), four different multiramp mixed screw-edge dislocations from 4 to 7 with the step of 1, four different normalized factors from 0.6 to 0.9 mm with the interval of 0.1 mm, and two different constants ($K = 0, 1$) are used to encode these 16 images. The 16 images are chosen from 0 to 9 and A to F. Here the parameters of each encoded image are shown in Fig. 13. The 16 OAM-selective holograms can be generated by encoding the different MHC phase modes into the corresponding OAM-preserved holograms. The α-m-r_0-K-encrypted MHC-OAM-multiplexed holography can be obtained by superposing those 16 selective holograms. Each target image can be reconstructed when the suitable MHC beams with $\phi(-\alpha, m, K, r_0)$ illuminate the multiplexed hologram. The experimental results are presented in Fig. 14.

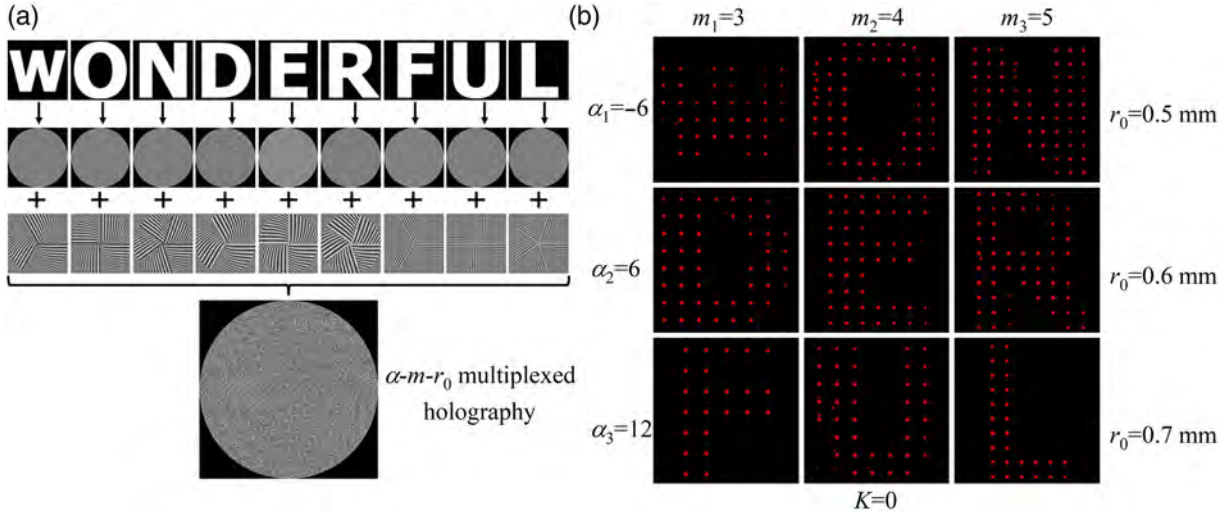

Fig. 11 Experimental reconstruction results of the α-m-r_0-K-encrypted MHC-OAM-multiplexed holography. (a) Design process and (b) experimental reconstruction results.

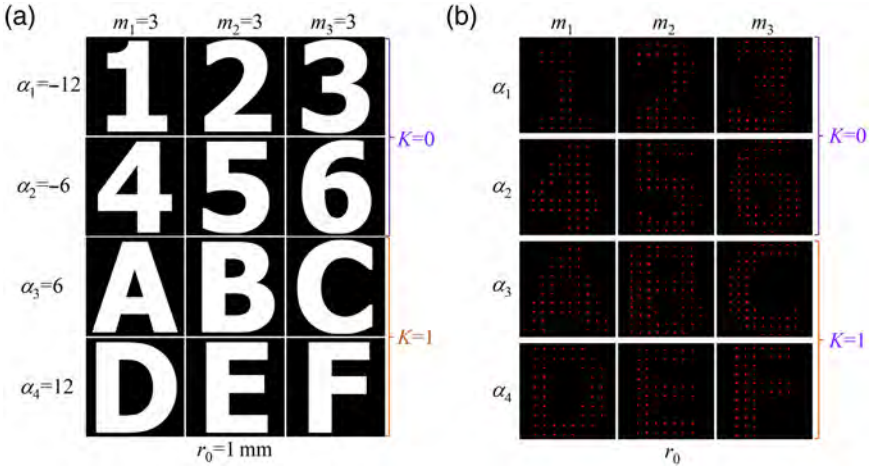

Fig. 12 Experimental reconstruction results of the α-m-K-encrypted MHC-OAM-multiplexed holography. (a) Design process and (b) experimental reconstruction results.

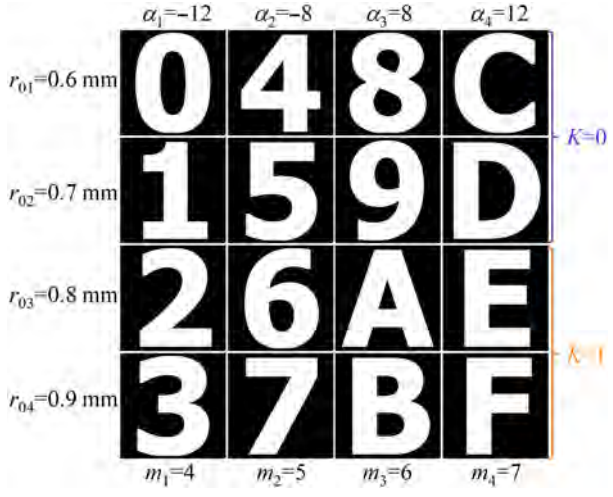

Fig. 13 The encrypted images are encoded by the parameters α, m, r_0, and K.

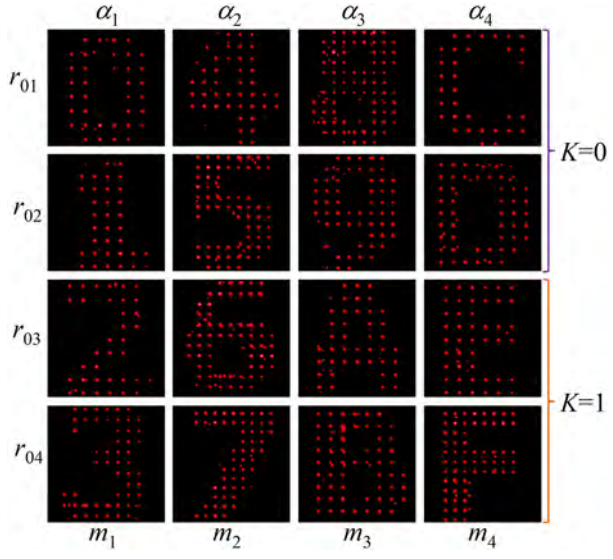

Fig. 14 Experimental reconstruction results of the α-m-r_0-K-encrypted MHC-OAM-multiplexed holography.

4 Conclusion

In summary, the MHC-OAMmultiplexed holography is proposed and experimentally implemented by introducing the number of multiramp mixed screw-edge dislocations, the normalized factor, and the constant K as new degrees of freedom. The MHC beams modulated with different parameters can be utilized as information encryption or decryption channels, which enhance the capability of holographic multiplexation. In the experiments, we have successfully realized 4-, 9-, 12- and 16-channel multiplexing by the combination of the four parameters of MHC beam. The results show that the encrypted image can be correctly reconstructed when the MHC-OAM hologram is illuminated by the incident MHC beam with an inverse TC, a customized number of multiramp mixed screw-edge dislocations, the normalized factor, and the constant K, while there is no image reconstructed with false MHC beam. The multiplexed holography proposed in this work can significantly improve the capability of the information encryption and storage and has potential applications in communication, 3D display, etc.

Acknowledgments

This work was supported by the National Natural Science Foundation of China (Grant No. 61775153) and the Priority Academic Program Development of Jiangsu Higher Education Institutions.

References

1. L. Hesselink, S. S. Orlov, and M. C. Bashaw, "Holographic data storage systems," *Proc. IEEE* **92**(8), 1231–1280 (2004).
2. Q. Dai et al., "A single-celled tri-functional metasurface enabled with triple manipulations of light," *Adv. Funct. Mater.* **30**(50), 2003990 (2020).
3. J. P. Balthasar Mueller et al., "Metasurface polarization optics: independent phase control of arbitrary orthogonal states of polarization," *Phys. Rev. Lett.* **118**(11), 113901 (2017).
4. D. Wen et al., "Helicity multiplexed broadband metasurface holograms," *Nat. Commun.* **6**(1), 8241 (2015).
5. X. Li et al., "Athermally photoreduced graphene oxides for three-dimensional holographic images," *Nat. Commun.* **6**(1), 6984 (2015).
6. L. Zou, L. Wang, and S. Zhao, "Turbulence mitigation scheme based on spatial diversity in orbital-angular-momentum multiplexed system," *Opt. Commun.* **400**, 123–127 (2017).

7. A. Mair et al., "Entanglement of the orbital angular momentum states of photons," *Nature* **412**(6844), 313–316 (2001).
8. C. Li and S. Zhao, "Efficient separating orbital angular momentum mode with radial varying phase," *Photonics Res.* **5**(4), 267–270 (2017).
9. L. Allen et al., "Orbital angular momentum of light and the transformation of Laguerre–Gaussian laser modes," *Phys. Rev. A* **45**(11), 8185 (1992).
10. Y. Liu et al., "Switchable second-harmonic generation of airy beam and airy vortex beam," *Adv. Optical Mater.* **9**(4), 2001776 (2021).
11. J. Berškys and S. Orlov, "Spherically polarized vector Bessel vortex beams," *Phys. Rev. A* **105**(1), 013502 (2022).
12. C. Sun et al., "Propagation dynamics of autofocusing circle Pearcey Gaussian vortex beams in a harmonic potential," *Opt. Express* **28**(1), 325–333 (2020).
13. X. Ouyang et al., "Synthetic helical dichroism for six-dimensional optical orbital angular momentum multiplexing," *Nat. Photonics* **15**(12), 901–907 (2021).
14. X. Fang et al., "High-dimensional orbital angular momentum multiplexing nonlinear holography," *Adv. Photonics* **3**(1), 015001 (2021).
15. H. Ren et al., "Metasurface orbital angular momentum holography," *Nat. Commun.* **10**(1), 2986 (2019).
16. X. Fang, H. Ren, and M. Gu, "Orbital angular momentum holography for high-security encryption," *Nat. Photonics* **14**(2), 102–108 (2020).
17. H. Ren et al., "Complex-amplitude metasurface-based orbital angular momentum holography in momentum space," *Nat. Nanotechnol.* **15**(11), 948–955 (2020).
18. H. Zhou et al., "Polarization-encrypted orbital angular momentum multiplexed metasurface holography," *ACS Nano* **14**(5), 5553–5559 (2020).
19. G. Zhu et al., "Ultra-dense perfect optical orbital angular momentum multiplexed holography," *Opt. Express* **29**(18), 28452–28460 (2021).
20. F. Wang et al., "Angular multiplexation of partial helical phase modes in orbital angular momentum holography," *Opt. Express* **30**(7), 11110–11119 (2022).
21. F. Wang et al., "Enhancing the information capacity with modulated orbital angular momentum holography," *IEEE Photonics J.* **14**(1), 5212905 (2022).
22. F. Li et al., "Multiple-dimensional multiplexed holography based on modulated chiro-optical fields," *Opt. Express* **30**(23), 41567–41579 (2022).
23. F. Li et al., "Multiple-image encryption using phase jump gradient factors-based OAM multiplexing holography," *Opt. Laser Eng.* **160**, 107303 (2023).
24. P. Cheng, S. Huang, and C. Yan, "Ellipticity-encrypted orbital angular momentum multiplexed holography," *J. Opt. Soc. Am. A* **38**(12), 1875–1883 (2021).
25. C. A. Alonzo, P. J. Rodrigo, and J. Glückstad, "Helico-conical optical beams: a product of helical and conical phase fronts," *Opt. Express* **13**(5), 1749–1760 (2005).
26. N. Hermosa, C. Rosales-Guzmán, and J. P. Torres, "Helico-conical optical beams self-heal," *Opt. Lett.* **38**(3), 383–385 (2013).
27. N. Bareza and N. Hermosa, "Propagation dynamics of vortices in helico-conical optical beams," *Opt. Commun.* **356**, 236–242 (2015).
28. J. Wen et al., "Fabrication of chiral 3D microstructure using tightly focused multiramp helico-conical optical beams," *Micromachines* **13**(10), 1771 (2022).
29. X. Li et al., "Controllable mode transformation in perfect optical vortices," *Opt. Express* **26**(2), 651–662 (2018).

Nian Zhang received his MS degree in optical engineering from the School of Optoelectronic Science and Engineering, Soochow University, Suzhou, China, in 2020. He is currently a PhD student in optical engineering at the School of Optoelectronic Science and Engineering, Soochow University, Suzhou, China. His research interests are holography and vortex beams.

Baoxing Xiong received his MS degree in optical engineering from the School of Optoelectronic Science and Engineering, Soochow University, Suzhou, China. He is an assistant researcher at the School of Optoelectronic Science and Engineering, Soochow University, Suzhou, China. His research interest is photothermal refractive glass.

Xiang Zhang received his MS and PhD degrees in optical engineering from the National Laboratory for Optoelectronics, Huazhong University of Science and Technology, Wuhan, China. He is a professor at the School of Optoelectronic Science and Engineering, Soochow University, Suzhou, China. His research interests are the preparation of photothermal refractive glass and Bragg volume diffractive devices, the theory and preparation of micro-nano-structure optical devices, advanced solid-state laser technology, and beam control.

Xiao Yuan is a Distinguished Professor at the School of Optoelectronic Science and Engineering, Soochow University, Suzhou, China. He was a visiting scientist at the University of Maryland from 1995 to 1997 and worked at the School of Optoelectronic Science and Engineering of Huazhong University of Science and Technology from 2002 to 2008. His research interests include high-power lasers and their applications, micro-nano-optical devices and technologies, laser materials and devices, nonlinear optics, and laser plasma physics. He has coauthored more than 100 publications in peer-reviewed journals.

Research Article

ADVANCED PHOTONICS NEXUS

Reconfigurable structured light generation and its coupling to air–core fiber

Yize Liang,[a,b,c] Hongya Wang,[a,b,c] Xi Zhang,[a,b,c] Jianzhou Ai,[a,b,c] Zelin Ma,[d] Siddharth Ramachandran,[d] and Jian Wang[a,b,c,*]

[a]Huazhong University of Science and Technology, Wuhan National Laboratory for Optoelectronics and School of Optical and Electronic Information, Wuhan, China
[b]Optics Valley Laboratory, Wuhan, China
[c]Shenzhen Institute of Huazhong University of Science and Technology, Shenzhen, China
[d]Boston University, College of Engineering, Boston, Massachusetts, United States

Abstract. Recently, structured light beams have attracted substantial attention in many applications, including optical communications, imaging, optical tweezers, and quantum optics. We propose and experimentally demonstrate a reconfigurable structured light beam generator in order to generate diverse structured light beams with adjustable beam types, beam orders, and beam sizes. By controlling the sizes of generated free-space structured light beams, free-space orbital angular momentum (OAM) beams and vector beams are coupled into an air–core fiber. To verify that our structured light generator enables generating structured light with high beam quality, polarization distributions and mode purity of generated OAM beams and vector beams in both free space and air–core fiber are characterized. Such a structured light generator may pave the way for future applications based on higher-order structured light beams.

Keywords: structured light beams; orbital angular momentum; vector beams; air–core fiber.

Received Feb. 15, 2023; revised manuscript received Apr. 6, 2023; accepted for publication May 12, 2023; published online Jun. 12, 2023.

[DOI: 10.1117/1.APN.2.3.036015]

1 Introduction

The explosive growth of global data traffic is driving an ever-increasing demand for higher data capacity and more efficient spectral usage in transmission links.[1–3] To address the coming capacity crunch, it is highly desirable not only to make full use of already well-known physical dimensions (e.g., amplitude, phase, frequency/wavelength, polarization, and time) but also to exploit additional degrees of freedom (e.g., spatial structure) of light waves. As a result, space-division multiplexing (SDM) exploiting the transverse spatial structure dimension of light waves has attracted more and more attention.[4,5] SDM technology employing orthogonal higher-order light modes multiplexing can be divided into two different application scenarios, including the free space[6,7] and the optical fiber.[8–11] Among them, the application scenario in optical fiber has the advantages of flexibility and long-distance transmission. Therefore, in recent years, optical fibers supporting high-order modes have been widely designed, fabricated, and used in SDM applications, such as few-mode fiber,[12,13] traditional multimode fiber,[14] ring–core fiber,[15,16] and air–core fiber.[17,18]

Traditional higher-order modes in fiber, also known as structured light beams due to their different transverse structures,[19–23] can be divided into three types: orbital angular momentum (OAM) beams, linearly polarized (LP) beams, and vector beams. Due to the low loss and flexibility of optical fiber transmission, such diverse structured light beams in optical fibers are widely used in optical communications,[24] optical tweezers,[25] rotating Doppler sensing,[26–29] superresolution imaging,[30,31] and quantum optics.[32,33] Therefore, generating various structured light beams in fiber are required in many applications. There are several approaches to producing structured light beams in fiber, such as mode-selective couplers (MSCs),[34] long-period fiber gratings (LPFGs),[35,36] fiber Bragg gratings,[37] and free-space-to-fiber coupling.[14–16] However, for generation of the fourth, fifth, and much higher-order structured light beams in

*Address all correspondence to Jian Wang, jwang@hust.edu.cn

optical fiber, the MSCs and LPFGs suffer from a greatly high intensity loss. Thus the method of producing high-order structured light beams in free space and then coupling them into optical fiber is the main way to generate structured light beams with orders higher than fourth in fiber. Remarkably, reconfigurable generation of these structured lights in free space requires a reconfigurable phase-modulation device, such as spatial light modulator (SLM). Different from LP beams and OAM beams, vector beams possess inhomogeneous polarization distributions. Thus approaches for reconfigurable generation of vector beams usually use such steps: splitting a Gaussian beam into two orthogonally polarized beams, modulating them into two OAM beams with opposite topological charges, and then recombining them. There are many experimental setups for generating vector beams based on this principle. In general, these setups can be divided into two categories: one is conventional interferometric setup,[38,39] the other is common-path interferometric loops.[40–43] For conventional interferometric setups, since the two OAM beams propagate along different optical paths, their relative phase difference may alter with time, which will cause the rotation of polarization distributions of a combined vector beam. Such an instability limits applications based on vector beams, including coupling them into optical fiber. In this article, we demonstrate that a common-path interferometric loop will lead to a higher robustness of generated vector beams compared to conventional interferometric setups.

We propose and experimentally demonstrate a reconfigurable structured light beams generator with adjustable beam types, beam orders, and beam sizes. OAM beams, LP beams, and cylindrical vector beams are produced by our scheme in free space. Since beams in the proposed scheme share a common optical path, generated vector beams feature more robustness compared to conventional approach. We measure the Stokes parameters to reconstruct the polarization distributions of beams for verifications. Then OAM beams and vector beams with fifth to seventh mode orders are coupled into a 5-m air–core fiber. At the fiber output, high beam quality and low coupling loss of output higher-order beams are demonstrated, showing that our scheme enables pure high-order structured light generation in optical fiber.

2 Results

2.1 Scheme of Reconfigurable Structured Light Beams Generator

We propose and experimentally demonstrate a single SLM loop for reconfigurable structured light beams generation. Figure 1(a) illustrates the concept of generating cylindrical vector beams in such a loop. As displayed in Fig. 1(a), the red lines show the track of spatial light, whereas the green and purple arrows represent the transmitting directions of orthogonally polarized beams. In order to produce vector beams, the input Gaussian beam should be 45 deg or −45 deg polarized. Half of the 45 deg polarized beam straightly propagates through the beam splitter (BS), and then it is divided into two orthogonal polarized beams by a polarization beam splitter (PBS). An x-polarized beam straightly propagates through PBS and transmits in clockwise direction, whereas the y-polarized beam reflects at PBS and transmits in counterclockwise direction. Gaussian beams are converted into OAM beams by hologram loaded onto SLM, expressed as

$$\mathrm{mod}[(l\varphi + n_g \cdot x - a \cdot r)/2\pi], \tag{1}$$

where the first two components are referred to as a forked phase hologram, which is generally used for generating a pure OAM mode. The $l\varphi$ term consists of the topological charge l, and azimuthal angle φ denotes the phase mask of an lth OAM beam, whereas the $n_g \cdot x$ term corresponds to the phase mask of an x direction grating that separates the modulated OAM beam from the unmodulated beam. In addition, the radial grating component $-a \cdot r$ is applied to form perfect OAM modes with adjustable size[44] (see S3 in the Supplementary Material). Noting that the phase-only SLM only works on x-polarized light, a half-wave plate (HWP) is inserted into this loop so as to match the polarization requirement of the SLM and the PBS. At the output of the BS, an x-polarized OAM beam and a y-polarized OAM beam are generated with opposite topological charges as a result of different reflected times. Propagating through a quarter-wave plate (QWP), x- and y-polarized OAM beams are converted into right-circularly and left-ircularly polarized OAM beams. The vector beam is obtained by superposition of these two OAM beams,

$$A_1 \cdot \exp(il\varphi)\begin{bmatrix}1\\ \pm i\end{bmatrix} + A_2 \cdot \exp(-il\varphi)\begin{bmatrix}1\\ \mp i\end{bmatrix} \cdot \exp(-i\Delta\Phi), \tag{2}$$

where $\mathrm{abs}(A_1)$ equals to $\mathrm{abs}(A_2)$ when generating a vector beam, as mentioned above. $\Delta\Phi$ describes the phase difference of two circularly polarized OAM beams. To further illustrate the relationship between different beam modes, we display the concept of the higher-order Poincaré sphere (HOPS) with $l = 1$, as displayed in Fig. 1(b). The poles of the HOPS represent scalar OAM beams (having helical wavefronts) with a uniform circular polarization (right circular at the north pole and left circular at the south pole). The superposition of two poles forms different vector beams with different polarization distributions due to diverse phase difference $\Delta\Phi$ of two circularly polarized OAM beams, as shown in Fig. 1 (b). In Eq. (2), the type of synthetic vector beams can be changed by adjusting the sign of A_1 and A_2. Changing the polarization of input Gaussian beam (e.g., +45 deg to −45 deg) means changing the sign of A_1 and A_2. Rotating the QWP enables the changing of circular polarization state. Therefore, four vector beams on the equator can be generated (see S1 in the Supplementary Material for details). When generating OAM beams employing this single SLM loop, one can just adjust the incident Gaussian beam to x or y polarization. Loading a ±OAM superposition phase hologram onto the SLM, LP beams are also generated. In addition, to generate arbitrary vector beams based on this single SLM loop, control of the phase difference of two OAM beams is requested. Many approaches can be utilized to arbitrarily control the phase difference of two OAM beams, including using another SLM or some polarization optics to adjust their phase delay (see S3 in the Supplementary Material for details). Furthermore, letting the x-polarized and y-polarized beams have a slight offset on SLM and then separately modulating them may be another approach to controlling the phase delay of two OAM beams.

A conventional interferometric setup for generation of vector beams obey the rules: splitting a Gaussian beam into two orthogonally polarized beams, modulating them into two OAM beams with opposite topological charges via two phase holograms, and then recombining them. In such a conventional setup, $\Delta\Phi$ alters, since the two OAM beams propagate along

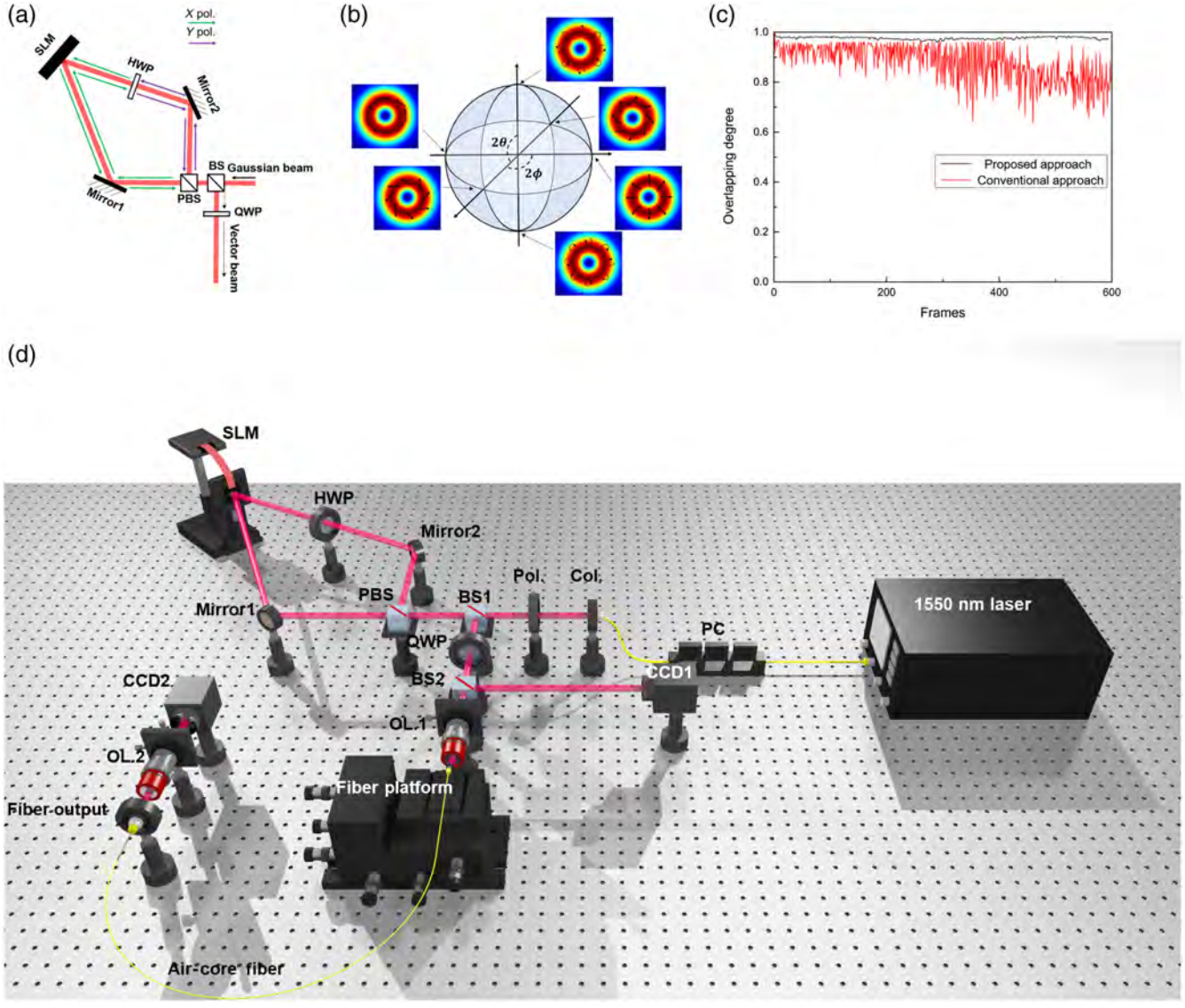

Fig. 1 (a) Concept of reconfigurable structured light beams generator employing a single SLM loop. (b) HOPS with $l = 1$. (c) Overlapping degree between polarization distributions of vector beams in initial frames and vector beams in subsequent frames. (d) Experimental setup of reconfigurable structured light beams generator and fiber-coupling system. PC, polarization controller; Col, collimator; BS, beam splitter; PBS, polarization beam splitter; HWP, half-wave plate; QWP, quarter-wave plate; OL, objective lens; CCD, charge-coupled device (Video 1, mp4, 12.2 MB [URL: https://doi.org/10.1117/1.APN.2.3.036015.s1; Video 2, mp4, 12.1 MB [URL: https://doi.org/10.1117/1.APN.2.3.036015.s2).

different paths. Such a rapid change of $\Delta\Phi$ may lead to vibration and rotation of the polarization distributions of vector beams, which may be a fundamental disadvantage of conventional approaches. In our approach, the two orthogonal OAM beams share the common optical path so that the polarization distribution of the generated vector beam is robust. An experiment is carried out to demonstrate this point. First, we use two different setups to generate higher-order vector beams. Let the generated vector beams propagate through a polarizer, and the LP-like intensity profiles of vector beams are recorded using a CCD run at 10 frames per second. For a conventional interferometric setup, the lobe jitters and rotates (see Video 1). For common-path interferometric loop in this work, the lobe are stable (Video 2). Taking the intensity profile of the first frame of recorded video as a reference, the overlapping degree between intensity profiles in other frames and the reference is calculated. As shown in Fig. 1(c), vector beams generated using the proposed approach are stable and robust.

After finishing the construction of reconfigurable structured light beam generator with adjustable beam types, beam orders, and beam sizes, we couple these diverse structured light beams into air–core fiber for testing. The specific experimental setup is shown in Fig. 1(d), with the red line describing the track of spatial light. A polarizer (Pol.) is used to adjust the polarization of the input Gaussian beam. After propagating through the single SLM loop mentioned above, a structured light beam is

generated at the output of the QWP. Then the beam passes through BS2 and is coupled into the air–core fiber by an objective lens (OL1). After the transmission in the air–core fiber, the structured light beam is collimated by OL2. CCD1 and CCD2 capture the intensity profiles of generated structured light beams before and after fiber transmission, respectively. Remarkably, BS2 is used for capturing the free-space structured light, whereas BS1 applied due to the SLM is a polarization-sensitive device. Such two BSs lead to a 9-dB loss, which is a disadvantage for power-limited structured light beam applications. Thus one can further improve the transmission efficiency of this setup by removing the two BSs (see S7 in the Supplementary Material for details).

2.2 Polarization Reconstruction of Structured Light Beams

To verify the generated structured light beams, an approach is developed to measure the polarization distributions of structured light beams, especially for vector beams. Figs. 2(a)–2(g) illustrate the polarization reconstruction process of vector beam with mode order $l = 1$, whereas Figs. 2(h)–2(n) correspond to mode order $l = 10$.

Noting that the polarization of the uniform polarized beam can be described by Stokes parameters, we achieve the polarization measurement of the vector beams by calculating the Stokes parameters of each point at the transverse plane. Stokes parameters are known to be calculated as

$$\begin{cases} S_0 = I_X + I_Y \\ S_1 = I_X - I_Y \\ S_2 = I_{+45} - I_{-45} \\ S_3 = I_R - I_L \end{cases}, \tag{3}$$

where $S_0 - S_3$ represent four Stokes parameters. I_X, I_Y, I_{+45}, and I_{-45} correspond to the intensity of light passing through a polarizer whose direction is adjusted to x, y, $+45$ deg, and -45 deg, respectively. I_R corresponds to the intensity of light passing through a $+45$ deg directional QWP and an x-directional polarizer, representing the right-circularly polarized component. I_L corresponds to the intensity of light passing through a $+45$ deg directional QWP and a y directional polarizer, representing the left-circularly polarized component. For cylindrical vector beams, by recording six different intensity profiles, one can easily calculate the Stokes parameters of each point at the beam transverse plane. Thus the function of the light field can be calculated employing the known Stokes parameters of each point, which can be written as

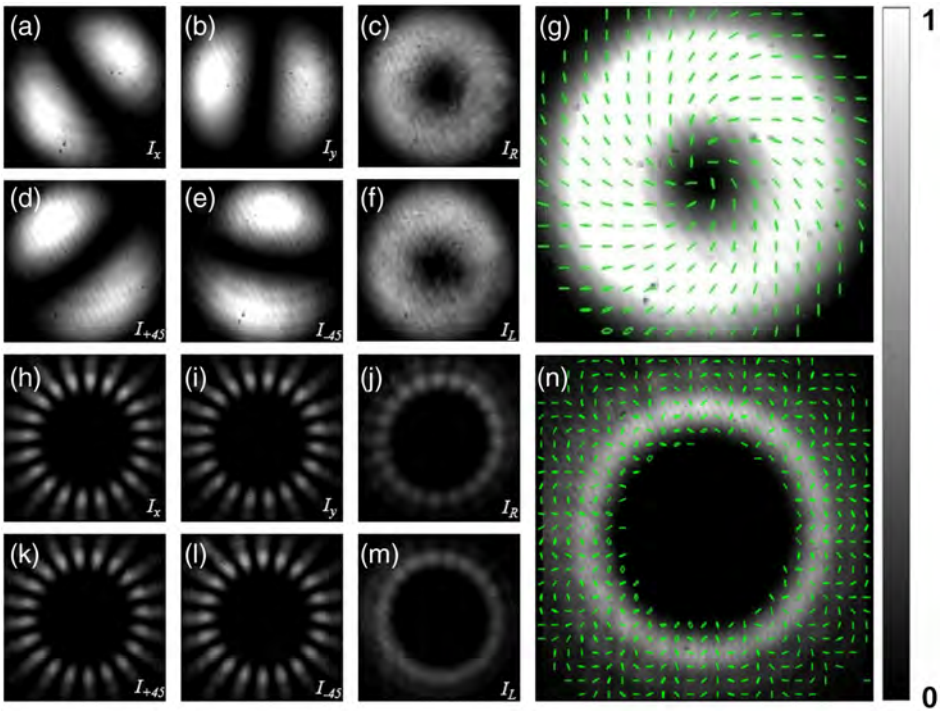

Fig. 2 Polarization reconstruction of cylindrical vector beams. Measured intensity profiles of a vector beam with mode order $l = 1$ after propagating through (a) an x-polarized polarizer; (b) a y-polarized polarizer; (c) a $+45$ deg directional QWP and an x-polarized polarizer; (d) a $+45$ deg polarizer; (e) a -45 deg polarizer; (f) a $+45$ deg directional QWP and a y-polarized polarizer; (g) intensity profile and polarization distribution of the vector beam with mode order $l = 1$. Measured intensity profiles of a vector beam with mode order $l = 10$ after propagating through (h) an x-polarized polarizer; (i) a y-polarized polarizer; (j) a $+45$ deg directional QWP and an x-polarized polarizer; (k) a $+45$ deg polarizer; (l) a -45 deg polarizer; (m) a $+45$ deg directional QWP and a y-polarized polarizer; (n) intensity profile and polarization distribution of the vector beam with mode order $l = 10$.

$$\begin{cases} E_X = \sqrt{(1+S_1/S_0)/2}\cdot\cos\ \varphi \\ E_Y = \sqrt{(1-S_3/S_2)/2}\cdot\cos[\varphi+\tan^{-1}(S_3/S_2)] \end{cases}, \tag{4}$$

where E_X and E_Y describe the simple harmonic vibration functions of light in two orthogonal directions. φ represents the transmission and vibration phase of light, usually described as $\varphi = k\cdot z - \omega\cdot t + \varphi_0$. Thus the trajectory of the beam vector determined by E_X and E_Y can be calculated by taking the value of φ from 0 to 2π in the parameter equation system about φ.

By capturing the intensity profiles of I_X, I_Y, I_{+45}, I_{-45}, I_R, and I_L, as shown in Figs. 2(a)–2(f) or Figs. 2(h)–2(m), respectively, we calculate the Stokes parameters and then give the polarization of each point. It is worth mentioning that all the intensity profiles are divided into many small matrices in order to facilitate the final marking of the polarization in the reconstruction figure, such as in Figs. 2(g) and 2(n).

2.3 Reconfigurable Structured Light Beams Generated in Free Space

Loading the seventh order hologram ($l = 7$) onto the SLM, by adjusting the polarization devices in the experimental setup, we obtain diverse structured light beams, such as x-polarized OAM beams, x-polarized LP beams, circularly polarized OAM beams, and vector beams in free space. CCD1 in Fig. 1(d) is used to capture the intensity profiles of the generated beams.

Figure 3 displays all types of structured light beams with the seventh order generated in our setup. We record the intensity profiles and reconstruct the polarization distributions of x-polarized OAM beams with opposite topological charges (i.e., $+7$ and -7), as shown in Figs. 3(a) and 3(b). Moreover, we record the intensity profiles of OAM beams interfering with Gaussian beams in order to verify the topological charge of OAM beams, as inserted into the right side of Fig. 3(b). The upper one denotes the interference intensity profile of OAM mode in Fig. 3(a),

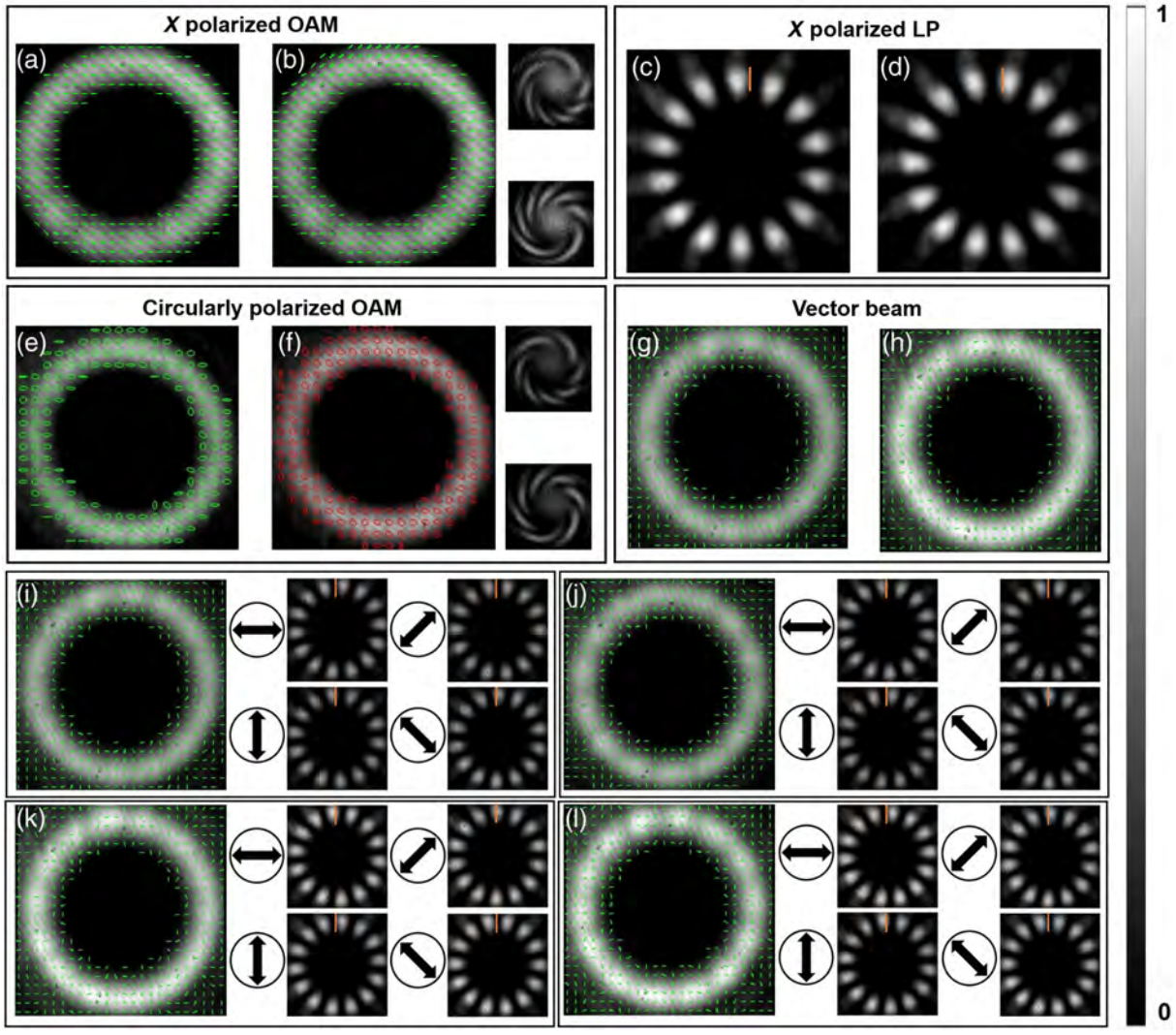

Fig. 3 Intensity profiles and polarization distributions of diverse seventh-order structured light beams generated in free space. (a), (b) x-polarized OAM beams, insets are interference intensity profiles of them. (c), (d) x-polarized LP beams. (e), (f) Circularly polarized OAM beams, insets are interference intensity profiles of them. (g), (h) Vector beams. (i)–(l) Four different vector beams; insets are intensity profiles of vector beams passing through different directional polarizers.

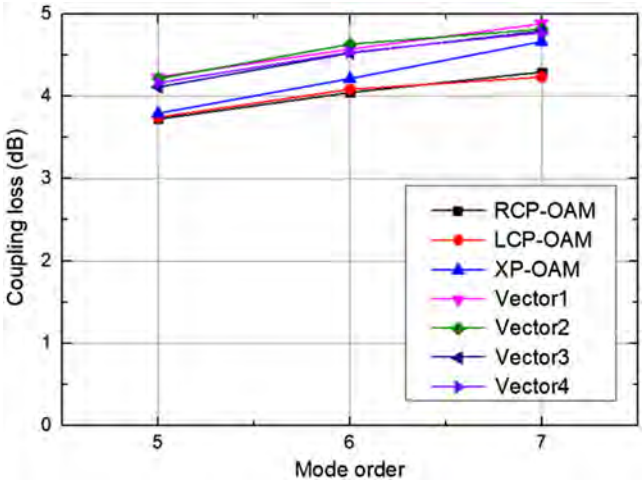

Fig. 4 Coupling losses of the fourth to seventh OAM and vector beams. RCP, right circular polarization; LCP, left circular polarization; and XP, *x* polarization.

whereas the bottom one corresponds to the interference intensity profile of OAM mode in Fig. 3(b). Figures 3(c) and 3(d) illustrate the obtained *x*-polarized LP beams, with orange vertical lines marked to distinguish different LP modes. Circularly polarized OAM beams with opposite topological charges, mentioned as poles on HOPS, are shown in Figs. 3(e) and 3(f). For circularly polarized OAM beams, green lines indicate the right circular polarizations, whereas red lines indicate the left circular polarizations. Similarly, interference intensity profiles are also inserted into the right side of Fig. 3(f). The upper one denotes the interference intensity profile of the OAM mode in Fig. 3(e), whereas the bottom one corresponds to the interference intensity profile of the OAM mode in Fig. 3(f). Figures 3(g) and 3(h) display the intensity profiles and polarization distributions of two different seventh-order vector beams.

Four vector beams with different polarization distributions are generated in this experimental setup by adjusting the polarization devices, as illustrated in Figs. 3(i)–3(l). They possess a measured average polarization purity of 94.0% (94.2%, 93.3%, 94.3%, and 94.3%) for four different vector beams, respectively (see S9 in the Supplementary Material for details).[45,46] Intensity profiles of four different vector beams passing through different directional polarizers are also displayed, as shown in Figs. 3(i)–3(l). Orange vertical lines are marked to distinguish these LP-like intensity profiles. With the rotation of polarizer (from horizontal to 45 deg, vertical, −45 deg), lobes in Figs. 3(i) and 3(k) rotate clockwise, whereas lobes in Figs. 3(j) and 3(l) rotate counterclockwise.

2.4 Diverse Structured Light Beams after Transmission through Air–Core Fiber

Noting that the air–core fiber is a strongly guiding fiber (LP beams are not supported in air–core fiber), only free-space vector beams and OAM beams are coupled into the air–core fiber. By adjusting the divergence of such free-space structured light, the size match between focused structured light and ring-shaped fiber core can be accomplished. Hence, fifth to seventh OAM beams and vector beams can be coupled into the air–core fiber with losses <5 dB, as displayed in Fig. 4. Vector 1 to vector 4 represent four different vector beams generated in the interferometric loop (see S1 in the Supplementary Material for details).

The quality of output beam is another way to prove that accurate coupling of higher-order modes is accomplished in our scheme. We accordingly capture the intensity profiles of OAM beams and vector beams output from the 5-m air–core fiber using CCD2, as shown in Fig. 5. It can be seen from Figs. 5(a)–5(d) that *x*-polarized and circularly polarized

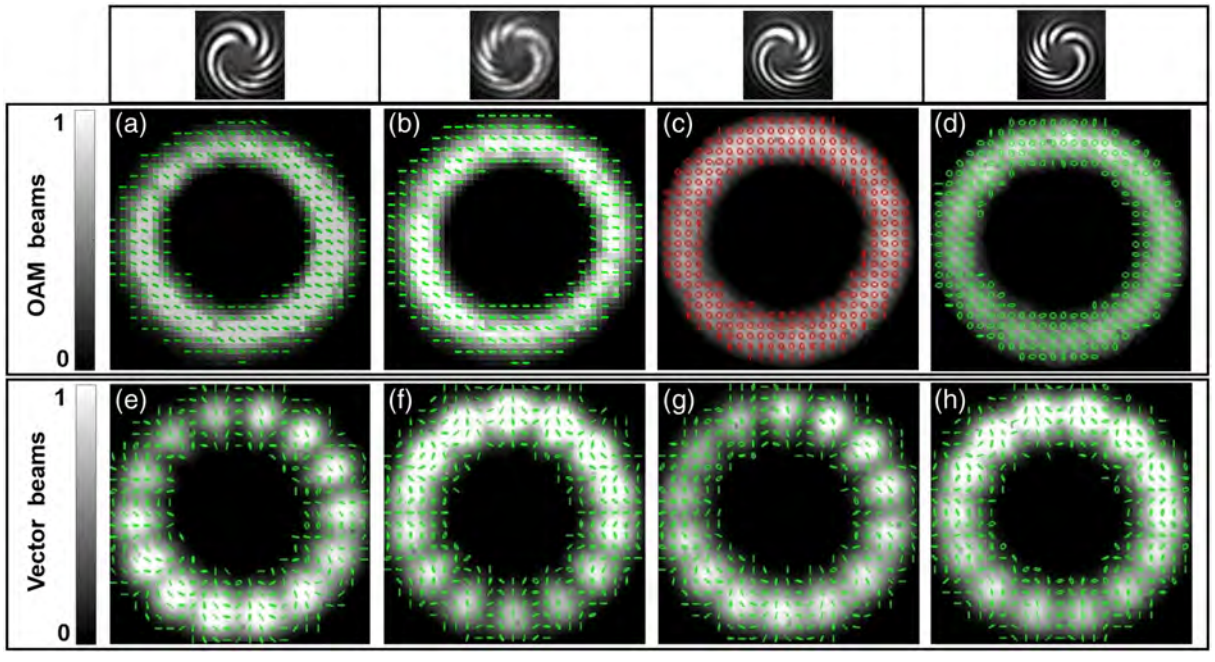

Fig. 5 Diverse seventh-order structured light beams after 5-m air–core fiber transmission, insets above figures (a)–(d) are their interference intensity profiles, respectively. (a), (b) *x*-polarized OAM beams; (c), (d) circularly polarized OAM beams; and (e)–(h) vector beams.

OAM beams still possess the same uniform polarization distributions after transmission of air–core fiber. In addition, all the interference intensity profiles of OAM beams and fundamental Gaussian beams are recorded, demonstrating the high purity of output OAM beams (see S8 in the Supplementary Material). For output vector beams, they still remain periodic polarization distributions, as shown in Figs. 5(e)–5(h). Polarization purity of the fiber-guided vector beams are also calculated, possessing an average polarization purity of 91.6% (92.9%, 90.8%, 91.1%, and 91.5%) for four different vector modes, respectively (see S9 in the Supplementary Material for details).

3 Conclusion

In summary, we propose and experimentally demonstrate a reconfigurable structured light beam generator. Diverse structured light beams, such as OAM beams, LP beams, and vector beams with controllable mode orders and sizes are generated in free space. For ring-shaped uniformly polarized OAM beams and ring-shaped nonuniformly polarized cylindrical vector beams, we measure the Stokes parameters of each point at the transverse plane to reconstruct the polarization distributions for distinguishing these two beams. In order to produce and transmit higher-order structured light beams in optical fiber, we couple the generated fifth- to seventh-order OAM beams and vector beams into 5-m air–core fiber. Low coupling loss (<5 dB for all supported modes) and high purity of structured light beams are obtained, further proving that we have produced and transmitted stable structured light beams in fiber.

There are already some other devices to generate structured light beams, including digital micromirror devices,[47] metasurfaces,[48] Q-plates,[49] and J-plates.[50] Digital micromirror devices are another kind of free-space device to tailor the spatial transverse structure of light beams, which might be used to replace the SLM in the interferometric loop. Although metasurfaces, Q-plates, and J-plates can also generate structured light with high robustness, they are usually not reconfigurable. Hence, the single-SLM Sagnac loop approach in this study takes advantage of both high robustness and reconfiguration. Such reconfigurable structured light beams generator may act as a useful scheme for various free-space and fiber-optic applications based on structured light beams, such as SDM communications, optical tweezers, optical sensing, superresolution imaging, and quantum optics.

Data Availability Statement

The data that support the findings of this study are available from the corresponding author upon reasonable request.

Acknowledgments

This work was supported by the National Natural Science Foundation of China (Grant Nos. 62125503 and 62261160388), the Key R&D Program of Hubei Province of China (Grant Nos. 2020BAB001 and 2021BAA024), the Key R&D Program of Guangdong Province (Grant No. 2018B030325002), the Shenzhen Science and Technology Program (Grant No. JCYJ20200109114018750), the Open Projects Foundation of State Key Laboratory of Optical Fiber and Cable Manufacture Technology (Grant No. SKLD2201), and the Innovation Project of Optics Valley Laboratory (Grant No. OVL2021BG004). The authors declare no conflicts of interest.

References

1. R. Essiambre et al., "Capacity limits of optical fiber networks," *J. Lightwave Technol.* **28**(4), 662–701 (2010).
2. R. Essiambre and R. W. Tkach, "Capacity trends and limits of optical communication networks," *Proc. IEEE* **100**(5), 1035–1055 (2012).
3. Y. Liang et al., "Experimental demonstration of visualized multi-core fiber coupling alignment system for inter-core cross talk measurement," *Opt. Lett.* **47**(12), 3071–3074 (2022).
4. G. Li et al., "Space-division multiplexing: the next frontier in optical communication," *Adv. Opt. Photonics* **6**(4), 413–487 (2014).
5. J. Wang, "Advances in communications using optical vortices," *Photonics Res.* **4**(5), B14–B28 (2016).
6. J. Wang et al., "Terabit free-space data transmission employing orbital angular momentum multiplexing," *Nat. Photonics* **6**(7), 488–496 (2012).
7. Y. Liang et al., "Adaptive turbulence compensation and fast auto-alignment link for free-space optical communications," *Opt. Express* **29**(24), 40514–40523 (2021).
8. N. Bozinovic et al., "Terabit-scale orbital angular momentum mode division multiplexing in fibers," *Science* **340**(6140), 1545–1548 (2013).
9. G. Zhu et al., "Scalable mode division multiplexed transmission over a 10-km ring-core fiber using high-order orbital angular momentum modes," *Opt. Express* **26**(2), 594–604 (2018).
10. J. Liu et al., "Direct fiber vector eigenmode multiplexing transmission seeded by integrated optical vortex emitters," *Light Sci. Appl.* **7**(3), 17148 (2018).
11. J. Zhang et al., "Mode-division multiplexed transmission of wavelength-division multiplexing signals over a 100-km single-span orbital angular momentum fiber," *Photonics Res.* **8**(7), 1236–1242 (2020).
12. H. Huang et al., "Mode division multiplexing using an orbital angular momentum mode sorter and MIMO-DSP over a graded-index few-mode optical fibre," *Sci. Rep.* **5**(1), 1–7 (2015).
13. Y. Liang et al., "2.6-km all-fiber orbital angular momentum (OAM) multiplexing link for data center networks (DCNs) using mode select coupler and commercial SFP+ transceivers," *presented at the CLEO: Sci. and Innov.* (2018).
14. A. Wang et al., "Directly using 8.8-km conventional multi-mode fiber for 6-mode orbital angular momentum multiplexing transmission," *Opt. Express* **26**(8), 10038–10047 (2018).
15. J. Zhang et al., "Orbital-angular-momentum mode-group multiplexed transmission over a graded-index ring-core fiber based on receive diversity and maximal ratio combining," *Opt. Express* **26**(4), 4243–4257 (2018).
16. H. Wang et al., "Low-loss orbital angular momentum ring-core fiber: design, fabrication and characterization," *J. Lightwave Technol.* **38**(22), 6327–6333 (2020).
17. P. Gregg, P. Kristensen, and S. Ramachandran, "Conservation of orbital angular momentum in air-core optical fibers," *Optica* **2**(3), 267–270 (2015).
18. K. Ingerslev et al., "12 Mode, MIMO-free OAM transmission," presented at *2017 Opt. Fiber Commun.Conference and Exhibit. (OFC)* (2017).
19. Q. Zhan, "Cylindrical vector beams: from mathematical concepts to applications," *Adv. Opt. Photonics* **1**(1), 1–57 (2009).
20. A. Forbes, M. de Oliveira, and M. R. Dennis, "Structured light," *Nat. Photonics* **15**(4), 253–262 (2021).
21. A. Rubano et al., "Q-plate technology: a progress review," *JOSA B* **36**(5), D70–D87 (2019).
22. M. Piccardo et al., "Roadmap on multimode light shaping," *J. Opt.* **24**(1), 13001 (2021).
23. H. Rubinsztein-Dunlop et al., "Roadmap on structured light," *J. Opt.* **19**(1), 13001 (2016).
24. Z. Xie et al., "Ultra-broadband on-chip twisted light emitter for optical communications," *Light Sci. Appl.* **7**(4), 18001 (2018).

25. M. Padgett and R. Bowman, "Tweezers with a twist," *Nat. Photonics* **5**(6), 343–348 (2011).
26. M. P. Lavery et al., "Detection of a spinning object using light's orbital angular momentum," *Science* **341**(6145), 537–540 (2013).
27. L. Fang, M. J. Padgett, and J. Wang, "Sharing a common origin between the rotational and linear Doppler effects," *Laser Photonics Rev.* **11**(6), 1700183 (2017).
28. Z. Wan et al., "Flexible and robust detection of a remotely rotating target using fiber-guided orbital angular momentum superposed modes," presented at *2020 Conf. Lasers and Electro-Optics (CLEO)* (2020).
29. Z. Wan et al., "Remote measurement of the angular velocity vector based on vectorial Doppler effect using air-core optical fiber," *Research (Wash D C)* **2022**, 9839502 (2022).
30. L. Yan, P. Kristensen, and S. Ramachandran, "Vortex fibers for STED microscopy," *APL Photonics* **4**(2), 022903 (2019).
31. J. Wang and Y. Liang, "Generation and detection of structured light: a review," *Front. Phys.* **9**, 263 (2021).
32. Y. Zhang et al., "Simultaneous entanglement swapping of multiple orbital angular momentum states of light," *Nat. Commun.* **8**(1), 1–7 (2017).
33. J. Liu et al., "Multidimensional entanglement transport through single-mode fiber," *Sci. Adv.* **6**(4), y837 (2020).
34. T. Wang et al., "Generation of femtosecond optical vortex beams in all-fiber mode-locked fiber laser using mode selective coupler," *J. Lightwave Technol.* **35**(11), 2161–2166 (2017).
35. Y. Zhao et al., "All-fiber mode converter based on long-period fiber gratings written in few-mode fiber," *Opt. Lett.* **42**(22), 4708–4711 (2017).
36. Y. Han et al., "Controllable all-fiber generation/conversion of circularly polarized orbital angular momentum beams using long period fiber gratings," *Nanophotonics* **7**(1), 287–293 (2018).
37. L. Wang et al., "Characterization of OAM fibers using fiber Bragg gratings," *Opt. Express* **22**(13), 15653–15661 (2014).
38. C. Maurer et al., "Tailoring of arbitrary optical vector beams," *New J. Phys.* **9**(3), 78 (2007).
39. H. Chen et al., "Generation of vector beam with space-variant distribution of both polarization and phase," *Opt. Lett.* **36**(16), 3179–3181 (2011).
40. S. Liu et al., "Generation of arbitrary spatially variant polarization beams with a trapezoid Sagnac interferometer," *Opt. Express* **20**(19), 21715–21721 (2012).
41. S. Li et al., "An efficient and robust scheme for controlling the states of polarization in a Sagnac interferometric configuration," *Europhys. Lett.* **105**(6), 64006 (2014).
42. P. Li et al., "Generation of perfect vectorial vortex beams," *Opt. Lett.* **41**(10), 2205–2208 (2016).
43. C. Yang et al., "Nonlinear frequency conversion and manipulation of vector beams in a Sagnac loop," *Opt. Lett.* **44**(2), 219–222 (2019).
44. P. Vaity and L. Rusch, "Perfect vortex beam: Fourier transformation of a Bessel beam," *Opt. Lett.* **40**(4), 597–600 (2015).
45. Z. E. Bomzon, V. Kleiner, and E. Hasman, "Formation of radially and azimuthally polarized light using space-variant subwavelength metal stripe gratings," *Appl. Phys. Lett.* **79**(11), 1587–1589 (2001).
46. G. Machavariani et al., "Birefringence-induced bifocusing for selection of radially or azimuthally polarized laser modes," *Appl. Opt.* **46**(16), 3304–3310 (2007).
47. K. J. Mitchell et al., "High-speed spatial control of the intensity, phase and polarisation of vector beams using a digital micromirror device," *Opt. Express* **24**(25), 29269–29282 (2016).
48. X. Yi et al., "Generation of cylindrical vector vortex beams by two cascaded metasurfaces," *Opt. Express* **22**(14), 17207–17215 (2014).
49. W. Ji et al., "Meta-q-plate for complex beam shaping," *Sci. Rep.* **6**(1), 25528 (2016).
50. Y. Huang et al., "Versatile total angular momentum generation using cascaded J-plates," *Opt. Express* **27**(5), 7469–7484 (2019).

Yize Liang received his BS degree from Huazhong University of Science and Technology in 2018. Currently, he is pursuing his PhD at Wuhan National Laboratory for Optoelectronics and School of Optical and Electronic Information at Huazhong University of Science and Technology. His research interests include structured light and multimode fibers.

Hongya Wang received his BS degree and his PhD from Huazhong University of Science and Technology in 2016 and 2023, respectively. He is currently an R&D engineer at the ZTE Corp. His research interests include intelligent optical transmission system and mode-division multiplexing over fibers.

Xi Zhang received his BE degree from Nanjing University of Technology, Nanjing, China. He is currently pursuing his PhD at Wuhan National Laboratory for Optoelectronicsand School of Optical and Electronic Information of Huazhong University of Science and Technology. His research interests include specialty passive optical fibers, active optical fibers, and high-speed optical communications.

Jianzhou Ai received his BS degree and master's degree from Huazhong University of Science and Technology in 2016 and 2019, respectively. He is currently an R&D engineer at Huawei Technologies Corp.

Zelin Ma received his BS degree from Sun Yat-sen University in 2015. Currently, he is pursuing his PhD in electrical engineering at High Dimensional Photonics Lab at Boston University. His research interests include light with orbital angular momentum in optical fibers for telecommunications.

Siddharth Ramachandran started his career at Bell Labs, and after a decade in industrial research labs, returned to academia, where he is currently a Distinguished Professor of engineering at Boston University. His work on the understanding and development of lightwave devices comprising spatial, vectorial and topological complexity have been applied in the fields of quantum computing, optical networks, brain imaging, as well as laser-based defense systems. For his contributions, he has been named a Distinguished Member of Technical Staff at OFS (2003), a fellow of Optica (2010), IEEE (2019), SPIE (2019), and APS (2022), an IEEE Distinguished Lecturer (2013 to 2015), a Distinguished Visiting Fellow of UK Royal Society of Engineering (2016), and a Vannevar Bush Faculty Fellow (2019). He serves the optics and photonics community in several capacities, including, currently, as a deputy editor for Optica.

Jian Wang received his PhD in physical electronics from Wuhan National Laboratory for Optoelectronics, Huazhong University of Science and Technology, China, in 2008. He worked as a postdoctoral research associate at the Optical Communications Laboratory, University of Southern California, United States, from 2009 to 2011. Currently, he is working as a professor at Wuhan National Laboratory for Optoelectronics, Huazhong University of Science and Technology, China. He is a vice director of Wuhan National Laboratory for Optoelectronics, Huazhong University of Science and Technology, China. He was elected as an OPTICA fellow (formerly OSA fellow) in 2020 and an SPIE fellow in 2022. He leads the Multi-dimensional Photonics Laboratory. His research interests include optical communications, optical signal processing, silicon photonics, photonic integration, orbital angular momentum, and structured light.

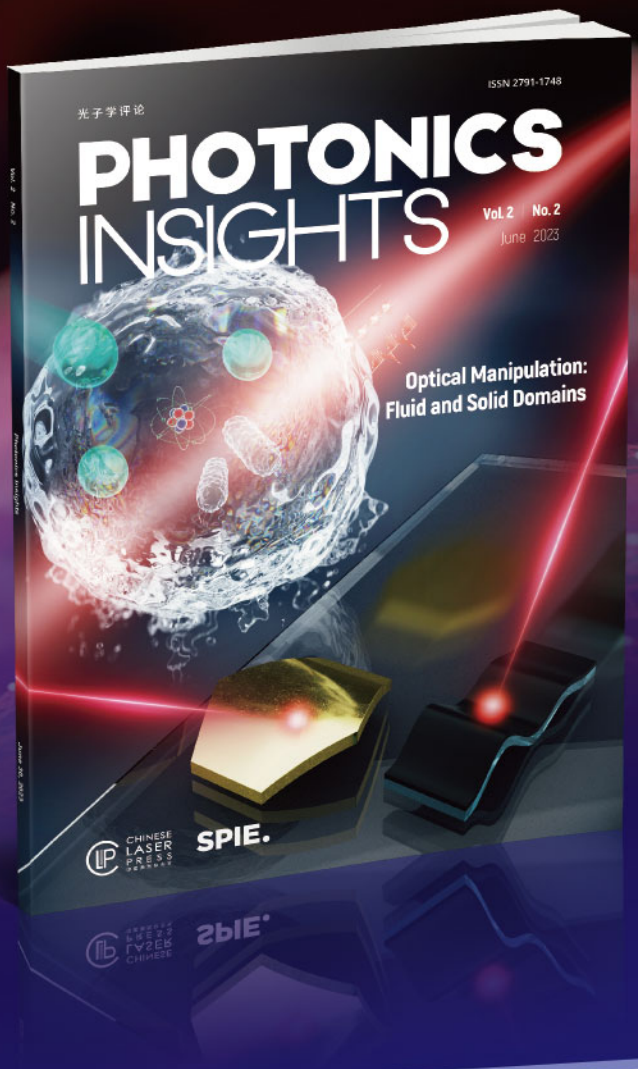

A high-quality, peer reviewed, diamond open access journal.

The first review journal in optics in China

PHOTONICS INSIGHTS

Co-Editors-in-Chief

Lei Zhou

China

Din Ping Tsai

China

Photonics Insights (PI) as a peer-reviewed, highly dedicated diamond open access review journal, co-published by Chinese Laser Press (CLP) and SPIE, and hosted by Shanghai Institute of Optics and Fine Mechanics (SIOM), Chinese Academy of Sciences. PI publishes high-quality, comprehensive review articles, mini review articles covering the whole area of optics and photonics and relevant interdisciplinary topics. It aims to be one of the best review journals in the world through publishing the best high-quality review articles in optics and photonics with academic leadership and guidelines.

SPIE.

CHINESE LASER PRESS 中国激光杂志社

http://www.photonicsinsights.org

http://pi.researching.cn